Heft 2011-2

Brazilian Test on Anisotropic Rocks – Laboratory Experiment, Numerical Simulation and Interpretation

von DINH, Quoc Dan

Freiberg 2011

Brazilian Test on Anisotropic Rocks - Laboratory Experiment, Numerical Simulation and Interpretation

Der Fakultät für Geowissenschaften, Geotechnik und Bergbau

der Technischen Universität Bergakademie Freiberg

eingereichte

DISSERTATION

zur Erlangung des akademischen Grades

Doktor-Ingenieur

Dr.-Ing.

vorgelegt

von Dipl.-Ing. DINH, Quoc Dan

geboren am 20.06.1972 in Vinh Phuc, Viet Nam

Gutachter: Prof. Dr.-Ing. habil. Heinz Konietzky , Freiberg

Prof. Dr.-Ing. habil. Jens Engel, Dresden

Prof. Dr.-Ing. Nguyen, Quang Phich, Hanoi

Tag der Verleihung: 02.09.2011

Acknowledgments

Abstract

The present work describes investigations on the anisotropic strength behavior of rocks in the splitting tensile test (Brazilian test). Three transversely isotropic rocks (gneiss, slate and sandstone) were studied in the Lab.

A total of more than 550 indirect tensile strength tests were conducted, with emphasis was placed on the investigation of the influence of the spatial position of anisotropic weakness plane to the direction of the load on the fracture strength and fracture or fracture mode. In parallel, analytical solutions were evaluated for stress distribution and developed 3D numerical models to study the stress distribution and the fracture mode at the transversely isotropic disc.

There were new findings on the fracture mode of crack propagation, the influence of the disc thickness, the influence of the applying loading angle and angle of the loading-foliation for transversely isotropic material.

Zusammenfassung

Inhalt der Arbeit sind Untersuchungen zum anisotropen Festigkeitsverhalten von Gesteinen beim Spaltzugversuch („Brasilianischer Test"). Laborativ wurden drei transversalisotrope Gesteine (Granit, Schiefer und Sandstein) untersucht.

Insgesamt wurden mehr als 550 Spaltzugversuche durchgeführt, wobei der Schwerpunkt auf die Untersuchung des Einflusses der räumlichen Lage der Anisotropieebene zur Richtung des Lasteintrages auf die Bruchfestigkeit und das Bruchbild bzw. den Bruchmodus gelegt wurde. Parallel dazu wurden analytische Lösungen zur Spannungsverteilung ausgewertet sowie numerische 3D-Modelle entwickelt, um die Spannungsverteilung sowie den Bruchmodus bei einer transversalisotropen Scheibe zu untersuchen.

Es wurden neue Erkenntnisse zum Bruchmodus, der Rissausbreitung, des Einflusses der Scheibendicke, dem Einfluss des Lasteinleitungswinkel sowie des Winkels Lasteintrag - Anisotropieebene für transversalisotropes Material gewonnen.

Table of Contents

List of Figures

List of Tables

Introduction

The Brazilian tensile strength test is a well-known indirect method of determining the tensile strength of rocks and other brittle materials using a circular plane disc under diametral compression. The Brazilian tensile strength test or the so-called splitting tensile test is widely applied in rock engineering because specimens are easy to prepare, the test is easy to conduct and uniaxial compression test machines are quite common.

The Brazilian test was developed in 1943 [1] and has found application mainly in investigations of homogeneous rocks; only a few studies covering tensile strength of anisotropic rocks. Theories relating to evaluation of the test results are still limited because full-field expressions of the stress-strain components and the anisotropic failure mechanisms have yet to be investigated in detail.

Based on these reasons, this work aims at assessing the influence of strength anisotropy on the measured peak strength in the Brazilian test. The test was carried out on a large number of four different types of rock samples ranging from isotropic to anisotropic. It was done parallel to "numerical laboratory tests" so as to evaluate both the characteristics and the influencing factors.

Importance and application of tensile strength

Besides compressive or shear strength, the tensile strength is a key parameter for determining the load bearing capacity of rocks, their deformation, damage and fracturing, crushing, etc. and is used in to analyze the stability and serviceability of rock structures. Tensile strength plays an important, often the most important role, because rocks are much weaker in tension than in compression.

(a) Tension cutoff   (b) Tension region
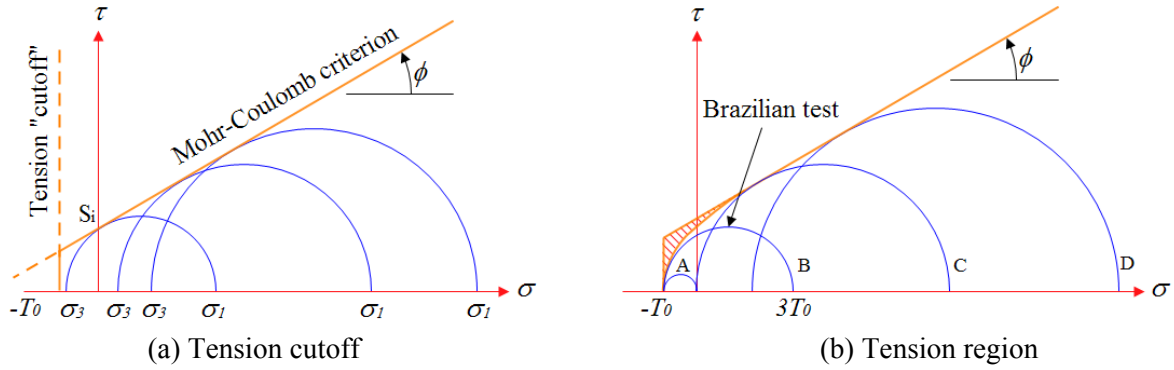
Figure I-1: 'Tensile strength" as illustrated by the Mohr-Coulomb failure criterion (a) Mohr-Coulomb failure criterion with a tension cut-off T_0 and cohesion S_i; (b) Comparison of empirical failure envelope and Mohr-Coulomb criterion with tension cut-off. (after Goodman [2]).

Tensile strength is frequently used as input parameter in many applications in civil engineering, mining and petroleum engineering.

Anisotropic rocks

Intact rock and rock mass are characterized by different degrees of heterogeneity and anisotropy depending on whether the rock is of igneous, sedimentary or metamorphic origin. The degree of anisotropy (aelotropy) of a particular rock type is shown by such defined by the presence of fabric elements such as bedding, stratification, layering, foliation, fissuring, or jointing. Evaluating the anisotropic properties helps predict the behavior of rock materials in the analysis, design and construction phases and improves on the quality and safety of these processes [3, 4]. Therefore, methods of determining the strength and deformation of anisotropic rocks in the laboratory and in situ have increasingly gained attention in recent years. However, rock anisotropy and its implications are still poorly understood in both theory and practice.

Objective of this work

Tensile strength of anisotropic rocks largely depends on the anisotropic character of the rock and especially on the orientation of the planes of rock anisotropy relative to the loading direction. The objective here is to combine experimental, analytical and numerical methods in order to determine the indirect tensile strength of intact rocks with anisotropic

properties varying from isotropic to transversely isotropic. Special attention is to be paid to both physical and geometrical numerical simulations using different constitutive laws and model parameters. The numerical simulation results are to be compared with results of lab tests and then analyzed in detail. Finally, recommendations for the practical application of the Brazil test and the correct interpretation of the test results are to be given.

Scope of work

This research encompasses the conventional Brazilian test used to determine indirect tensile strength by diametral compressive loading of a disc between two-plates of a compressive test machine, as proposed by the International Society of Rock Mechanics [5]. The validity of diametral compression tests for indirect measurement of tensile strength is investigated theoretically and experimentally. Well-designed tests are conducted on sandstone, gneiss and slate and the experimental results compared with theoretical predictions. The research focuses on investigating the influences of anisotropy on the test results. Numerical analyses are also done in order to investigate the effects of the boundary conditions, loading angle and sample size. Anisotropic elastic-plastic constitutive laws are used to investigate the failure process in detail and to estimate the tensile strength of the rock.

Research procedure

A combination of experimental tests and numerical simulation was undertaken so as to achieve the abovementioned research goals. In the light of this, two main aspects have been distinguished in the methodology of this thesis:

1. Well-designed laboratory experiments which carefully test all the bedding-plane orientations and loading directions of both isotropic and anisotropic specimen.
2. Numerical simulation of such underlying mechanical processes as damage, fracturing, failure and plastifications taking into account, different orientations of the weakness planes in relation to the loading direction.

Significance of the work

Firstly, characterizing anisotropic rocks is to be completely and systematically investigated in both laboratory experiments and numerical simulations of the Brazilian tensile strength test.

Secondly, the planes of weakness are to be explicitly simulated by laminated planes (smeared-crack model) which enable distinction, both in tension and in compression, between failure inside the rock matrix and along the planes of weakness. It will be the first time that the failure behavior of such an anisotropic rock was comprehensively investigated in 3-dimensional during the Brazilian test.

Layout

The thesis is structured into mainly three sections. The first section, Chapters 1 and 2, contain the theoretical background and a comparison between the elastic theory and the analytical and numerical solutions as a means of evaluating the Brazilian test. The second section, Chapter 3, documents the Brazilian tests as carried out on sandstones, gneisses and slates. The last section, Chapters 4 - 5, focuses on detailed numerical simulations and comparisons with results from lab tests. This is the most important section of this thesis because it presents:

(I.)   Several proposals explaining observations of the experimental results and

(II.)   Conclusions and recommendations on how to perform and evaluate the Brazilian tests on anisotropic materials.
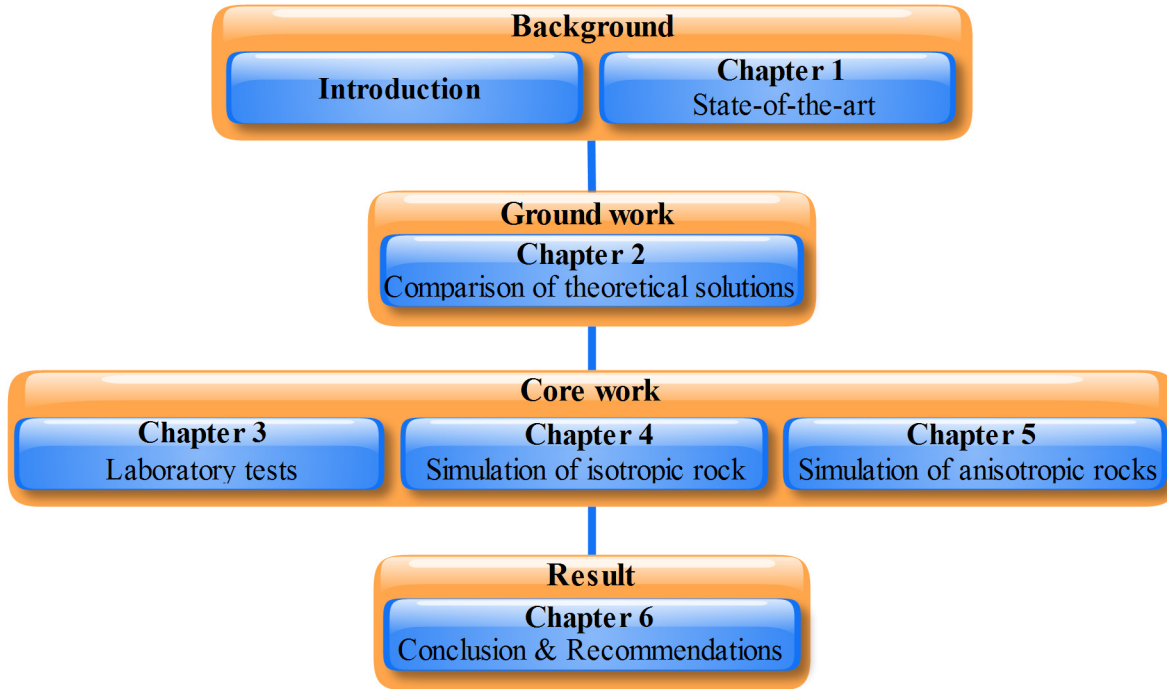
Figure I-2: Thesis structure.

The work presented in this thesis is subdivided into the following chapters Figure I-2:

Chapter 1 highlights the theoretical background of the research. It presents literature review of the tensile strength test (State-of-the-Art) and defines the background and main aspects of this work, specially focusing on the conventional Brazilian test on anisotropic rocks. This chapter also defines terms and notations used throughout the work.

Chapter 2 deals with the analytical and semi-analytical 2- and 3-dimensional mathematical formulations of the elastic stress distribution inside the disc under diametral compressive strip loading.

Chapter 3 describes the lab experiments and discusses the results obtained. Laboratory tests for determining strength and deformation parameters can be divided into dynamic and static methods. The ultrasonic pulse test, uniaxial and triaxial compression tests, and a series of Brazilian tensile tests provide information on geomechanical properties which are used later as input parameters for numerical analyses. A total of 555 Brazilian tests were conducted on four different types of rocks: sandstone, slate and gneiss. The choice of these four rock types should help highlight the whole spectrum of isotropic to anisotropic characteristics of these materials.

Chapter 4 contains numerical simulations of isotropic rocks; to be exact, of the Postaer Sandstone from Pirna in Saxony, Germany. Also highlighted here are factors such as size effect, loading area, etc and material properties like Young's modulus and Poisson's ratio which affect the results.

Chapter 5 focuses on the numerical simulation of anisotropic rocks, in this case, the Freiberger and Leubsdorfer Gneisses from Saxony and the Mayen Mosel-Slate from Rheinland-Pfalz, all in Germany. Numerical 3D-models using FLAC^{3D} - *Fast Lagrangian Analysis of Continua in 3 Dimensions* [6] were used to investigate the stress-strain field and failure pattern under consideration of different orientation planes of weakness in relation to loading direction. The numerical analyses reveal failure modes of the disc and the differences in strength between the lab test procedure and the simulation results when taking into account the anisotropy associated with foliation and orientation of the weakness planes.

Chapter 6 reflects evaluation of the splitting tensile strength of anisotropic rocks, makes recommendations on experimental test procedures and gives back final conclusions arrived from the study and briefly explains further research possibilities.

Chapter 1

State of the art

1.1 Review of the Brazilian tensile strength test

1.1.1 General overview

The Brazilian tensile strength test, also called the 'splitting tensile test' or 'indirect tensile test', is a plane disc test used to determine tensile strength, especially of quasi-brittle materials such as concrete or rocks whose compressive strength are much higher than their tensile strength. The easy sample preparation and simple test procedure have made the Brazilian test a highly useful and popular experimental method. Under uniform distributed loading along two symmetric peripheral arcs, a sample fails either in tensile or tensile-shear mode [3, 7-9]. A nearly bi-axial (compressive in vertical and tensile in horizontal) stress state develops along the diametral line through the center of the sample. Theoretically, the tensile failure occurs along the loaded diameter, splitting the disc (or cylinder) into two halves [8].
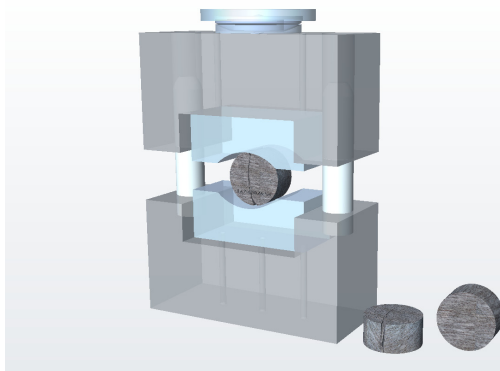
(a) Experimental set-up   (b) Splitting in a sandstone specimen

Figure 1-1: The Brazilian test as proposed by ISRM [5].

Today, the Brazilian tensile strength test is a major standardized test method internationally recommended by ASTM D3967-08 [10], BS EN12390-6 [11], Recommendation Nr.10 of

the German Society of Geotechnical Engineering (DGGT) [12] and the ISRM-recommendations in particular [5]. Brazilian test procedures and specimen preparations as specified by ASTM, DGGT and ISRM show a few but differences. ISRM and DGGT suggest a special test apparatus hold the specimen whereas ASTM recommends placing cardboard or plywood between the plates and the specimen to reduce stress concentrations where forces are applied as at the boundary areas. The advantage of the ISRM and DGGT recommendations is that the loading angle (2α) develops automatically.

Determining tensile strength by the direct tension test ranks amongst the most difficult test methods. Several technical difficulties originate from fragmentation whilst gripping and then applying the load parallel to the axis of the specimen so as to avoid development of bending or torsion moments caused by misalignment [13, 14]. These difficulties lead to replacement of the direct tension test by simpler ones; example the diametral compression test on discs and rings, the three- or four-point bedding test, the hydraulic tension and the diametral compression tests on cylinders or cubes. Obviously, the stress state during these tests is far from the one theoretically characterized as uniaxial, hence the results obtained often subject to serious criticisms. Besides, many such brittle materials as rocks have non-linear stress-strain characteristics in reality, their inherent defect structures having dimensions not much smaller than certain dimensions of the test specimens. Thus, there are serious discrepancies between theoretical and actual behavior [7].

The Brazilian test also has grave disadvantages, nonetheless. The expansion of the contact loading area completely depends on the deformation (stiffness) of the specimen. It is therefore important to specify or measure the form of the loading area. In addition, frictional effects at the point of contact between the loading plates and the sample have to be taken into account in laboratory tests.

(a) simple tension   (b) compression and tension
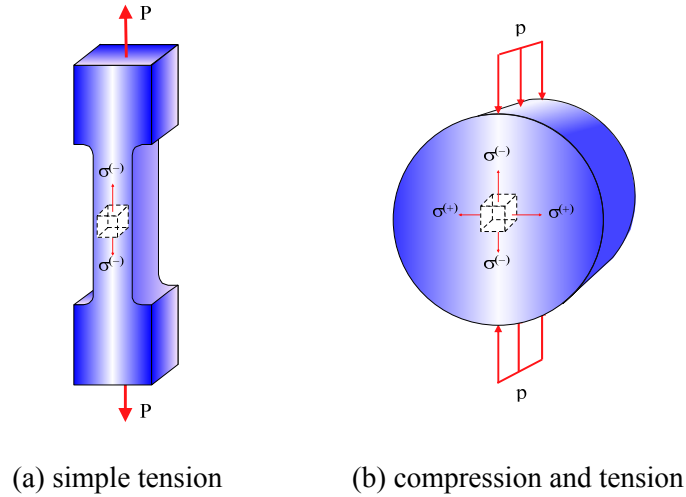
Figure 1-2: Basic physical models characterizing the mechanical behavior of materials: (a) direct tensile strength test with dogbone-shaped specimen and (b) the conventional Brazilian test [15].

In spite of all this, the Brazilian tensile strength test remains a simplified and widely used method of testing rocks and other brittle materials. And as the name implies, especially in determining tensile strength of anisotropic materials, though recent developments have enabled determinations of fracture toughness and elastic modulus as well [3]. In principle, the stress field, which induces tensile failure when the disc is compressed diametrally, can be fully determined, provided the material is linear elastic, homogeneous and isotropic up to the point of failure.

1.1.2   Development of the Brazilian tensile strength test

The Brazilian test was first introduced by Professor Carneiro, a Brazilian, who invented the splitting tensile test for measuring the tensile strength of concrete in 1943 [1]. He observed that concrete fractures develop almost in a vertical plane connecting the line of contact between the cylindrical specimen and the compression plates. This observation brought up the idea of developing a test that could be performed on cylinders. Using simple formulas based on the elasticity theory, Carneiro developed a procedure to deduce the tensile strength based on measured peak load at failure. At about the same time, Akazawa also presented a similar method [16]. The Brazilian test has been researched by many scientists from all over the world ever since then.

In 1978, the International Society of Rock Mechanics (ISRM) suggested the method be used for determining indirect tensile strength [5]. The justification here being that experimentally, most rocks in biaxial stress fields fail in tension if one principal stress is tensile and the other finite principal stress compressive, with a magnitude not exceeding a threefold of the tensile principal stress. This suggestion is still useful today and finds application in laboratories all around the world. It can be said thus, that the ISRM-suggestion has had a significant impact on the development of the Brazilian tensile test.

Before the proposal of the ISRM

Long before the ISRM-suggestion, the Brazilian disc test had been investigated by many scientists [6, 17-30] and various points of criticism discussed in relation to the data obtained therewith and those from direct tension tests. Berenbaum and Brodie [17] assessed this test and indicated its superiority in the light of its simplicity and usefulness as in material property determinations like anisotropic tensile strength. Hondros [18] proposed an analytical solution of the problem for a thin disc, assuming that the material is homogeneous, isotropic and linear elastic and the load distribution is along two symmetric finite arcs at the periphery of the specimen. He derived the complete stress field by using the series expansion technique and compared his solutions with experimental data on cement mortars and concrete. Fairhurst [19] analyzed the failure of specimen based on a Griffith-type fracture criterion. He indicated that when materials have low compression to tension ratios, the initial failure might occur away from the center of the disc for small angles in loading contact areas. Fairhurst concluded that the tensile strength of a rock with a compressive to tensile strength ratio of 8 would be underestimated by 30% especially for a plate contact width of $2\alpha \approx 15°$. Hobbs [20] proposed using specimens with a small hole at the centre as a modification of the Brazilian disc test so as to mitigate some of the drawbacks of the conventional test. His results are also presented in a study on the relationship between tensile strength and lamination orientation and that between uniaxial compressive strength and tensile strength for laminated and massive rocks. Hooper [21] examined the influence of the tensile stresses in the contact region and the frictional effects at the interface. Hooper's results showed that Hondros' two-dimensional analysis predicts the presence of exclusively compressive stresses at the contact area and that fracture always initiates at the contact surface and not within the disc as suggested by conventional theory.

This phenomenon is caused by the three-dimensional stress state in the contact region and by the frictional effects at the interface.

After the ISRM proposal

Since the ISRM proposal, the Brazilian disc test has undergone intensive research by many authors [3, 13, 15, 22-35]: Wijk (1978); Nova et al. (1990); Guo et al. (1993); Andreev (1995); Chen et al (1998); and recently [8, 9, 36-51] as Sarris et al. (2005); Ma and Hung (2008); Lanaro et al. (2008); Ma et al. (2008); Kwaśniewski (2009); Markides et al. (2010); Tang et al. (2010), to name a few. In order to take the effect of other factors such as the influence of the loading device or the anisotropy of rocks or rock-like materials into account, many suggestions relating to the experimental procedure and the shape of the specimens, as well as new analytical or numerical solutions for the stress-strain field have been proposed [3, 33, 43, 46, 50-53]. Especially noteworthy are, the more recent studies by Amadei (1996); Hakala et al. (2007); Ke et al. (2008); Shahnazari et al. (2010); Tavallali et al. (2010); Markides et al. (2010) are notable. Most recent studies were conducted with the aid of the Finite Element Method (FEM), the Boundary Element Method (BEM) and the Discrete Element Method (DEM) [36, 38, 45, 47, 54]. These methods have given a better understanding of the test by explicitly illustrating the stress- and strain field at any point inside the specimen.

1.1.3   The Brazilian tensile strength test on anisotropic rocks

Anisotropy is a typical characteristic of intact foliated metamorphic rocks (slates, gneisses, phyllites, schists) and intact laminated, stratified or bedded sedimentary rocks (shales, sandstones, siltstones, limestones, coal, etc.) [55, 56]. The anisotropy results from complex physical and chemical processes associated with transportation, deposition, compaction, cementation, etc. In these rocks, the fabric can be expressed in different ways. It is worthy to note that rocks which have undergone several formation processes, may present more than one direction of planar anisotropy such as foliation and bedding planes in slates. These rocks tend to split into planes as a result of the parallel orientation of microscopic grains of mica, chlorite or other platy minerals [3]. The majority of the discs tests confirm that failure along the loaded diameter largely depends on the microstructure.

Rock anisotropy plays an important role in civil, mining and petroleum engineering, especially in terms of the following aspects [57]:

> ➢ Long- and short-term stability of underground structures (tunnels, caverns, shafts and other openings);
> ➢ Determination of excavation methods (drill-and-blast or TBM and raise-boring);
> ➢ Design of rock support systems;
> ➢ Prediction of rock bursts;
> ➢ Thermo-hydro-mechanical behavior of the rock;
> ➢ Design of grout methodology;
> ➢ Fluid flow and contaminant transport;
> ➢ Fracturing and fracture propagation.

Stress state and failure envelop including tensile strength are necessary as input values for the above mentioned engineering tasks. However, determination of the tensile strength of anisotropic rock is still untrod territory; particularly, when the load directions and bedding-planes are inclined to each other, the stress- and strain field can not be obtained by analytical solutions and the influence of anisotropy on the tensile strength remains an unsolved problem. In fact, combining experimental, analytical and numerical methods in order to analyse the results of the Brazilian test for intact foliated metamorphic and intact laminated, stratified or bedded sedimentary rocks has yet to be undertaken.

1.1.4   Summary

The Brazilian test is widely used in engineering to indirectly obtain the tensile strength of rocks and rock-like materials, thanks to its practicality in the way of specimen preparation and simple test procedure. The Brazilian test has been constantly updated by new theories and experimental techniques for many years now, both in relation to its dependence on the foliation angle, loading methods and in combination of analytical and numerical solutions for continuous and discontinuous, homogenous and inhomogeneous, isotropic and anisotropic, elastic and plastic media. Nevertheless, many questions still remain to be answered especially in its evaluation of strongly anisotropic rocks.

1.2   Analytical aspects

The splitting tensile test is based on the fact that tensile stresses developed when a circular solid disc is compressed between two diametrally opposed forces. The maximum tensile stress develops perpendicular to the loading direction and is proportional to the applied load. Results of the test largely rely on the important hypothesis that fracture is initiated by tensile stresses. Because failure occurs along the diametral plane of the applied load, it is commonly assumed that the nominal tensile stress causes the disc to fail.

Simulation results obtained by FLAC^{3D} for homogeneous material also confirm that plastifications occur at areas near the applied load and at the center of the disc. The intensified tensile stresses towards the applied load are greater at the center than at any other point. Therefore, failure is initiated at the center of the disc. Simulations done by other authors yielded similar results [36, 58].

Besides, the strength values obtained in diametral compression tests are often much lower than those obtained in other uniaxial, three- and four-point bending and direct tensile tests. The reasons for these differences could be [59]:

> ➤ The formula used for calculating the tensile strength relative to the load is based on the assumption that the material behavior follows Hooke's law. However, many quasi-brittle materials do not exactly follow Hooke's law.
> ➤ Quasi-brittle materials obey the maximum tensile strain criterion rather than the maximum tensile strength criterion.

In addition, the initial crack is not always observed at the center of the disc as implied by theoretical solutions. Some authors [21, 60] believe that failure is initiated under the load points or somewhere near the center. Because of this, disagreements on the true mechanism of failure have ensued. The results of numerical simulations obtained by FLAC^{3D} for gneiss and slate under different orientations of the planes of weakness to the loading direction indicate the important role of anisotropy in strength determinations and failure patterns. Similar conclusions have also been drawn by other authors like Chen [39], Yu [61] and Markides [62], etc..

1.2.1   Hypotheses for the conventional Brazilian test

The determination of tensile strength for brittle materials assumes that the material is homogeneous, isotropic and linearly elastic. The first theoretical solution was obtained in 1881 by Hertz. An enhancement, accounting for the uniform distribution of the load over strips of finite width, was made by Hondros in 1959 [18].

(a) Brazilian   test,   showing   notations used

(b) Stresses along the cross sectional line YY' for a Brazilian test with strip load angle $\alpha = \tan^{-1}\frac{1}{12}$
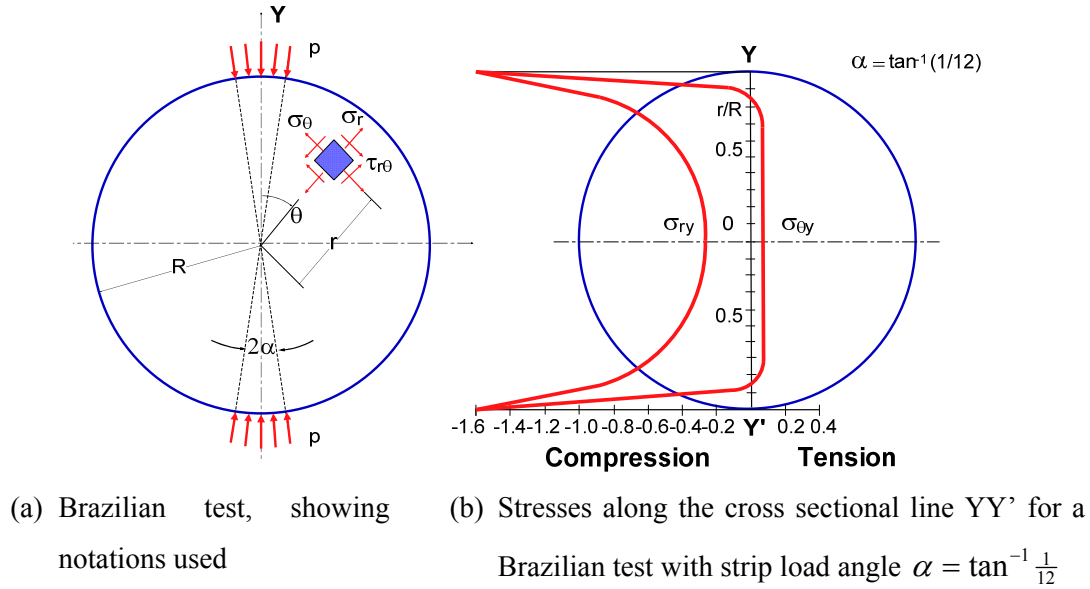
Figure 1-3: Stress distribution inside a thin disc under uniform radial pressure applied over a small arc of the circumference at each end of the diameter (after Hondros [18]).

In Figure 1-3, the compression (p) induces tensile stresses $\left(\sigma_{\theta y}\right)$ which are nearly constant over a large part in the inner area of the sample. The tensile strength is calculated based on the assumptions that failure occurs at the point of maximum tensile stress (i.e. at the center) and that the radial compressive stress $\left(\sigma_{ry}\right)$ has no influence on the failure [19].

From these observations, the Brazilian tensile test assumes the following:

➢ Rocks in biaxial stress states fail in tension when their uniaxial tensile strength is exceeded by the tensile principal stress.

➢ The compressive principal stress has a magnitude, which does not exceed a threefold of the tensile principal stress and does not therefore, produce shear failure.

> ➢ The failure is governed by the Griffith criterion or the maximum tensile stress criterion when the initial point of crack is at the center of the disc. This means that, this criterion is valid only as long as the compressive strength of the rock is greater by far than its tensile strength [63].

Under these assumptions, the fundamental mathematical problem in emulating a real experiment is, achieving linear elasticity for a solid disc. The exact center of the disc is the only point where the conditions for tensile failure are met. The principal stresses there are:

$$\sigma_{\theta y} = +\frac{2p}{\pi}(\sin 2\alpha - \alpha) \cong \frac{2p\alpha}{\pi} \qquad (1.1)$$

When α is small $(\alpha < D/10)$ and (r/R) approaches zero, then $\dfrac{P}{Dt} = p\alpha$

substituting this in Eq. (1.1) yields:

$$\sigma_{\theta y} = \frac{2P}{\pi Dt} \qquad (1.2)$$

$$\sigma_{ry} = -\frac{6P}{\pi Dt} \qquad (1.3)$$

and $\sigma_{ry} = -3\sigma_{\theta y}$ (1.4)

Following Fairhurst [19], the error introduced by using the approximate expression $\sigma_{\theta y}$, with an arc contact $2\alpha \approx 15°$, is 2%.

In reality, Eq. (1.1) is a function of p, α and t. According to the ISRM proposal [5], the contact length between the disc and the loading jaws is considered a finite arc rather than a single point. It is also assumed that the contact between the disc and the loading jaws can be simulated by uniform radial compressive pressure acting on two arcs of the perimeter of the disc, symmetric to its center. The only stress acting on the contact area is radial compressive. Any frictional forces created at the disc–jaw interface can be ignored. And, the problem can also be considered as a state of plane stress.
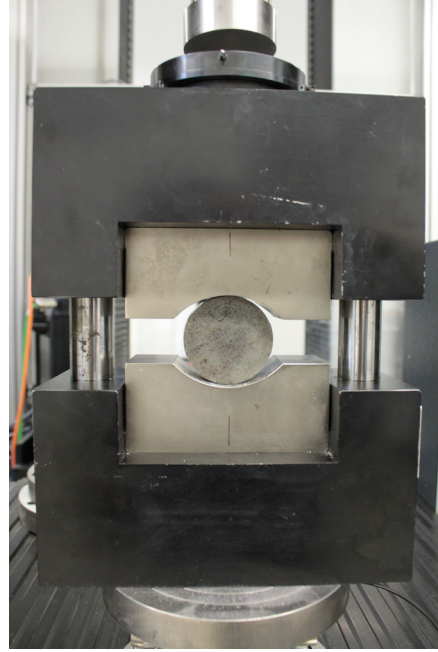
Figure 1-4: Loading jaws in a Brazilian test equipment (after ISRM [5]).

1.2.2   Failure criteria

Rock materials are usually weaker in tension and comparatively stronger in compression, so cracking or failure often occurs essentially in tension. The foregoing relationships give the stress distribution along the lines where cracks are known to initiate and propagate. However, in order to decide where failure begins in a real material, it is necessary to introduce a failure criterion, i.e. a characteristic relationship between the principal stresses at failure.

Mohr-Coulomb failure criterion

The Mohr-Coulomb failure criterion is the simplest and best-known criterion for failure of rocks. As shown in Figure I-1:(a, b), the Mohr envelope touches all the Mohr circles which represent critical combinations of principal stresses. The ultimate equilibrium in terms of normal and shear stresses on the failure plane is represented by the envelope tangent to the Mohr circle.

$$\tau_p = S_i + \sigma \tan \phi \qquad\qquad (1.5)$$

Eq. (1.5) can be interpreted as follows. Failure occurs when the actual shear stress τ_p, diminished by the frictional resistance associated with the normal stress on the failure plane

is equal to shear strength S_i. On the plane of failure, the minimum principal stress σ_3 can be tensile as long as σ_1 remains compressive. Other theories of failure (e.g., the Griffith theory) describe the tensile failure region in more detail. The Mohr-Coulomb criterion is derived by extrapolating the Mohr-Coulomb line into the tensile region up to the point where σ_3 becomes equal to the uniaxial tensile strength $-T_0$. The minor principal stress can never be less than $-T_0$ [2].

In Figure I-1:(a, b), a "tension cutoff" superimposed on the Mohr-Coulomb criterion is taken as a constraint for the failure criterion. The actual envelope of critical Mohr's circles with one negative principal stress lies beneath the Mohr-Coulomb criterion (Figure I-1:(b)). Consequently, it is necessary to reduce the tensile strength $-T_0$ and the shear strength intercept S_i when applying this simplified failure criterion to any practical situation.

Griffith failure criterion

Although the Mohr-Coulomb criterion is easy to handle practically, the Griffith theory delivers a more precise criterion of failure for any rock when the envelopes are fitted to Mohr's circles. The Griffith theory of failure predicts a parabola in the tensile stress region. This theory assumes the presence of randomly oriented fissures which create local stress concentrations and new cracks. However, the Griffith theory does not hold physically regions where both principal stresses are compressive. Jaeger and Cook (1976) and Hoek (1968) demonstrated that the failure envelopes for most rocks lie between a straight line and a parabola.

It is generally accepted that the Griffith failure criterion is the most satisfactory explanation for the fracture of brittle materials. According to this criterion, failure occurs when:

$$\sigma_3 = \sigma_T \quad where \quad \sigma_1 + 3\sigma_3 \geq 0 \tag{1.6}$$

and: $\quad \left(\sigma_1 - \sigma_3\right)^2 = 8\sigma_T\left(\sigma_1 + \sigma_3\right) \quad if \quad \sigma_1 + 3\sigma_3 \leq 0 \tag{1.7}$

Where σ_1 is the major principal stress, σ_3 the minor principal stress, and σ_T the uniaxial tensile strength of the material (tension positive) and the intermediate principal stress σ_2 is assumed as having no influence on failure. It is usually assumed that failure occurs in accordance with conditions in Eq. (1.6), thus initiating at the center of the disc. Fairhurst

generalized the Griffith criterion to account for the variations in *n, the* uniaxial compression/tension strength ratio. The rate may vary considerably from the theoretical value *n=8* implying that in practice, the conditions for failure may not conform to the simplified Griffith criterion [7].

Hoek-Brown failure criterion

The criterion starts from the properties of intact rocks and then introduces factors that reduce these properties based on the joint characteristics in a rock mass.

Applying the Mohr-Coulomb failure criterion, the rock mass strength is defined by the cohesive strength *c'* and the friction angle ϕ', the relationship between the major and minor principal stresses linear. Meanwhile, this relationship is non-linear in the Hoek-Brown criterion [64]. Moreover, determining *c'* and ϕ' for disturbed in-situ rock masses is difficult.

The generalized Hoek-Brown criterion is expressed as [65]

$$\sigma_1' = \sigma_3' + \sigma_{ci}\left(m_b \frac{\sigma_3'}{\sigma_{ci}} + s\right)^a \tag{1.8}$$

where m_b is a reduced value of material constant m_i and is given by

$$m_b = m_i \exp\left(\frac{GSI - 100}{28 - 14D}\right) \tag{1.9}$$

s and *a* are constants of the rock mass given by the following relationship:

$$s = \exp\left(\frac{GSI - 100}{9 - 3D}\right) \tag{1.10}$$

$$a = \frac{1}{2} + \frac{1}{6}\left(e^{\frac{-GSI}{15}} - e^{\frac{-20}{3}}\right) \tag{1.11}$$

D is a factor which depends on the degree of disturbance to which the rock mass has been subjected by blast damage and stress relaxation. It varies from 0 for disturbed in situ rock masses to 1 for very disturbed rock masses. And, GSI is the value of the **G**eological **S**trength **I**ndex of the rock mass.

The empirical uniaxial compressive strength is obtained by assuming $\sigma_3' = 0$ in Eq.(1.8):

$$\sigma_c = \sigma_{ci}.s^a \tag{1.12}$$

The empirical tensile strength is obtained by assuming $\sigma_1' = \sigma_3' = \sigma_t$ in Eq.(1.8):

$$\sigma_t = -\frac{s\sigma_{ci}}{m_b} \tag{1.13}$$

1.2.3 Crack initiation and propagation

One of the assumptions of the conventional evaluation of the Brazilian test is that the crack should initiate at the disc center during loading and then propagate along the loading diameter [5, 12]. In fact, the crack initiates in regions other than the center of the disc, for example somewhere near the load arc or especially along weak planes in transverse anisotropic rock specimens (Figure 1-5).
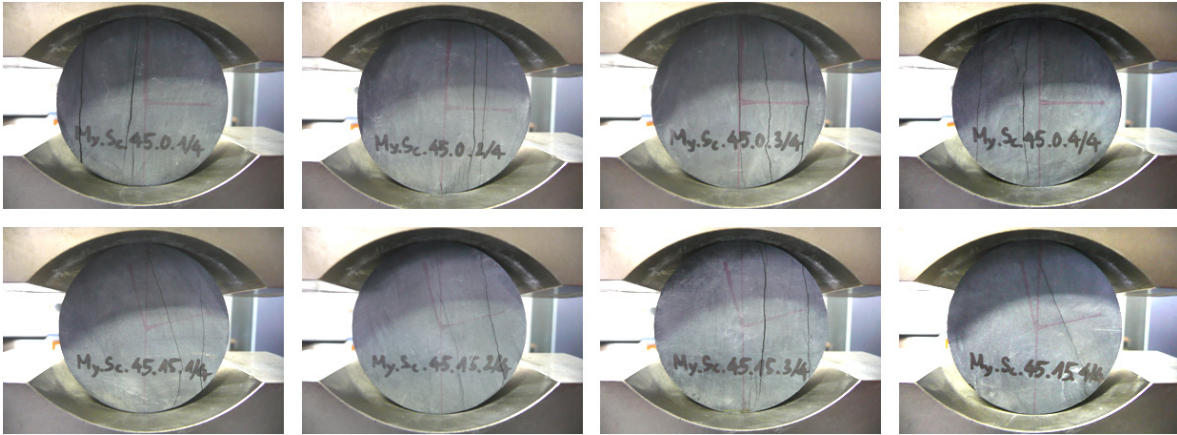
Figure 1-5: Some typical fracture patterns in the slates at orientation angle (ψ) 45^0 and foliation-loading angles (β) 0^0 and 15^0 (for My.Sc.45.0 & My.Sc.45.15, respectively).

As indicated in Figure 1-5, the fractures do not always go through the center and separate the disc in two halves, as the simple theory predicts. Details of fracture patterns are given in Chapter 3 and Appendices 3.1, 3.2, 3.3 and 3.4.

Fairhurst [19] first discussed the validity of the Brazilian test. Based on results obtained from tests with different loading angles (2α) he suggested that failure might occur away from the center of the test disc for small angles in the loading contact area. Intensive local stress concentrations inside the sample may exceed such a level that cracks initiates and propagation of relatively small cracks starts. With larger loading angles, e.g. $2\alpha \approx 15°$, the

deduced tensile strength becomes more representative of the whole specimen rather than the strength of one single point in it.

The intact continuum is assumed to be flawless. In this model, failure can be initiated either when the tension or shear failure criterion is reached. It is known meanwhile that in anisotropic rocks, material heterogeneity generates local stress concentrations at micropores of flaws causing tensile or shear crack development when the critical stress intensity is reached locally. Fracture toughness of rocks, one of the basic material parameters in fracture mechanics, is defined as the resistance to crack propagation. In other words, fracture toughness can also be defined as the critical value of the stress intensity factor (SIF) when a crack propagates. There are three stress intensity factors which correspond to three basic fracture modes - opening, sliding and tearing. Most of the previous studies on rock fracture mechanics have mainly focused on the opening mode fracture (mode-I) until now. Investigations into sliding and mixed-mode fractures are limited in literature [28, 46]. In general, fracture toughness is greatly influenced by the microstructural properties of anisotropic rocks. Mode-I fracture toughness is highest when measured orthogonal to a bedding plane (i.e. weakness plane) and is lowest for cracks propagating along the bedding plane.

Rock materials are characterized by grain, pore and crack structures, so that they can only be considered as homogeneous in large volumes compared to the dimensions of these structural elements. Probability, size etc. of structural defects becomes more critical with increasing sample volume. Thus, although the most critical stress conditions may exist at a certain point in the specimen, the most critical defect might occur at some other point and therefore, the failure may initiate at any point inside the sample, where a critical combination of stress and structure defects occur.

With the rapid development in simulation programs in recent years, it has become much easier to observe the initiation and propagation of cracks through analysis of digital images obtained from small sections [4, 66]. These modeling programs take the direct measurements of crack length, orientation, grain size etc. into account and can provide the complete stress-strain field on a small scale. Apart from which, those programs enable researchers to handle the representative assessment of microstructural properties and failure mechanisms in a much more efficient way.

1.2.4 Summary

Due to the simplicity of its experimental set-up and theoretical analysis, the Brazilian test has become an important method of determining the tensile strength of rocks.

However, the analytical stress-strain solutions deduced for circular discs (plane stress) and cylinders (plane strain) highly depend on boundary and initial conditions, which are largely ignored by theoretical analyses. In fact, the theoretical closed-form solutions do not consider pre-existing or newly initiated flaws or other inhomogeneities. Besides, cracks affect the stress distribution inside the samples to such an extent that it violates the hypothesis of material continuity and homogeneity.

Anisotropic rocks have been widely investigated in rock mechanics but relevant information on their complete tensile fracture behavior is significantly limited. Rock failure in tension results from the propagation of one or more cracks and can thus be investigated using the theory of fracture mechanics.

The best way to judge any of the aforementioned indirect tension test methods is to compare their results with those from the direct tension tests.

1.3   Numerical considerations

In recent years, the enormous development in numerical analyses codes has offered new insights into simulating the Brazilian test. These new techniques have been successfully applied in solving different problems involving the determination of the full stress-strain field, the consideration of the microstructural composition and the fracture propagation in rocks. Most of the research and development in terms of numerical simulations for the Brazilian test has focused on understanding various problems of homogeneous and heterogeneous geomaterials under 2-dimensional conditions. However, mechanical problems in geomaterials are generally 3-dimensional [4, 14, 58, 62, 63, 66]. So far, the extension of the numerical investigations towards 3D so as to cover the behavior of heterogeneous geomaterials is quite rare. Relevant details on the self-designed 3-dimensional numerical models will be presented in the section below and in Chapter 5.

The numerical simulation of the Brazilian test has several advantages, some of which are:

> ➢ Conducting parameter or sensitivity studies

> ➢ Investigation of the influence of boundary, geometrical and initial conditions on test results.

> ➢ Studying stress distribution induced by the initiated cracks inside the model.

> ➢ Analyzing failure mechanisms assuming elasto-plastic or damage / fracture mechanical behavior of materials.

> ➢ Investigation of anisotropic behavior of materials.

1.3.1   Numerical methods

Most of the recent numerical studies have been carried out with the aid of the following methods: **F**inite **E**lement (FEM), the **B**oundary **E**lement (BEM) and the **D**iscrete **E**lement (DEM) [56], [67]. Numerical simulations of the Brazilian test have concentrated on the determination of the stress-strain distribution, the crack initiation, propagation and coalescence.

BEM is suitable for modeling problem of rapidly changing stresses and stress singularities. It finds application in the case of elastic problems and has been used to simulate crack propagation during loading by such researches as Malan et al. [68]; Chen at el. [33]; Wang et al. [69]; Pan et al. [70]; Van de Steen et al. [71] and Lanaro et al. [40]. In Malan's studies [68], fracture growth using the small strain dislocation theory was controlled by evaluating the stress field at a set of potential growth sites. These sites comprise "seed" points either at arbitrary positions in the medium or at the junctions between existing elements or at the tips of growing fracture segments. The first application of 2-dimensional BEM to anisotropic half-plane problems were done by Pan [70]. For half-plane problems using the Kelvin-type Green's functions, 2-dimensional BEM has provided very accurate results using relative coarse discretizations. Numerical applications of the 2-dimensional BEM in rock mechanics, for example, clearly showed that the degree of rock anisotropy and the orientation of the anisotropy can have a great impact on the stress distributions.

1.3.2   Summary

In recent years, the rapid development of computing power, interactive computer graphics and topological data structure, has led to computer simulation becoming a more and more attractive alternative of investigating the complete of stress-strain field and fracturing. The

numerical constitutive models are more and more compatible with intrinsic properties of materials and so are the testing simulations to the experimental tests.

The Brazilian test should considers more and more, the numerical calculation of the stress components at each point of the disc, especially in the critical domains, i.e. at the center of the disc and the crack tip; the numerical determination of any stress concentration at the crack tips and the determination of the orientation angle, at which the rock is considered an anisotropic medium.

1.4 Conclusion

The Brazilian test has been evaluated and confirmed as a simple way of measuring the tensile strength of brittle materials. Tensile strength of rocks is among the most important parameters influencing rock deformation and crushing. Recent developments with respect to Brazilian tests include fracture mechanical approaches, determination of elastic modulus, etc, ranging from isotropic to anisotropic material behavior. Many specific lab test arrangements have been developed with results that are almost impossible to interpret analytically.

To deduce the tensile strength from Brazilian tests, one must know the principal tensile stress, especially at the disc center of the rock, however cracks initiate in most though not all cases. Indeed, for uniform distributed load, it has been shown that under certain circumstances the failure is due to shear and compressive stresses at the loading points. Also, failure may initiate not at the center, but at the point where a critical combination of stress and fabric structures occur.

Numerical simulations provide a powerful instrument for investigating the complete stress-strain field and simulating the failure pattern even for anisotropic and inhomogeneous materials.

An efficient method based on a combination of analytical, experimental and numerical solutions for the analysis of the Brazilian tests of anisotropic rocks is the aim and objective of this thesis.

Chapter 2

Diametral compression in a solid disc – Compilation of analytical and semi-analytical solutions

2.1 Introduction

This chapter deals with the analytical and semi-analytical solutions of the stress distribution in a solid disc under diametral compressive loading. Different solutions for 2- and 3-dimensional considerations of isotropic materials are presented. Remarks which extend the solutions to anisotropic materials are also made. This Chapter also concentrates on the comparison and interpretation of existing solutions.

2.2 Diametral compressive stress distribution in an isotropic elastic disc

The starting point in studying diametral compression of a solid disc is the determination of the stress field, assuming that the material is homogeneous, isotropic, and linearly elastic.

The theoretical solutions assume isotropism, homogeneity, linear elasticity and half-space. Since Hertz' initial proposal in 1883 this solution has been expanded on by many researches like Frocht (1948) [72]; Timoshenko (1951) [73]; Sokolnikoff (1956) [74]; Muskhelishvili (1975) [75]; Timoshenko and Goodier (1982) [76]; Poulos (1991) [77]; Martin (2005) [78] and others.

The problem of a disc in diametral compression as used in experimental stress analysis in the Brazilian test has had many contributions made to it for several decades now. Currently, theoretical solutions for solid discs under opposing point loads or load

distribution over a small arc of the disc's circumference have been developed for 2-D and 3-D.

2.2.1   Elastic theory of line load

The theoretical solution was first proposed in 1883 by H. R. Hertz. This bothered many mathematicians for a long time. One of the theoretical contributions put forward by Timoshenko [73] considers a constant line force acting at the surface of an isotropic, homogeneous, linearly elastic half-space (Figure 2-1).
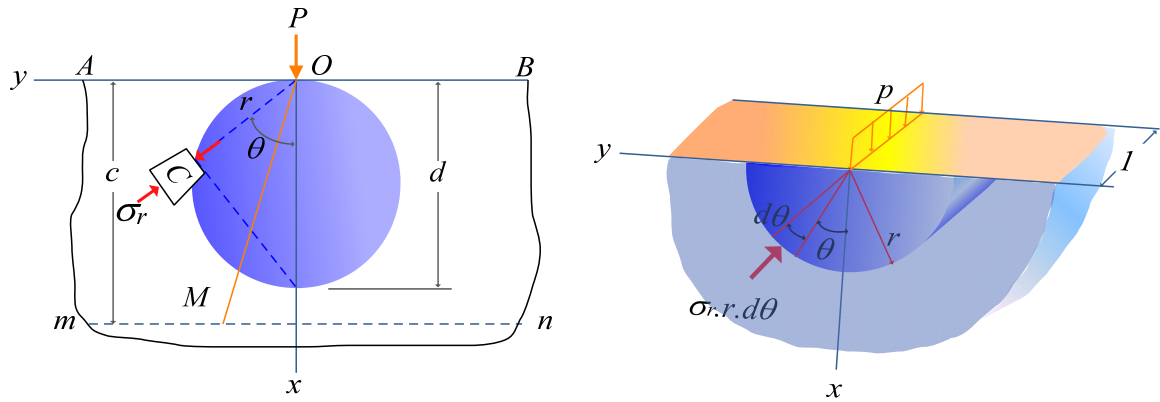
Figure 2-1: Uniform line load acting at the surface of a half space (after Timoshenko, [73]). The solution to this problem was found by Bousssinesq based on a three-dimensional solution put forward by Flamant in 1892 [79].

The stress in an elastic half-space shows a radial distribution. Any element *C* at a distance *r* from the point where the load is applied is subject to a simple compression in the radial direction.

$$\sigma_r = -\frac{2P}{\pi}\frac{\cos\theta}{r} \tag{2.1}$$

The stress analysis of a circular disc subjected to concentrated forces has been discussed further by Frocht (1948) [72]; Timoshenko (1951) [73]; Sokolnikoff (1956) [74]; Muskhelishvili (1975) [75]; Poulos (1991) [77] and others.

Analytical solutions for a pair of diametrally opposite, symmetric and compressive line loads applied to a disc of isotropic rock material have been provided by Muskhelishvili

(1975) [75]; Timoshenko and Goodier (1982) [76] and Martin (2005) [78] so that the stress distribution inside the disc is known.

Indirect tensile test   Flamant solution (1)   Flamant solution (2)   radial tension solution (3)
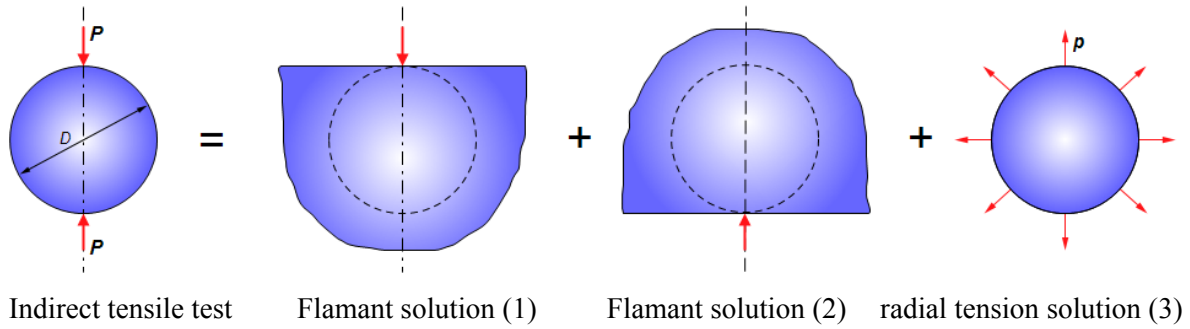
Figure 2-2: Disc under diametral compression – superposition solution (after Martin [78]).

2.2.2 2D analytical solutions

Based on the theory of elasticity for isotropic medium, Timoshenko and Goodier [76] provided comprehensive solutions for the stress distribution induced by line loads on a disc.

To compare these theoretical results with actual material behavior photoelasticity was used to illustrate the stress field experimentally [80]. The obtained isochromatic fringe patterns were compared with theoretical solutions. As Figure 2-3 documents only neglectable deviations were found [78].

Theoretical contours   Photoelastic contour
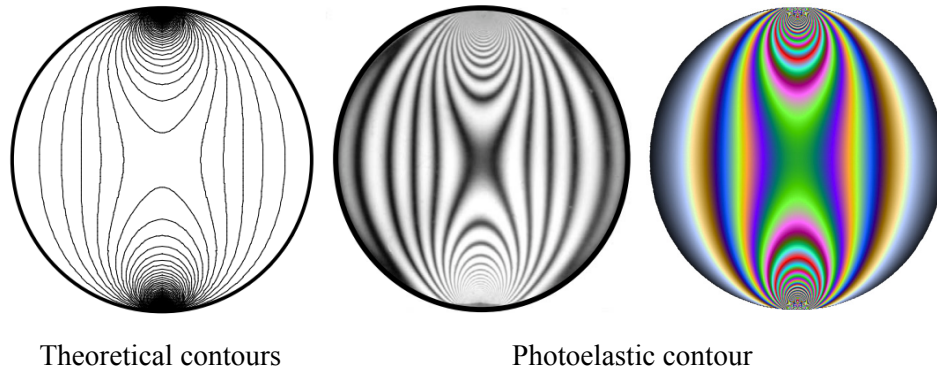
Figure 2-3: Maximum shear stress contours obtained by analytical solution and the corresponding photoelastic isochromatic fringe patterns for a disc under diametral compression. (after Martin [78])

The mode of load application has an important influence of the induced stress pattern. Figure 2-4 illustrates and compares near-field photoelastic fringe patterns for a rectangular plate under four different loading conditions.

| point loading | uniform loading | flat punch loading | cylinder contact loading |
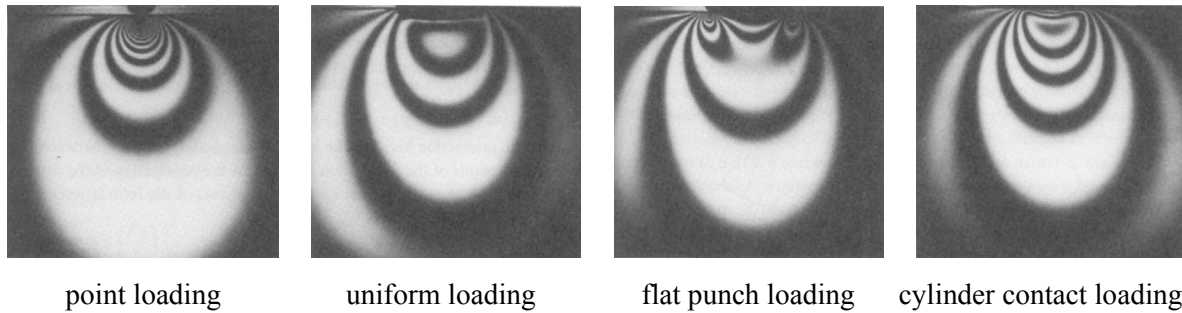
Figure 2-4: Isochromatic photoelastic fringe patterns for several contact loadings along a half plane. (after Martin [78]).

The effect of a finite loading area on the stress distribution is important and was investigated experimentally. The Saint-Venant's principle applied to circular discs subjected to diametral loading was examined by comparing the stress field obtained by concentrated compression with those from distributed compression over a small angle. The methods of photoelasticity and Moiré interferometry were used (Figure 2-5).
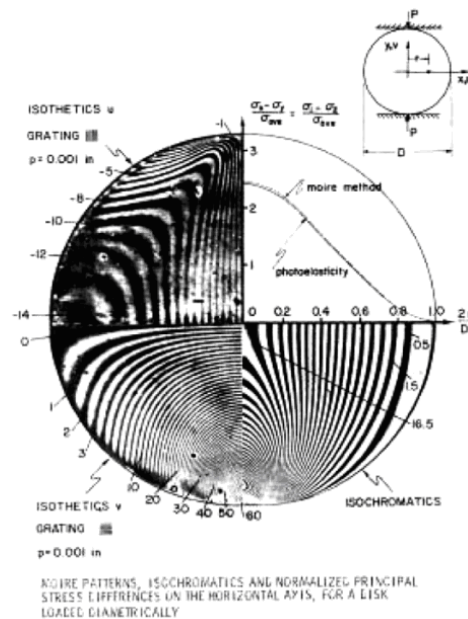
Figure 2-5: Experimental results of Moiré interferometry and photoelasticity (after Timoshenko [76]).

2.2.2.1 Plane disc under diametral compressive line load

This problem was fully resolved by Timoshenko [73] as illustrated in Figure 2-1. Based on the radial solution, the stress distribution can easily be converted into a Cartesian coordinate system as illustrated in Figure 2-6.
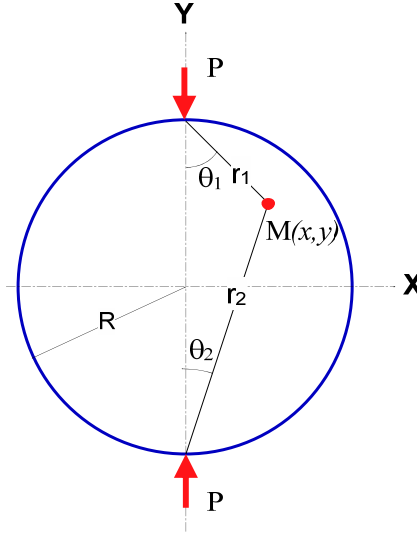
Figure 2-6: A plane disc subjected to line load

The Cartesian stress components at any point M on a horizontal plane *mn* at a distance *c* from the surface of the half-space (Figure 2-1) can be calculated from the compression (P) in the radial direction:

$$\sigma_x = \sigma_r \cos^2 \theta = -\frac{2P}{\pi} \frac{\cos^2 \theta}{r} = -\frac{2P}{\pi c} \cos^4 \theta$$

$$\sigma_y = \sigma_r \sin^2 \theta = -\frac{2P}{\pi c} \sin^2 \theta \cos^2 \theta \qquad (2.2)$$

$$\tau_{xy} = \sigma_r \sin \theta \cos \theta = -\frac{2P}{\pi} \frac{\sin \theta \cos^2 \theta}{r} = -\frac{2P}{\pi c} \sin \theta \cos^3 \theta$$

On the other hand, the equilibrium equation for two-dimensional solutions is given in polar coordinates:

$$\frac{\partial \sigma_r}{\partial r} + \frac{\sigma_r - \sigma_\theta}{r} + \frac{1}{r} \frac{\partial \tau_{r\theta}}{\partial \theta} = 0$$

$$\frac{1}{r} \frac{\partial \sigma_\theta}{\partial \theta} + \frac{\partial \tau_{r\theta}}{\partial r} + \frac{2\tau_{r\theta}}{r} = 0 \qquad (2.3)$$

Figure 2-2 is an illustration of an alternative method which utilizes the superposition principle of three particular stress fields. This method combines the two Flamant solutions and that of the uniformly loaded disc and these yields the final stress field for an XY-coordinate system:

$$\sigma_x = -\frac{2P}{\pi}\left[\frac{(R-y)x^2}{r_1^4} + \frac{(R+y)x^2}{r_2^4} - \frac{1}{D}\right]$$

$$\sigma_y = -\frac{2P}{\pi}\left[\frac{(R-y)^3}{r_1^4} + \frac{(R+y)^3}{r_2^4} - \frac{1}{D}\right] \qquad (2.4)$$

$$\tau_{xy} = \frac{2P}{\pi}\left[\frac{(R-y)^2 x}{r_1^4} - \frac{(R+y)^2 x}{r_2^4}\right]$$

where $r_{1,2} = \sqrt{x^2 + (R \pm y)^2}$.

On the Y-axis in particular, (where X=0), the stresses are:

$$\sigma_x(0,y) = \frac{2P}{\pi D}$$

$$\sigma_y(0,y) = -\frac{2P}{\pi D}\left[\frac{2}{D-2y} + \frac{2}{D+2y} - \frac{1}{D}\right] \qquad (2.5)$$

$$\tau_{xy}(x,0) = 0$$

Thus, along the loaded diameter at X=0, the body experiences a uniform tensile stress of $\sigma_x = 2P/\pi D$. This formula serves as a basis for calculating the tensile strength in the Brazilian test.

To record the strain, Jianhong et al. [81] used two strain gauges fixed at the center of a Brazilian disc both measuring parallel and perpendicular to the line load direction. In addition, a force sensor was used to record the applied force. The stress–strain curve was then determined. The tensile elastic modulus E_t and strength were derived from a linear elastic, isotropic finite-element analysis and the regression fitting test data. The analytic solution for a pair of diametrally opposed, symmetrical and compressive loads on an isotropic Brazilian disc could thus be written as:

$$\sigma_x = \frac{2P}{\pi t}\left[\frac{(R-y)x^2}{\left((R-y)^2+x^2\right)^2}+\frac{(R+y)x^2}{\left((R+y)^2+x^2\right)^2}-\frac{1}{D}\right]$$

$$\sigma_y = \frac{2P}{\pi t}\left[\frac{(R-y)^3}{\left((R-y)^2+x^2\right)^2}+\frac{(R+y)^3}{\left((R+y)^2+x^2\right)^2}-\frac{1}{D}\right] \qquad (2.6)$$

$$\tau_{xy} = \frac{2P}{\pi t}\left[\frac{(R-y)^2 x}{((R-y)^2+x^2)^2}+\frac{(R+y)^2 x}{((R+y)^2+x^2)^2}\right]$$

Eq. (2.6) deduced by Jianhong et al. [81] is identical with the solution given by Martin [78].

To highlight the differences in the above given solutions, the stress distribution along the loading plane at X=0 was calculated under the same boundary condition (i.e., the same radius, thickness and load, in concrete as: *D=50 mm; t=25 mm* and *P=25 kN.*).
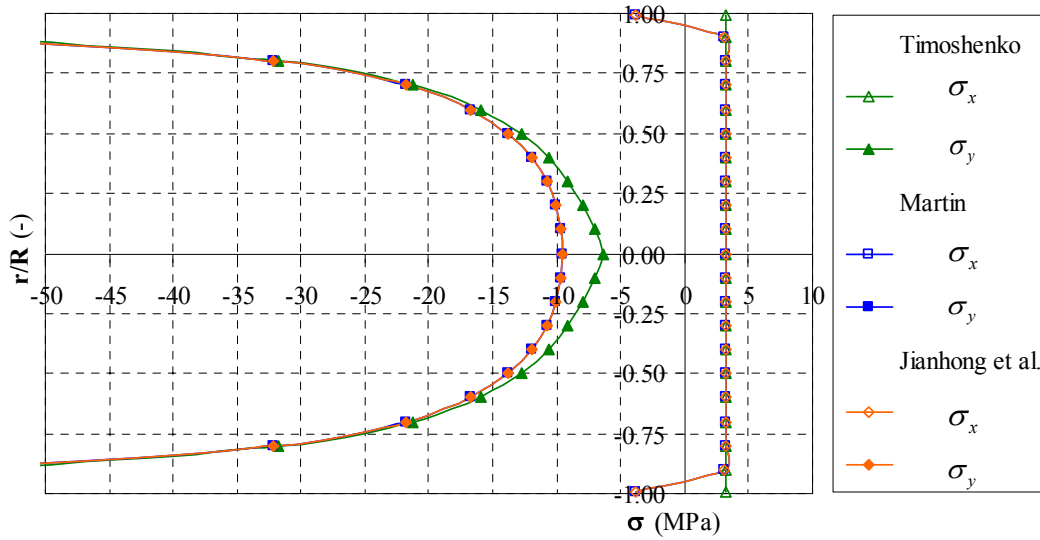
Figure 2-7: Distribution of stress components relative to Eqs. (2.2), (2.5) & (2.6)

From Figure 2-7, it is obvious that the stress at the load entry points is infinite. In all three solutions the distribution of tensile stress σ_t is constant along the plane X=0. The predicted vertical compressive stress obtained from the Timoshenko-solution deviates from that of Martin and Jainhong, which both demonstrate identical values.

2.2.2.2 Plane disc under diametrally compressively distributed load

An analytical solution for a disc with partially distributed compression was developed by Hondros [18]. This solution is valid for both plane stress (discs) and plane strain (cylinders). Since then, many other investigators such as Fairhurst (1964) [19]; Hobbs (1964) [20]; Jaeger (1967) [82]; Colback (1967) [83]; Hudson et al. (1972) [60]; Wijk (1978) [35]; Guo et al. (1983) [28] ; Andreev (1991) [25]; Hung et al. (2003) [37]; Wang et al. (2004) [41]; Ma et al. (2008) [8]; Ma and Hung (2008) [8]; Markides, et al. (2010) [9] have carefully reviewed and expanded on these solutions.
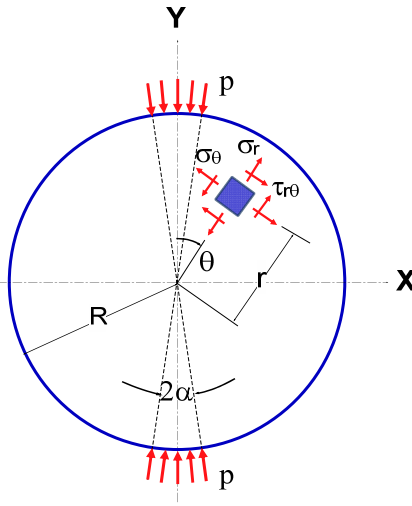
Figure 2-8: Configuration of a plane disc subjected to compressive load distributed along a curved line

Hondros' solution for an elastic homogeneous linear isotropic material gives the following stress fields:

(a) Stresses along the vertical diameter (OY)

$$\sigma_{\theta y} = +\frac{2p}{\pi}\left[\frac{\left(1-r^2/R^2\right)\sin 2\alpha}{\left(1-2r^2/R^2\cos 2\alpha + r^4/R^4\right)} - \tan^{-1}\frac{\left(1+r^2/R^2\right)}{\left(1-r^2/R^2\right)}\tan\alpha\right]$$

$$\sigma_{ry} = -\frac{2p}{\pi}\left[\frac{\left(1-r^2/R^2\right)\sin 2\alpha}{\left(1-2r^2/R^2\cos 2\alpha + r^4/R^4\right)} + \tan^{-1}\frac{\left(1+r^2/R^2\right)}{\left(1-r^2/R^2\right)}\tan\alpha\right] \qquad (2.7)$$

$$\tau_{r\theta} = 0$$

(b) Stresses along the horizontal (OX)

$$\sigma_{\theta x} = -\frac{2p}{\pi} \left[\frac{\left(1-r^2/R^2\right)\sin 2\alpha}{\left(1+2r^2/R^2 \cos 2\alpha + r^4/R^4\right)} + \tan^{-1}\frac{\left(1-r^2/R^2\right)}{\left(1+r^2/R^2\right)}\tan \alpha \right]$$

$$\sigma_{rx} = \frac{2p}{\pi} \left[\frac{\left(1-r^2/R^2\right)\sin 2\alpha}{\left(1+2r^2/R^2 \cos 2\alpha + r^4/R^4\right)} - \tan^{-1}\frac{\left(1-r^2/R^2\right)}{\left(1+r^2/R^2\right)}\tan \alpha \right] \qquad (2.8)$$

$$\tau_{r\theta} = 0$$

Hondros' solution (Eqs. (2.7) & (2.8)), valid for a very thin plane disc subjected to a uniformly distributed pressure applied radially over a short strip at the circumference predicts intensive local stress concentrations near the applied load. In practice though, due to the deformation of the specimen and plates, the actual loads are always only distributed over a finite portion of the disc.

Focusing on the stresses near the load entry arc, Sarris et al. [36] expanded on the Hondros' solution:

$$\sigma_{\theta} = \frac{2p}{\pi} \left\{ \frac{\sin 2\alpha}{1-2(r/R)^2 \cos 2\alpha + (r/R)^4} \left[1 - (r/R)^2\right] - \arctan\left[\frac{(r/R)^2 \sin 2\alpha}{1-(r/R)^2 \cos 2\alpha} \right] - \alpha \right\}$$

$$\sigma_{r} = \frac{2p}{\pi} \left\{ \frac{\sin 2\alpha}{1-2(r/R)^2 \cos 2\alpha + (r/R)^2} \left[(r/R)^2 - 1\right] - \arctan\left[\frac{(r/R)^2 \sin 2\alpha}{1-(r/R)^2 \cos 2\alpha} \right] - \alpha \right\} \qquad (2.9)$$

Instead of using series expansion, Ma and Hung [8] successfully expanded on Hondros' formula and obtained an analytical solution with explicit expressions. For the special case where $\alpha \to 0$ the problem can be reduced to a disc subjected to concentrated forces acting along the diameter in which the stress solutions are simplified as follows:

$$\sigma_r\big|_{\alpha \to 0} = \frac{P}{\pi R t} \left\{ \frac{\left(1-(r/R)^2\right)^2\left((r/R)^4 + 2(r/R)^2 - 1 - 2\cos 2\theta\right)}{\left((r/R)^4 + 1 - 2(r/R)^2 \cos 2\theta\right)^2} \right\}$$

$$\sigma_\theta\big|_{\alpha \to 0} = \frac{P}{\pi R t} \left\{ \frac{(r/R)^8 + 4(r/R)^4 - 4(r/R)^2 - 1 + 2\left(-2(r/R)^6 + (r/R)^4 + 1\right)\cos 2\theta}{\left((r/R)^4 + 1 - 2(r/R)^2 \cos 2\theta\right)^2} \right\} \qquad (2.10)$$

$$\tau_{r\theta}\big|_{\alpha \to 0} = \frac{P}{\pi R t} \left\{ \frac{2\left(1-(r/R)^4\right)\left(1-(r/R)^2\right)\sin 2\theta)}{\left((r/R)^4 + 1 - 2(r/R)^2 \cos 2\theta\right)^2} \right\}$$

To compare the different solutions, the stress distribution was calculated under the same boundary condition using radius, thickness, load and loading angle 2α. Precisely put, the

conditions are $D = 50$mm; $t = 25$mm; Poisson's ratio $\mu = 0.25$; applied load $P = 25$kN; and loading angle $2\alpha = 20^0$.
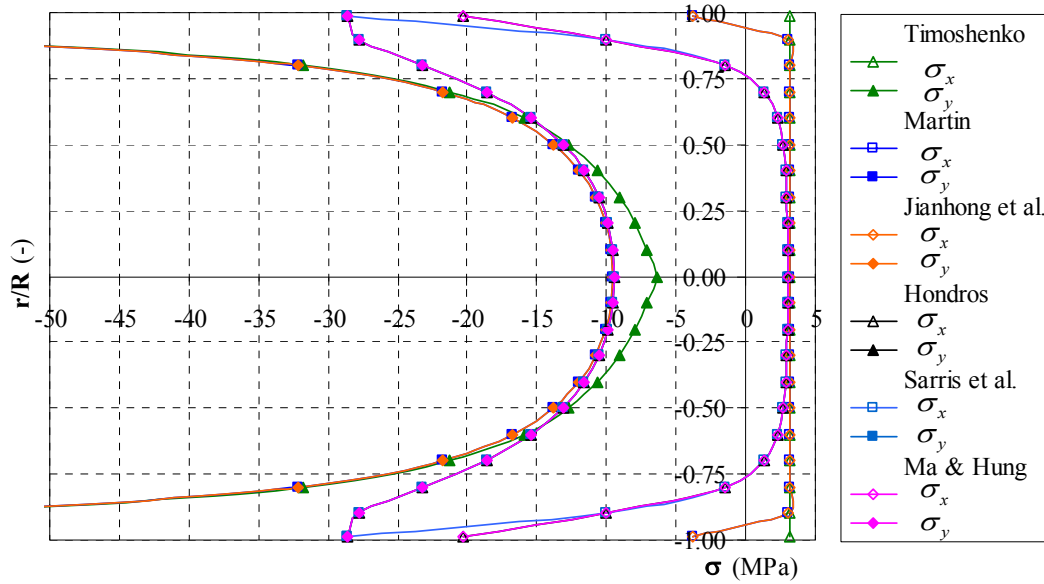
Figure 2-9: Stress component distribution in 2D theoretical solutions

Figure 2-9 shows a comparison of the stress distributions along the axes X=0 obtained from the different solutions mentioned above. The solution of Sarris et al. has improved on the stress prediction near the load entry. However, the stresses at the center of the disc are more or less equal to Hondros's values.

In general, Hondros's solution can be considered as the basic means of determining the tensile strength. This approach of taking the applied load into account is much closer to reality than the original method which only considered the concentrated line loads. However, the approximate expressions derived for the stress components often provide only insufficient in-depth error analysis. It is also difficult to realize the required uniform and radially oriented load distributed over a pair of arcs in real experiments. Consequently, there are always differences between the actual stress state and the predictions obtained by the analytical or semi-analytical solutions.

2.2.3 3D disc under line and diametral compressive distributed loads

From the theory of elasticity, it is well known that some solutions [73, 78, 84, 85] for stress, strain or displacement fields are very sensitive to Poisson's ratio μ. In other words, the tensile stress produced by the Brazilian test has to be taken as a function of the Poisson's ratio for the material and consequently, another advanced calculation scheme for the determination of the tensile strength has to be used.

2.2.3.1 3-dimensional solution for a cylindrical disc under line load

Mindlin [86] expanded on the solution proposed by Boussinesq in 1885 for a force applied on the boundary of a semi-infinite body and found the corresponding 3-dimensional solution. Subsequently, the solution for two concentrated forces P acting on the plane of a cylinder was worked out by Timoshenko [73]. The expressions for the stress components at any point on the equatorial plane are given in the cylinder co-ordinate system:

$$\sigma_r = \frac{P}{2\pi}\left\{(1-2\mu)\left[\frac{1}{r^2}-\frac{z}{r^2}(r^2+z^2)^{-1/2}\right]-3r^2z(r^2+z^2)^{-5/2}\right\}$$

$$\sigma_z = -\frac{3P}{2\pi}z^3(r^2+z^2)^{-3/2}$$

$$\sigma_\theta = \frac{P}{2\pi}(1-2\mu)\left\{-\frac{1}{r^2}+\frac{z}{r^2}(r^2+z^2)^{-1/2}+z(r^2+z^2)^{-3/2}\right\} \tag{2.11}$$

$$\tau_{rz} = -\frac{3P}{2\pi}rz^2(r^2+z^2)^{-5/2}$$

In relation to Boussinesq's problem, Martin [78] has shown that the stress distribution within the specimen under 3-dimensional conditions is a function of Poisson's ratio:

$$\sigma_r = \frac{P}{2\pi R^2}\left[-\frac{3r^2z}{R^3}+\frac{(1-2\mu)R}{R+z}\right]$$

$$\sigma_\theta = \frac{(1-2\mu)P}{2\pi R^2}\left[\frac{z}{R}-\frac{R}{R+z}\right]$$

$$\sigma_z = -\frac{3Pz^3}{2\pi R^5} \tag{2.12}$$

$$\tau_{rz} = -\frac{3P.r.z^2}{2\pi R^5}$$

2.2.4   3D solution under diametral compressive distributed load

Wijk [35] suggested a 3D 'correction' of the 2D analytical solution for the Brazil test. Under certain conditions, the elastic solution of a 2-dimensional problem may be used to construct a solution for the corresponding 3-dimensional problem. For a thin disc, the 3D solution is converted into a 2D solution.

Based on the assumption that the material is homogeneous and the behavior linear elastic with a Young's modulus E and Poisson's number m, the three-dimensional equation for the middle plane is given as:

$$\sigma_x(x=0,y,z) = -\frac{2p}{\pi}\left\{ \begin{array}{l} \dfrac{(1-\rho^2)\sin 2\alpha}{1-2\rho^2\cos 2\alpha+\rho^4} - \arctan\left(\dfrac{1+\rho^2}{1-\rho^2}\tan\alpha\right) + \\[4mm] \dfrac{4z^2\tan\alpha}{(m+1)R^2}\dfrac{(1-\rho^2)(1+3\rho^2)+(1+\rho^2)(1-3\rho^2)\tan^2\alpha}{\left((1-\rho^2)^2+(1+\rho^2)^2\tan^2\alpha\right)^2} \end{array} \right\} \tag{2.13}$$

To show the 3D-effect and the influence of the different parameters on the solution more clearly, a special case of Eq. (2.13) with a vanishing loading angle of 2α is deduced;

$$\lim_{\alpha\to 0}\sigma_x(x=0,y,z) = -\frac{F}{\pi Rt}\left[1+\frac{4z^2(1+3\rho^2)}{(m+1)R^2(1-\rho^2)^3}\right] \tag{2.14}$$

where $\rho = \dfrac{r}{R} = \dfrac{\sqrt{(x^2+y^2)}}{R}$
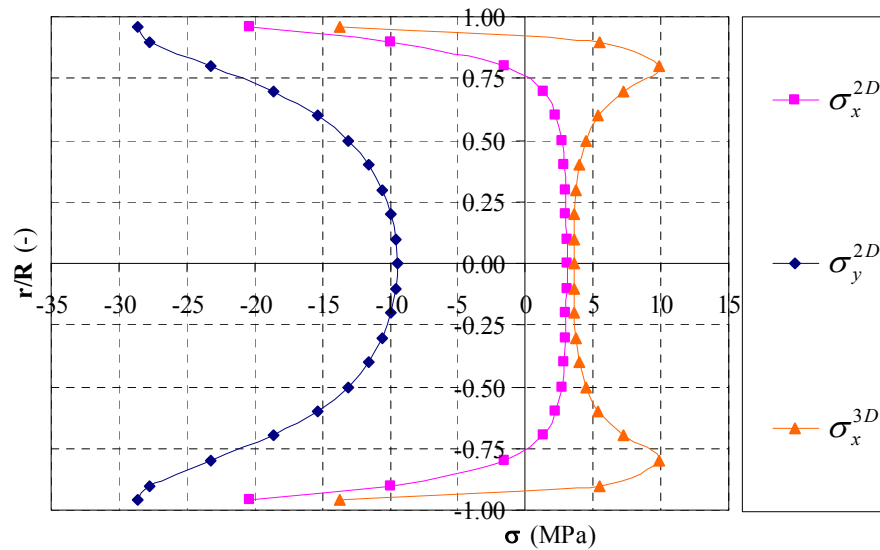
Figure 2-10: Stress component distribution along the middle plane of a disc with a thickness-to-diameter ratio L/D = ½ after Wijk, Eq. (2.14)

2.2.4.1 Effect of finite disc thickness and loading angle after Wijk's solution

Based on the Wijk's three-dimensional formula (Eq. (2.13)), the effect of finite thickness and Poisson's ratio on the stress distribution can be demonstrated as follows.
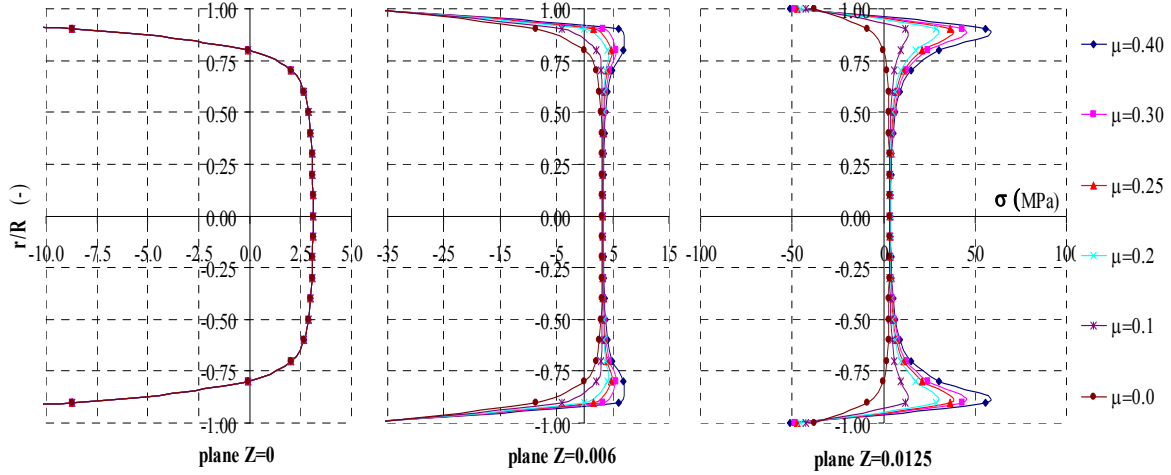
Figure 2-11: Effect of Poisson's ratio and the above plane on distribution of the horizontal stress component in accordance with Wijk's solution, where $2\alpha = 25°$; L/D = ½.

It can be observed in Figure 2-11 that the stress distribution is independent of the Poisson's ratio along the middle plane of the disc, i.e. for Z = 0. In contrast, the stress distributions at Z ≠ 0 show pronounced differences depending on Poisson's ratios and the planes under observations. The higher the Poisson's ratio and the further away from the center plane, the more pronounced the stress peaks close to the load entry area.
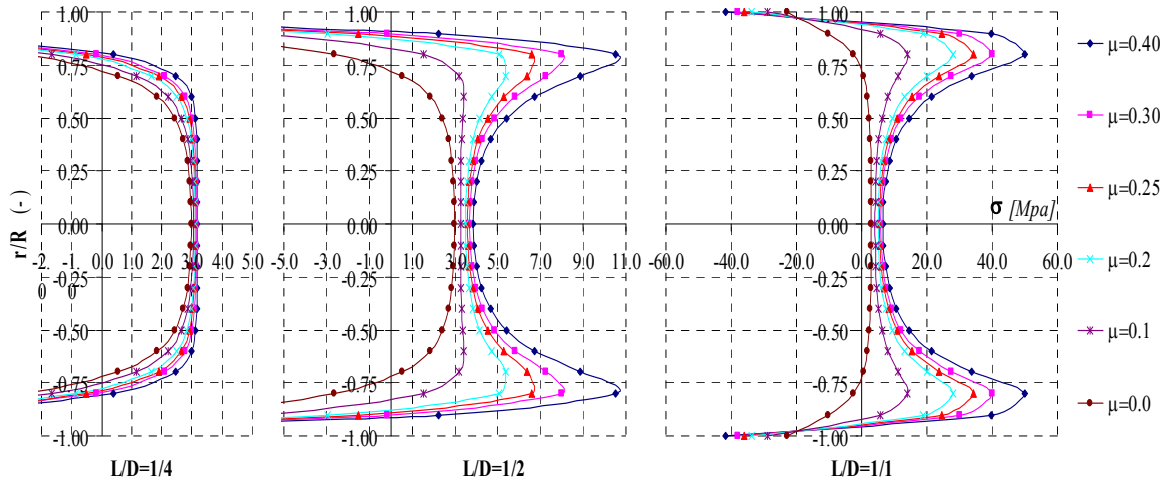
Figure 2-12: Effect of finite thickness of the sample on distribution of the horizontal stress component in accordance with Wijk's solution, where $2\alpha = 25°$.

Figure 2-12, the stress distribution here indicates distinct differences in the effect of thickness. The thinner the disc and the smaller the Poisson's ratio, the more the stress distributions converge with a corresponding reduction in concentrated stress in the load entry area.
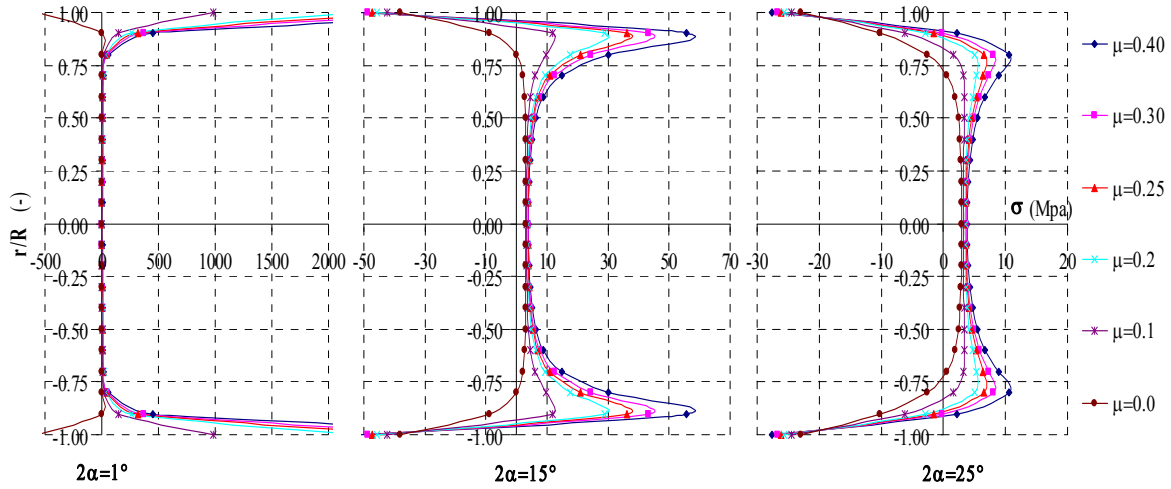
Figure 2-13: Effect of loading angle and Poisson's ratio on distribution of the horizontal stress component along the middle plane after Wijk's solution, where L/D = ½.

According to Wijk's solution, the horizontal stress component is rather inhomogeneous except for very small loading angles, where extreme values only occur immediately at the load entry point. For larger loading angles, two local stress peaks can be predicted depending on the loading angle - one in the immediate region of the load entry area, i.e. at $r/R \to 1$ (local compression) and another in the region around $r/R = 0.8 \div 1.0$ (local tension). From the stress distribution diagram, Wijk's solution predicts the largest tensile stresses not at the center of the disc but closer to the boundary. This solution also predicts extremely large values.

Wijk's 3D solution has some drawbacks [63]. The stress predictions for planes away from the center are particularly questionable. They are not backed up by experimental data or numerical simulation results.

2.3 Stress and strain in an isotropic solid disc

Based on the theory of elasticity, the strain can be normally obtained by applying Hooke's law for plane strain conditions in polar coordinates (r, θ).

$$\varepsilon_r = \frac{1}{E}(\sigma_r - \mu\sigma_\theta); \quad \varepsilon_\theta = \frac{1}{E}(\sigma_\theta - \mu\sigma_r); \quad \varepsilon_{r\theta} = \frac{1}{G}\tau_{r\theta} \tag{2.15}$$

The strain-displacement relationship for small strains is given by:

$$\varepsilon_r = \frac{\partial u_r}{\partial r}; \qquad \varepsilon_\theta = \frac{u_r}{r} + \frac{1}{r}\frac{\partial u_\theta}{\partial \theta}; \qquad \varepsilon_{r\theta} = \frac{1}{r}\frac{\partial u_r}{\partial \theta} + \frac{\partial u_\theta}{\partial r} - \frac{u_\theta}{r} \tag{2.16}$$

The strains given by Timoshenko [73] for a line force (Figure 2-1) where u_r and u_θ are the components of displacements in the radial and tangential directions, respectively are:

$$\varepsilon_r = \frac{\partial u_r}{\partial r} = -\frac{2P}{\pi E}\frac{\cos\theta}{r}; \; \varepsilon_\theta = \frac{u_r}{r} + \frac{\partial u_\theta}{r\partial\theta} = \mu\frac{2P}{\pi E}\frac{\cos\theta}{r}; \; \varepsilon_{r\theta} = r\frac{\partial u_r}{\partial\theta} + \frac{\partial u_\theta}{\partial r} - \frac{u_\theta}{r} = 0 \tag{2.17}$$

Integrating Eq. (2.17) provides the displacement u. Substituting u_r and u_θ in Eq. (2.15) gives

$$f(\theta) = -\frac{(1-\mu)P}{\pi E}\theta\sin\theta + A\sin\theta + B\cos\theta, \qquad F(r) = Cr \tag{2.18}$$

where A, B and C are constants of integration determined by the conditions of constraint. The expressions for the radial and tangential displacements deduced from the integrated equations u_r and u_θ are:

$$u_r = -\frac{2P}{\pi E}\cos\theta\log r - \frac{(1-\mu)P}{\pi E}\theta\sin\theta + A\sin\theta + B\cos\theta \tag{2.19}$$

$$u_\theta = \frac{2\mu P}{\pi E}\sin\theta + \frac{2P}{\pi E}\log r\sin\theta - \frac{(1-\mu)P}{\pi E}\theta\cos\theta + \frac{(1-\mu)P}{\pi E}\sin\theta + A\cos\theta - B\sin\theta + Cr$$

Based on the results of Cauwellaert et al. [29], Wang [41] developed an approximate displacement solution for the flat-end region of the specimen exposed by uniformly distributed load along the load arc (Figure 1-3):

$$\Delta u_\theta = \frac{2P}{\pi E t}\left[(1-\mu) - \ln\left(1 + \frac{4}{\sin^2\alpha}\right)\right]\frac{\alpha}{\sin\alpha} \tag{2.20}$$

Recently, Ma and Hung [8] explored the normal strains and displacements along the $X(\theta = \pi/2)$ and $Y(\theta = 0)$ axis for partially distributed compressions where the shear strain along these two lines is zero.

For $\theta = 0$, normal strains $\varepsilon_r = \varepsilon_y$ and $\varepsilon_\theta = \varepsilon_x$, the solutions can therefore be reduced as follows:

$$\varepsilon_r(\rho,0) = \varepsilon_y(\rho,0) = -\frac{2p}{\pi E}\left\{(1+\mu)\frac{(1-\rho^2)\sin 2\alpha}{\rho^4 + 1 - 2\rho^2 \cos 2\alpha} + (1-\mu)\tan^{-1}\left(\frac{1+\rho^2}{1-\rho^2}\tan\alpha\right)\right\} \quad (2.21)$$

$$\varepsilon_\theta(\rho,0) = \varepsilon_x(\rho,0) = -\frac{2p}{\pi E}\left\{-(1+\mu)\frac{(1-\rho^2)\sin 2\alpha}{\rho^4 + 1 - 2\rho^2 \cos 2\alpha} + (1-\mu)\tan^{-1}\left(\frac{1+\rho^2}{1-\rho^2}\tan\alpha\right)\right\} \quad (2.22)$$

where $\rho = r/R$

For $\theta = 0$, the displacements can be obtained as follows:

$$u_r(\rho,0) = u_y(\rho,0) = -\frac{2pR}{\pi E}\left\{(1-\mu)\rho\tan^{-1}\left(\frac{1+\rho^2}{1-\rho^2}\tan\alpha\right) + \sin\alpha\ln\left|\frac{1+\rho^2 + 2\rho\cos\alpha}{1+\rho^2 - 2\rho\cos\alpha}\right|\right.$$

$$\left. -(1-\mu)\cos\alpha\left[\tan^{-1}\left(\frac{\rho\sin\alpha}{1+\rho\cos\alpha}\right) + \tan^{-1}\left(\frac{\rho\sin\alpha}{1-\rho\cos\alpha}\right)\right]\right\} \quad (2.23)$$

$$u_\theta(\rho,0) = u_x(\rho,0) = 0$$

For $\theta = \pi/2$, displacements are obtained as follows:

$$u_r(\rho,\pi/2) = u_y(\rho,\pi/2) = -\frac{2pR}{\pi E}\left\{(1-\mu)\rho\tan^{-1}\left(\frac{1+\rho^2}{1-\rho^2}\tan\alpha\right) + \sin\alpha\ln\left|\frac{1+\rho^2 + 2\rho\cos\alpha}{1+\rho^2 - 2\rho\cos\alpha}\right|\right.$$

$$\left. -(1-\mu)\cos\alpha\left[\tan^{-1}\left(\frac{\rho\sin\alpha}{1+\rho\cos\alpha}\right) + \tan^{-1}\left(\frac{\rho\sin\alpha}{1-\rho\cos\alpha}\right)\right]\right\} \quad (2.24)$$

$$u_\theta(\rho,\pi/2) = u_x(\rho,\pi/2) = 0$$

2.4 Stress and strain in anisotropic rocks

Anisotropy is a typical characteristic of intact foliated metamorphic rocks and laminated, stratified or bedded sedimentary rocks. The deformability and strength of anisotropic media are different from those of isotropic media. As discussed in detail above, the indirect tensile strength is deduced by means of equations derived from the theory of isotropic elasticity and does not consider the anisotropic character of rocks. Consequently, the deduced tensile strength may be not correct.

In relation to stress and strain in anisotropic rocks, Amadei [3, 87] culled together an excellent review from the many available lab and field techniques. Lekhnitskii [84] used the complex stress function method to express the relationship between stress and strain in a thin disc of anisotropic material under diametral loading. Amadei and Jonsson [88] and Chen et al. [89] have applied theoretical solutions to tensile strength measurements in anisotropic rocks in the lab. The mechanical properties of intact anisotropic rocks are usually determined by using test samples with different loading angles relative to the apparent planes of anisotropy. The effect of anisotropy on the indirect determination of tensile strength of rocks using the Brazilian test was investigated by Berenbaum and Brodie [17] on coal, Hobbs [20] on siltstone, sandstone and mudstone, McLamore and Gray [90] on shale, and Barla [91] on gneiss and schist.

Stress and strain in anisotropic rocks are commonly analyzed using the theory of elasticity under assumption of Hooke's law. The general equation for the constitutive relations of homogeneous anisotropic elastic media in a Cartesian (XYZ) coordinate system can be written as follows [87]:

$$[\varepsilon]_{xyz} = [A] \times [\sigma]_{xyz} \tag{2.25}$$

where $[\varepsilon]_{xyz}$ and $[\sigma]_{xyz}$ are $[6 \times 1]$ column matrices representing the strain and stress tensors in the (XYZ) coordinate system, respectively, and $[A]$ is a $[6 \times 6]$ matrix for the elastic constants whose components are $a_{i,j}(i, j = 1 \div 6)$. In general, matrix $[A]$ has 21 distinct elastic constants; this number reducing when symmetry occurs in the inherent structure of the anisotropic medium. Precisely put, the number reduces to 13 if the medium possesses a

plane of elastic symmetry perpendicular to one of three axes X, Y or Z, 9 if the medium is orthotropic, 5 if transversely isotropic (i.e. isotropic within a plane perpendicular to one of the three coordinate axes) and 2 if isotropic [3, 87, 92].

For transversely isotropic rocks with planar fabric, e.g. assuming the plane of symmetry is Y-Z, Hooke's law can be defined for a local coordinate system (X'Y'Z') [92]:

$$[\sigma'] = [D'] \times [\varepsilon']$$
(2.26)

(a) line load with components X_n and Y_n (b) distributed pressure over an angle of 2α

(after Chen et al. [33])   (after Amadei, et al. [93])
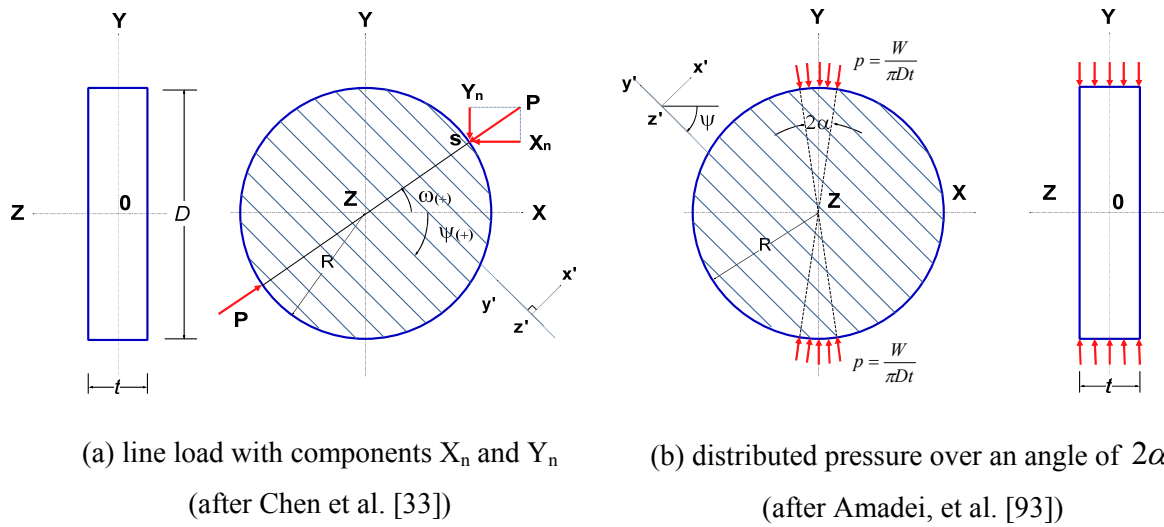
Figure 2-14: Configuration of a transverse anisotropic disc under diametral compressive loading with global Cartesian coordinate (XYZ) and local coordinate (X'Y'Z').

Lekhnitskii [84], Claesson and Bohloli [94], Amadei [3, 90], Chen et al. [55], Lemmon [31] and Exadaktylos et al. [95] have attempted to account for the influence of anisotropy on the distribution of stress. Lekhnitskii [84] developed a complex stress function equation to express the relationship between stress and strain within a disc of anisotropic material under diametral loading. Applying this theory, Chen et al. [55] especially focused on finding a solution for a linear elastic, homogeneous and transversely isotropic thin disc.

According to Figure 2-14(a), the load components X_n, Y_n are the surface forces measured per unit area in the *x* and *y* directions. The surface forces are assumed to act along the boundary area of the disc. The equilibrium and compatibility equations, the constitutive relationships and the boundary conditions are all expressed in terms of average values of stress, strain and displacement relative to the thickness of the disc. Therefore, the mean

stress, strain and displacement components should all satisfy the same equations that govern the classical plane strain formulation in the (XY) plane [84]. Hooke's law expressed in Eq. (2.26) for the (XY) plane can be written as follows [33]:

$$
\begin{bmatrix} \varepsilon_x \\ \varepsilon_y \\ \gamma_{xy} \end{bmatrix} = \begin{bmatrix} a_{11} & a_{12} & a_{16} \\ a_{12} & a_{22} & a_{26} \\ a_{16} & a_{26} & a_{66} \end{bmatrix} \times \begin{bmatrix} \sigma_x \\ \sigma_y \\ \tau_{xy} \end{bmatrix}
$$

(2.27)

where $a_{i,j}(i, j = 1-6)$ are compliance components calculated in the (XY) coordinate system. These components are a function of the angle ψ and the elastic constants in the (X'Y'Z') coordinate system. The constants are Young's moduli *(E, E'),* Poisson's ratios *(μ, μ')* and shear modulus *(G')* in a normal direction and in the plane of transverse isotropy, respectively. The shear modulus *G* in the plane of transverse isotropy is equal to $E / 2(1 + \mu)$.

$$
a_{11} = \frac{\sin^4 \psi}{E'} + \frac{\cos^4 \psi}{E} + \frac{\sin^2 2\psi}{4} \left(\frac{1}{G'} - \frac{2\mu'}{E'} \right)
$$

$$
a_{12} = \frac{\sin^2 2\psi}{4} \left(\frac{1}{E'} + \frac{1}{E} - \frac{1}{G'} \right) - \frac{\mu'}{E'} \left(\cos^4 \psi + \sin^4 \psi \right)
$$

$$
a_{16} = \sin 2\psi \left[\left(\frac{\sin^2 \psi}{E'} - \frac{\cos^2 \psi}{E} \right) + \left(\frac{1}{2G'} - \frac{\mu'}{E'} \right) \cos 2\psi \right]
$$

$$
a_{22} = \frac{\cos^4 \psi}{E'} + \frac{\sin^4 \psi}{E} + \frac{\sin^2 2\psi}{4} \left(\frac{1}{G'} - \frac{2\mu'}{E'} \right)
$$

(2.28)

$$
a_{26} = \sin 2\psi \left[\left(\frac{\cos^2 \psi}{E'} - \frac{\sin^2 \psi}{E} \right) - \left(\frac{1}{2G'} - \frac{\mu'}{E'} \right) \cos 2\psi \right]
$$

$$
a_{66} = \sin^2 2\psi \left(\frac{1}{E'} + \frac{1}{E} + \frac{2\mu'}{E'} \right) + \frac{\cos^2 2\psi}{G'}
$$

Letting F be a stress function such that:

$$
\sigma_x = \frac{\partial^2 F}{\partial y^2}, \qquad \sigma_y = \frac{\partial^2 F}{\partial x^2}, \qquad \tau_{xy} = \frac{\partial^2 F}{\partial x \partial y},
$$

(2.29)

And substituting Eqs. (2.28) & (2.29) into Eq. (2.27), the following differential equation is obtained:

$$a_{22}\frac{\partial^4 F}{\partial x^4} - 2a_{26}\frac{\partial^4 F}{\partial x^3 \partial y} + (2a_{12} + a_{66})\frac{\partial^4 F}{\partial x^2 \partial y^2} - 2a_{16}\frac{\partial^4 F}{\partial x \partial y^3} + a_{11}\frac{\partial^4 F}{\partial y^4} = 0 \qquad (2.30)$$

Inserting the root, $\mu_i\,(i = 1 \div 4)$, into the general solution equation above yields the characteristic equation:

$$a_{11}\mu^4 - 2a_{16}\mu^3 + (2a_{12} + a_{66})\mu^2 - 2a_{26}\mu + a_{22} = 0 \qquad (2.31)$$

Substituting Eq. (2.28) into Eq. (2.30), the first derivatives of F with respect to x and y can be expressed, according to Lekhnitskii [84], as:

$$\frac{\partial F}{\partial x} = 2\,\mathrm{Re}[\phi_1(z_1) + \phi_2(z_2)]$$
$$\frac{\partial F}{\partial y} = 2\,\mathrm{Re}[\mu_1\phi_1(z_1) + \mu_2\phi_2(z_2)] \qquad (2.32)$$

where $\phi_k(z_k)(k = 1,2)$ are analytical functions of the complex variables $z_k = x + \mu_k y$ and *Re* defines the real part of the complex expression in the brackets (2.32). Combining Eqs. (2.30) & (2.32) can yield a general expression for the stress components:

$$\sigma_x = 2\,\mathrm{Re}[\mu_1^2\phi_1'(z_1) + \mu_2^2\phi_2'(z_2)]$$
$$\sigma_y = 2\,\mathrm{Re}[\phi_1'(z_1) + \phi_2'(z_2)] \qquad (2.33)$$
$$\tau_{xy} = -2\,\mathrm{Re}[\mu_1\phi_1'(z_1) + \mu_2\phi_{21}'(z_2)]$$

where $\phi_k'(z_k)(k = 1,2)$ are the first derivatives of $\phi_k(z_k)$ with respect to z_k. General expressions for the functions $\phi_k(z_k)$ and relation $z_k / R = \cos\varpi + \mu_k \sin\varpi$ (Figure 2-14) were proposed by Lekhnitskii [84]. The stress components σ_x, σ_y and τ_{xy} (Eq. (2.33)) can then be computed for any point *(x, y)* inside the disc.

Using a polar coordinate system, as shown in Figure 2-14(a), this stress distribution can be approximated by the following Fourier series for the angle ω:

$$\sigma_r = A_0 + \sum_{n-1}^{N-1}(A_n \cos n\omega + B_n \sin n\varpi) \qquad (2.34)$$

with $\quad A_0 = 2p\alpha / \pi, \quad A_n = \frac{2p}{\pi}\left(\frac{1 + (-1)^n}{n}\right)\cos\frac{n\pi}{2}\sin n\alpha, \quad B_n = 0 \qquad (2.35)$

There is no shear stress applied along the contour of the disc. The surface tractions X_n, Y_n depend only on p and can then be expressed as Fourier's series for $\cos(n\omega)$ and $\sin(n\omega)$ with n varying between *1* and *N*.

If the geometry presented in Figure 2-14(b) is considered, with a disc subjected to distributed pressure applied over a small angular width of 2α, the rock assumed to be orthotropic with one of its three planes of anisotropy parallel to the disc (XY) plane and the X'- and Y'-axes inclined at an angle ψ with respect to the X- and Y-axes, Amadei [3] has proposed the following stress concentration factors for stress components at the center of the disc:

$$\sigma_x = q_{xx}\frac{W}{\pi Dt}; \quad \sigma_y = q_{yy}\frac{W}{\pi Dt}; \quad \tau_{xy} = q_{xy}\frac{W}{\pi Dt} \tag{2.36}$$

The stress concentration factors q_{xx}, q_{yy} and q_{xy} have complex expressions, which depend on the coordinates (x, y) at the point of interest, the loading angle (2α), and the compliance components $a_{i,j}(i, j = 1\div 6)$ as well as the strike angle (ψ).

For a Brazilian test on isotropic media and small values of the loading angle 2α $(2\alpha \leq 15°)$ [3], stress concentration factors at the center of the disc can be approximated by q_{xx}= -2, q_{yy}= 6 and q_{xy}= 0. The Eq. (2.27) can then be written as follows:

$$\frac{\pi Dt}{W}\begin{bmatrix} \varepsilon_x \\ \varepsilon_y \\ \gamma_{xy} \end{bmatrix} = \begin{bmatrix} 1/E & -\mu/E & 0 \\ -\mu/E & 1/E & 0 \\ 0 & 0 & 2(1+\mu)/E \end{bmatrix} \times \begin{bmatrix} -2 \\ 6 \\ 0 \end{bmatrix} \tag{2.37}$$

Despite the often pronounced anisotropic characteristics of rocks, the evaluation of the indirect tensile strength test is still based on the isotropic elasticity theory. However, as documented in detail in the Chapters above, this can be quite misleading.

2.5   Conclusion

The distribution of stress and strain in a disc under diametral compression has been investigated by many researchers with the help of analytical solutions. A majority of the studies focusing on theoretical solutions have only been for isotropic rocks, solutions for anisotropic rocks being much more difficult to obtain. Exact analytical solutions for

anisotropic rocks are not available so that either numerical analysis or semi-analytical solutions have to be used.

The following conclusions can be drawn from the analytical solutions:

➢ If a finite disc thickness is assumed, the magnitude of the stresses inside the disc can be said to be strongly influenced by the loading angle (2α) and the plane under consideration.

➢ Brazilian test on isotropic discs with a low thickness to diameter ratio almost produce maximum tensile stresses at the center of the disc.

➢ There are local stress concentration phenomena in the region near the loading points which can lead to shear or mixed-mode failure if the loading angle is very low. When the loading angle increases, the stress concentration phenomena reduce [19] and the induced tensile stress dominates in the failure of the material.

➢ Analytical solutions indicate that under certain circumstances tensile stress may be produced not at the center but more closely to the boundary of the disc, depending on the Poisson's ratio, thickness and loading angle.

The analytical solutions discussed above show up several still unsolved problems regarding the stress distribution:

➢ The analytical solutions only do consider plane-stress situations.

➢ Only the 3D semi-analytical solution after Wijk's does explain the effect of Poisson's ratio and finite thickness, predicting though, extreme stress values for planes away from the center. These values are not however supported by numerical analysis or results of lab tests.

➢ The analytical solutions do not consider the effect of friction between the loading jaws and the disc.

➢ They do not consider inhomogeneities inside the disc.

➢ And they do not consider anisotropy.

The discussions in the Chapter above show that the interpretation of the Brazilian tensile strength test is much more complicated than usually thought and needs further investigations in order to tackle the still unsolved problems, especially with respect to anisotropy in rocks.

The tensile strength in relation to anisotropy can be investigated by numerical simulation, which could provide the full stress-strain field and the failure mechanisms, as well as by systematic lab tests.

Both were undertaken within the framework of this work and will be explained in the succeeding Chapters.

Chapter 3

Laboratory tests

3.1 Introduction

Very few systematic studies on the influence of anisotropy (bedded, laminated or schistose rocks) on tensile strength have been conducted so far [20, 59, 101]. Also, results from experimental studies using the Brazilian test with specimens in various orientations of the loading axis to the planes of weakness are rather limited. All this makes it difficult to give a sound interpretation of the measured data in terms of tensile strength values.

In this Chapter results of lab tests are presented on three different rock types with different degrees of anisotropy: sandstone, gneiss and slate, which stand for both bedded sedimentary tendentious isotropic and foliated, highly anisotropic rocks. In total, 555 Brazilian tests were carried out in order to determine the tensile strength in directions relative to the planes of schistosity, ranging from 0° to 90° (in incremental steps of 15°).
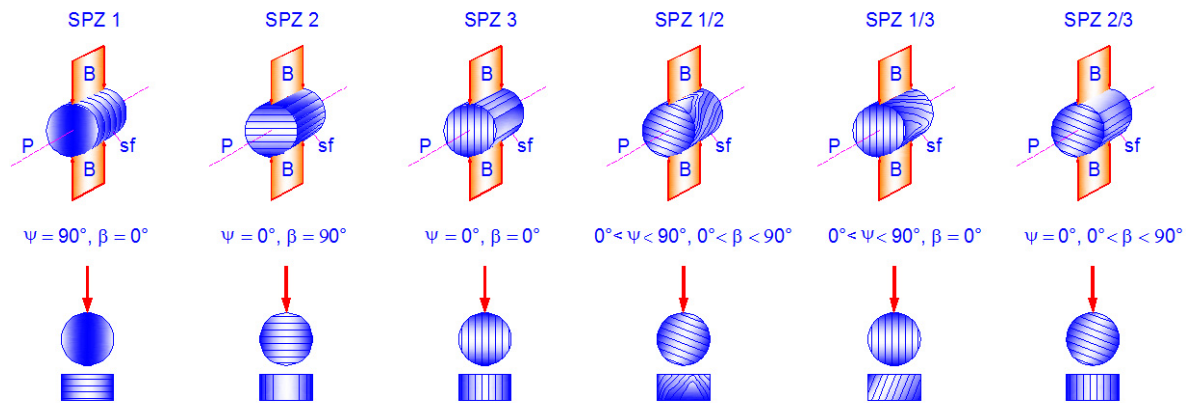
Figure 3-1: Experimental arrangement for testing rock anisotropy relative to Orientation (ψ) and Foliation-Loading (β) angles[1][2] using the Brazilian test. Combining $[\psi]$ and $[\beta]$ in 15° increments creates a $[7 \times 7]$ matrix of angles.

---

[1] Orientation angle (ψ) is an angle between the foliation planes and the test specimen axis.

[2] Foliation-Loading angle (β) is an angle between the foliation plane and loading direction.

Selection of materials for the lab tests

In petrology, rocks are classified into three principal groups according to their geological origin: igneous rocks, sedimentary rocks and metamorphic rocks. Anisotropy is a pronounced characteristic of intact foliated metamorphic rocks such as slates, gneisses, phyllites or schists.

In metamorphic rocks, foliation is often expressed as alternate layers of differing mineral compositions as in gneiss or slate. It is worthy to note that rocks which have undergone several processes of formation may present more than one direction of planar anisotropy as in foliation and bedding planes in slates [3]. These directions may not necessarily be parallel to each other. In addition, linear features such as lineations can be superimposed on the planar features. Due to their distinct anisotropy, metamorphic rocks were selected for this study. The following four types of rocks were chosen specifically for this study: Freiberger Gneiss from Halsbrücke near Freiberg in Saxony (FG.Gs), Leubsdorfer Gneiss from the Flöha-Valley in Saxony (Le.Gs) and Mosel Slate from Mayen-Koblenz in Rheinland-Pfalz (My.Sc). Anisotropy is also characteristic of laminated, stratified or bedded sedimentary rocks such as shales, sandstones, siltstones, limestones or coal. In these rocks, the anisotropy results from complex physical and chemical processes associated with transportation, deposition, compaction, cementation, etc. However, the Postaer Sandstone from Pirna in Saxony (FG.Ss) with a medium-grained size varying from 0.01 to 1.0 *mm* and occasionally containing some larger mineral spots, reaching 2.0 and 3.0 *mm*, is an almost isotropic rock and was therefore chosen as a reference material for homogeneous isotropic rocks.

3.2   Laboratory test program

Laboratory tests were carried out to determine both deformation and strength parameters. Although the whole test program comprises uniaxial and triaxial compressive tests and ultrasonic wave speed measurements, its main focus is on the Brazilian tests. The arrangements for the Brazilian tests are described by a $[7 \times 7]$ matrix, which contains 7 values for the orientation angle ψ and another 7 for the foliation-loading angle β, each ranging from 0° to 90° at 15° intervals. The other lab tests were done only either parallel or

perpendicular to the plane of anisotropy. Table 3-1 gives an overview of the lab tests conducted, all at the Rock Mechanics Laboratories in the Geotechnical Institute of the Technical University Bergakademie in Freiberg. Figure 3-2 documents the sample nomenclature used.

Type of test	Sample material				Total number of samples
	Gneiss		Slate		
	$\parallel$	$\perp$	$\parallel$	$\perp$	
Ultrasonic analysis		3		3	6
Uniaxial compression test	3	3	3	3	12
Triaxial compression test (conventional)	1	1	1	1	4
Triaxial compression test (multi-stage)		3		3	6
Brazilian tensile strength test					555

Table 3-1: Laboratory test program ($\parallel$: loading direction parallel to plane of anisotropy, $\perp$: loading direction perpendicular to plane of anisotropy).
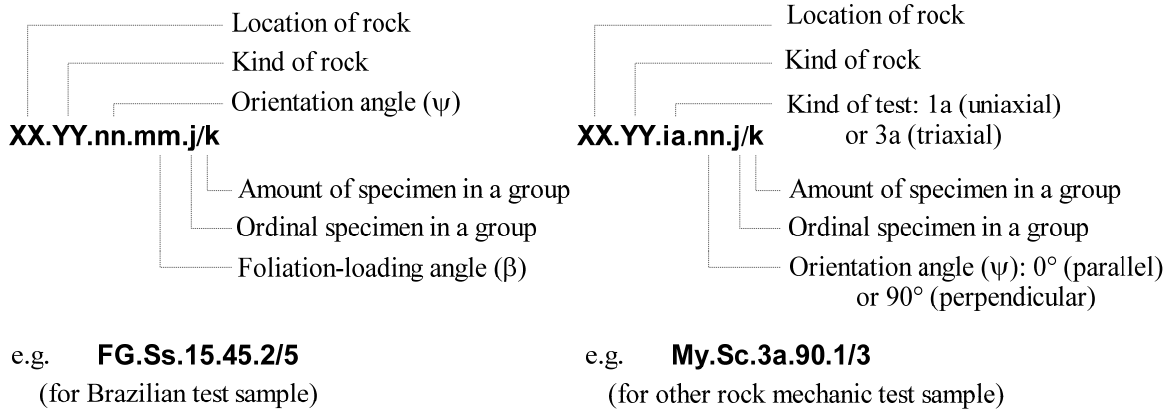
Figure 3-2: Specimen nomenclature

3.3 Sample preparation

At the beginning of the sample preparations, cylindrical cores with a diameter of 50 mm were drilled out of larger rock blocks. It was especially ensured that the axis of the cylindrical cores have a predefined direction to the bedding planes: ψ = 0°, 15°, 30°, 45°, 60°, 75° and 90°. The cores were then cut into test specimens of suitable length, the end

faces ground and polished. After the specimen's dimensions had been measured and found to meet standards, they were stored in dry air at room temperature.

The experimental arrangement for the Brazilian tests is illustrated in Figure 3-1. The foliation planes were found to be the true planes of weakness, characterized by very small cohesive and tensile strength. The sample preparations and tests strictly followed the stipulations of the International Society for Rock Mechanics [5]. The specimens were all disc-shaped with a diameter $D = 50$ mm and a thickness $t = 25$ mm. A sum total of 555 Brazilian tensile tests were carried out: Postaer Sandstone (**FG.Ss**) with a total of 97 specimens, Freiberger Gneiss (**FG.Gs**) - 126, Leubsdorfer Gneiss (**Le.Gs**) - 160 and Mayen Mosel-Slate (**My.Sc**) - 172.

Further tests were carried out to determine additional geophysical and geomechanical properties. Ultrasonic measurements were used to determine effective porosity, elastic wave velocity, density and dynamic elastic constants while uniaxial and triaxial compression tests were used to obtain Young's modulus, Poisson's ratio, friction angle and cohesion. The Brazilian tests were carried out in accordance with the ISRM- and DGGT-recommendations for cylindrical samples with diameter $D = 50$ mm and height to diameter ratio $h/D = 0.5$.

3.4   Ultrasonic measurements

Sample	My.Sc.3a. 90.1/3	My.Sc.3a. 90.2/3	My.Sc.3a. 90.3/3	Le.Gs.3a. 90.1/3	Le.Gs.3a. 90.2/3	Le.Gs.3a. 90.3/3
Length (cm)	10.09	10.16	10.15	9.99	10.15	10.15
Diameter (cm)	5.01	5.01	5.01	5.01	5.01	5.01
Density (kg/m^3)	2774	2774	2774	2716	2716	2716
Dynamic Poisson's ratio (-)	0.40	0.36	0.40	0.20	0.41	0.39
Dynamic Young's modulus (GPa)	21.36	20.02	18.79	50.15	22.15	19.20
Dynamic shear modulus (GPa)	7.63	7.37	6.69	20.83	7.88	6.92
Pulse-wave (Hz)	13428	12970	12512	21362	13733	12817

Table 3-2: Le.Gs and My.Sc sample data and ultrasonic measurements results.

3.5 Uniaxial and triaxial compression tests

To determine the constitutive model parameters of the rock structure components, uniaxial and triaxial tests were carried out on cylindrical test specimens with diameter $D = 50$ mm and a height to diameter ratio $h/D = 2.0$.

To determine the anisotropic properties, tests were done in which the planes of anisotropy were either parallel or perpendicularly oriented to the loading direction.

3.5.1 Uniaxial compression test

The peak strength σ_D was obtained during the uniaxial compression tests and the Young's modulus determined at 50% peak load E_{50} (Table 3-3) from deformation measurements.

Sample	σ_D (MPa)	E_{50} (GPa)
Le.Gs.1a.0.1/3	171.41	16.60
Le.Gs.1a.0.2/3	177.19	14.67
Le.Gs.1a.0.3/3	180.19	13.61
Average	176.26	14.96
Le.Gs.1a.90.1/3	173.84	12.43
Le.Gs.1a.90.2/3	179.32	14.43
Le.Gs.1a.90.3/3	190.67	14.36
Average	181.28	13.74
My.Sc.1a.0.1/3	79.58	11.78
My.Sc.1a.0.2/3	122.62	16.46
My.Sc.1a.0.3/3	148.70	18.48
Average	116.97	15.57
Le.Gs.1a.90.1/3	203.97	12.95
Le.Gs.1a.90.2/3	218.63	12.74
Le.Gs.1a.90.3/3	225.93	12.21
Average	216.18	12.63
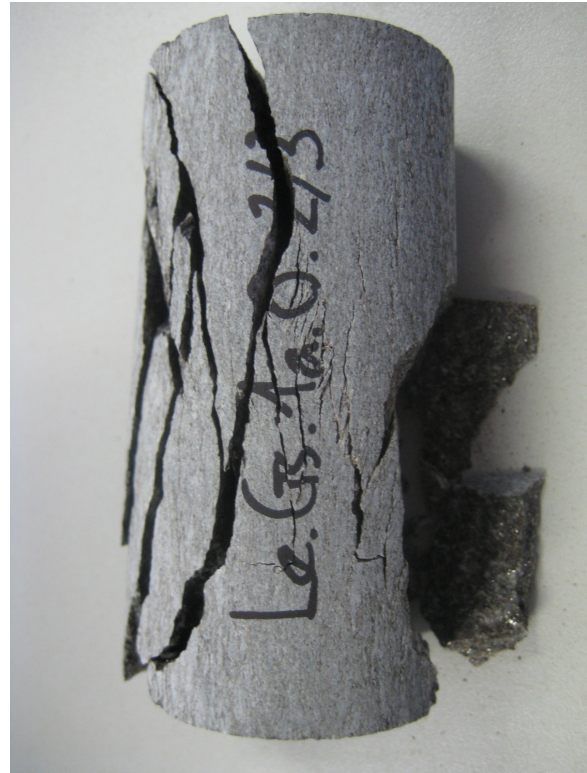
Table 3-3: Results of unconfined compression tests on Le.Gs and My.Sc

Figure 3-3: Typical failure patterns in Le.Gs.1a.2/3 under unconfined compression test

3.5.2   Triaxial compression tests

The triaxial tests were carried out either in single- (Table 3-4), or multi-stages (Figure 3-4 and Table 3-5)

$\psi = 90°$	σ_3 (MPa)	σ_1 (MPa)	
		Le.Gs.0.1/2	My.Sc.0.1/2
	4.9	225.1	-
	6.51	-	163.47
$\psi = 0°$	σ_3 (MPa)	Le.Gs.90.1/2	My.Sc.90.1/2
	2.39	194.03	-
	3	-	233.12

Table 3-4: Results of single-stage triaxial compression tests on Le.Gs and My.Sc

From the triaxial tests, peak and residual strength values were obtained. The multi-stage triaxial test has the advantage of obtaining several peak and residual strength values from a single specimen under different confining pressures.
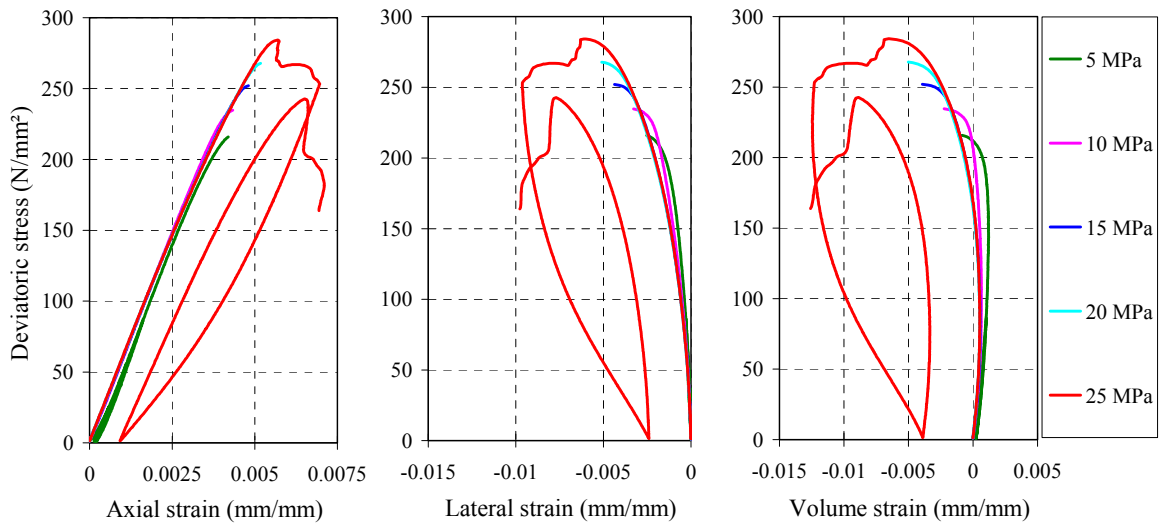
Figure 3-4: Results of multi-stage tests on Le.Gs.3a.90.3/3 samples.

$\psi = 90°$	σ_3 (MPa)	σ_1 (MPa)					
		My.Sc.3a. 90.1/3	My.Sc.3a. 90.2/3	My.Sc.3a. 90.3/3	Le.Sc.3a. 90.1/3	Le.Sc.3a. 90.2/3	Le.Sc.3a. 90.3/3
	5	253	241	253	151	98	215
	10	278	219	149	160	246	235
	15	284	206	207	174	268	252
	20	261	233	140	189	287	268
	25	273	276	321	202	297	284

Table 3-5: Results of multi-stage triaxial compression tests on Le.Gs and My.Sc

The failure envelopes for the Mohr-Coulomb- and Hoek-Brown-failure criteria deduced from the multi-stage triaxial compression tests are presented in Figure 3-5 & 3-6.
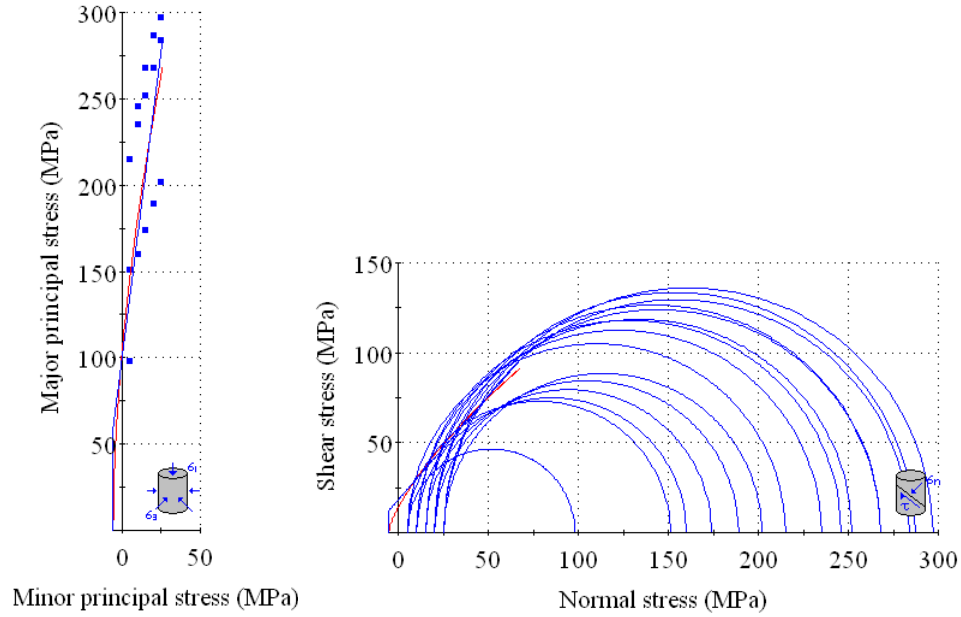
Figure 3-5: Results of multi-stage triaxial compression tests on Le.Gs.3a.90 samples
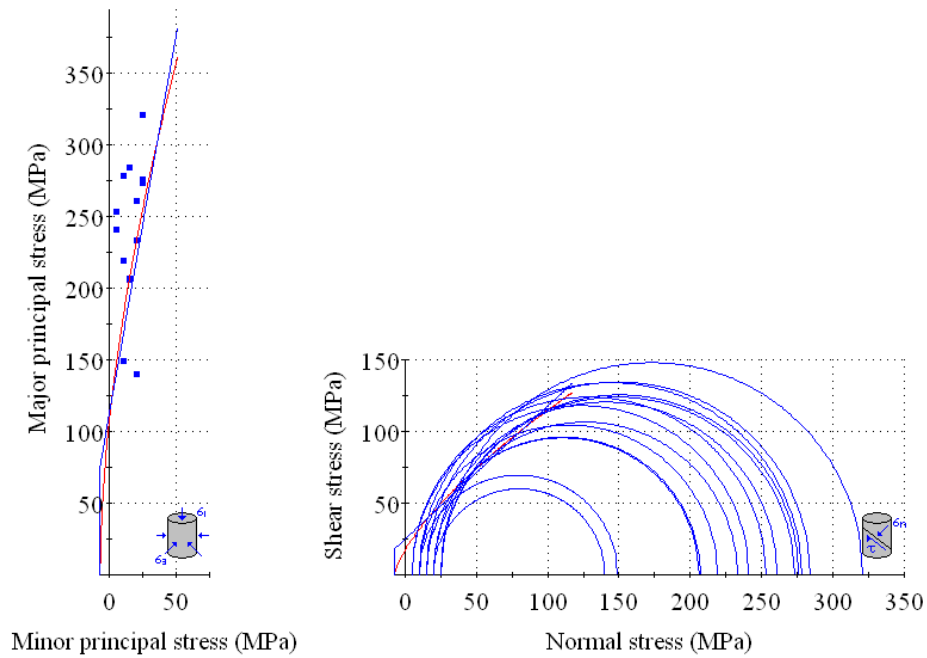
Figure 3-6: Results of multi-stage triaxial compression tests on My.Sc.3a.90

3.6   Brazilian tensile strength tests

3.6.1   Test apparatus

The rock mechanics test system MTS 20/M (Figure 3-7) was employed for the indirect tensile tests. MTS 20/M is a computer servo-controlled machine with a maximum load capacity of ±100 kN and an accuracy of 0.01%. The TestWorks-4-System-Software was used to conduct computer controlled tests. Tests on stress or strain control in tension or in compression could be performed. The load is measured by the load cell, the displacement by a linear variable differential transformer (LVDT) and the strain by an extensometer with an accuracy of up to 0.0002%. The discs with an unchanged loading rate of 200 N/sec, were loaded up to failure.

ISRM [5] suggests that the load be applied via two steel loading jaws in contact with a disc-shaped specimen, the radius of the jaws 1.5 times the specimen radius and that the disc loading jaw contact be a finite arc rather than a single point.

Figure 3-7: Loading jaws of rock mechanics test system MTS 20/M [3].

---

[3] The pictures were taken in the Rock Mechanics Laboratories, Geotechnical Institute, TU Bergakademie Freiberg.

3.6.2 Laboratory test results

3.6.2.1 Postaer Sandstone (FG.Ss): (97 tests)

Tensile strength of the FG.Ss samples (MPa)							
Sample	**β=0°**	**β=15°**	**β=30°**	**β=45°**	**β=60°**	**β=75°**	**β=90°**
FG.Ss.0.0-90	3.232	3.486	3.819	-	3.563	3.720	3.025
	3.338	3.621	4.030	2.750	3.580	3.830	3.204
	3.387	3.720	4.242	3.074	3.871	4.065	3.536
	3.741	4.181	4.269	3.595	3.910	4.107	3.578
	3.952	4.208	4.289	3.842	4.482	4.487	3.610
FG.Ss.15.0-90	3.154	-	3.100	-	3.085	-	1.769
	3.448	-	3.255	-	3.554	-	3.849
	3.749	-	3.941	-	3.557	-	4.126
FG.Ss.30.0-90	3.031	-	2.907	-	3.251	-	2.945
	3.519	-	3.333	-	3.425	-	3.461
	3.589	-	3.397	-	3.488	-	3.693
FG.Ss.45.0-90	3.161	-	2.908	-	3.583	-	3.117
	3.487	-	3.341	-	3.591	-	3.169
	3.765	-	4.048	-	3.621	-	3.377
FG.Ss.60.0-90	2.774	-	2.738	-	2.674	-	2.852
	3.199	-	3.546	-	3.208	-	3.400
	3.787	-	3.768	-	-	-	3.416
FG.Ss.75.0-90	3.085	-	3.084	-	2.137	-	3.141
	3.251	-	3.197	-	3.178	-	3.245
	3.689	-	3.678	-	3.693	-	3.747
FG.Ss.90	3.820	-	3.820	-	3.820	-	3.820

Table 3-6: Results of Brazilian tensile strength test on FG.Ss

Average tensile strength of the FG.Ss samples (MPa)							
	ψ = 0°	**ψ = 15°**	**ψ = 30°**	**ψ = 45°**	**ψ = 60°**	**ψ = 75°**	**ψ = 90°**
β = 0°	3.489	3.450	3.379	3.471	3.253	3.850	3.820
β = 15°	3.759	-	-	-	-	-	-
β = 30°	4.136	3.521	3.365	3.694	3.142	3.437	3.820
β = 45°	3.396	-	-	-	-	-	-
β = 60°	3.781	3.399	3.388	3.599	2.941	3.003	3.820
β = 75°	4.065	-	-	-	-	-	-
β = 90°	3.391	3.987	3.577	3.247	3.408	3.193	3.820

Table 3-7: Average results of Brazilian tensile strength test on FG.Ss

(a) Polar diagram   (b) Linear diagram
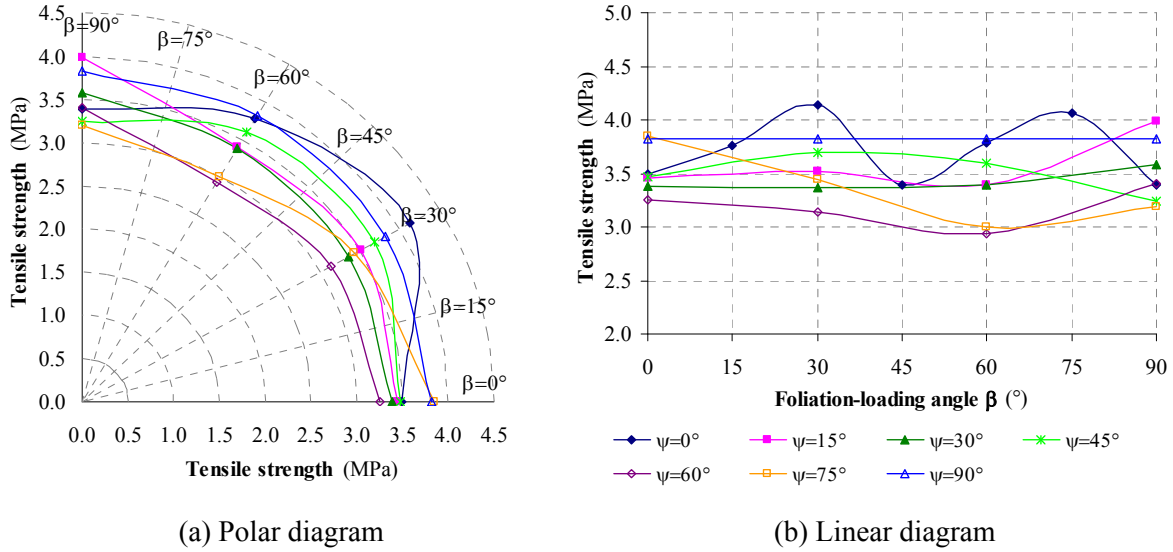
Figure 3-8: Average tensile strength results of FG.Ss samples as functions of foliation-loading direction (β) and orientation angle (ψ)
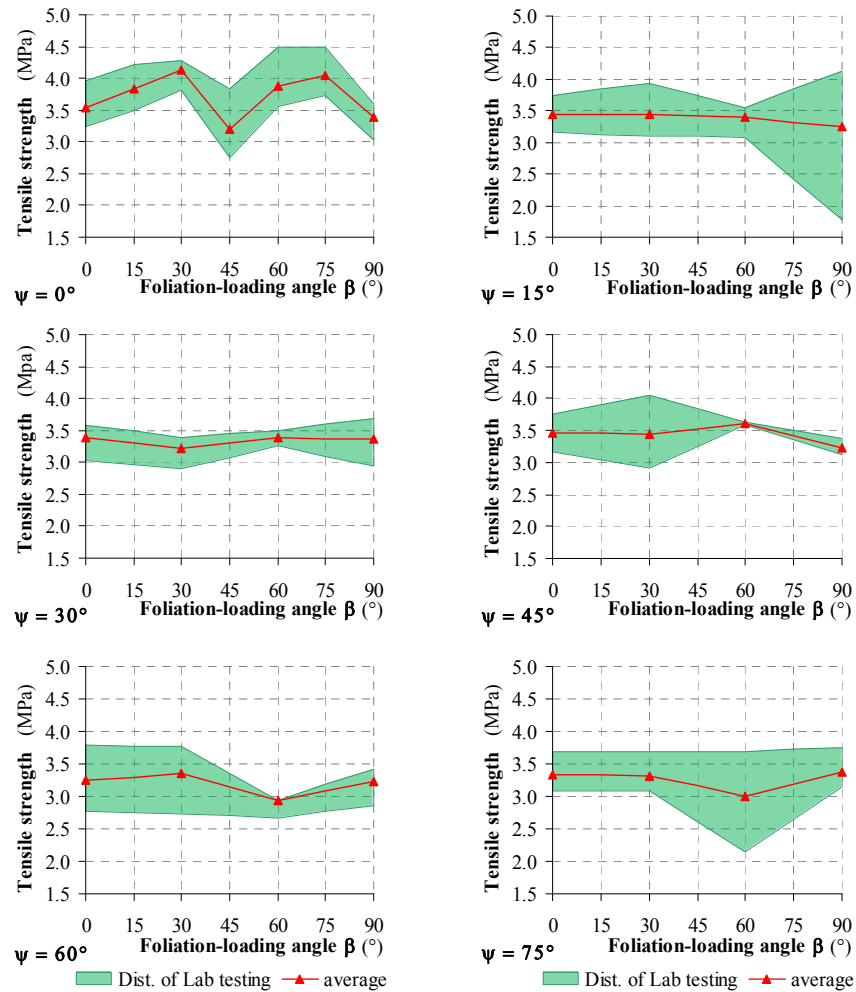
Figure 3-9: Tensile strength results of FG.Ss samples as functions of foliation-loading direction (β) and orientation angle (ψ) with minimum and maximum values; green: Min-Max-Ranges.
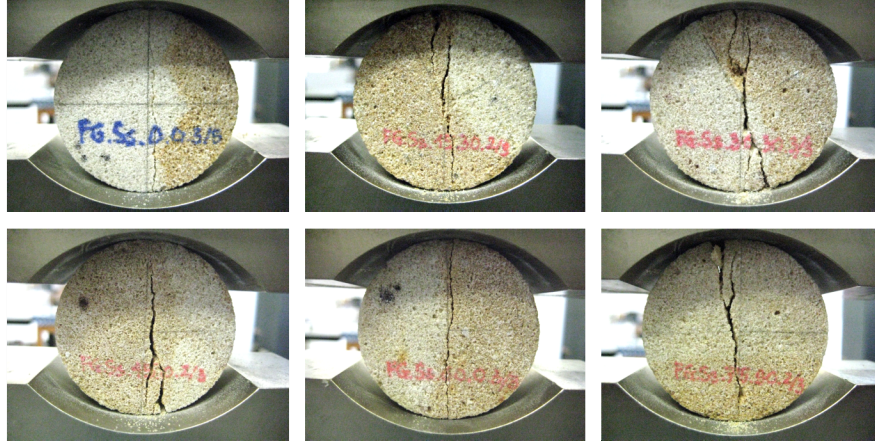
Figure 3-10: Typical fracture patterns in FG.Ss specimens (see also Appendix 3.1)
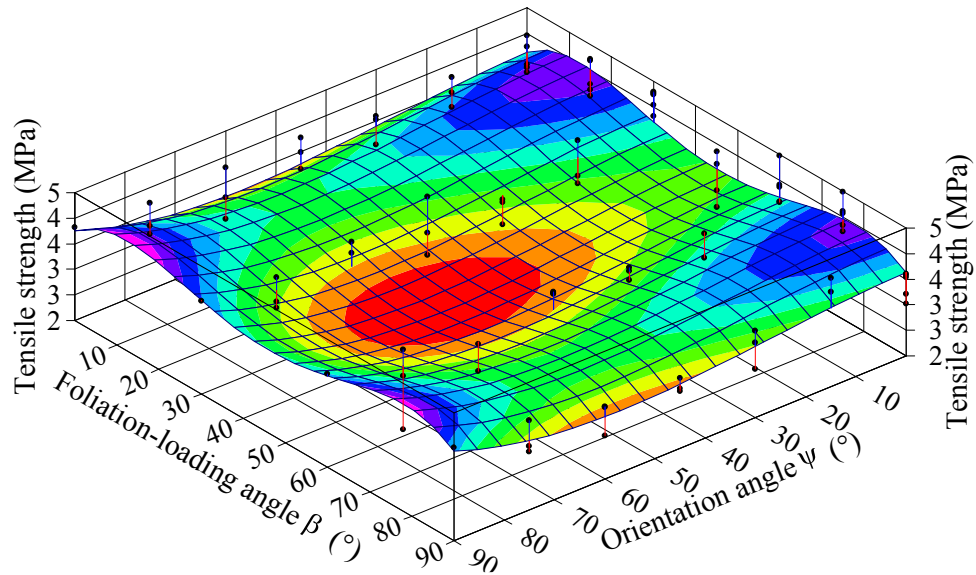
Number of observations = 97
Coefficient of Multiple Determination (R^2) = 0.314

Figure 3-11: Tensile strength results of FG.Ss samples as functions of foliation-loading direction (β) and orientation angle (ψ) with regression surface deduced from multiple regression analysis and determined by coefficient of multiple determination.

3.6.2.2 Postaer Sandstone (FG.Gs): (126 tests)

Tensile strength of the FG.Gs samples (MPa)							
Sample	β=0°	β=15°	β=30°	β=45°	β=60°	β=75°	β=90°
FG.Gs.0.0-90	5.556	5.413	6.804	7.734	7.666	5.441	13.735
	5.939	5.973	7.230	8.236	7.908	10.416	15.038
	6.566	6.019	7.768	8.343	8.259	10.757	16.463
	6.764	7.070	8.479	8.839	9.434	11.623	16.751
FG.Gs.15.0-90	6.106	-	5.682	8.290	8.441	-	16.540
	10.020	-	7.192	9.104	8.572	-	16.687
	11.403	-	8.530	9.944	8.680	-	16.842
	-	-	8.760	10.183	10.394	-	18.550
FG.Gs.30.0-90	7.112	-	4.196	7.568	9.702	-	11.234
	8.195	-	5.233	7.605	11.341	-	13.625
	8.650	-	5.852	9.558	11.444	-	14.027
	9.061	-	13.627	11.638	12.502	-	14.948
FG.Gs.45.0-90	11.270	-	12.476	12.062	12.062	-	14.239
	13.730	-	15.008	13.366	13.006	-	14.843
	14.403	-	-	16.271	14.117	-	15.373
	14.730	-	-	-	15.061	-	16.448
FG.Gs.60.0-90	16.328	-	8.074	15.739	13.278	-	14.283
	16.558	-	10.046	15.818	13.785	-	14.613
	16.563	-	15.027	17.057	15.050	-	14.923
	17.631	-	15.086	-	15.289	-	15.357
FG.Gs.75.0-90	12.574	-	15.402	13.466	14.960	-	12.661
	13.733	-	16.537	14.518	15.734	-	14.835
	14.235	-	16.593	16.277	16.979	-	15.172
	17.114	-	17.662	16.533	18.193	-	16.446
FG.Gs.90	18.994	19.836	20.605				

Table 3-8: Results of Brazilian tensile strength tests on FG.Gs

Average tensile strength of the FG.Gs samples (MPa)							
	ψ = 0°	ψ = 15°	ψ = 30°	ψ = 45°	ψ = 60°	ψ = 75°	ψ = 90°
β = 0°	6.206	9.176	8.635	14.288	16.483	13.514	19.812
β = 15°	5.802	-	-	-	-	-	19.812
β = 30°	7.768	8.161	5.094	13.742	12.058	16.548	19.812
β = 45°	8.288	9.743	8.244	13.9	16.205	15.199	19.812
β = 60°	7.944	8.564	11.762	13.561	14.35	16.466	19.812
β = 75°	10.416	-	-	-	-	-	19.812
β = 90°	16.751	16.69	14.2	14.818	14.794	15.484	19.812

Table 3-9: Average results of Brazilian tensile strength test on FG.Gs

(a) Polar diagram   (b) Linear diagram
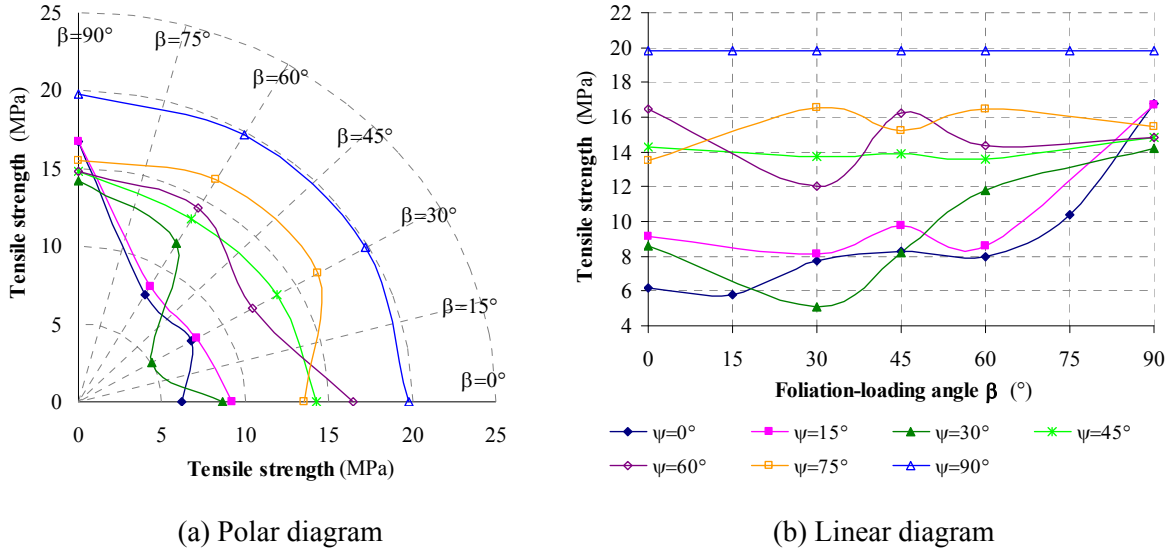
Figure 3-12: Average tensile strength results of FG.Gs samples as functions of foliation-loading direction (β) and orientation angle (ψ)
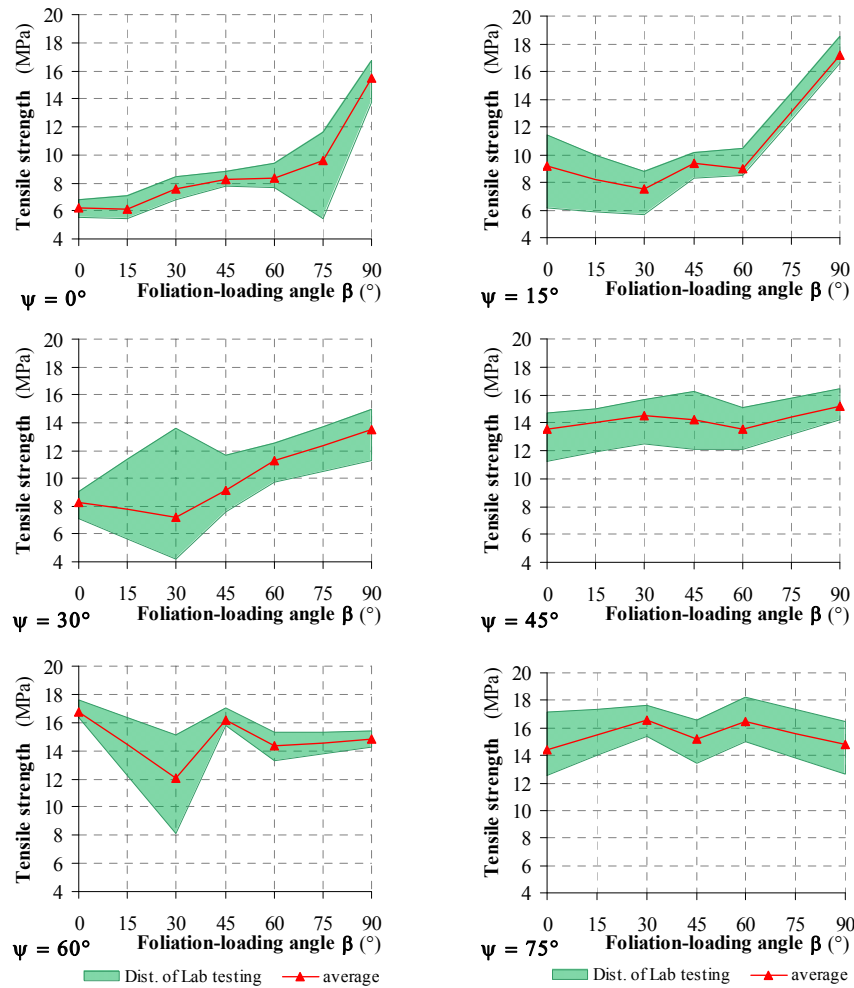
Figure 3-13: Tensile strength results of FG.Gs samples as functions of foliation-loading direction (β) and orientation angle (ψ) with minimum and maximum values; green: Min-Max-Ranges.
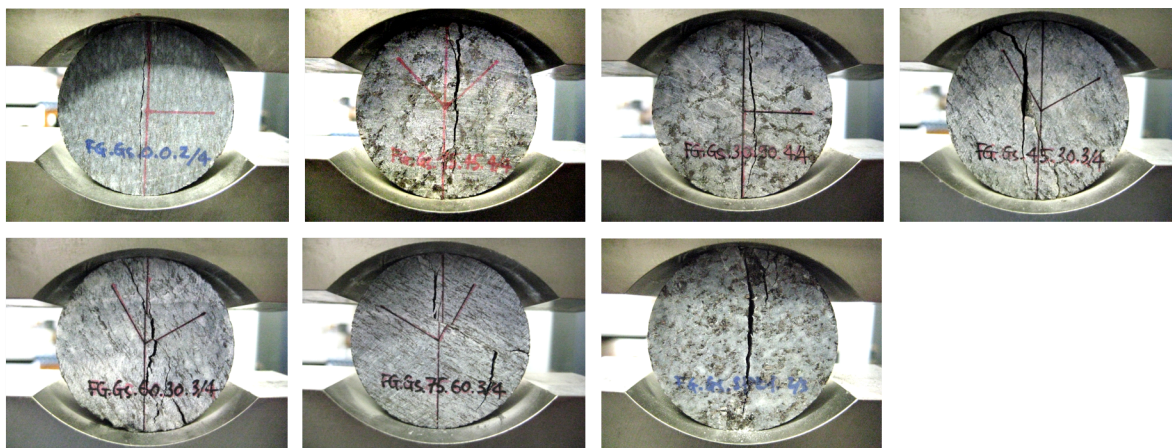
Figure 3-14: Typical fracture patterns of FG.Gs specimen (see also Appendix 3.2)

Number of observations = 126
Coefficient of Multiple Determination (R^2) = 0.870

Figure 3-15: Tensile strength results of FG.Gs samples as functions of foliation-loading direction (β) and orientation angle (ψ) with regression surface deduced from multiple regression analysis and determined by coefficient of multiple determination.

3.6.2.3 Leubsdorfer Gneiss (Le.Gs): (160 tests)

Tensile strength of the Le.Gs samples (MPa)							
Sample	β=0°	β=15°	β=30°	β=45°	β=60°	β=75°	β=90°
Le.Gs.0.0-90	7.686	7.845	8.827	11.500	12.835	14.312	12.830
	8.608	8.864	9.306	11.807	13.048	16.167	18.745
	9.035	9.219	10.145	12.674	14.221	16.615	19.323
	9.345	10.025	10.761	-	14.450	17.425	19.739
Le.Gs.15.0-90	7.992	6.269	8.637	12.835	9.870	13.878	16.186
	8.453	9.289	9.452	13.021	13.703	16.352	16.611
	8.578	9.338	10.337	13.211	14.170	16.450	16.766
	10.357	10.356	11.609	-	14.298	17.103	19.972
Le.Gs.30.0-90	11.706	11.501	10.311	-	15.263	7.992	16.271
	12.799	12.089	13.781	12.835	16.672	8.453	17.096
	13.452	12.811	13.900	13.021	18.110	8.578	17.102
	14.207	14.065	14.998	13.211	18.205	10.357	17.266
Le.Gs.45.0-90	13.918	14.850	14.871	17.212	15.244	16.256	15.907
	16.232	16.745	15.539	17.219	15.433	16.681	17.129
	16.494	17.010	16.899	17.322	17.295	17.675	17.136
	20.693	17.095	17.414	-	17.537	18.299	18.266
Le.Gs.60.0-90	11.667	4.060	14.673	-	16.419	15.892	18.421
	16.921	9.478	16.917	17.251	17.850	17.472	18.567
	18.599	16.886	16.986	20.754	19.634	17.916	18.798
	19.580	19.117	18.138	21.239	20.595	18.299	20.155
Le.Gs.75.0-90	20.393	22.191	14.623	21.522	12.951	15.559	15.951
	22.503	22.206	17.155	23.665	19.491	21.581	16.384
	23.421	24.585	22.533	23.746	22.086	22.370	18.968
Le.Gs.90	16.750	18.328	22.530	24.653			

Table 3-10: Results of Brazilian tensile strength test on Le.Gs

Average tensile strength of the Le.Gs samples (MPa)							
	ψ = 0°	ψ = 15°	ψ = 30°	ψ = 45°	ψ = 60°	ψ = 75°	ψ = 90°
β = 0°	8.669	8.845	13.041	16.834	16.692	22.106	20.565
β = 15°	8.988	8.813	12.617	16.425	12.385	22.994	20.565
β = 30°	9.760	10.009	13.247	16.181	16.678	18.104	20.565
β = 45°	11.994	13.023	13.023	17.251	19.748	22.978	20.565
β = 60°	13.638	13.010	17.062	16.377	18.625	18.176	20.565
β = 75°	16.130	15.946	8.845	17.228	17.395	19.837	20.565
β = 90°	17.659	17.384	16.934	17.110	18.986	17.101	20.565

Table 3-11: Average results of Brazilian tensile strength test on Le.Gs

(a) Polar diagram
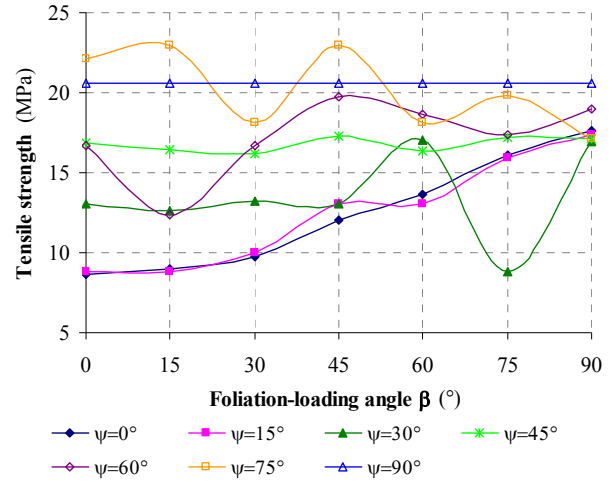
(b) Linear diagram

Figure 3-16: Average tensile strength results of Le.Gs samples as functions of foliation-loading direction (β) and orientation angle (ψ)
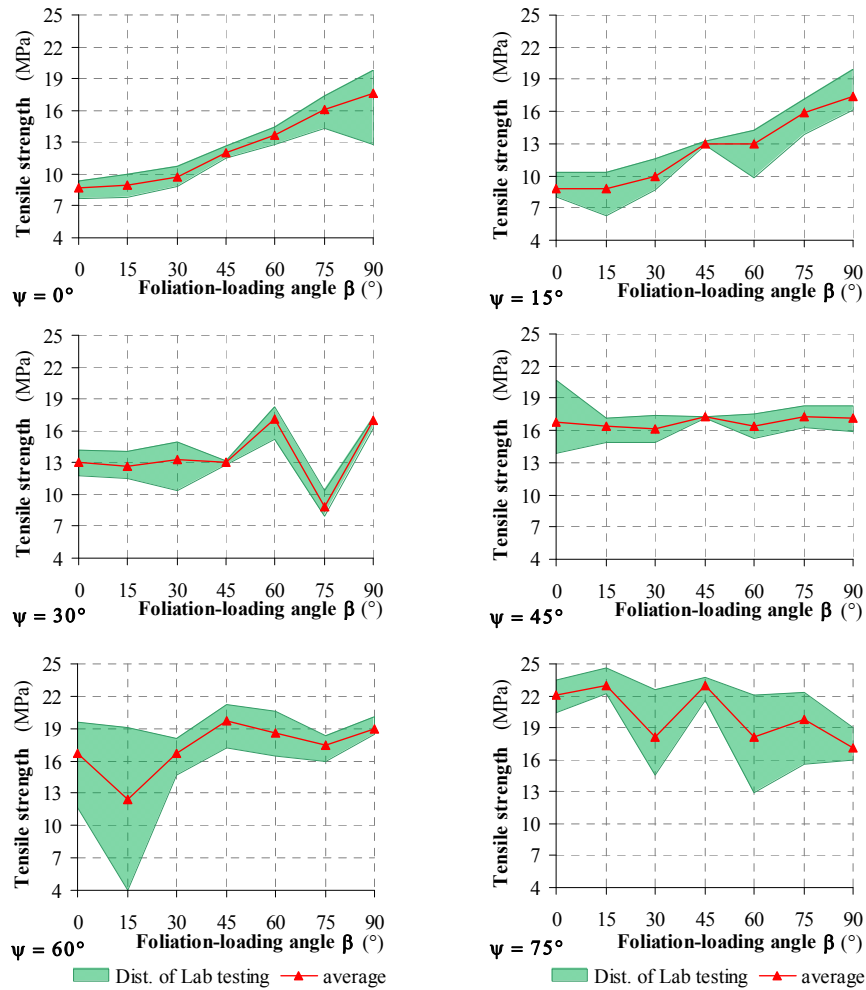
Figure 3-17: Tensile strength results of Le.Gs samples as functions of foliation-loading direction (β) and orientation angle (ψ) with minimum and maximum values; green: Min-Max-Ranges.
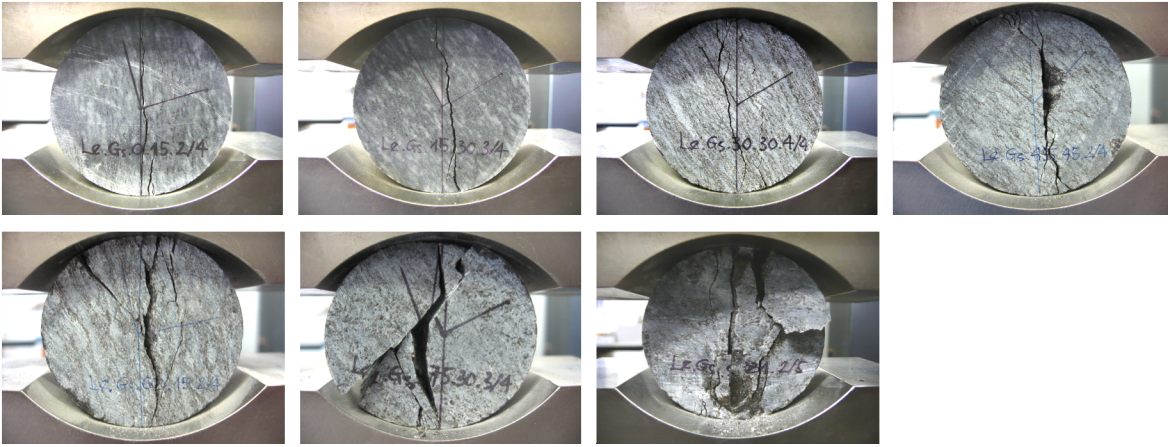
Figure 3-18: Typical fracture patterns of Le.Gs specimen (see also Appendix 3.3)

Number of observations = 160
Coefficient of Multiple Determination (R^2) = 0.708
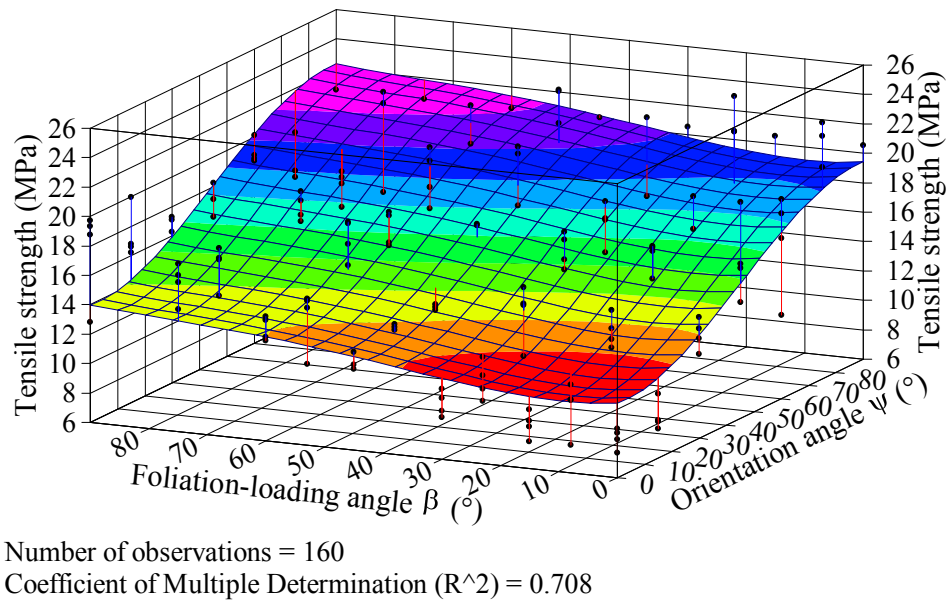
Figure 3-19: Tensile strength results of Le.Gs samples as functions of loading direction (β) and orientation angle (ψ) with regression surface deduced from multiple regression analysis and determined by coefficient of multiple determination.

3.6.2.4 Mayen Mosel-Slate (My.Sc): (172 tests)

Tensile strength of the My.Sc samples (MPa)							
Sample	**β=0°**	**β=15°**	**β=30°**	**β=45°**	**β=60°**	**β=75°**	**β=90°**
My.Sc.0.0-90	2.385	2.595	2.375	3.390	3.389	8.106	14.878
	3.143	3.225	3.670	5.631	3.670	8.925	15.013
	5.353	4.581	4.579	5.972	3.846	9.419	15.312
	5.985	4.782	4.975	6.582	7.811	10.189	17.022
My.Sc.15.0-90	5.170	3.002	3.368	-	7.210	6.226	7.878
	5.254	4.281	3.731	5.334	7.449	7.091	8.583
	6.318	5.562	4.562	6.005	7.953	9.647	11.084
	6.940	5.817	6.287	6.130	8.363	10.204	11.739
My.Sc.30.0-90	6.443	6.930	6.284	-	5.028	4.800	7.928
	6.481	7.069	6.523	7.492	7.545	5.822	10.627
	8.726	8.212	8.103	8.528	7.909	7.854	11.302
	9.397	8.426	8.297	8.729	8.151	9.487	12.395
My.Sc.45.0-90	9.892	8.298	8.049	-	8.244	7.518	9.913
	11.013	8.639	8.158	6.330	8.518	9.301	10.003
	11.092	8.763	8.623	8.471	8.733	9.846	12.023
	11.338	12.446	10.585	10.058	9.043	10.150	12.036
My.Sc.60.0-90	13.287	12.088	11.571	-	5.465	10.470	8.100
	13.313	12.145	11.692	9.104	8.965	10.950	10.184
	14.807	14.469	13.897	11.676	11.407	11.394	12.176
	18.367	18.240	17.007	12.316	11.549	11.531	12.226
My.Sc.75.0-90	13.091	17.499	17.677	-	12.389	17.499	13.301
	20.469	21.217	22.679	18.509	12.506	21.217	15.147
	21.781	21.900	23.977	18.895	13.119	21.900	19.916
	23.348	23.026	24.166	19.600	19.730	23.026	22.114
My.Sc.90	18.164	18.759	19.454	19.869	21.195	22.124	23.446

Table 3-12: Results of Brazilian tensile strength test on My.Sc

Average tensile strength of all My.Sc specimens (MPa)							
	ψ = 0°	**ψ = 15°**	**ψ = 30°**	**ψ = 45°**	**ψ = 60°**	**ψ = 75°**	**ψ = 90°**
β = 0°	4.216	5.921	7.762	10.834	14.943	19.672	21.721
β = 15°	3.796	4.666	7.659	9.537	14.236	20.911	21.721
β = 30°	3.900	4.487	7.302	8.854	13.542	22.125	21.721
β = 45°	5.394	5.823	8.250	8.286	11.032	19.001	21.721
β = 60°	4.679	7.744	7.158	8.634	9.347	14.436	21.721
β = 75°	9.160	8.292	6.991	9.204	11.086	20.911	21.721
β = 90°	15.556	9.821	10.563	10.994	10.671	17.619	21.721

Table 3-13: Average results of Brazilian tensile strength test on My.Sc
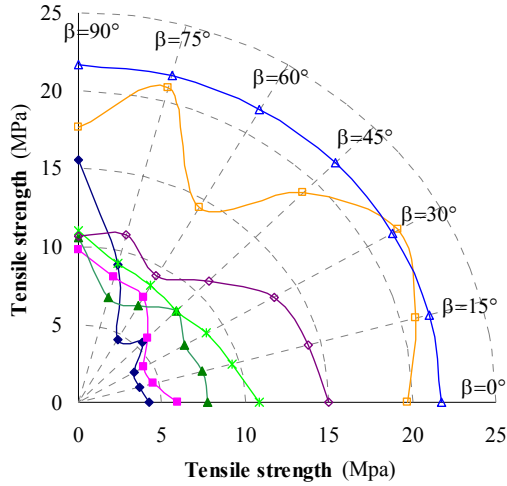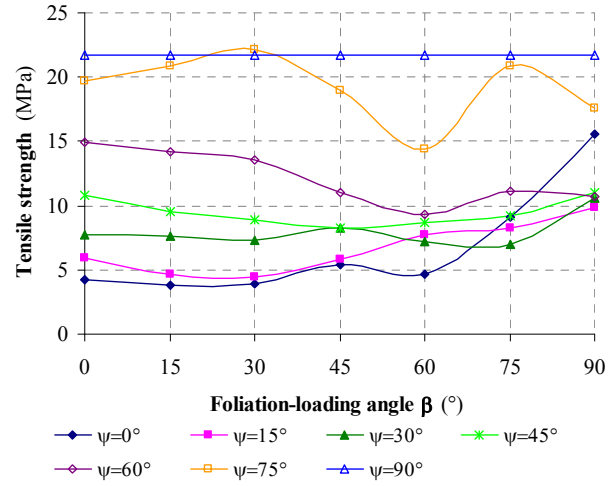
(a) Polar diagram   (b) Linear diagram

Figure 3-20: Average tensile strength results of My.Sc samples as functions of foliation-loading direction (β) and orientation angle (ψ)
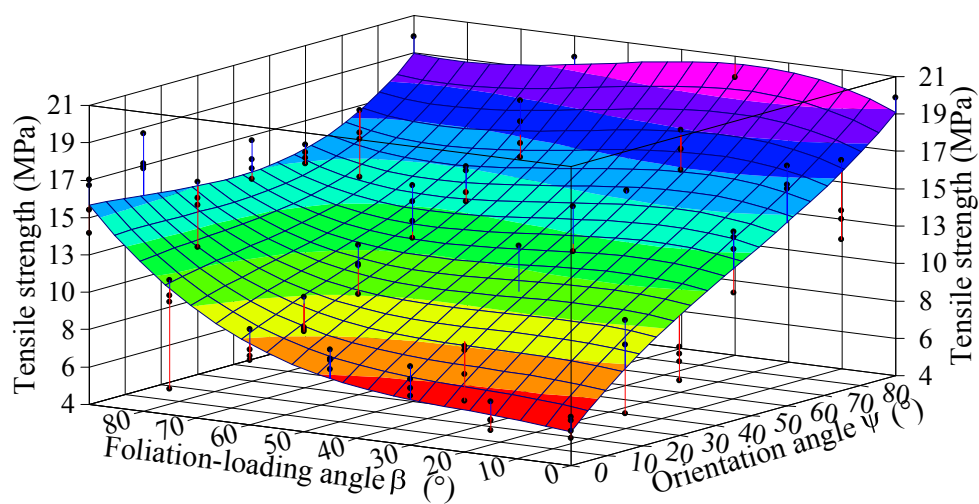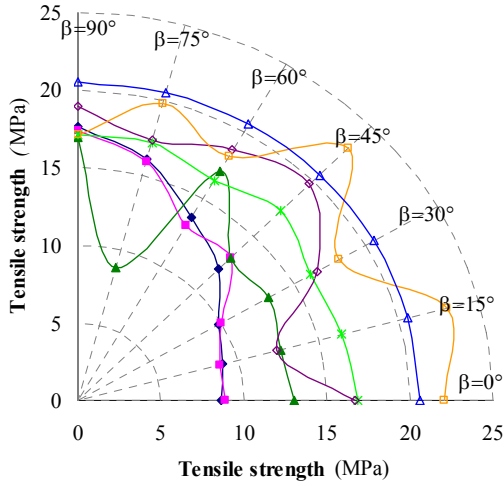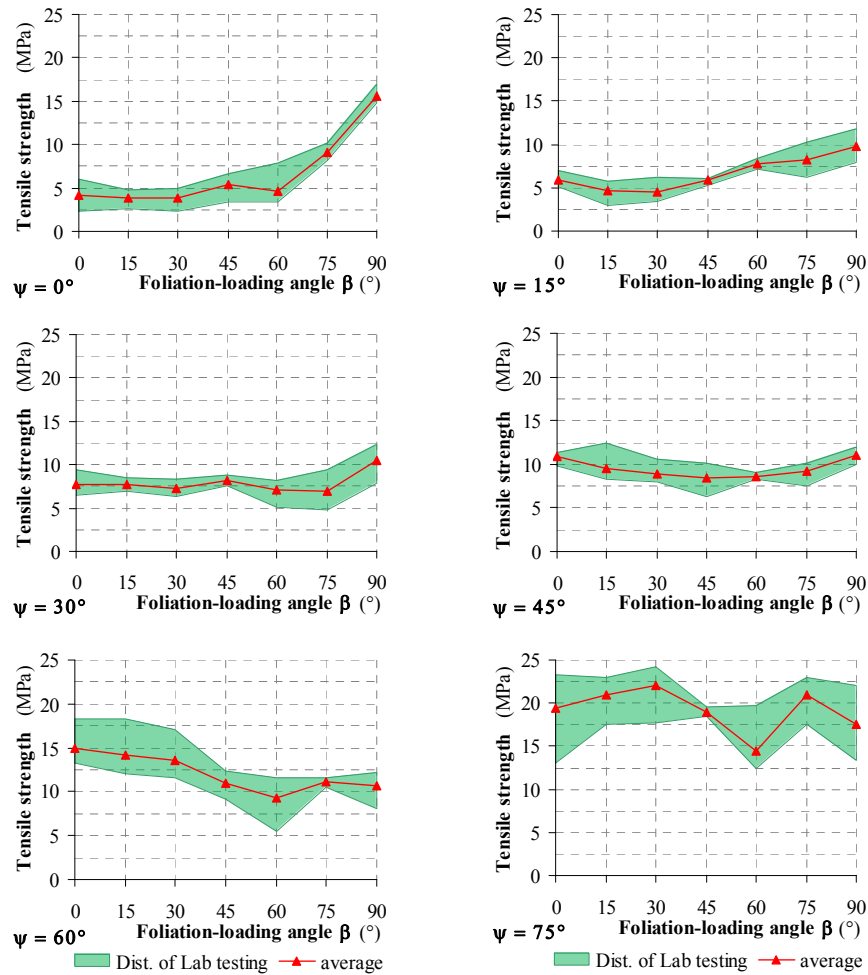

Figure 3-21: Tensile strength results of My.Sc samples as functions of foliation-loading direction (β) and orientation angle (ψ) with minimum and maximum values; green: Min-Max-Ranges.
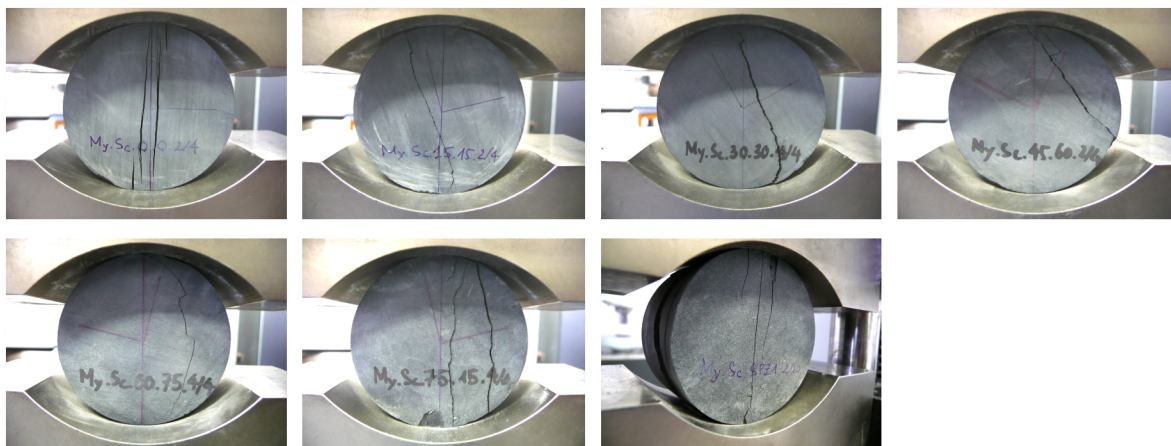
Figure 3-22: Typical fracture patterns of My.Sc specimen (see also Appendix 3.4)
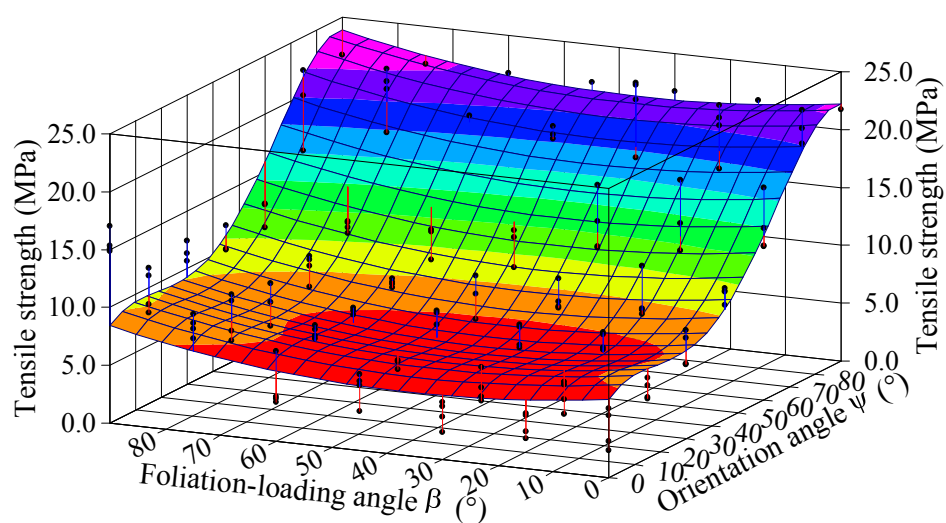
Number of observations = 172
Coefficient of Multiple Determination (R^2) = 0.871

Figure 3-23: Tensile strength results of My.Sc samples as functions of foliation-loading direction (β) and orientation angle (ψ) with regression surface deduced from multiple regression analysis and determined by coefficient of multiple determination.

3.6.3 Interpretation of the test results

3.6.3.1 Interpretation of tensile strength values

Variant Statistics				
Rock	**FG.Ss**	**FG.Gs**	**Le.Gs**	**My.Sc**
Count	97	126	160	172
Median	3.546	12.833	16.244	9.408
Standard Deviation	0.458	3.961	4.231	5.692
Variance	0.210	15.693	17.905	32.401
Standard Error	0.046	0.353	0.335	0.434
Coefficient of variation	13 %	31 %	26 %	61 %

Table 3-14: Total tensile strength variant statistic values of the rock materials

The FG.Ss material has revealed relatively low standard deviations and consequently low coefficients of variations (below 13% according to Table 3-14). The fracture pattern of all FG.Ss samples was more or less identical and is characterized by a central tensile crack independent on the sample orientation (see Appendix 3.1). Therefore, this Sandstone can be considered as quasi-isotropic and orientation of sample in relation to loading jaws is practically unimportant.

	ψ	β	FG.Ss	FG.Gs	Le.Gs	My.Sc
ψ	1.00000	-0.05336	-0.27708	0.69157	0.60162	0.79195
β	-0.05336	1.00000	-0.02948	0.28078	0.28568	0.04580
FG.Ss	-0.27708	-0.02948	1.00000	-0.09302	0.01118	0.01959
FG.Gs	0.69157	0.28078	-0.09302	1.00000	0.73853	0.75364
Le.Gs	0.60162	0.28568	0.01118	0.73853	1.00000	0.66316
My.Sc	0.79195	0.04580	0.01959	0.75364	0.66316	1.00000

Table 3-15: Tensile strength correlation coefficients of the rock materials

The correlation results given in Table 3-15 indicates that influence of the orientation angle ψ is stronger than the loading direction β on the tensile strength in all Gneisses and Slate, especially the correlation coefficient is 0.69157 and 0.28078 for FG.Gs Gneiss, 0.60162 and 0.28568 for Le.Gs Gneiss, 0.79195 and 0.04580 for My.Sc Slate with respect to ψ and β.

The Student's *t*-distribution was used to determine the mean value and standard deviation for each group of specimen with either the same orientation angles or foliation-loading angle (Table 3-16 & 3-17).

Statistics of tensile strength values as a function of orientation angle (ψ)																
Rock	FG.Ss				FG.Gs				Le.Gs				My.Sc			
Orient. Angle	N - sample	Mean	Std. Dev.	Coef. Var.	N - sample	Mean	Std. Dev.	Coef. Var.	N - sample	Mean	Std. Dev.	Coef. Var.	N - sample	Mean	Std. Dev.	Coef. Var.
ψ = 0°	34	3.72	0.31	8 %	28	9.03	3.72	41 %	27	12.41	3.55	29 %	27	6.67	4.33	65 %
ψ = 15°	12	3.59	0.27	8 %	19	10.47	3.53	34 %	27	12.43	3.40	27 %	27	6.68	1.99	30 %
ψ = 30°	12	3.43	0.10	3 %	20	9.59	3.50	36 %	27	13.54	2.81	21 %	27	7.96	1.23	15 %
ψ = 45°	12	3.50	0.19	5 %	17	14.06	0.50	4 %	27	16.77	0.44	3 %	27	9.48	1.06	11 %
ψ = 60°	11	3.19	0.20	6 %	19	14.78	1.77	12 %	27	17.22	2.43	14 %	27	12.12	2.10	17 %
ψ = 75°	12	3.37	0.37	11 %	20	15.44	1.23	8 %	21	20.19	2.50	12 %	27	19.24	2.58	13 %
ψ = 90°	4	3.82	-	-	3	19.81	-	-	4	20.57	-	-	10	21.72	-	-

Table 3-16: Statistics of tensile strength values as a function of orientation angle (ψ)

Statistics of tensile strength values as a function of orientation angle (β)																
Rock	FG.Ss				FG.Gs				Le.Gs				My.Sc			
Orient. angle	N - sample	Mean	Std. Dev.	Coef. Var.	N - sample	Mean	Std. Dev.	Coef. Var.	N - sample	Mean	Std. Dev.	Coef. Var.	N - sample	Mean	Std. Dev.	Coef. Var.
β = 0°	34	3.53	0.22	6 %	28	12.59	4.81	38 %	27	15.25	5.31	35 %	27	12.15	6.82	56 %
β = 15°	12	3.79	0.04	1 %	19	12.81	9.91	77 %	27	14.68	5.52	38 %	27	11.79	7.36	62 %
β = 30°	12	3.59	0.33	9 %	20	11.88	5.24	44 %	27	14.93	4.09	27 %	27	11.7	7.67	66 %
β = 45°	12	3.61	0.30	8 %	17	13.06	4.43	34 %	27	16.94	4.33	26 %	27	11.36	6.47	57 %
β = 60°	11	3.42	0.35	10 %	19	13.21	4.22	32 %	27	16.78	2.71	16 %	27	10.53	5.76	55 %
β = 75°	12	3.94	0.17	4 %	20	15.11	6.64	44 %	21	16.56	3.83	23 %	27	12.48	6.16	49 %
β = 90°	4	3.52	0.30	9 %	3	16.08	1.91	12 %	4	17.96	1.34	7 %	10	13.85	4.55	33 %

Table 3-17: Statistics of tensile strength values as a function of foliation-loading angle (β)

Based on the data given in Table 3-16 & 3-17 box plots and Gaussian distribution plots were drawn up (Figure 3-24 to Figure 3-31).

(a) box-plot of tensile strength values   (b) Gaussian distribution of tensile strength
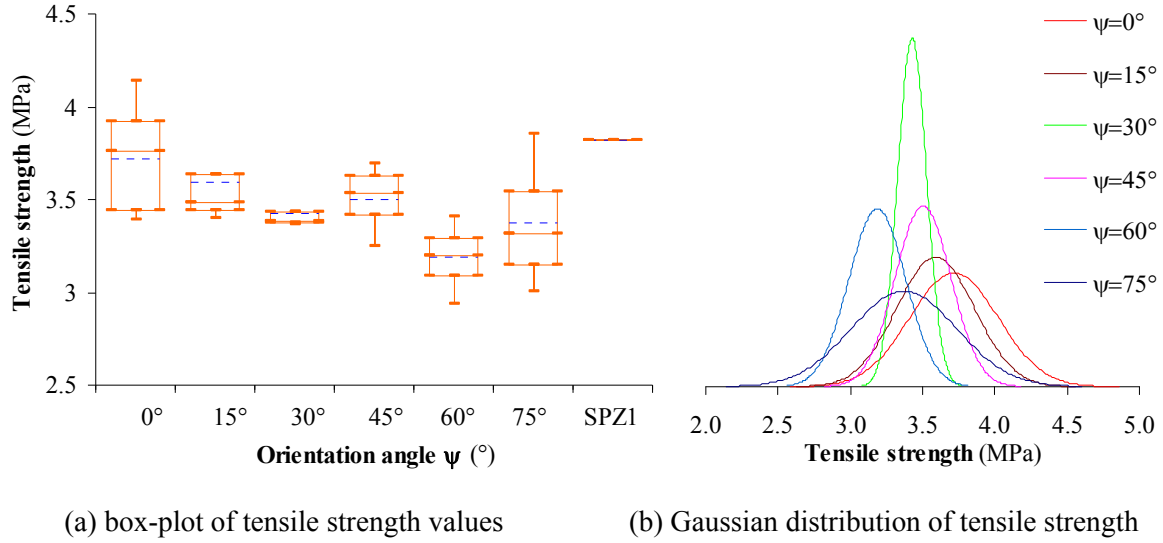
Figure 3-24: Box and Gaussian distribution plots of FG.Ss samples as a function of orientation angle ψ

(a) box-plot of tensile strength values   (b) Gaussian distribution of tensile strength
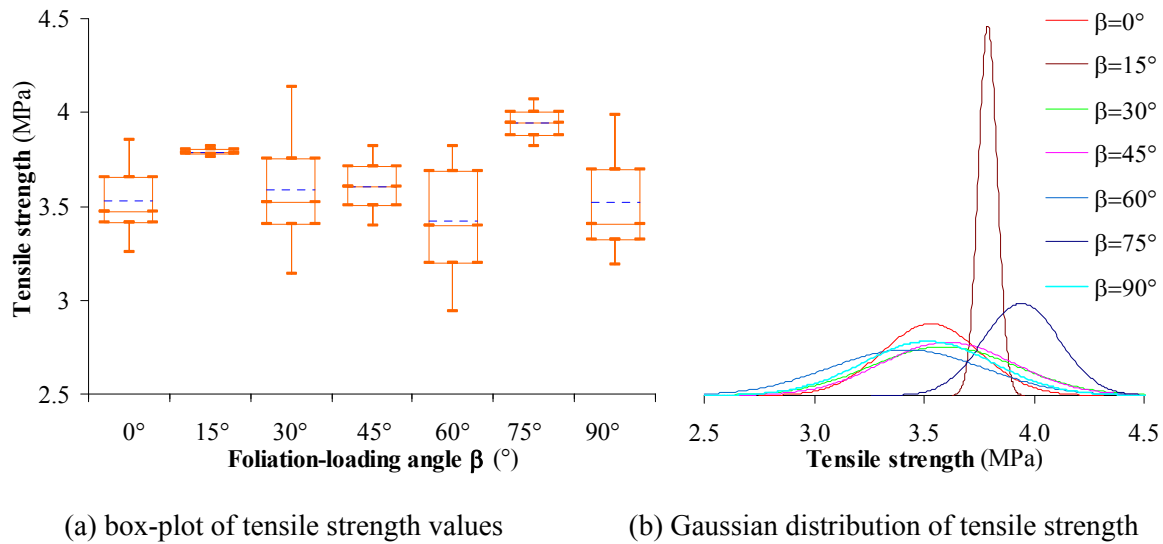
Figure 3-25: Box and Gaussian distribution plots of FG.Ss samples as a function of foliation-loading angles β

(a) box-plot of tensile strength values   (b) Gaussian distribution of tensile strengths
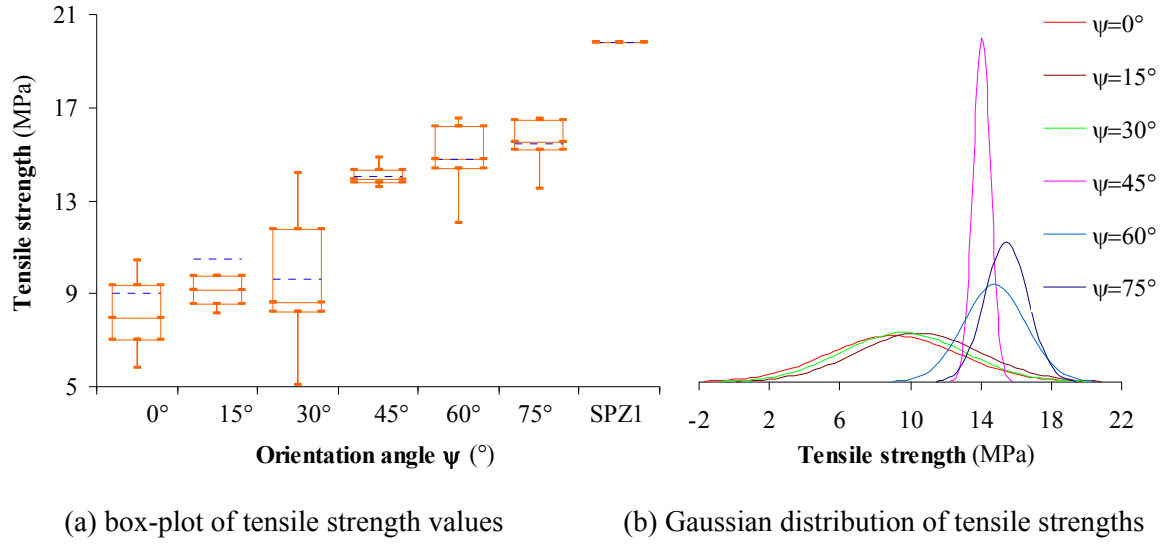
Figure 3-26: Box and Gaussian distribution plots of FG.Gs samples as a function of orientation angle ψ

(a) box-plot of tensile strength values   (b) Gaussian distribution of tensile strength
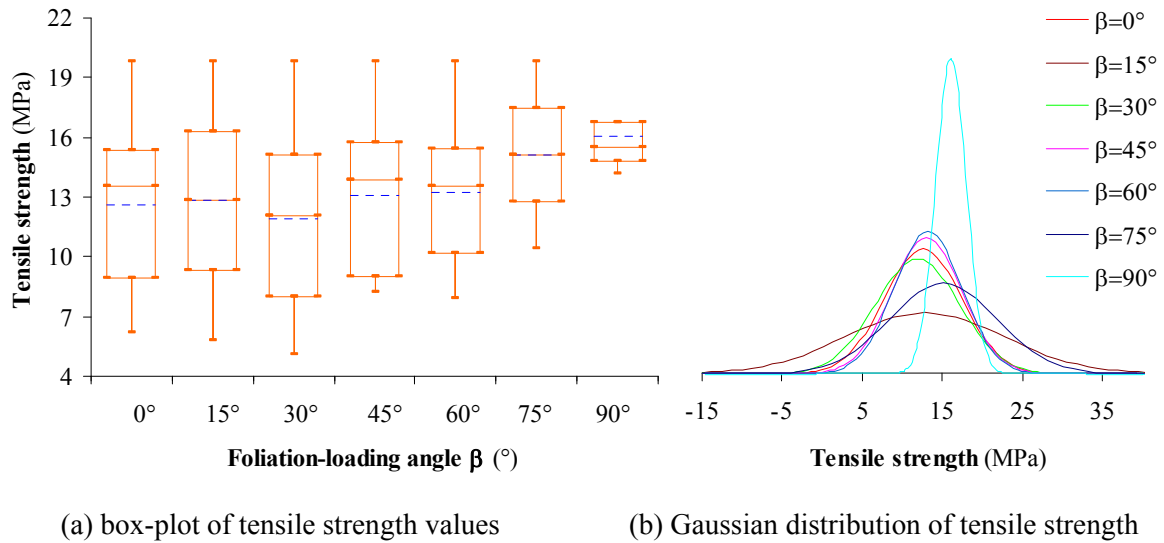
Figure 3-27: Box and Gaussian distribution plots of FG.Gs samples as a function of foliation-loading angles β
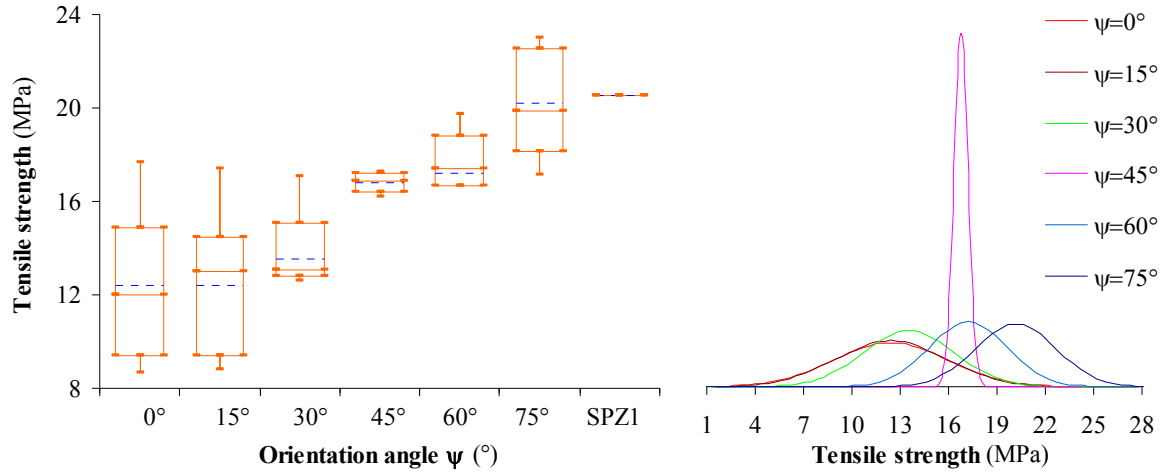
(a) box-plot of tensile strength values (b) Gaussian distribution of tensile strength

Figure 3-28: Box and Gaussian distribution plots of Le.Gs samples as a function of orientation angle ψ
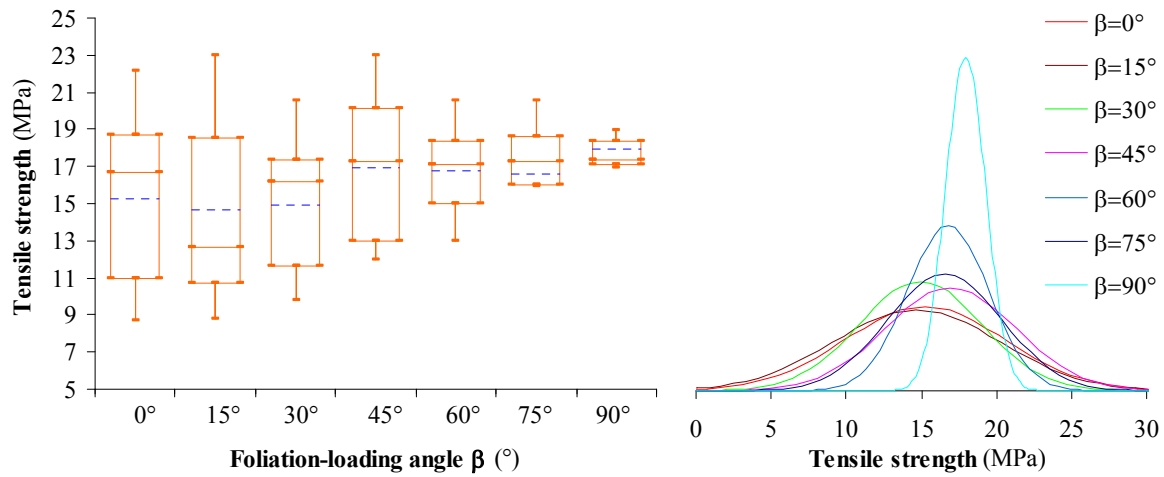
(a) box-plot of tensile strength values (b) Gaussian distribution of tensile strength

Figure 3-29: Box and Gaussian distribution plots of Le.Gs samples as a function of foliation-loading angles β

(a) box-plot of tensile strength values   (b) Gaussian distribution of tensile strength
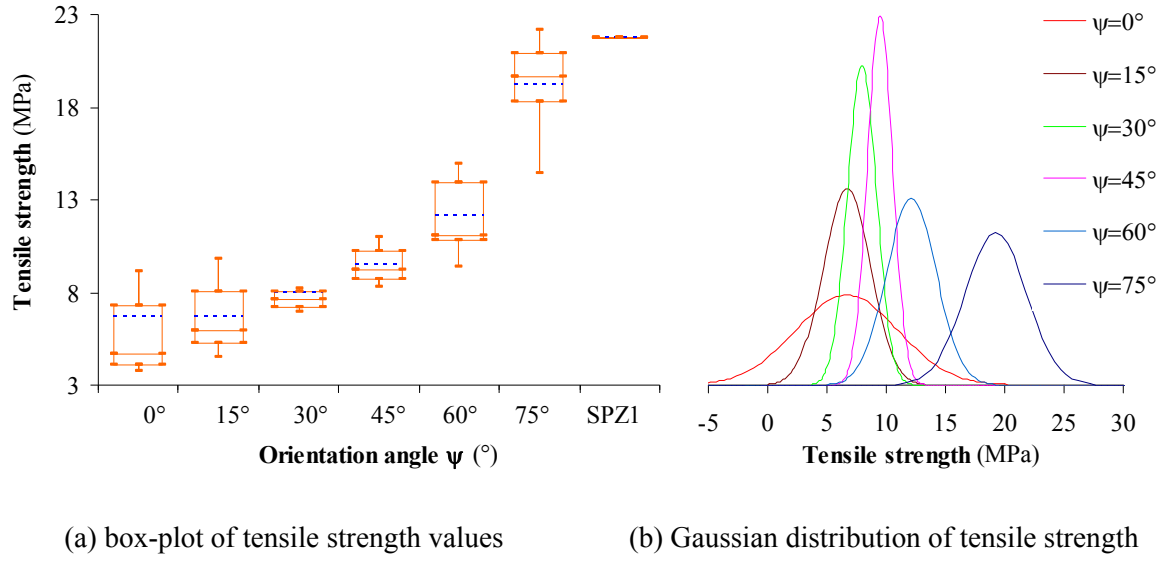
Figure 3-30: Box and Gaussian distribution plots of My.Sc samples as a function of orientation angle ψ

(a) box-plot of tensile strength values   (b) Gaussian distribution of tensile strength
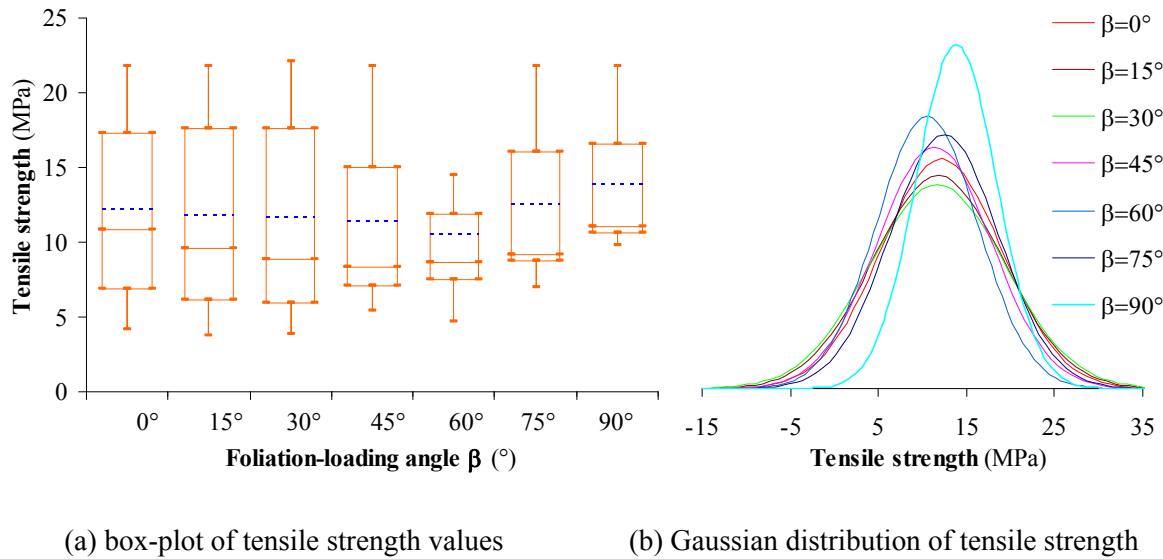
Figure 3-31: Box and Gaussian distribution plots of My.Sc samples as a function of foliation-loading angles β

Compared to the Sandstone, the Gneiss and Slate materials showed much higher coefficients of variations with values of up to 77%. This indicates that the orientation of the sample in relation to the loading direction is very sensitive for the measured peak strength. As the fracture patterns reveal (see Appendices 3.2, 3.3 and 3.4), the crack development follows, to a large degree, the weak anisotropy planes (bedding planes, schistosity planes).

Hence, a material characterized by a high degree of anisotropy will have the orientation of the sample influencing the fracture pattern (fracture type, fracture orientation) in relation to the loading direction and consequently the measured peak load.

3.6.3.2 Interpretation of fracture pattern

The digital pictures shown in Figure 3-10, 3-14, 3-18 & 3-22; and Appendices 3.1, 3.2, 3.3, & 3.4 document observations of the failure pattern after the peak strength had been reached during the Brazilian tests. Typical of the FG.Ss Sandstone is a distinct pattern of fracture which splits the sample into two. Sometimes, wedges are formed immediately under the loading jaws. In the FG.Gs and Le.Gs Gneisses in contrast, and especially in the My.Sc Slate, the fracture pattern is strongly influenced by the orientation of the weak planes (anisotropy). In many cases, the fracture pattern is characterized by sub-parallel crack along the existing weak planes (like in step faults or staircase-shaped fractures).

A high-speed camera was used to try to capture the crack development. However, the fracture process was so fast, that even a camera with a speed of 10.000 pictures/minute could not catch it. It was thus impossible to find out where the crack first appeared and how it developed with time.

3.6.3.3 Compilation of material data set

The data in Table 3-18 were compiled based on the whole set of mechanical rock properties determined above, relevant literature material on similar rock types and lab tests carried out in previous projects.

Mechanical rock parameter	Set of material parameters [4][5][6]	
	Gneiss	Slate
Young's modulus E (GPa)	45.0 – 54.7	35.0 – 47.0
Poisson's ratio μ (-)	0.3 – 0.4	0.3 – 0.45
Cohesion matrix C_m (MPa)	17.9 – 31.5	10.3 – 32.0
Cohesion joint C_j (MPa)	5.0 – 19.0	5.0 – 13.2
Friction matrix ϕ_m (°)	27.6 – 54.8	43.7 – 49.0
Friction joint ϕ_j (°)	35.7 – 43.2	22.6 – 44.4
Cohesion residual matrix $C_{res\text{-}m}$ (MPa)	1.0 – 13.7	4.84 – 13.7
Cohesion residual joint $C_{res\text{-}j}$ (MPa)	1.0 – 10.0	4.84 – 9.3
Friction residual matrix $\phi_{res\text{-}m}$ (°)	20.0 – 32.4	21.2 – 31.0
Friction residual joint $\phi_{res\text{-}j}$ (°)	22.0 – 35.0	21.0 – 34.5

Table 3-18: Summary of material parameters from lab and reference results [2, 102, 103].

3.7   Conclusion

The laboratory tests have shown that the degree of anisotropy has a strong influence on the measured peak strength obtained in the Brazilian test. Whereas the orientation of the sample in relation to the loading direction is unimportant for nearly isotropic materials, strongly anisotropic materials, like Gneiss and Slate reveal a strong dependence of the peak strength on the sample orientation relative to the loading direction. Also, isotropic materials show distinct tensile cracks along the centerline in contrast to the latter, where the fracture pattern is more complicated and composed of cracks along the weak planes and the matrix.

Several different laboratory tests were done in order to enable the determination of a set of material parameters for a ubiquitous joint model, this comprising strength data for the matrix and the weak planes as well as for the orientation of the latter.

---

[4] Walter, K. and Konietzky, H. Bericht der *Standsicherheitsberechnungen/Dimensionierung für das Dachschieferbergwerk Katzenberg*. 2009, Technische Universität Bergakademie Freiberg.

[5] Hoek, E., ed. *Practical rock engineering*. 2000, Rocscience

[6] Goodman, R. E., ed. *Rock Mechanics*. 1989, John Wiley & Sons

Chapter 4

Numerical simulation of isotropic materials - Comparison with analytical solutions

4.1   Introduction

For homogeneous and isotropic elastic materials, a handful of comprehensive analytical or semi-analytical solutions exist (see Chapters 1 & 2). Some of them deal in depth with the influence of Poisson's ratio, the thickness of the specimen and the loading arc under which the loading jaws act.

Some of these solutions are used here for comparison with the numerical 3-dimensional simulations. In the forefront of this comparison was the investigation of the different numerical meshes. The numerical simulation results were then compared with the lab results of the Postaer Sandstone.

4.2   Numerical simulation of isotropic materials

4.2.1   FLAC^{3D} simulation program

FLAC^{3D} - **F**ast **L**agrangian **A**nalysis of **C**ontinua - is a 3-D explicit finite-difference code for engineering mechanical simulations [6]. The explicit, Lagrangian calculation scheme and the mixed-discretization zoning technique used in FLAC^{3D} ensure that plastic collapse and flow are modeled very accurately.

4.2.2   Simulation procedure

A comprehensive parameter study was done using the analytical solutions of Hondros [18] and Wijk [35] as well as the 3-dimensional numerical model developed by them.

Brazilian tests were carried out with different thickness-to-diameter ratios, different material parameters and different loading angles (2α) but identical initial and boundary conditions. The sample diameter and elastic modulus were also fixed and the same uniform loading, i.e., 1000 N/mm disc thickness, applied. The following aspects were investigated:

➢ **Mesh structure:** three different mesh types - radial, orthogonal and tetrahedral grids - were investigated (Figure 4-1). In the middle section, where the load acts and most of the fracturing takes place, the mesh structure was refined.

➢ **Thickness-to-diameter ratio (L/D):** in order to investigate the slenderness, Brazilian test samples with a thickness-to-diameter ratio equal to ¼, ½, and $\frac{1}{1}$ and a disc diameter of D=50 mm were designed and investigated.

➢ **Site of section under investigation:** the stress state inside the specimen was investigated along the edge-, quarter- and middle-section.

➢ **Influence of Poisson's ratio:** the influence of three different Poisson's ratios ($\mu =$ 0.15, 0.25 and 0.35) on the state of the stress was investigated at constant Young's modulus.

➢ **Loading angle (2α):** different loading angles (2α = 1°, 5°, 10°, 15°, 20° and 25°) were selected to calculate the internal stress in the sample.

4.2.3   Numerical model setup

Three models with very different mesh techniques were designed using FLAC^{3D} (Figure 4-1). All three meshes have a fine mesh pattern on the surface where the load was applied.

(a) radial model	(b) orthogonal model	(c) tetrahedral model
(with 21021 gridpoints)	(with 54621 gridpoints)	(with 76692 gridpoints)
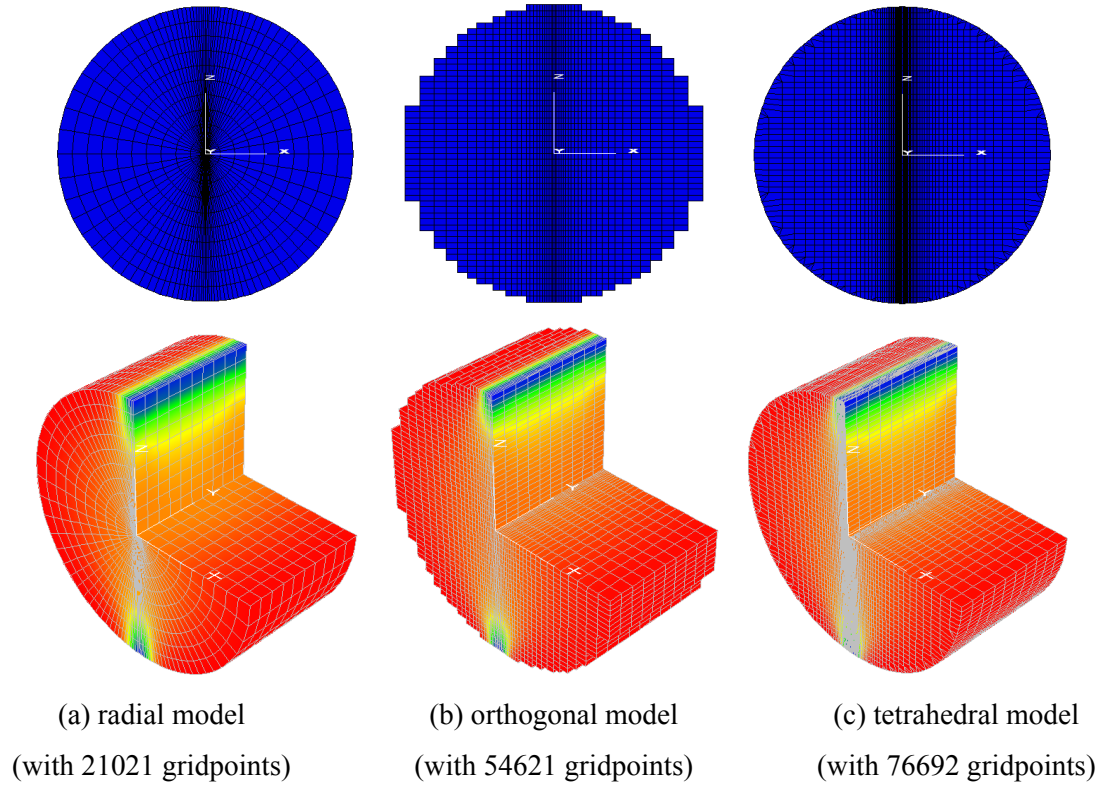
Figure 4-1: 3D models showing mesh structure (thickness-to-diameter ratio L/D = ½)

4.2.4   Influence of mesh type

As is well known, the meshing influences the results of numerical simulations. Figure 4-2 shows the stress distribution of the horizontal stress component along the vertical center line for different loading angles but otherwise identical conditions.

(a) radial model	(b) orthogonal model	(c) tetrahedral model
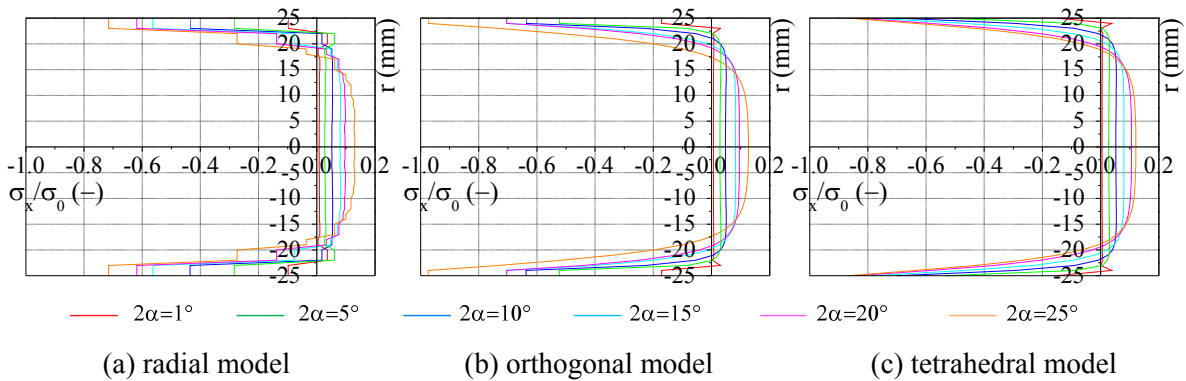
Figure 4-2: Influence of mesh type on σ_x along the center with $\mu = 0.25$ and thickness-to-diameter ratio L/D = ½

The radial mesh (see Figure 4-1a & 4-2a) is relatively coarse and not optimized in terms of mesh refinement and areas of high stress gradients. Also the zones are not adjusted to the

stress profiles of interest, e.g. the vertical center line. Therefore, the obtained stress profiles, as shown in Figure 4-2a, show a rather wave-like or step-wise curve progression.

The orthogonal mesh (see Figure 4-1b & 4-2b) is generated only by brick elements so that the outer boundary is somewhat jagged. A mesh refinement done on the central part of the model resulted in a good stress profile, except around the boundary areas where the jagged surface yielded slightly wrong results.

The tetrahedral mesh (see Figure 4-1c & 4-2c) has the highest resolution and most appropriate mesh structure for the underlying problem. All the elements inside of the specimen are orthogonal, tetrahedral elements used only at the boundary. A mesh refinement at the center of the model was also carried out here, the element boundaries parallel and perpendicular to the Cartesian axes. Compared to the radial and orthogonal mesh, the tetrahedral mesh revealed the best performance and was therefore used in all the subsequent studies. Further results on the tetrahedral model are presented in Appendices 4.1 & 4.2.

4.2.5   Influence of specimen thickness

Up until now, nearly all analytical, numerical and lab test results have not considered the effect of thickness. In fact the test specimens are either thin discs or cylinders. ASTM [10] stipulates that the diameter of the specimen be at least 10 times larger than the largest mineral grain constituent and that the thickness-to-diameter ratio (L/D) lie between 0.2 and 0.75. According to ISRM [5] and DGGT [12] the thickness should be approximately equal to the radius.

The influence of specimen thickness on the tensile stress and the strength, was investigated on the tetrahedral model using different loading angles (2α) and thickness-to-diameter ratios. The results were normalized, with the tensile strength calculated using the analytical solutions given in Eq. (1.2) at a constant load of $P = 10$ kN (see Table 4-1).

2α	L/D = ¼				L/D = ½				L/D = 1/1			
	Edge section	Quar. section	Middle section	Dev. (max/min)	Edge section	Quar. section	Middle section	Dev. (max/min)	Edge section	Quar. section	Middle section	Dev. (max/min)
1°	1.000	0.995	0.973	1.028	1.000	0.920	0.895	1.117	1.000	0.867	0.873	1.153
5°	5.650	5.611	5.499	1.027	5.650	5.196	5.051	1.119	5.653	4.890	4.924	1.156
10°	10.623	10.499	10.340	1.027	10.628	9.758	9.471	1.122	10.645	9.169	9.229	1.161
15°	16.236	15.970	15.796	1.028	16.270	14.893	14.429	1.128	16.339	13.970	14.052	1.170
20°	21.826	21.392	21.200	1.030	21.898	20.000	19.279	1.136	22.200	18.638	18.650	1.191
25°	24.788	24.255	25.566	1.054	24.975	22.717	21.941	1.138	25.180	21.267	21.395	1.184

Table 4-1: Normalized tensile stress values at the center of the disc as function of thickness-to-diameter ratio and loading angles (2α) with μ=0.25.
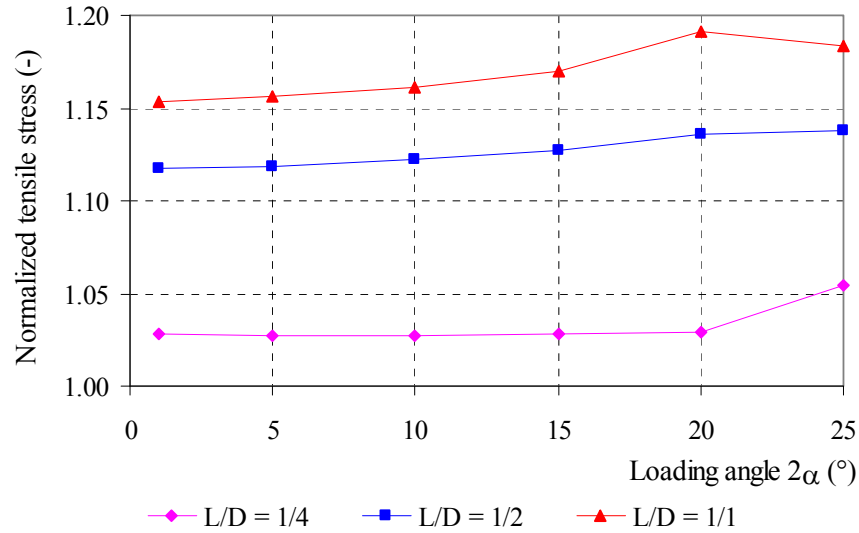
Figure 4-3: Deviation of tensile stress as function of thickness to diameter ratio and load angle (2α) in the tetrahedral model.

The influence of thickness-to-diameter ratio on the tensile stress is shown in Table 4-1 and Figure 4-3 with the tensile stress values normalized and the deviations between maximum and minimum tensile stresses compared. The results make some differences as in the following cases:

➢ For L/D = ¼, the tensile stresses obtained for the different sections are nearly identical, the amplitude $\sigma_{max}/\sigma_{min}$ (Table 4-1) ranging from 1.028 to 1.054.

However, in Figure 4-3, this difference increases steeply with a large loading angle ($2\alpha > 20°$).

➢   For L/D = ½, an indication that the tensile stresses at the edge of the section increase can already clearly be seen. The amplitude $\sigma_{max}/\sigma_{min}$ (Table 4-1) ranges from 1.117 to 1.138.

➢   For L/D = ⅟₁ , the increase in tensile stress at the edges is even more pronounced. The amplitude $\sigma_{max}/\sigma_{min}$ (Table 4-1) ranges from 1.153 to 1.191, a nearly 20% increase compared to the stress at the center.

➢   Figure 4-3 shows the significance of the influence of thickness of a specimen. The increase in the L/D ratio tends to raise the difference 12.5% in tensile strength on the plane section located within the sample.

Although a very small thickness is advantageous from a theoretical point of view, in order to avoid eccentric loading, misalignment and buckling, it is suggested that the upper limit of L/D be less than ⅟₁ and the lower limit not smaller than about ¼. Such considerations are governed more by reasons of practicability and expediency like material availability, uniform loading across the thickness of the specimen and size and capacity of the test machine.

4.2.6   Influence of Poisson's ratio

Based on the assumption of the rock materials being linearly elastic and homogeneous, the influence of Poisson's ratio was investigated. The analytical 2D solution after Hondros [18] was used parallel to adequate numerical simulations. A Young's modulus of 8.5 GPa was chosen with reference to the lab results of the numerical calculations.
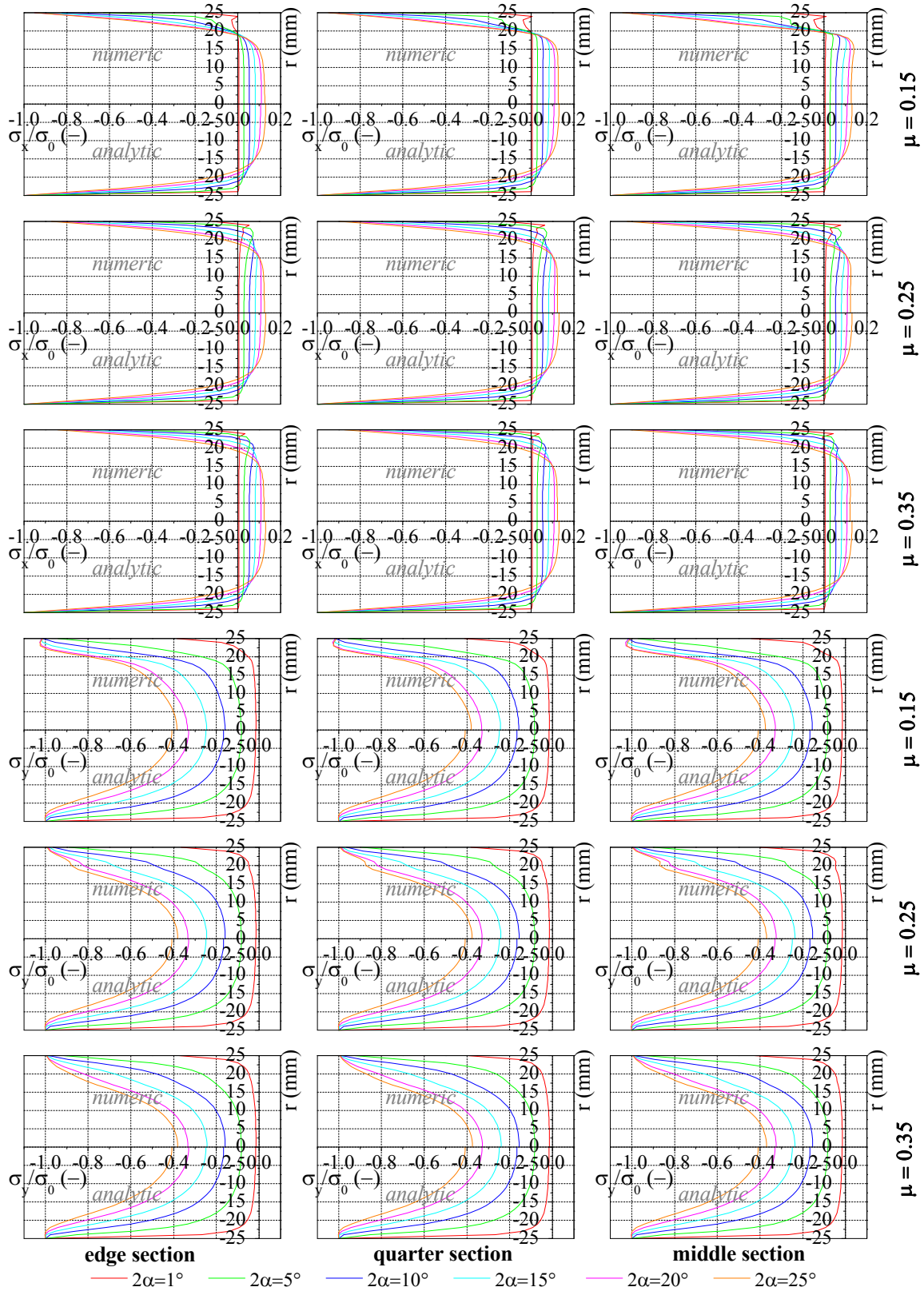
Figure 4-4: Influence of Poisson's ratio μ on σ_x and σ_y along middle, quarter and edge sections in the tetrahedral model with a thickness-to-diameter ratio L/D = ¼ (3D numerical and 2D analytical solutions).

Figure 4-5: Influence of Poisson's ratio μ on σ_x and σ_y along middle, quarter and edge sections in the tetrahedral model with a thickness-to-diameter ratio $L/D = \frac{1}{2}$ (3D numerical and 2D analytical solutions).
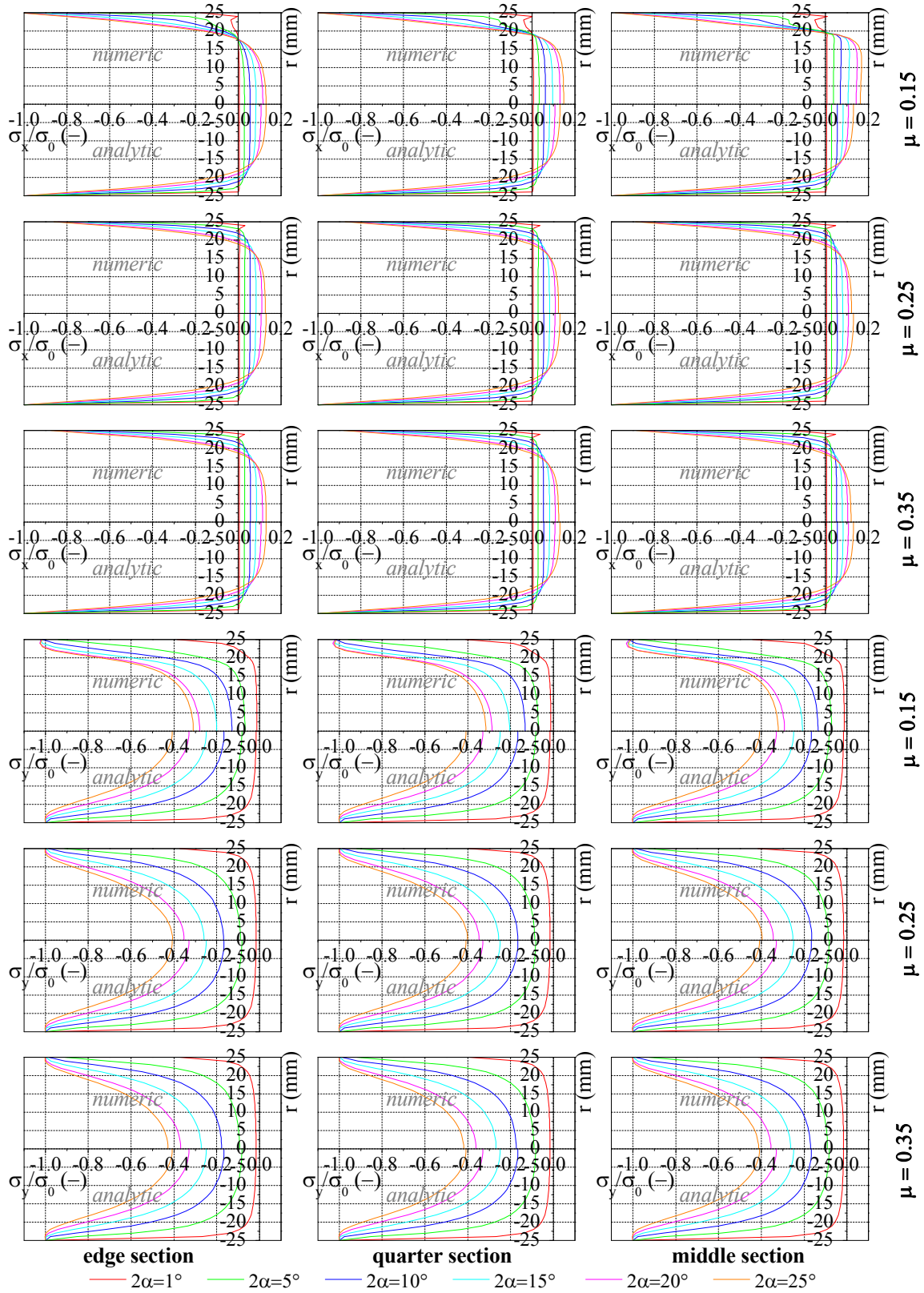
Figure 4-6: Influence of Poisson's ratio μ on σ_x and σ_y along middle, quarter and edge sections in the tetrahedral model with a thickness-to-diameter ratio L/D = 1/1 (3D numerical and 2D analytical solutions).

Figure 4-4, 4-5 & 4-6 illustrate that, firstly, when Poisson's ratio decreases, the influence of Poisson's ratio and loading angle on the stress components also increases. Secondly, the analytical and numerical solutions show qualitatively the same behavior and that the quantitative differences between analytical and numerical solutions are quite small.

4.2.7   Influence of loading angle (2α)

A more detailed analysis of the influence of loading angle on the tensile stress was done using the tetrahedral model (Figure 4-7, 4-8 & 4-9). The results indicate that the loading angle (2α) can play a significant role in the Brazilian test because the peak tensile stress does not develop any further at the center under certain conditions but more at the periphery of the disc. This can happen in combinations of very large loading angles and small Poisson's ratios as documented by the Figure 4-7, 4-8 & 4-9.

Figure 4-7: Influence of the loading angle (2α) on σ_x and σ_y in the tetrahedral model with a thickness-to-diameter ratio $L/D = \frac{1}{4}$ (3D numerical and 2D analytical solutions)
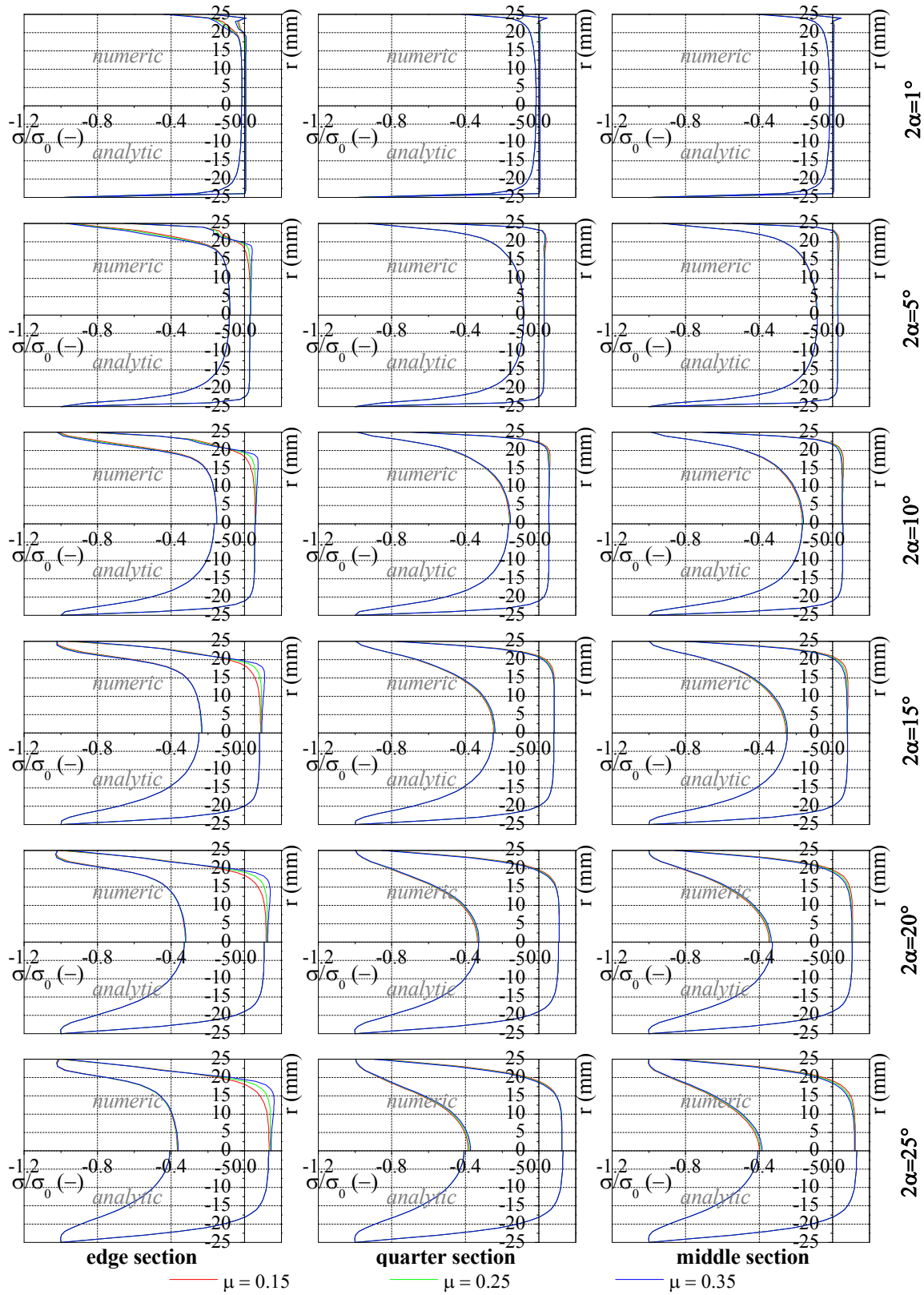
Figure 4-8: Influence of the loading angle (2α) on σ_x and σ_y in the tetrahedral model with a thickness-to-diameter ratio L/D = ½ (3D numerical and 2D analytical solutions)

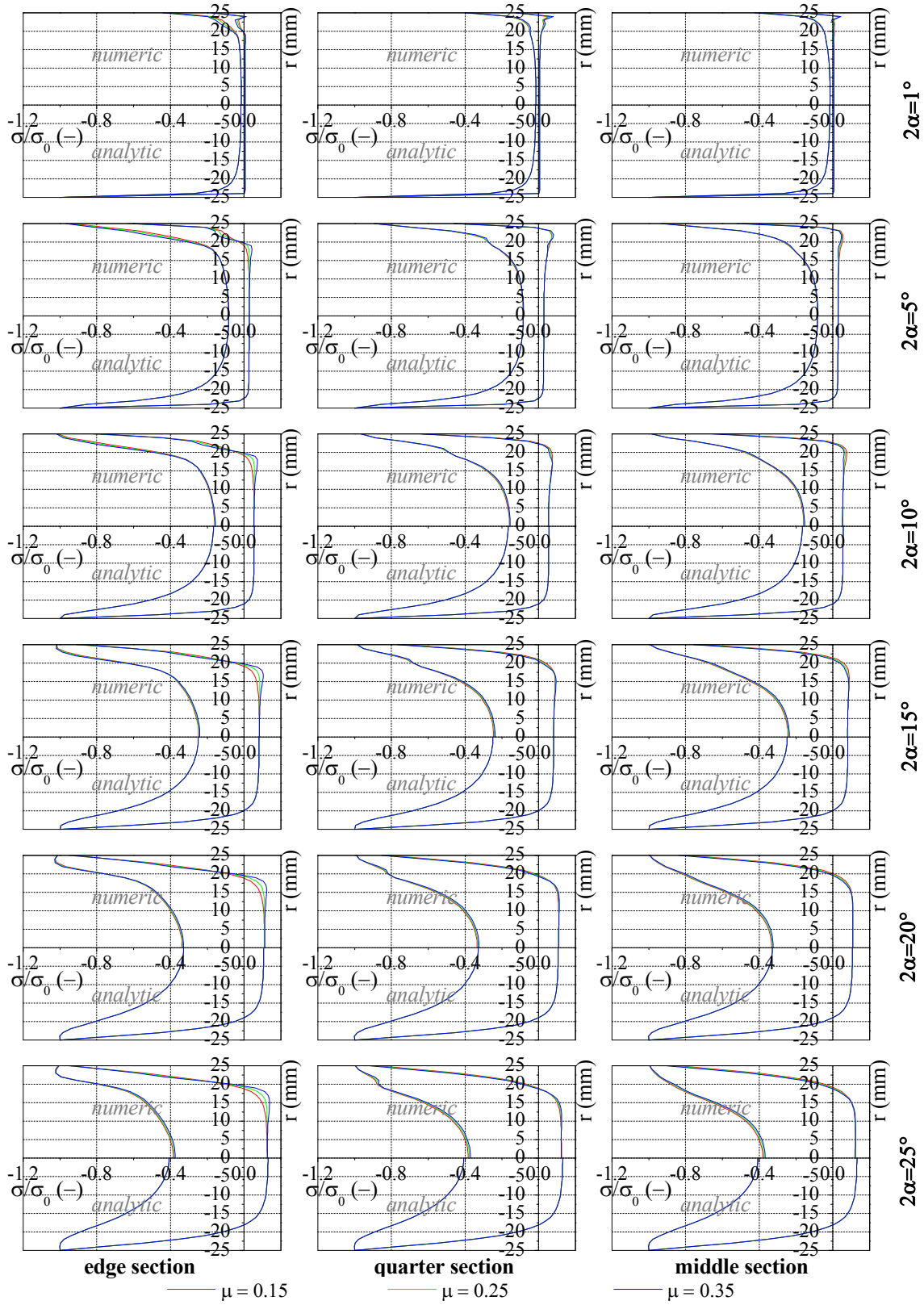**Figure 4-9:** Influence of the loading angle (2α) on σ_x and σ_y in the tetrahedral model with a thickness-to-diameter ratio L/D = $\frac{1}{1}$ (numerical 3D and analytical 2D solutions)

4.2.8   Comparison of 3D analytical and numerical results

Wijk's formula [35] is the only 3-dimensional quasi-analytical solution available today for the Brazilian test. As Figure 4-10 reveals, the analytical solution is in close agreement with the numerical solutions and consequently, also with the 2-dimensional analytical solutions for a broad range of loading angles and Poisson's ratios in relation to the middle section. For small loading angles and moving away from the middle section towards the sample edge, the analytical solutions give very questionable (even wrong) results.
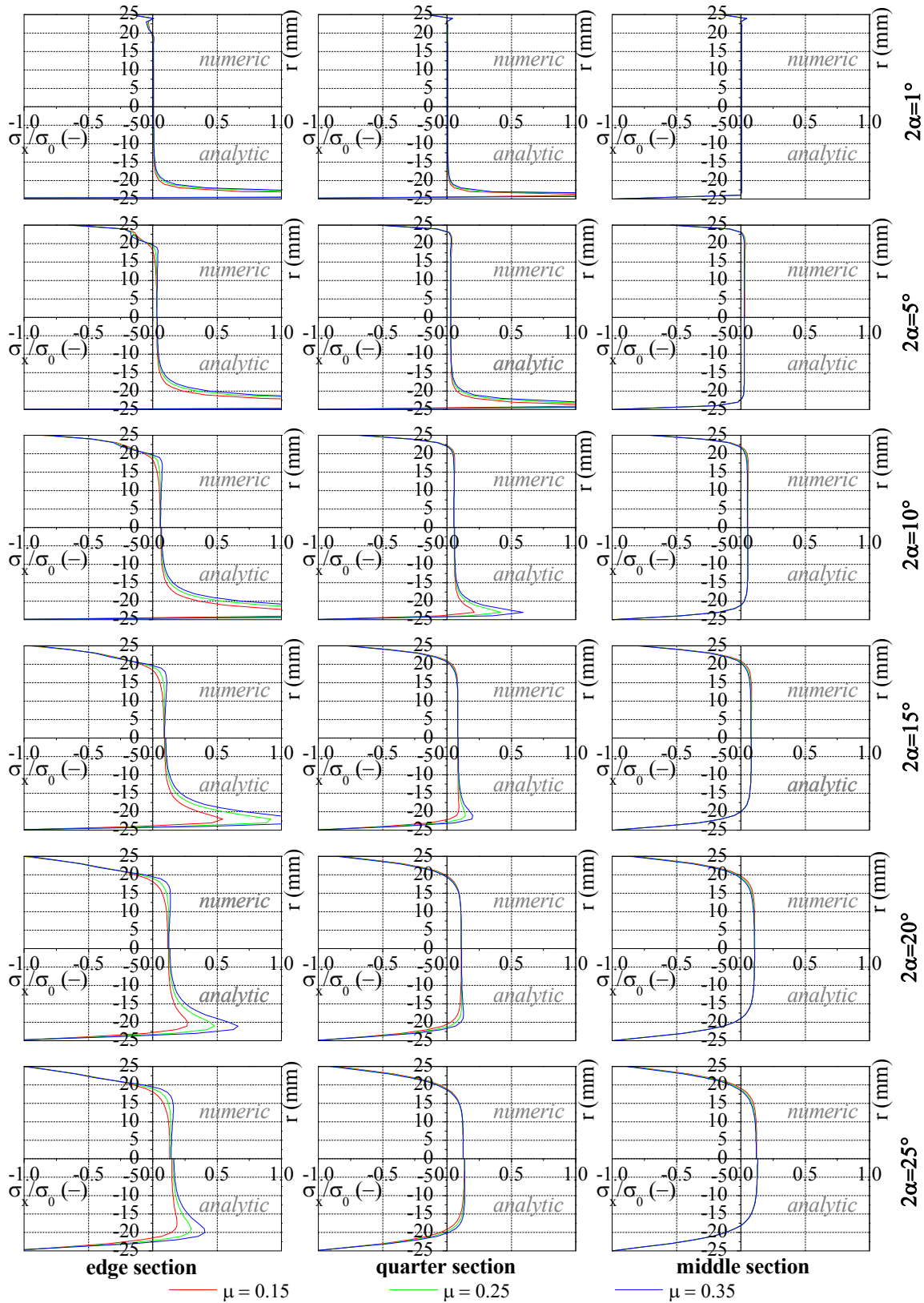
Figure 4-10: Tensile stress in the tetrahedral model with a thickness-to-diameter ratio L/D = ½ (3D numerical and analytical solutions)

4.2.9   Influence of stress concentration at the loading jaws

Stress concentrations at the loading jaws are a problem in Brazilian tests [96]. The classical analytical solutions ignore this effect though. In fact, the specimen can be destroyed in the initial stages of stress concentration under the loading areas instead of at its center where the tensile stress is nearly uniform (see also Figure 4-4 to Figure 4-10. This can then make it impossible to evaluate the Brazilian test in the classical way.

4.3   Comparison with experimental results of Postaer Sandstone (FG.Ss)

The numerical simulations are based on the laboratory results of the Postaer Sandstone (FG.Ss), which is taken as a homogeneous material (see Chapter 3). Assuming that the specimen is a continuous, isotropic and homogeneous elastic body, the stress distribution at failure is determined from the model at the stage where the simulated load is close to the failure load measured in the laboratory (Table 4-2). The specimen models an elastic isotropic solid with the following characteristics: E = 8.5 GPa; $\mu = 0.25$.

Parameter	Measured Values	Simulation Values	Explanations
Force (N)	7181	7111	[1] average lab results as in Eq. (1.2)
Tensile strength (MPa)	3.535 [1]	3.0 – 3.6 [2]	
Axial strain (mm/mm)	1.72E-4	1.70E-4	[2] distribution from center to edge [3] approximate values
Length of loading arc (mm)	11[3]	13	
Loading angle 2α (°)	27°[3]	32°	

Table 4-2: Laboratory and numerical simulation results of the Brazilian test on FG.Ss

(a) σ_x (MPa) in plane XZ   (b) σ_y (MPa) in plane XZ
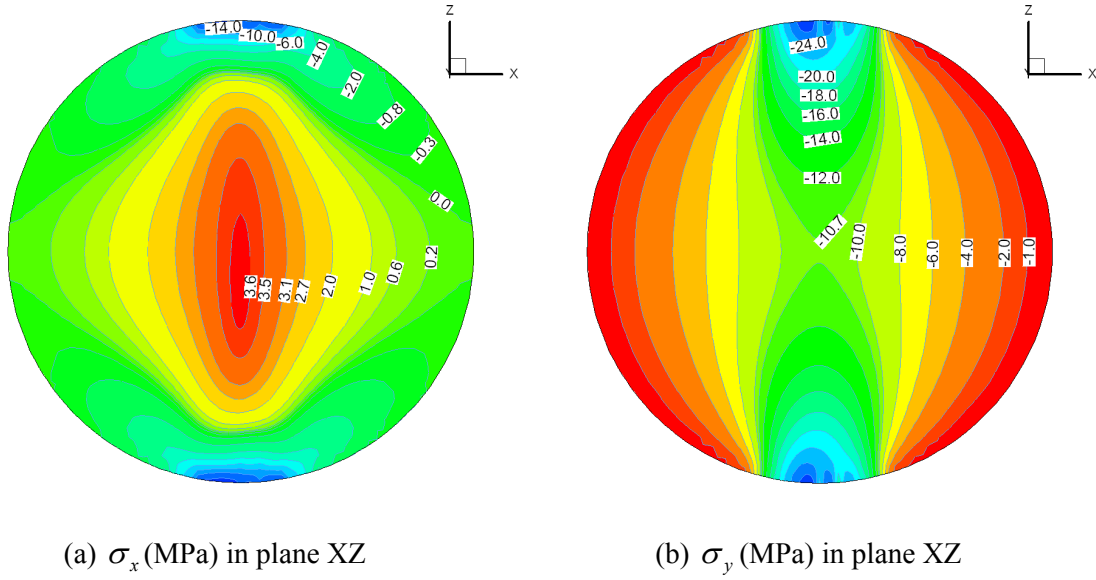
Figure 4-11: Numerical simulation of tensile (a) and compressive (b) stress distributions in a specimen with a thickness-to-diameter ratio L/D = ½ along the edge section.

(a) σ_x (MPa) in 3-D   (b) σ_y (MPa) in 3-D
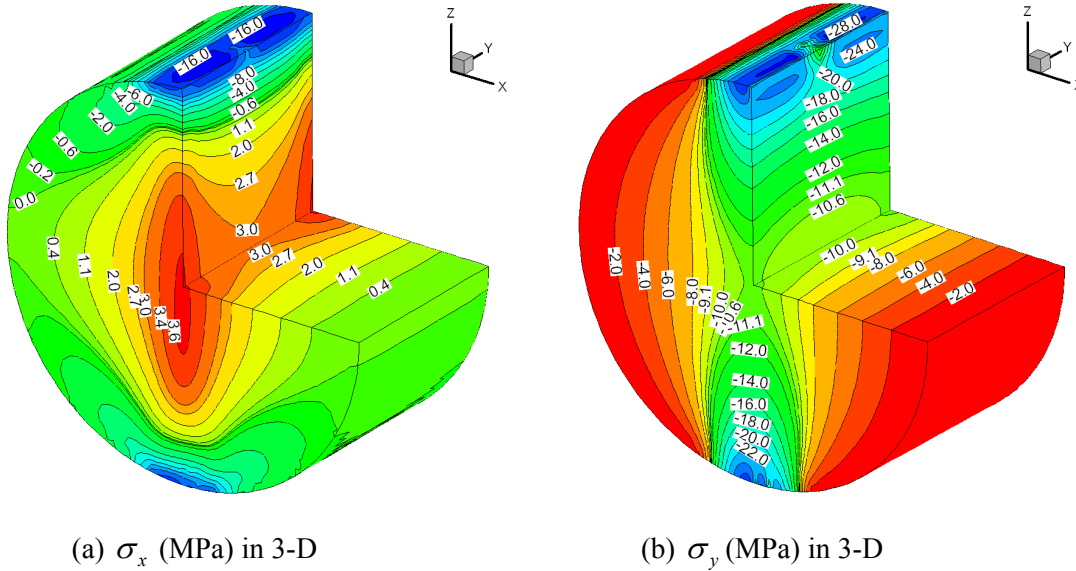
Figure 4-12: Numerical simulation of tensile (a) and compressive (b) stress distributions in a specimen with a thickness-to-diameter ratio L/D = ½.

The numerical simulation results are in close agreement with those of the lab tests. Figure 4-11 & 4-12 show the tensile and compressive stresses σ_x and σ_y immediately before the point of failure is reached. At the center of the disc, the tensile stress reaches σ_x = 3.0 MPa, which is somewhat (about 15%) lower than the average lab result of 3.535 MPa. At the edge however, the tensile stress σ_x reaches 3.6 MPa, which is slightly higher than the

average lab value of 3.535 MPa. The classical analytical 2D solutions assume that the fracture starts at the center, where the highest tensile stress is expected. The numerical model in contrast predicts the highest tensile stresses at the edges. Thereby the initiation of the fracture process in the end sections of the disc.

The stress component σ_y is always compressive and shows a significant concentration under the loading jaws. This can lead, as quite often observed during the lab tests, to shear failure and inclined fracture close to the loading area.

In general, Figure 4-12 documents that a quite complex 3-dimentional stress state is produced inside the disc under diametral compressive loading even for a homogeneous isotropic elastic material.

4.4   Conclusion

➢ The stress distribution near the center of a disc under diametral loading is quite the same in both 2D and 3D analytical solutions and 3D numerical simulations.

➢ The tensile stresses in the edge sections of the disc can be slightly smaller or even higher than those at the center depending on the parameters (loading angle, Poisson's ratio and L/D).

➢ The loading angle $2\alpha \geq 10°$ is in accordance with the ISRM [5] recommendations; Fairhurst's [19] suggestion, $2\alpha = 15°$ and Hondros [18] use of $2\alpha = 10°$ are for endless specimens.

➢ The lower and upper limits for the length-to-thickness ratios should be in the range $¼ \leq L/D \leq \frac{1}{1}$;

➢ The specimen can be initially fractured by the stress concentration at the loading jaws. This means that fracture initiation can be triggered in this region instead of the center of the disc as usually assumed.

➢ The formula usually used for calculating the tensile strength is derived from a 2D analytical elastic solution. It ignores however, the effect of the loading angle (2α),

the thickness-to-diameter ratio (L/D), the Poisson's ratio (μ) and the stress concentrations at the loading jaws and may hence disagrees with experimental results.

➢ The developed and tested 3-dimensional numerical model for the stress and failure analyses of the Brazilian test seems to be suitable not only for isotropic, but more generally also for anisotropic and inhomogeneous materials.

Chapter 5

Numerical simulation of anisotropic materials – Comparison with laboratory tests

5.1 Introduction

The mechanical behavior of anisotropic rocks under compression and/or tension is directional [3, 92]. This characteristic is a product of well-defined fabric elements which may form in the rock as bedding, stratification, layering or foliation. This chapter focuses on the modeling of Le.Gs Gneiss and My.Sc Slate as transversely isotropic materials.

In Chapter 3, laboratory tests carried out on Le.Gs Gneiss and My.Sc Slate are documented with deducing the mechanical rock parameters. This chapter also presents the results of corresponding numerical simulations for those rocks. The results, obtained from both procedures were compared and then used for interpretations.

A constitutive law which explicitly considers weakness planes in transverse isotropic rocks is the so-called *bilinear strain-hardening/softening ubiquitous-joint* FLAC³ᴰ model. The plane of weakness can be created in any desired direction. To enable a direct comparison with the lab results, seven discrete bedding-plane orientations (ψ) and loading directions (β) each were chosen to cover the full spectrum of potential constellations for the simulations.

5.2 General procedure for simulating the Brazilian test using FLAC³ᴰ

FLAC³ᴰ [97] is a powerful and globally applied 3-dimensional numerical simulation method especially developed to solve rock- and soil mechanical problems. The code is based on the explicit Finite-Difference method and enables simulation of highly non-linear problems. Figure 5-1 illustrates the simulation procedure used here.
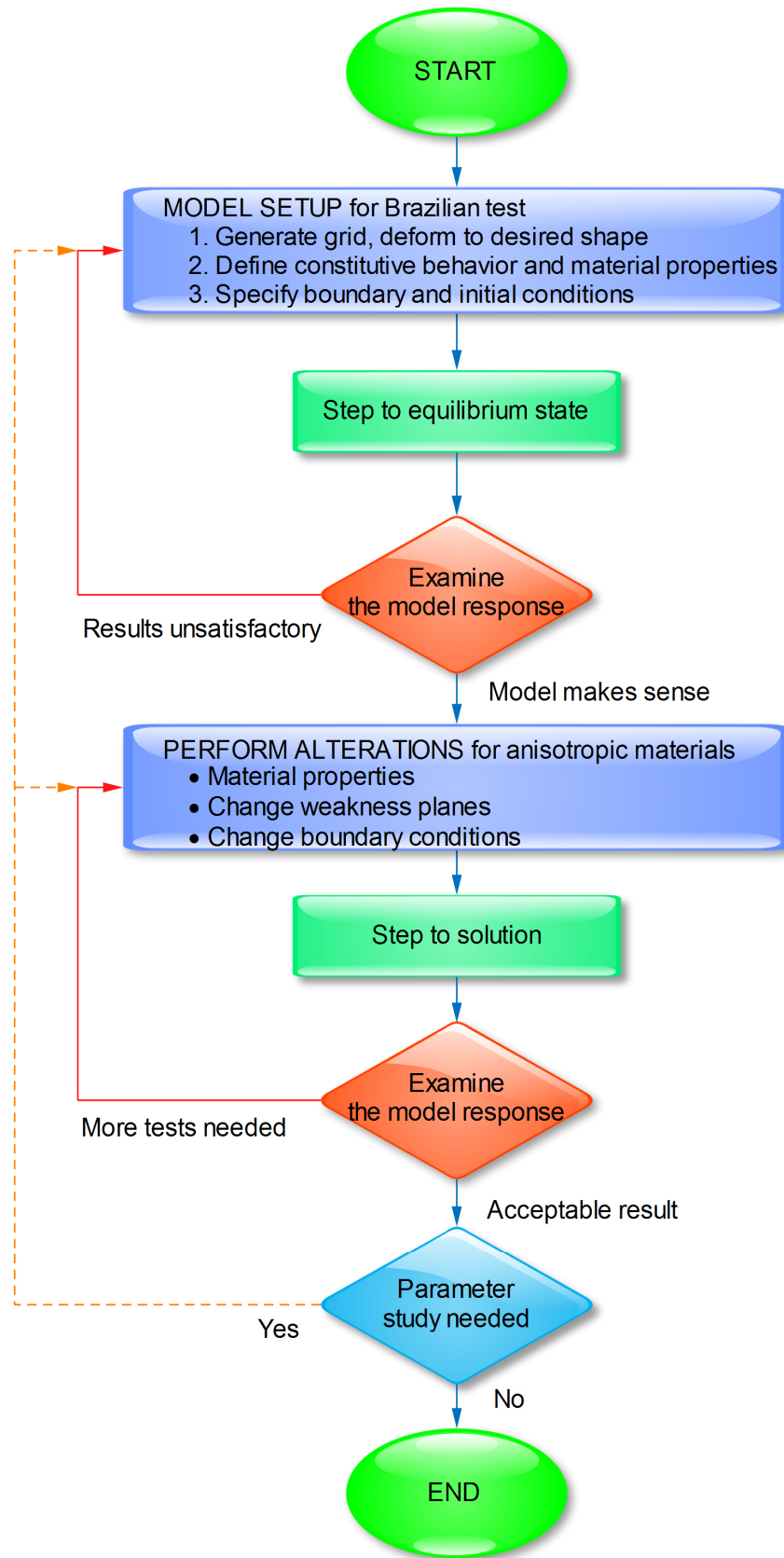
Figure 5-1: Solution procedure simulating Brazilian tests on anisotropic materials (after Itasca [97])

5.2.1   Conceptual model

The conceptual model is based on the experiences gained from the simulation of isotropic materials as described in detail in Chapter 4. A high resolution tetrahedral mesh, inclusive a frictional interface, was selected for all the tests and the loading jaw simulations so that the frictional contact between the loading jaws and the disc could be taken into account in the load entry area (Figure 5-2).
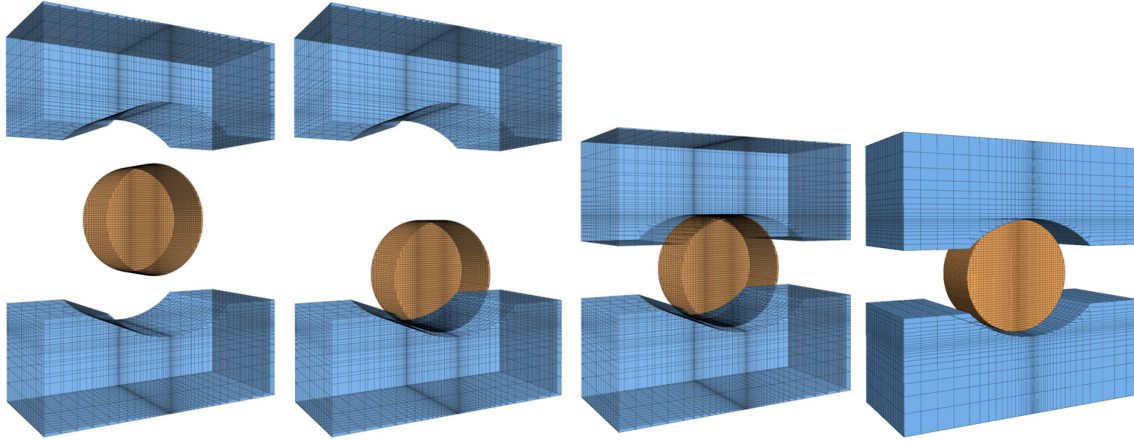
Figure 5-2: General model for simulating the Brazilian test: disc and upper and lower loading jaws

A tetrahedral mesh with 81.549 gridpoints and 73.584 zones (see also Chapter 4) and a higher mesh resolution in the center region duplicated the lab tests in a standard model. The extreme mesh resolution was necessary in order to duly illustrate the locally large stress gradients and complicated failure patterns.

5.2.2   Boundary Conditions

During the Brazilian test simulations, load was applied by two loading jaws. The force between the loading jaws and the disc was transmitted via an interface. The load was generated by applying a constant but reversed velocity to the two loading jaws. In addition, no displacements were allowed along the perpendicular to loading direction X-Y-plane:

```
fix   x y  range x -0.0576 -0.0574 y -0.0251 -0.0249
fix   x y  range x  0.0576  0.0574 y  0.0251  0.0249
apply zvel @_nvel  range z  0.0575  0.0585
apply zvel @_nvel1 range z -0.0575 -0.0585
```
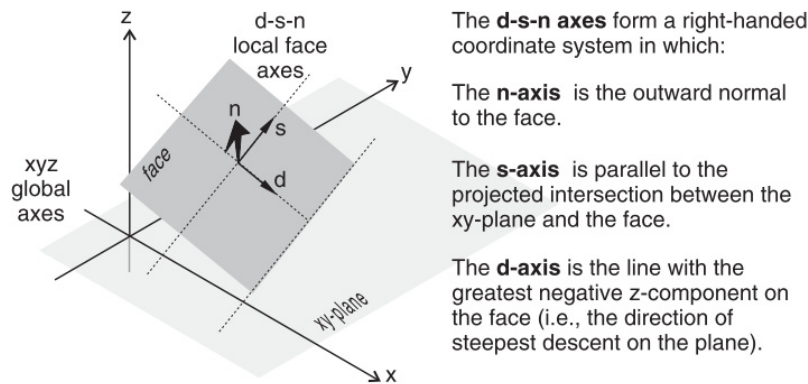
The codes apply for all model boundary gridpoints falling between $0.0575 \leq z \leq 0.0585$ for the top jaw and $-0.0575 \leq z \leq -0.0585$ for the bottom jaw.

The interface elements used incorporate automatic contact detectors so that deformation of the disc due to increase in the loading contact area with increasing load can be considered.
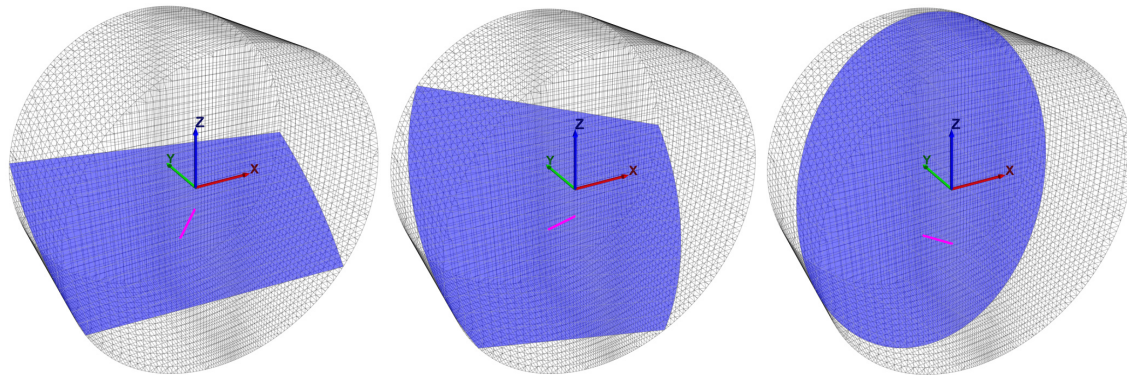
5.2.3   Numerical model set-up

The numerical model set-up mainly considers the orientation of the weakness planes in relation to the loading direction, this requiring the definition of a corresponding reference coordinate system. The orientation of the weakness plane here is given by a unit normal vector in the global x-, y-, z- coordinate system. A local system of reference axes is defined by the x'-axis pointing downward in the direction of dip, the y'-axis in the plane and z' pointing in the direction of the unit normal (n). All the orientation (ψ) and foliation-loading (β) angles have to be transformed into dip (dip) and dip direction (dd) in FLAC^{3D}.

 The d-s-n-axes form a right-angled co-ordinate system in which:

The **d-s-n axes** form a right-handed coordinate system in which:

The **n-axis** is the outward normal to the face.

The **s-axis** is parallel to the projected intersection between the xy-plane and the face.

The **d-axis** is the line with the greatest negative z-component on the face (i.e., the direction of steepest descent on the plane).

Figure 5-3: Local axes defined by the dip (d) strike (s) and normal (n) in FLAC^{3D} [97].

(a) dip plane = 150° dd = -10°   (b) dip plane = 130° dd = -15°   (c) dip plane = 105° dd = -15°

Figure 5-4: An arbitrary orientation of a plane of weakness inside the numerical model.

5.3   Constitutive model

5.3.1   Choice of constitutive model

FLAC^{3D} provides a library of build-in constitutive models. Each model is developed to represent a specific type of constitutive behavior commonly associated with specific geologic materials.

The most suitable model for simulating Brazilian tests on anisotropic rocks is the so-called *bilinear strain-softening ubiquitous-joint* model. This model enables simulation of both the softening and hardening of rock matrix materials and the weak planes using preset variations of the ubiquitous-joint model properties (cohesion, friction, dilation, tensile strength) as functions of accumulated plastic shear and tensile strain.

For the loading jaws, isotropic linear elastic constitutive laws were applied because the loading level was far below the failure state or plasticity threshold and linearity could be assumed.

### 5.3.2   Bilinear Strain-Hardening/Softening Ubiquitous-Joint Model [98]

The *bilinear strain-hardening/softening ubiquitous-joint* model [98] is a generalization of the *ubiquitous-joint* model which is an anisotropic plastic model that contains weak planes of specific orientation embedded in a Mohr-Coulomb solid. In the bilinear model, the failure envelopes for the matrix and joint planes are a combination of two Mohr-Coulomb criteria with a tension cut-off that can be hardened or softened according to laid down laws. A non-associated flow rule is used for the shear-plastic flow and an associated flow rule for the tensile-plastic flow.

The softening behavior of the matrix and the joint are specified relative to four independent hardening parameters (two for the matrix and two for the joint) which measure the amount of plastic shear and tensile strain. In this numerical model, a general failure is first detected for the step with relevant plastic corrections made, the new stresses analyzed for failure on the weak plane and then accordingly updated. In this numerical model, general failure is determined first for the step and relevant plastic corrections made and then the new stresses analyzed for failure on the weak plane and accordingly updated. The hardening parameters

are increased where plastic flow had taken place and the cohesion, friction, dilation and tensile strength parameters adjusted for the matrix and the joint using tables.

Failure Criterion for the Matrix

The matrix failure criterion used in this model is sketched in the principal stress plane (σ_1, σ_3) in Figure 5-5. (Compressive stresses are negative and by convention, $\sigma_1 \leq \sigma_2 \leq \sigma_3$.)
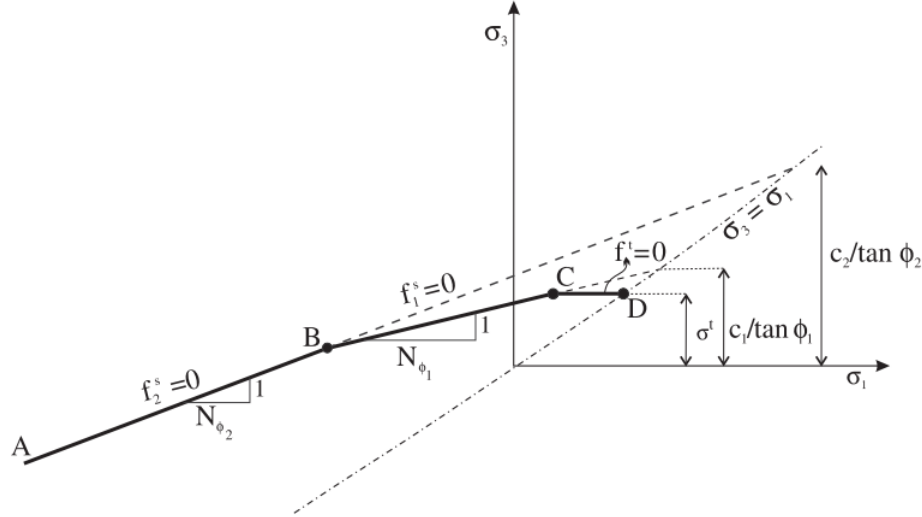
Figure 5-5: FLAC3D bilinear matrix failure criterion [98]

The failure envelope is defined by two Mohr-Coulomb failure criteria $f_2^s = 0$ and $f_1^s = 0$ for segments $A - B$ and $B - C$ and a tension failure criterion $f^t = 0$ for segment $C - D$. The shear failure criterion has the general formula $f^s = 0$. The criterion is characterized by a cohesion, c_2, and a friction angle, ϕ_2, for segment $A - B$, and by a cohesion, c_1, and a friction angle, ϕ_1, for segment $B - C$. The tensile failure criterion is specified by means of the tensile strength, σ^t (positive value), thus:

$$f^s = \sigma_1 - \sigma_3 N_\phi + 2c\sqrt{N_\phi} \qquad (5.1)$$

$$f^t = \sigma_3 - \sigma^t \qquad (5.2)$$

where

$$N_\phi = \frac{1+\sin(\phi)}{1-\sin(\phi)}$$ (5.3)

The tensile cap acts on segment B − C of the shear envelope and, for a material with non-zero frictional angle ϕ_1, the maximum value of the tensile strength is given by

$$\sigma^t_{max} = \frac{c_1}{\tan\phi_1}$$ (5.4)

Failure Criterion for the Weak Plane

The stresses, corrected for plastic flow in the matrix, are resolved into components parallel and perpendicular to the weak plane and then tested for ubiquitous-joint failure. The failure criterion is expressed in relation to the magnitude of the tangential traction component, $\tau = \sqrt{\sigma^2_{1'3'} + \sigma^2_{2'3'}}$, and the normal traction component, $\sigma_{3'3'}$, on the weak plane.
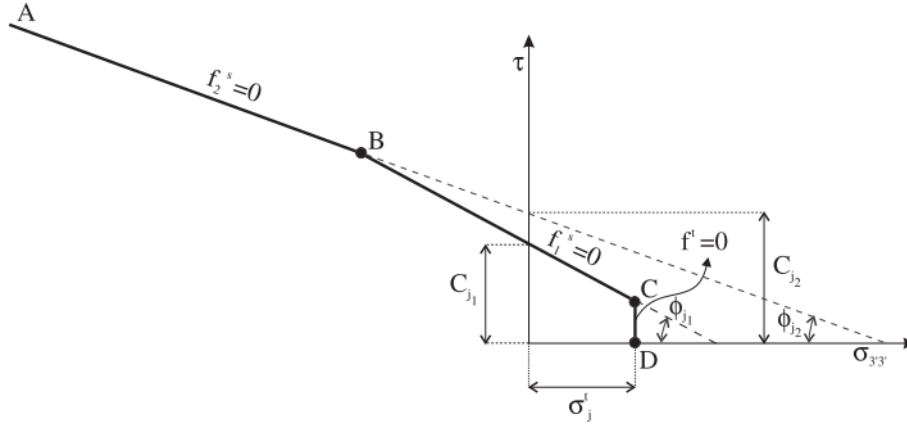
Figure 5-6: FLAC3D bilinear joint failure criterion [98]

This failure criterion is presented in Figure 5-6 and corresponds to two Mohr-Coulomb failure criteria: $f_2^s = 0$ for segment A − B, and $f_1^s = 0$ for segments B − C; and a tension failure criterion $f^t = 0$ for segment C − D. Each shear criterion has the general form $f^s = 0$, and is characterized by a cohesion and a friction angle c_j, ϕ_j equal to c_{j2}, ϕ_{j2} along segment A − B, and c_{j1}, ϕ_{j1} along segment B − C. The tensile criterion is specified by means of the tensile strength, σ^t_j (positive value), thus:

$$f^s = \tau - \sigma_{3'3'} \tan\phi_j - c_j \tag{5.5}$$

$$f^t = \sigma_{3'3'} - \sigma_j^t \tag{5.6}$$

For a weak plane with non-zero frictional angle ϕ_{j1}, the maximum value of the tensile strength is given by

$$\sigma_{j\,max}^t = \frac{c_{j1}}{\tan\phi_{j1}} \tag{5.7}$$

5.4   Parameter calibration

Parameter calibration involves adjusting the simulation parameters in such a way as to match the simulation results with those obtained in the laboratory. Lab results with statistical variability were used as input parameters.

5.4.1   Material parameters used

The material parameters in FLAC^{3D} are generally categorized into elastic deformation (Young's modulus and Poisson's ratio) and strength (cohesion, friction angle and tensile strength) properties. The laboratory test program for gneiss and slate paid particular attention to the foliation in the rocks. In fact, loading was applied parallel and perpendicular to the planes of weakness (joint planes) in order to determine the strength parameters of the rock matrix and the planes of weakness. The material parameters described in Chapter 3 were derived from the lab tests conducted by the author with additional values from literature.
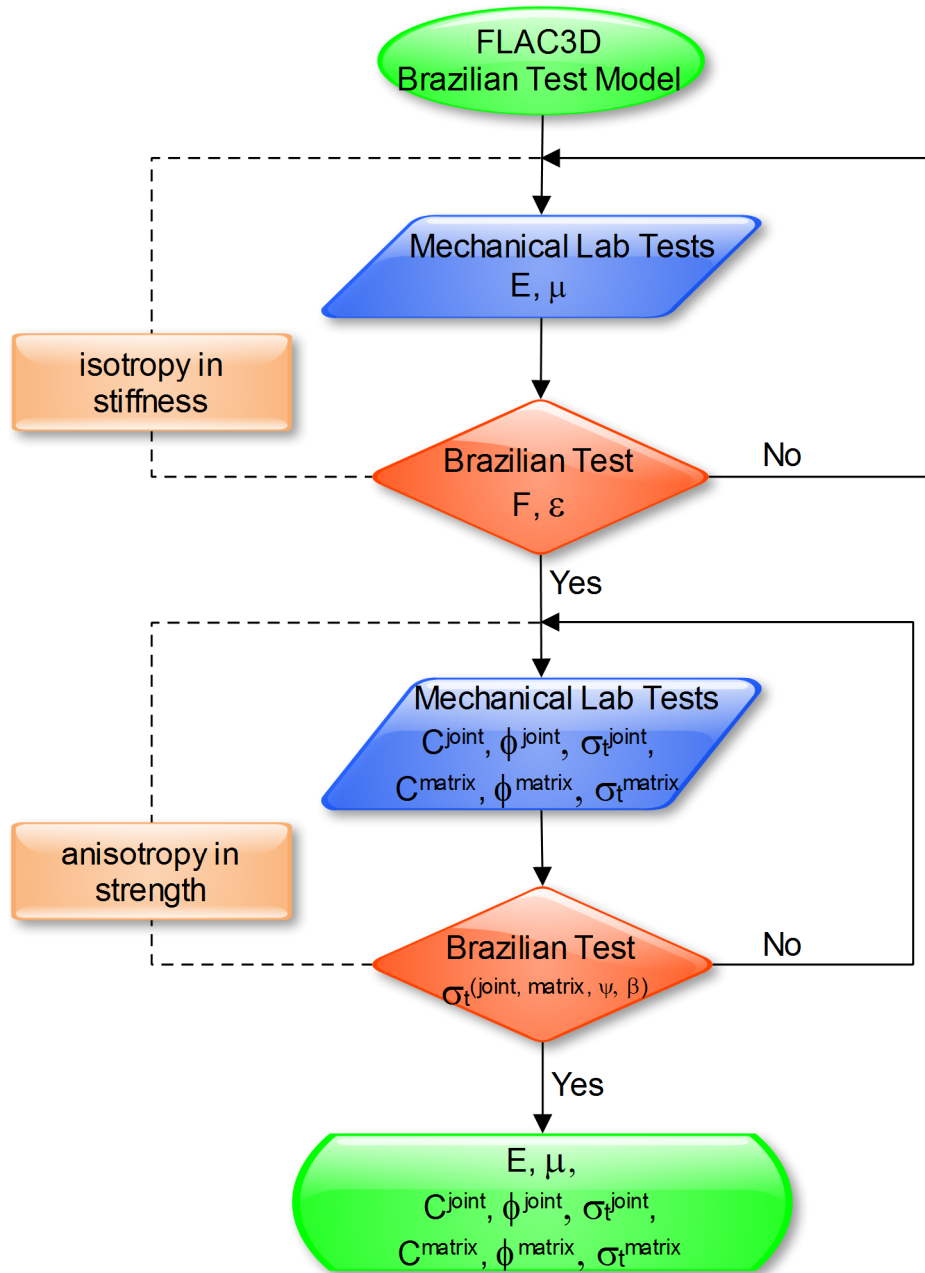
Figure 5-7: Material parameter calibrating procedure

Based on the calibration procedure in Figure 5-7, the following final input parameters were used for the *bilinear strain-hardening/softening ubiquitous-joint* model (Table 5-1):

Model Parameters		Le.Gs Gneiss Parameters	My.Sc Slate Parameters
global	_emod =	55.0e9	45.0e9
global	_ny =	0.33	0.33
Global	_tens_matrix =	23.0e6	21.7e6
Global	_tens_joint =	9.5e6	6.5e6
global	_coh_matrix =	38.0e6	32.0e6
global	_coh_joint =	18.0e6	12.5e6
global	_fric_matrix =	46.0	51.0
global	_fric_joint =	43.0	41.0
global	_tens_matrix_re =	1.0e6	1.0e6
global	_tens_joint_re =	0.5e6	0.5e6
global	_coh_matrix_re =	5.0e6	2.5e6
global	_coh_joint_re =	2.0e6	1.5e6
global	_fric_matrix_re =	33.0	33.0
global	_fric_joint_re =	30.0	30.0

Table 5-1: Material parameters (SI units) used in the numerical simulations

5.4.2　Contact between disc and loading jaws

As already described in Chapter 4, the loading angle (2α) plays an important role in the Brazilian tensile strength tests. During the test, the load is applied by means of loading jaws and transferred via an interface to the rock disc. This interface creates the link between the sub-grids in the calculations. The contact plane represents a physical discontinuity between two different materials (rock and steel).

FLAC^{3D} uses triangular elements for the interface each of which is defined by three nodes (interface nodes). Each interface node has a representative area associated with it such that the total area of the entire interface is divided into active interface nodes. Generally, interface elements are attached to a zone surface. Each quadrilateral zone face is defined by two triangular interface elements so that interface nodes are automatically created at every interface element vertex. When another grid surface comes into contact with an interface element, the contact is detected at the interface node and is characterized by normal and shear stiffnesses as well as sliding properties (friction).

The fundamental relationship at the contact is defined by the interface node and a zone surface, also known as the target face. The normal direction of the interface force is determined by the orientation of the target face. This means, for instance, that the compressive stresses on the target face are also diametrally compressive on the disc.

The material properties are related to the steel, rock parts and the interface via the following codes:

```
model elas range group jaw_top jaw_bottom
prop bulk 1.6e11 shear 7.7e10 range group jaw_top jaw_bottom
global _kn = (_bulk + 1.3333 * _shear) * 12.5
interface 1 face range z 0.0375,0.05        &
  cylinder end1 (0,-0.0125,0.025) end2 (0,0.0125,0.025) radius 0.0251 &
  cylinder end1 (0,-0.0125,0.025) end2 (0,0.0125,0.025) radius 0.0249 not
interface 2 face range z 0.0125,0          &
  cylinder end1 (0,-0.0125,0.025) end2 (0,0.0125,0.025) radius 0.0251 &
  cylinder end1 (0,-0.0125,0.025) end2 (0,0.0125,0.025) radius 0.0249 not
interface 1 prop kn=@_kn ks=@_kn fric 15
interface 2 prop kn=@_kn ks=@_kn fric 15
```
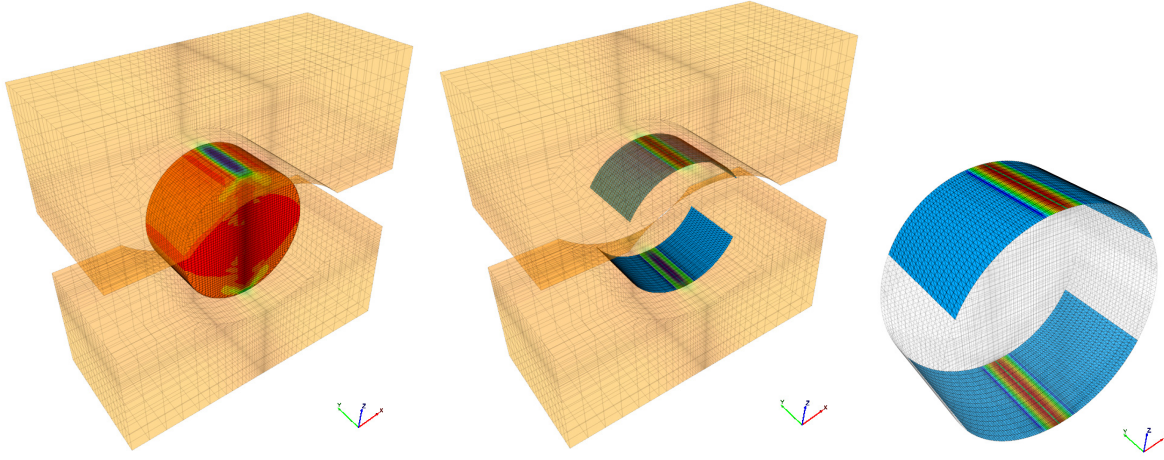

Figure 5-8: Interface reaction beneath loading jaws during the Brazilian test. Colored areas indicate potential and real contacts between disc and loading jaws.

Shear and normal stiffness have to be taken as the minimum prerequisite. A good thumb of the rule as found in FLAC^{3D} manuals is, that *kn* and *ks* be set at tenfold the equivalent stiffness of the stiffest neighboring zone. The apparent stiffness of a zone in the normal direction expressed in stress per unit distance, is:

$$\max\left[\frac{(K + \tfrac{4}{3}G)}{\Delta z_{min}}\right] \tag{5.8}$$

where: K & G are the bulk and shear moduli, respectively;

Δz_{min} is the smallest width of an adjoining zone in the normal direction.

The interface parameters used in the simulations are given in Section 5.4.2. Contact area, loading angle and contact force components were determined by the author's developed so-called Fish-functions based on the internal program language.

### 5.4.3   Post-failure deformation properties

The post-failure behavior was inserted in the simulation. Initiating material hardening or softening is a gradual process once plastic yield begins. At failure, deformation becomes more and more inelastic as a result of micro-cracking. This leads to degradation in strength of these materials and the initiation of shear bands or tensile cracks.

The bilinear strain-hardening/softening ubiquitous-joint model is based on the FLAC^{3D} Mohr-Coulomb model with non-associated shear and associated tension flow rules. If peak strength values (cohesion, friction, dilation and tensile strength) are reached for the matrix and/or the joints, they will be automatically modified according to infinite linear laws demarcated as input functions. Cohesion, friction and dilation are then defined as infinite-linear functions of the accumulated plastic shear strain. An infinite-linear softening law is used for the tensile strength, this being a function of the accumulated plastic tensile strain.

For example, the user-defined hardening/softening parameters for My.Sc Slate are:

```
table 101    0,@_tens_matrix   1e-4,0.1    2e-4,0.75   1e-3,0.95
             5e-3,@_tens_matrix_re
table 102    0,@_tens_joint    1e-4,0.1    2e-4,0.75   1e-3,0.95
             5e-3,@_tens_joint_re
table 103    0,@_fric_matrix   1e-3,0.1    2e-3,0.75   4e-3,0.95
             5e-3,@_fric_matrix_re
table 104    0,@_fric_joint    1e-3,0.1    2e-3,0.75   4e-3,0.95
             5e-3,@_fric_joint_re
table 105    0,@_coh_matrix    1e-3,0.1    2e-3,0.75   4e-3,0.95
             5e-3,@_coh_matrix_re
table 106    0,@_coh_joint     1e-3,0.1    2e-3,0.75   4e-3,0.95
             5e-3,@_coh_joint_re
```

Figure 5-9 & 5-10 document the softening functions used for the two anisotropic materials investigated in this thesis.
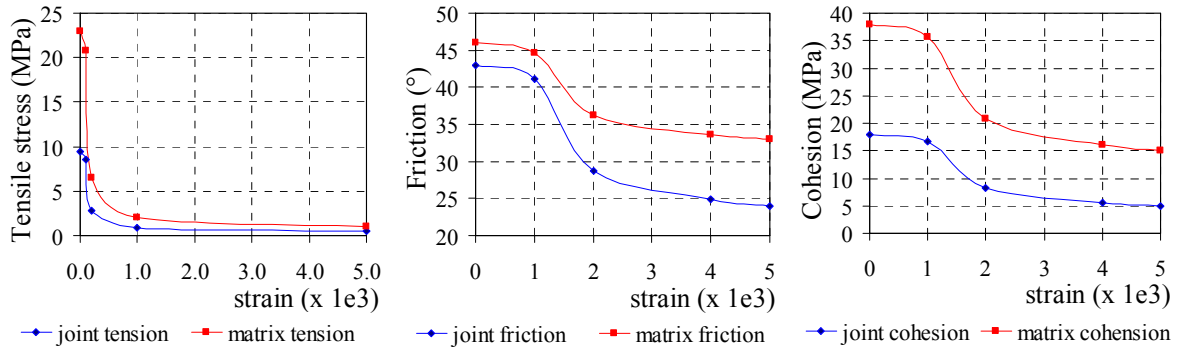
Figure 5-9: User-defined softening functions analyzed with respect to tensile stress, friction and cohesion for Le.Gs Gneiss.
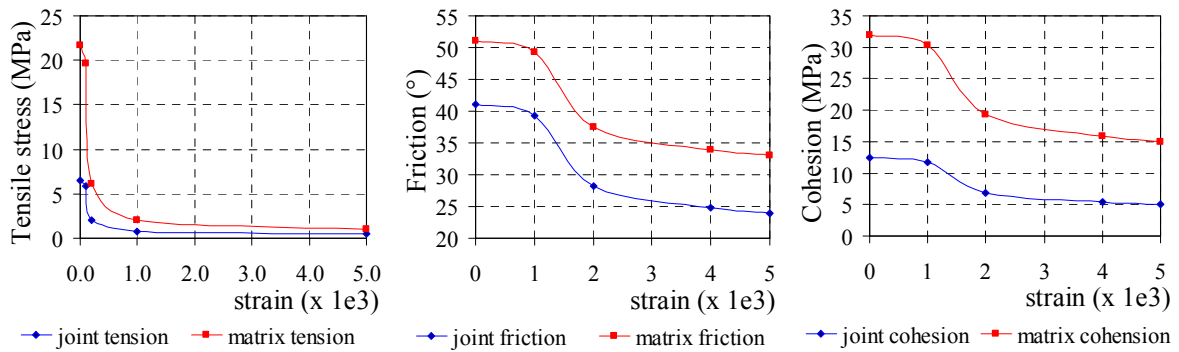

Figure 5-10: User-defined softening functions analyzed with respect to tensile stress, friction and cohesion for My.Sc Slate.
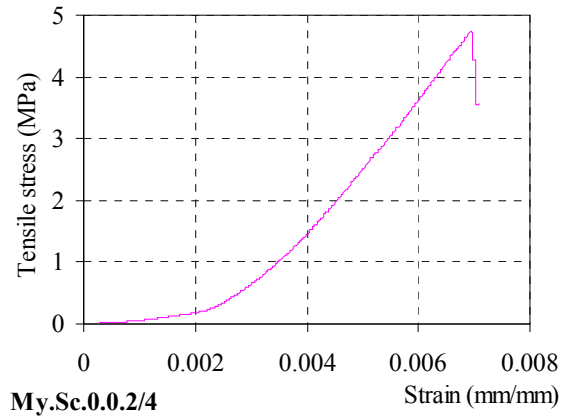
Hardening and softening parameters were calibrated for each and every one of the analyses and the values generally back-calculated from the laboratory test results.

5.4.4 Tension cut-off

Tensile failure is characterized by pronounced softening within very small ranges of plastic tensile strain (Figure 5-9 & 5-10).
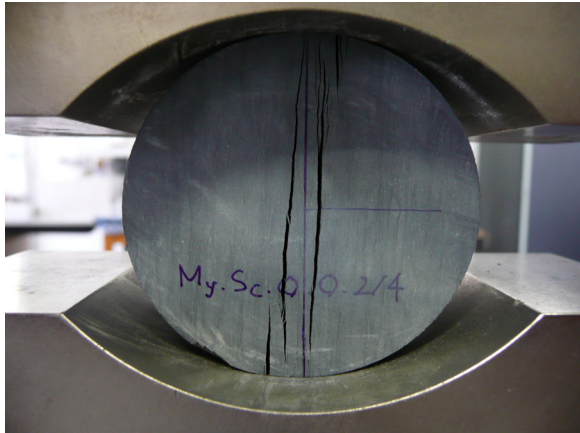
(a) Final fracture pattern   (b) Tensile stress vs. strain

Figure 5-11: Brazilian lab test results of My.Sc.0.0.2/4 specimen (compare Figure 5-12)
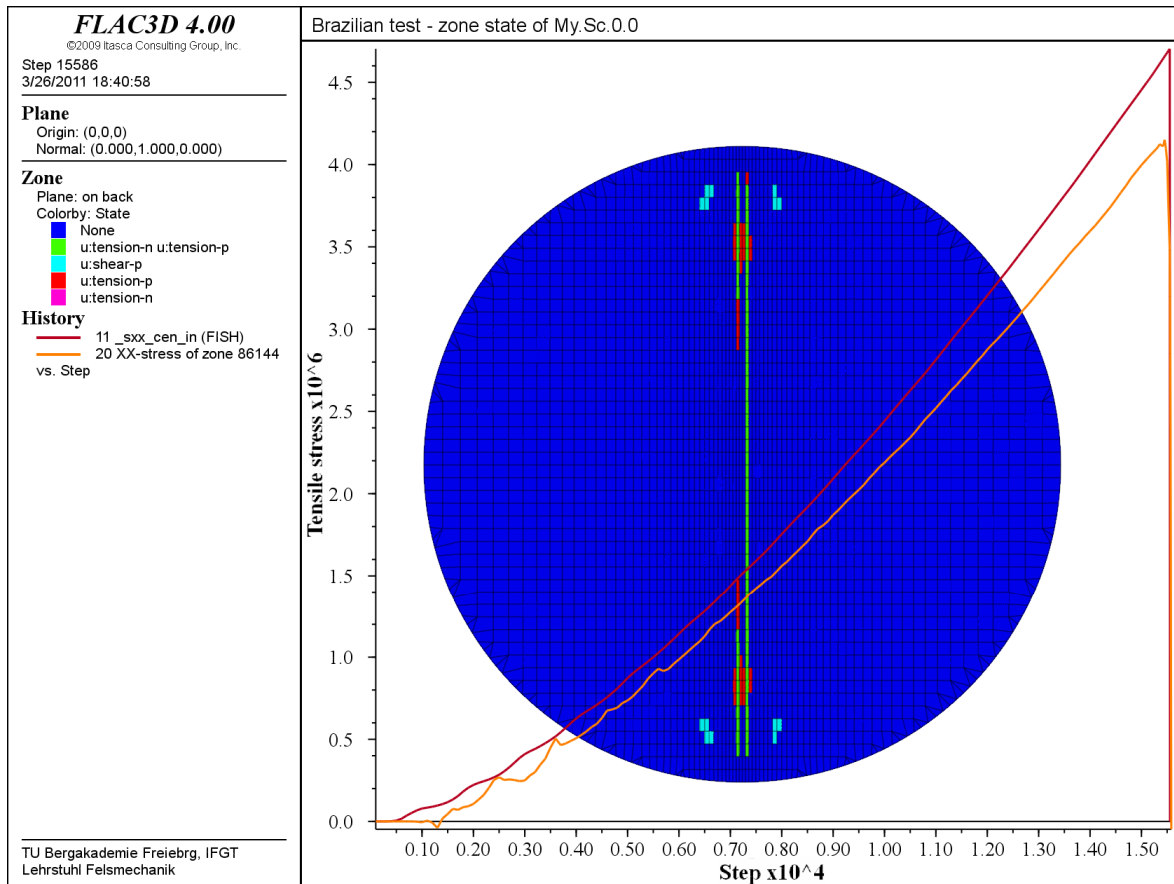
Figure 5-12: Numerical simulation results of My.Sc.0.0 specimen (compare Figure 5-11). Tensile stress (Pa) vs. calculation steps.

Figure 5-11 (b) & 5-12 show that the peak strength (tensile failure) reached in the lab is more or less identical with the result of the numerical simulation. After reaching the peak, a sudden drop is observed (brittle behavior in tension). The tensile stress values given in Figure 5-11 & 5-12 are based on Eq. 1.2 and therefore directly proportional to the load of the loading jaws. Figure 5-12 reveals that tensile failure starts to develop at the center line of the disc. This tensile failure determines the peak load and the subsequent softening.

5.5   Numerical simulation results

5.5.1   Introduction

The investigation of the damage and failure pattern is of prime importance because the Brazilian test is an indirect test method. This means that the deduced strength (mainly tensile strength) is not measured directly but requires correct interpretation.

Exemplarily, Figure 5-13 shows a series of Mohr's circles together with the linear envelopes for the joint planes (the red dash lines) and matrix (the magenta dash lines) given by Eq. (5.2). The failure envelopes correspond to the Mohr-Coulomb failure criterion with a tension cut-off.
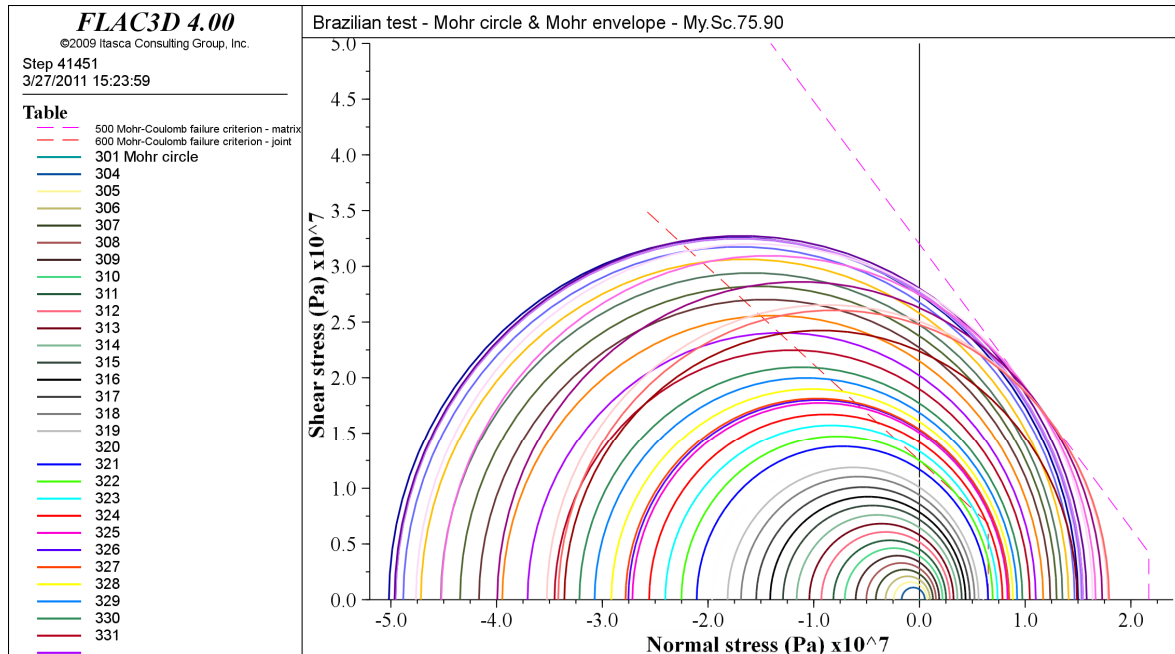
Figure 5-13: Development of Mohr's circles for the center zone under loading until peak strength of My.Sc.75.90 and failure envelopes for the joints and matrix plane.

Figure 5-13 exemplarily shows the development of the Mohr's stress circle for the center element of the disc with loading. The circle development starts at (0, 0) and increases step by step, first moving decidedly towards the left and later back to the right and finally reaching the shear failure envelope. The stress state at the center of the disc never reaches the tension cutoff of the matrix. The failure mechanism at the center of the specimen is therefore shear failure. This is also evident in Figure 5-14. The shear failure (shear-n or u:shear-n) dominates the pattern of plasticity. A mixed-mode fracture pattern is observed as indicated by Figure 5-14. In contrast, the classical evaluation procedure suggests, that this sample (orientation of weak planes perpendicular to loading direction) would fail in matrix tension.
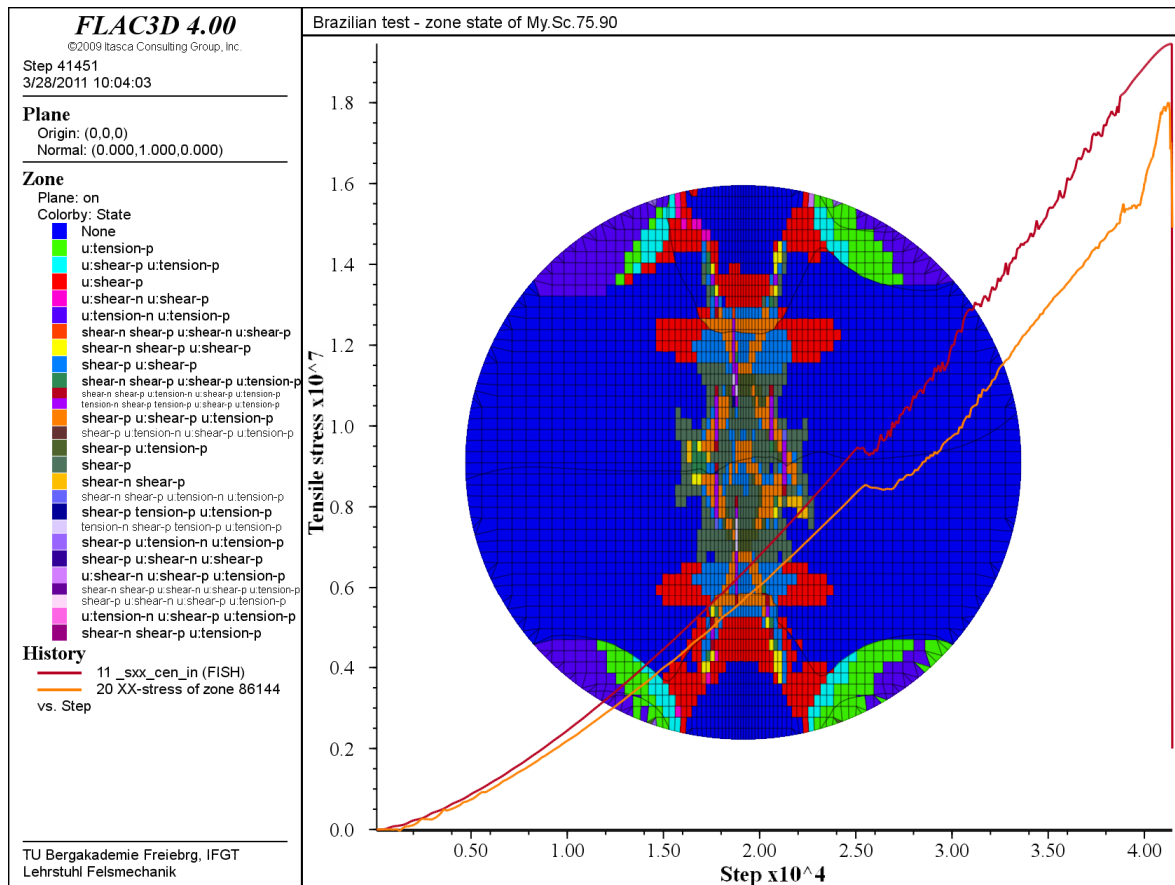
Figure 5-14: Plasticity (failure) pattern at peak strength for Le.Gs.75.90

This example shows that for anisotropic rocks, the failure pattern can be quite complex and a careful stress and fracture pattern analysis has to be undertaken to deduce the right strength values from the Brazilian test.

5.5.2 Stress distribution and failure state

(Continued)

(Continued)
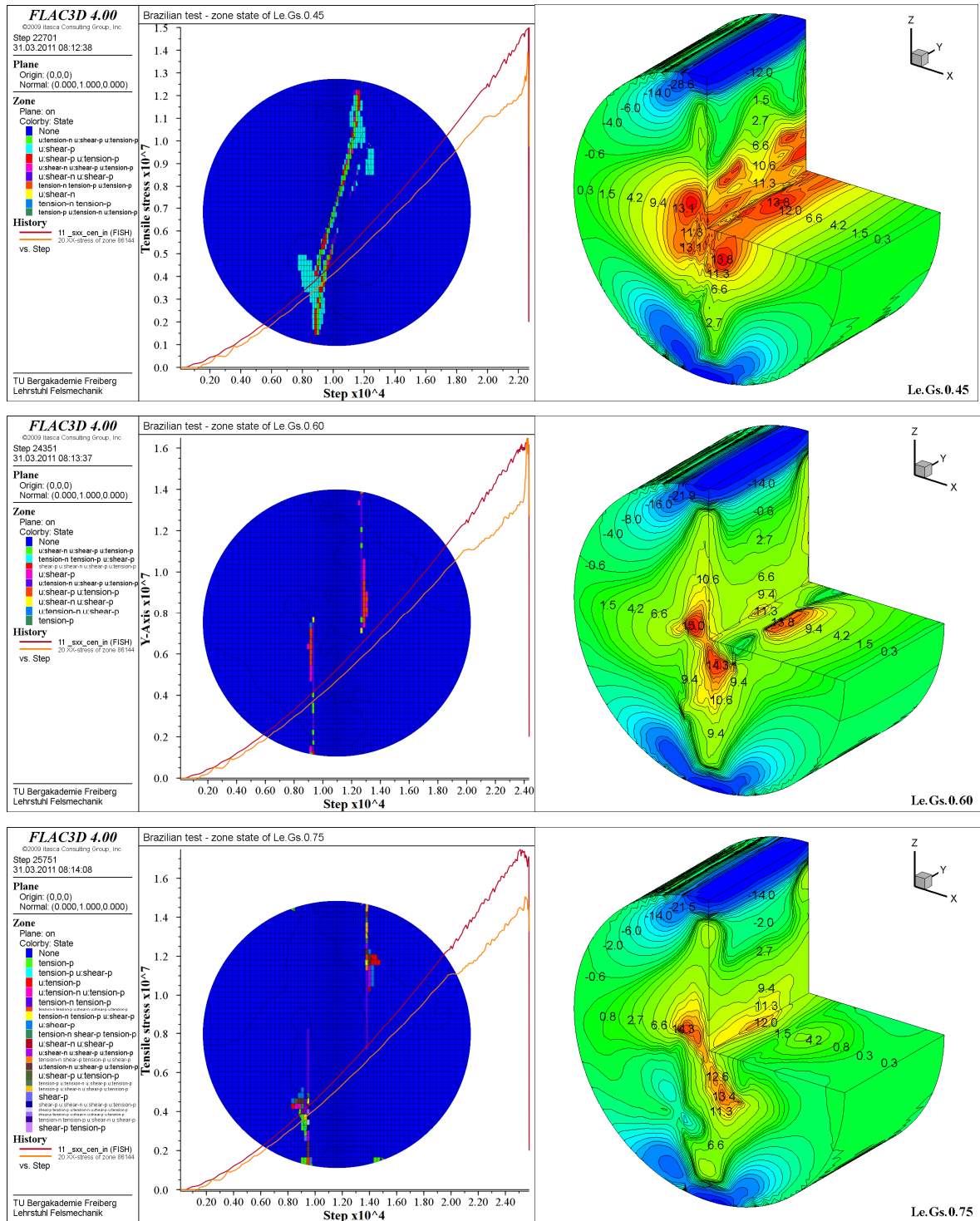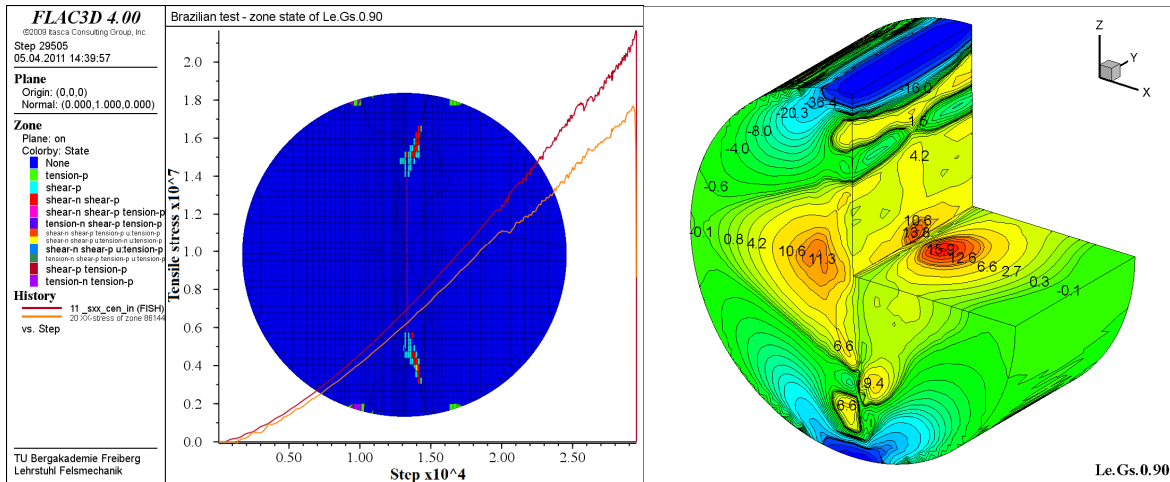
(a) Plasticity state in the middle plane at peak strength and development of "tensile" stress at the center of the specimen relative to Eq. 1.2

(b) Horizontal stress (MPa) contours at peak strength

Figure 5-15: Plasticity state at peak strength in the middle plane and the development of "tensile" stress in the center element relative to Eq. 1.2; (a) and (b) horizontal stress component contours at peak strength for Le.Gs Gneiss ($\psi = 0°$ and $\beta = 0° \div 90°$).

The plastic zone state, the "tensile" stress calculated from the standard Eq. 1.2 for the center of the specimen and the horizontal stress component contours of a disc of Le.Gs.0.0/15/30/45/60/75/90 are presented in Figure 5-15. When $\beta = 0°$, plastic zones develop quickly and move towards the center of the sample. Tensile failure appears exactly along the weakness planes at the center of the disc. For $\beta = 15°$, the plastic zone development is first under the loading jaws and then suddenly re-orients quickly along the center line in the direction parallel to the weakness planes. Clearly, tensile failure at the center still dominates. For $30° < \beta < 75°$, the plasticized area increases in width and shows a symmetric pattern with respect to the load direction. Shear plastification dominates and tensile failure appears within the plasticized area (several parallel tensile fractures) at the ubiquitous joints. As a result, strongly localized tensile failure at the center of the specimen is not observed any more but now along the joints and in the matrix. Where $\beta = 90°$, the plasticized area appears first at the rim of the disc along the weakness planes, then develops under the loading jaws and finally moves in a direction perpendicular to the weakness plane along the center line. The results show that tensile matrix failure dominates in this case.

In general, results of the simulations using various orientation (ψ) and foliation-loading angles (β) indicate that tensile strength depends very strongly on the orientation of the bedding or weakness planes and is relative to the loading direction.

Brazilian tests were performed in order to assess the effect of changes in ψ and β angles on the strength and fracture pattern of Le.Gs Gneiss and My.Sc Slate. The results are shown in Appendices 5.1 and 5.2.

5.5.3   Stress state in an isotropic elastic medium with arbitrary orientation planes

This section focuses on the state of stress in an isotropic elastic material as a function of the orientation of the planes (ψ) in relation to the loading direction (β). The shear/tensile stress states directly relate to the location and type of failure in the joint planes or the matrix. Particularly after yielding has started, the stress-strain behavior is no longer elastic and stress redistributions occur.

In a first step, the stress components for arbitrarily oriented planes are investigated. This procedure can indicate the conditions under which tensile or shear failure is to be expected.

Assuming isotropic elastic behavior, stress tensor components obtained from the theoretical transformation equations [92] were compared with the simulation results in order to specify the different potential failure mechanisms with respect to ψ and β.

The three dimensional stress transformation equations can be obtained when the primed coordinate system is derived from the unprimed system by rotating the angles of dip (dip) and dip direction (dd) as defined in Figure 5-16, linking the orientation angle (ψ) and foliation-loading angle (β).
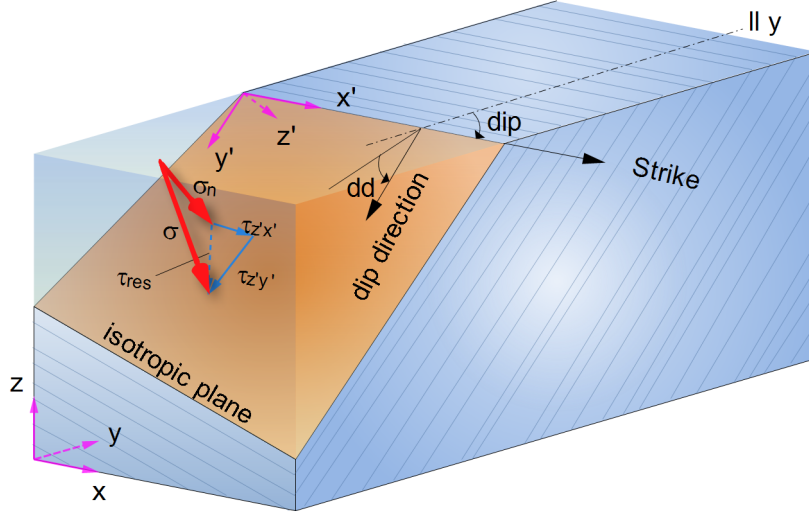
Figure 5-16: Relationship between fixed global coordinates (XYZ) and transverse plane orientations (X'Y'Z'); $(0° \leq dip \leq 360°)$; $(0° \leq dd \leq 90°)$ (after Wittke [92]).

The transformation of the stress tensor $\{\sigma\}$ from the global co-ordinate system into the local x'-y'-z' system is given by: $\{\sigma'\} = [T]\{\sigma\}$. For transversely isotropic materials, an equation is obtained for the required shear and normal stress component [92] by:

$$\tau_{y'z'} = \sigma_x l_2 l_3 + \sigma_y m_2 m_3 + \sigma_z n_2 n_3 + \tau_{xy}(l_2 m_3 + l_3 m_2) + \tau_{yz}(m_2 n_3 + m_3 n_2) + \tau_{zx}(n_2 l_3 + n_3 l_2)$$

$$\tau_{z'x'} = \sigma_x l_3 l_1 + \sigma_y m_3 m_1 + \tau_{xy}(l_1 m_3 + l_3 m_1) + \tau_{yz} m_1 n_3 + \tau_{zx} n_3 l_1 \tag{5.9}$$

$$\sigma_{z'} = \sigma_x l_3^2 + \sigma_y m_3^2 + \sigma_z n_3^2 + 2\tau_{xy} l_3 m_3 + 2\tau_{yz} m_3 n_3 + 2\tau_{zx} n_3 l_3$$

in which

$$l_1 = \sin(dip) \qquad m_1 = \cos(dd) \qquad n_2 = -\sin(dip)$$
$$l_2 = \cos(dd)\cos(dip) \qquad m_2 = -\cos(dip)\sin(dd) \qquad n_3 = -\cos(dip)$$
$$l_3 = -\sin(dip)\cos(dd) \qquad m_3 = \sin(dip)\sin(dd)$$

Parallel to the analytical solution, the stress state at the center of the numerical model was determined and then rotated into the same local co-ordinate system. The results obtained from both methods with respect to ψ and β are compared in Figure 5-17 & 5-18 for the Le.Gs Gneiss and the My.Sc Slate respectively. To make the comparison easier, the tensile stress value for $\psi = 0°$ was normalized to one.
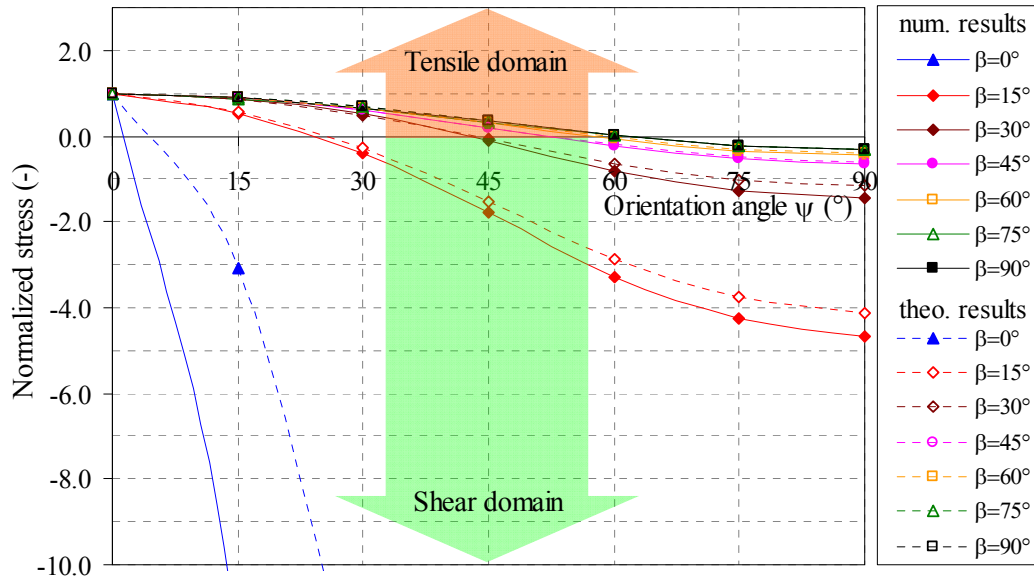
Figure 5-17: Comparison of normalized tensile stress with ψ for Le.Gs Gneiss.
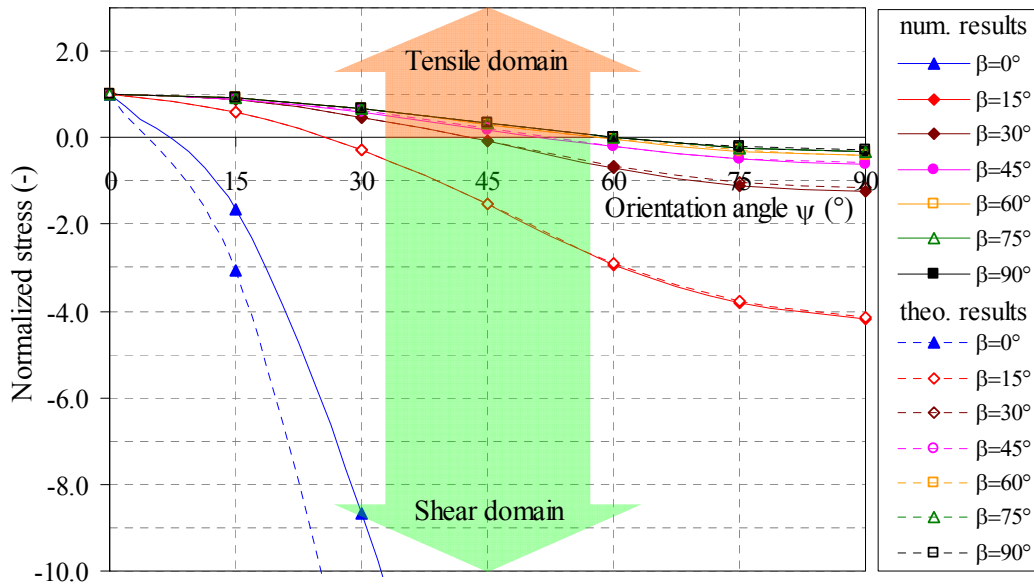
Figure 5-18: Comparison of normalized tensile stress with ψ for My.Sc Slate.

Figure 5-17 & 5-18 illustrate that there is only a small difference between theoretically calculated and numerically simulated stress states. In fact, this small difference only occurs when ψ and β angles are small, i.e. when $(\psi, \beta) \leq 30°$ for Gneiss and $(\psi, \beta) \leq 15°$ for Slate. This means that the influences of the elastic parameters on the stress state are negligible in relation to the orientation of the local planes (ψ) and the loading directions (β).

Meanwhile, a clear distinction between potential tensile and shear failure domains has been shown as a function of ψ and β. Depending on the loading direction, β ≤ 8°; ψ ≤ 60°, both shear and tensile failure are possible. Below ψ < 8°, only tensile failure is possible and shear failure only when ψ > 60°. In other words, shear failure should be considered as a potential failure mechanism over a large span of possible anisotropic plane orientations. One should keep in mind that the actual failure mechanism depends on several factors, on the strength ratios, for instance.

5.5.4 Plasticity states

Plastic zones display the state in which the stresses satisfy the yield criterion. The plasticity pattern across entire width of disc indicate which failure mechanism has developed. Two principal failure mechanism types can be distinguished: shear and tension failure. In the ubiquitous-joint model, shear failure along the joint planes is designated u:shear and tensile failure u:tension in the plasticity plots. The plots also indicate whether stresses within a zone are currently at the yield surface (i.e., the zone is in active failure now, -n), or the zone has failed earlier but the stresses currently fall below the yield surface (the zone failed in the past, -p). Plastic flow can occur at a certain point in time during the simulation but subsequent stress re-distributions may lead to partial unloading so that the yield criterion is no longer satisfied. This is indicated by shear-p or tension-p (on plots of the plasticity state).

Figure 5-19 illustrates the different plasticity states in the Le.Gs.0.45 sample shortly after the peak strength had been reached.
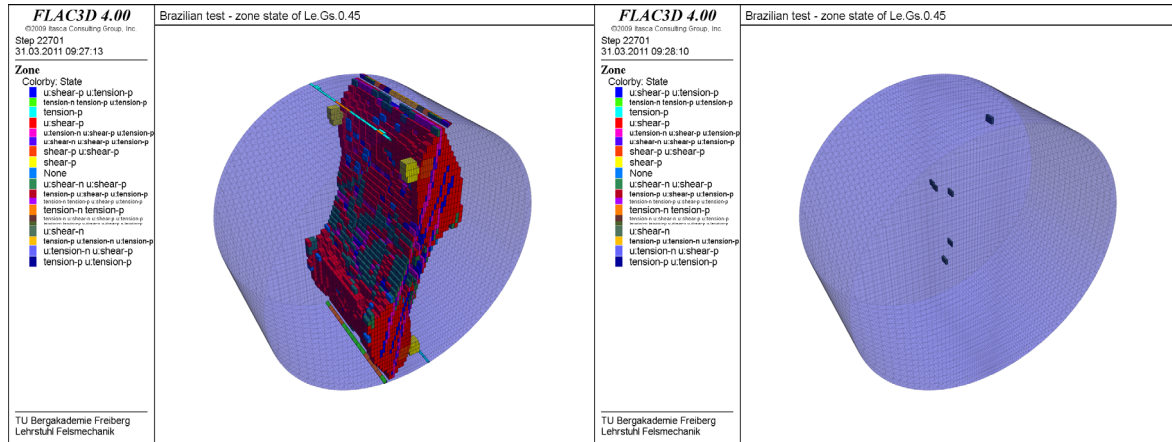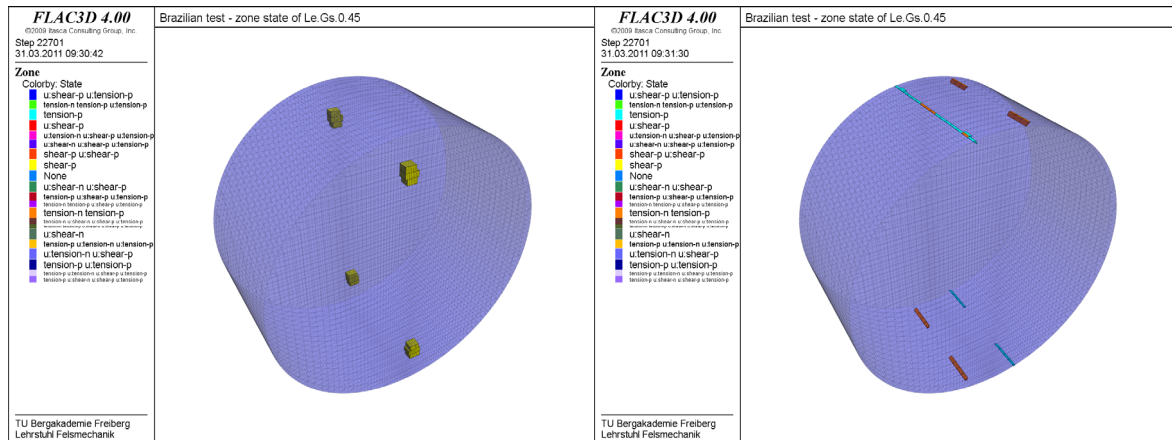
(a) Whole plasticized zones

(b) Joint_shear_now plastic zones
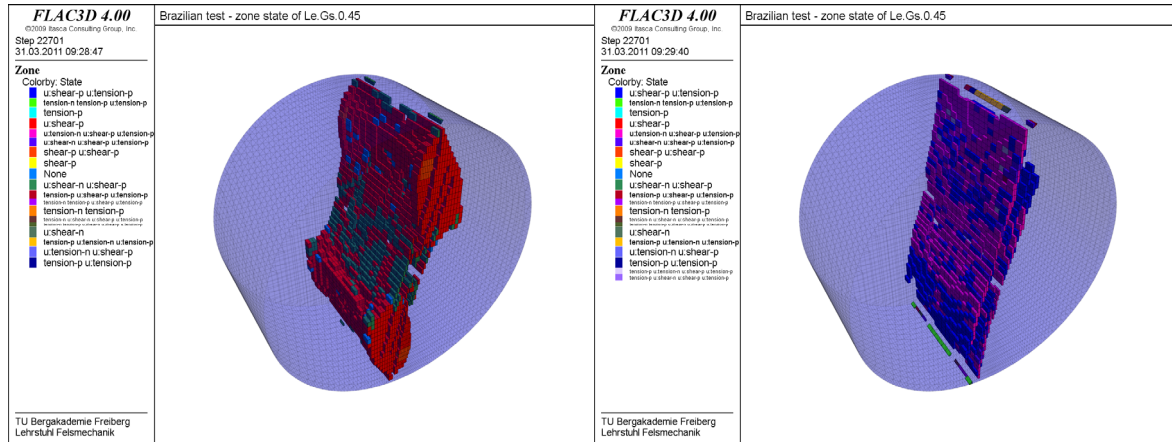
(c) Joint_shear_past plastic zones

(d) Joint_tension_past plastic zones

(e) Matrix_shear_past plastic zones

(f) Matrix_tension_past plastic zones

Figure 5-19: Plasticity state in the Le.Gs.0.45 specimen.

FLAC^{3D} is a continuum code and as such, crack propagation cannot be explicitly modeled. However, based on the development of stresses and the appearance and development of plastic states in each step of the numerical calculations, development of the plasticity pattern can be interpreted as a fracture propagation process.

5.5.5 Damage and fracture process

Figure 5-20 & 5-21 illustrate the process of damage development whereby different stages are considered in the numerical simulations; example:

➢ First, tensile plastic zones appear at r/R = 0.72 in Le.Gs.0.0 and at r/R = 0.76 in Le.Gs.0.90 and then spread towards the center of the disc.

➢ In the middle plane, tensile plastic zones do not only first appear at the center but also at r/R = 0.44 and 0.48 in Le.Gs.0.0 and Le.Gs.0.90, respectively. This means that the initial damage does not occur at the center of the disc but that triggered by the initial damage; secondary tensile plastic zones rapidly develop along the sample's center line.

➢ Tensile strength of joints (9.5 MPa) in Le.Gs.0.0 reaches its maximum along the center plane, leading to tensile failure. Figure 5-20 indicates that apparently not all elements really reached their ultimate strength. But this is misleading then the plastification indicates that at least one of the 10 sub-elements had reached the critical stress state. In such a case, the whole element is considered to be in the state of failure and softening begins, this being extremely strong for tensile failure and therefore leading to a sudden drop in stress.

➢ As indicated by Figure 5-21, matrix tensile failure dominates in Le.Gs.0.90. The elements along the central plane therefore only reach peak values of about 23 MPa.

➢ The damage in anisotropic materials during the Brazilian test is a very complicated process comprising tensile and shear fracturing.
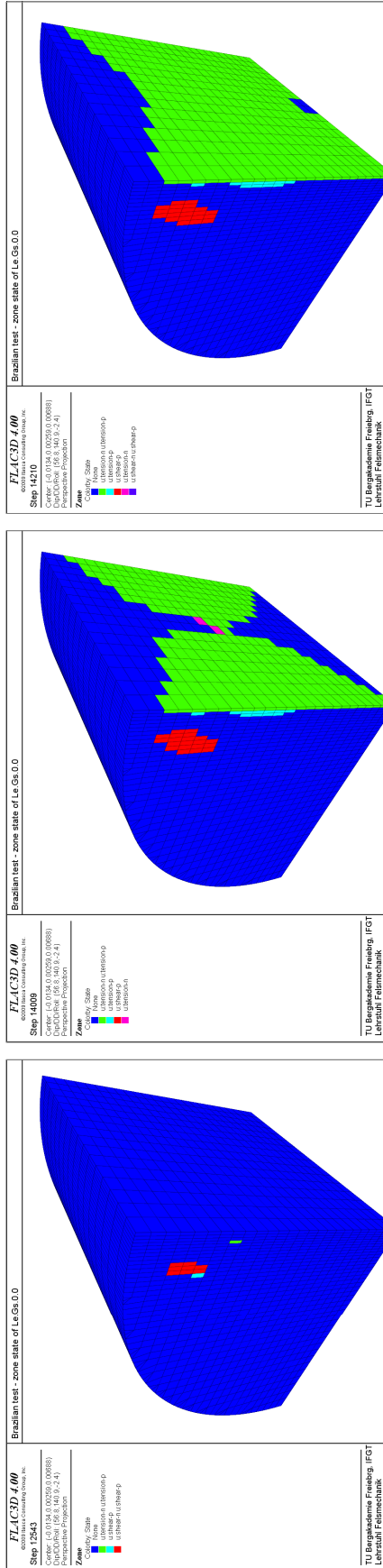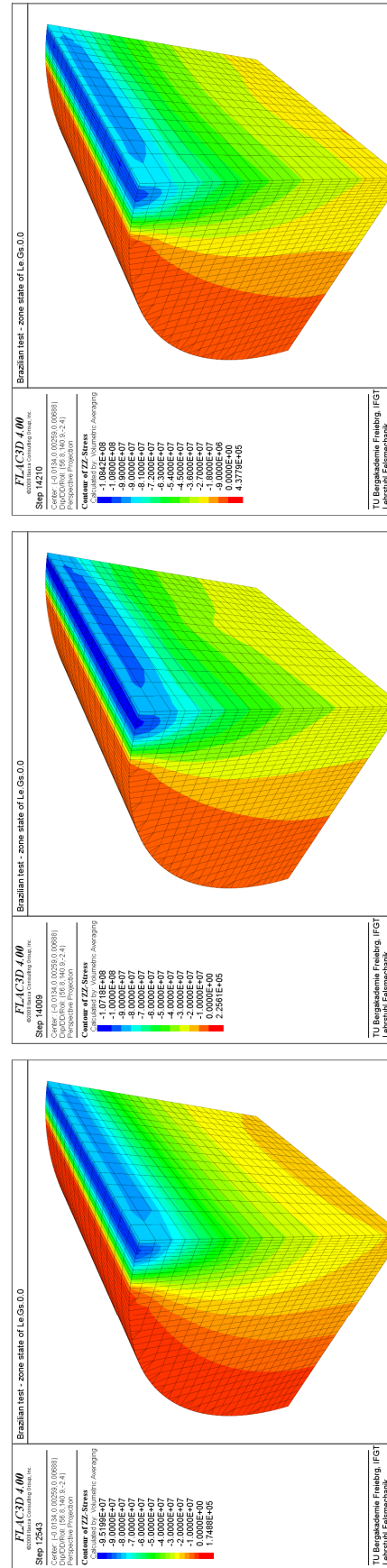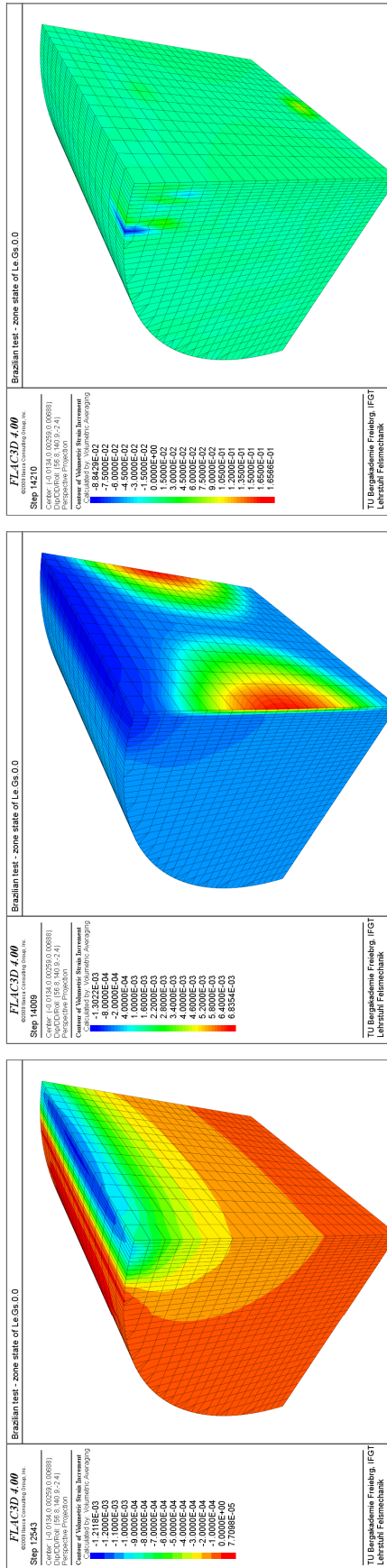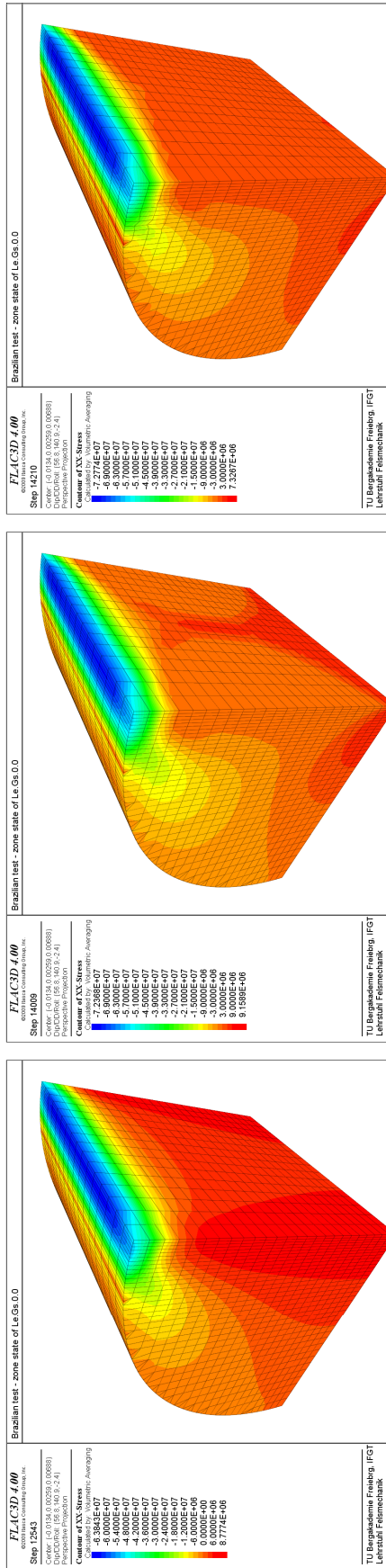
Plastic tensile zone
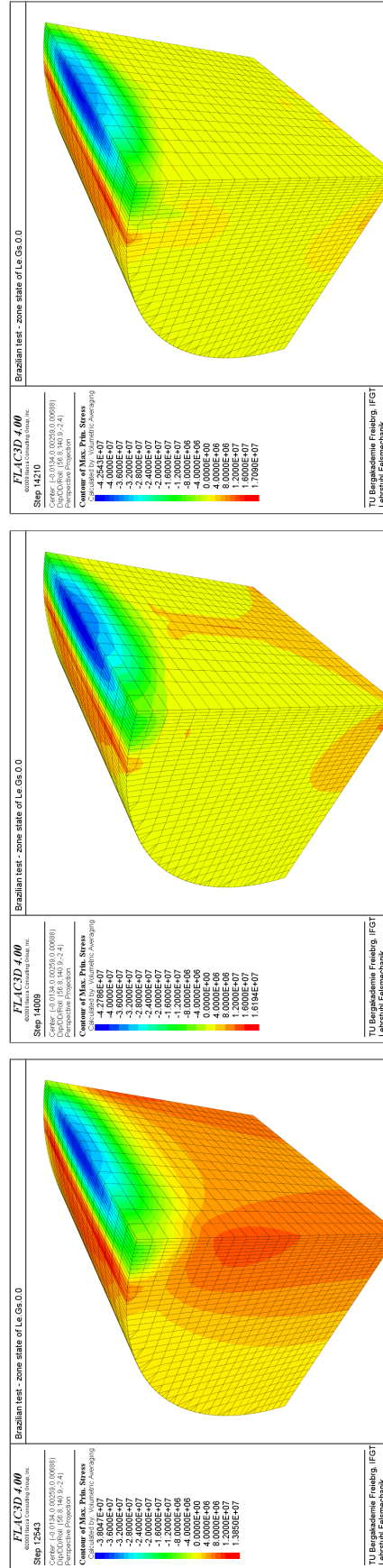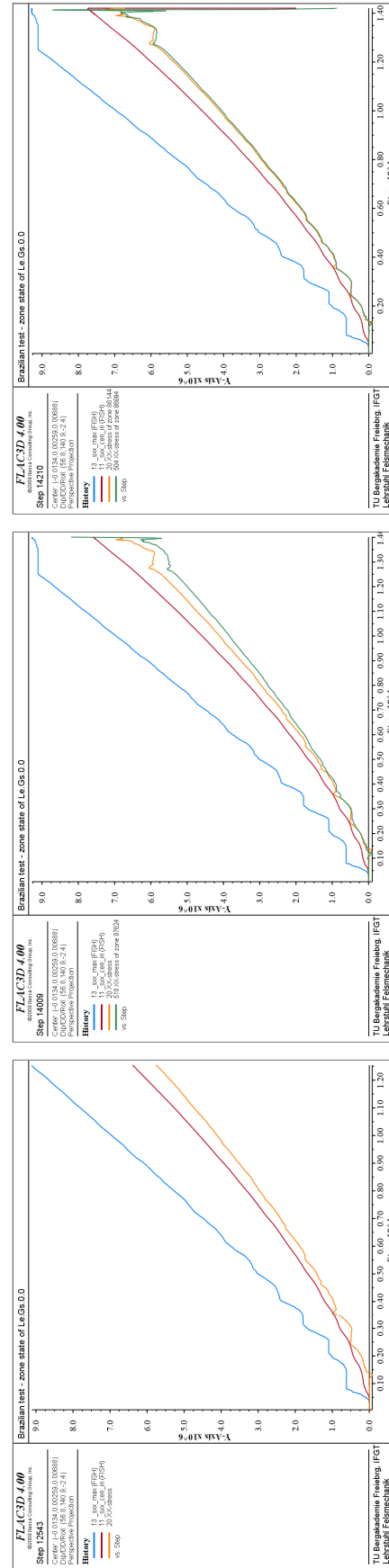

Max. principal stress (Pa)

(Continued)

Volume strain increment (-)

Vertical stress component (Pa)

(Continued)

Horizontal stress component (Pa)

(a) calculating at step 12543   (b) calculating at step 14009   (c) calculating at step 14210

Tensile stress (Pa) at selected points of observation close to the center of the disc

Figure 5-20: Damage development in the Le.Gs.0.0 specimen
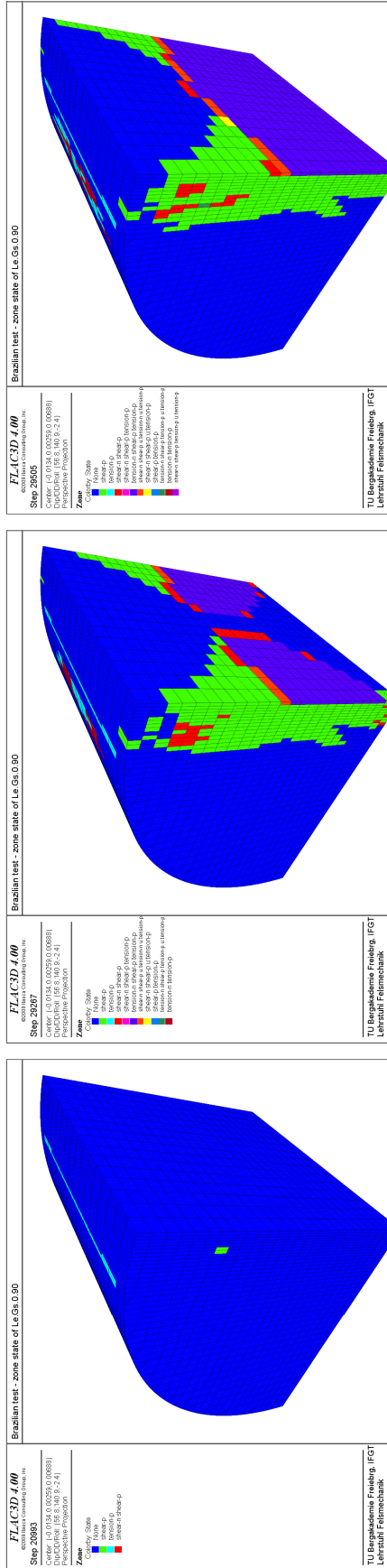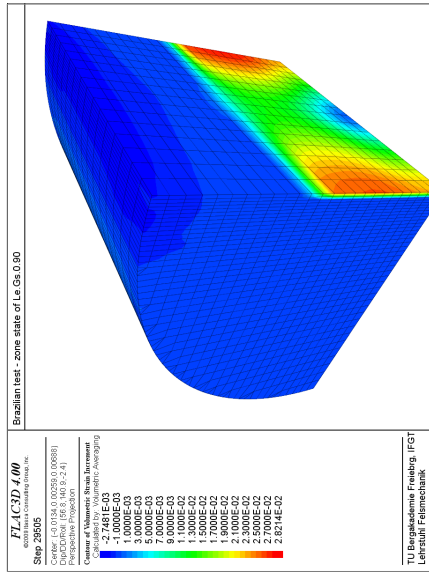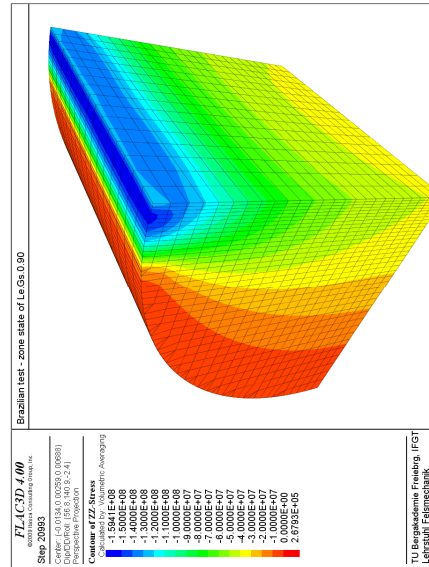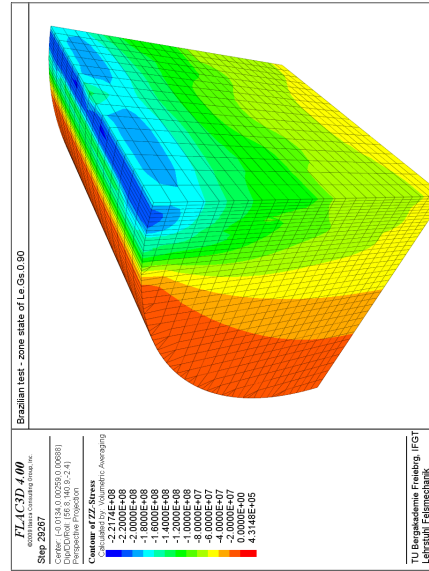
Plastic tensile zone
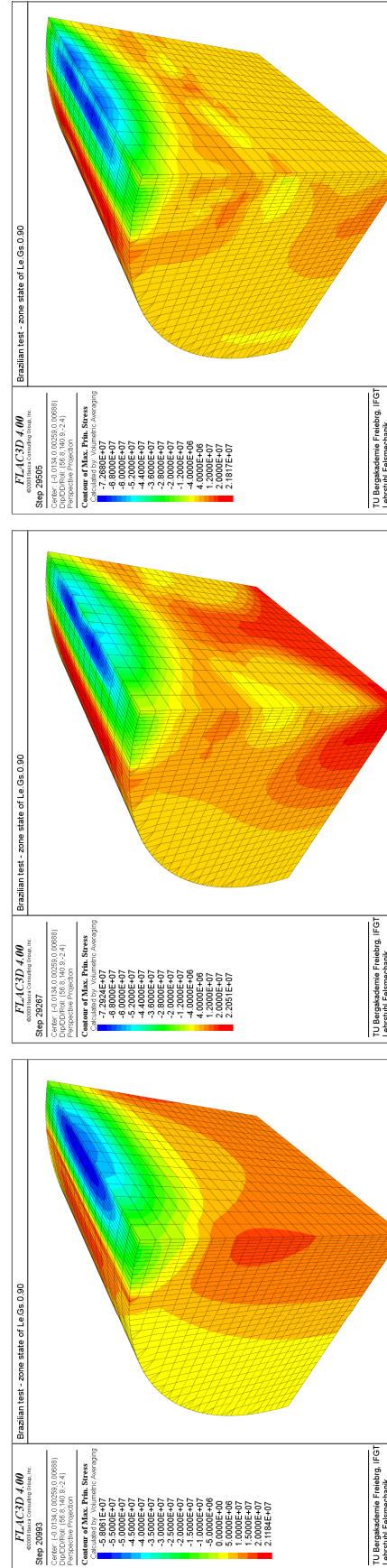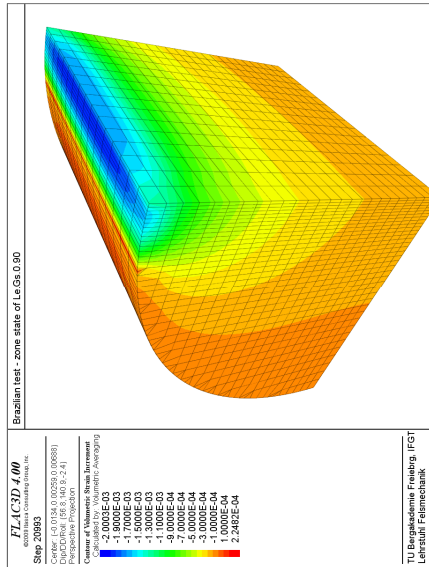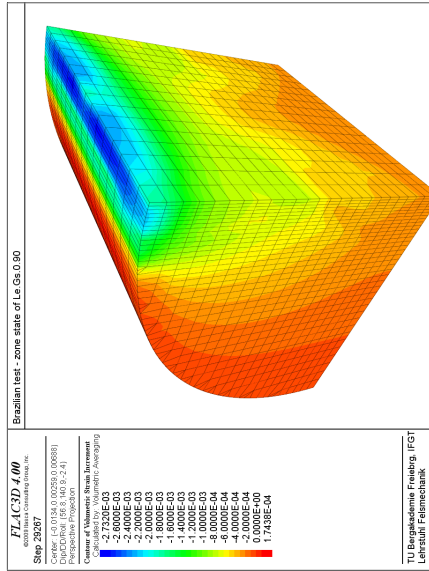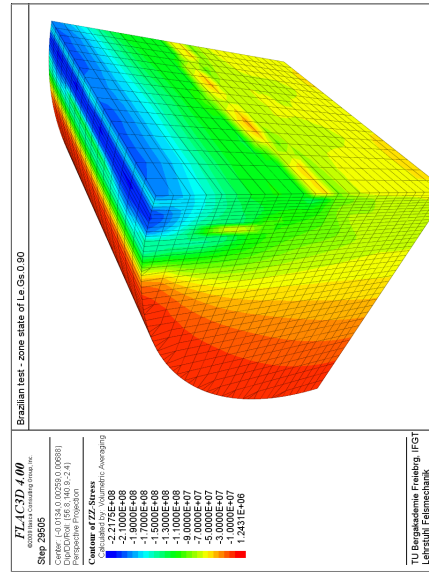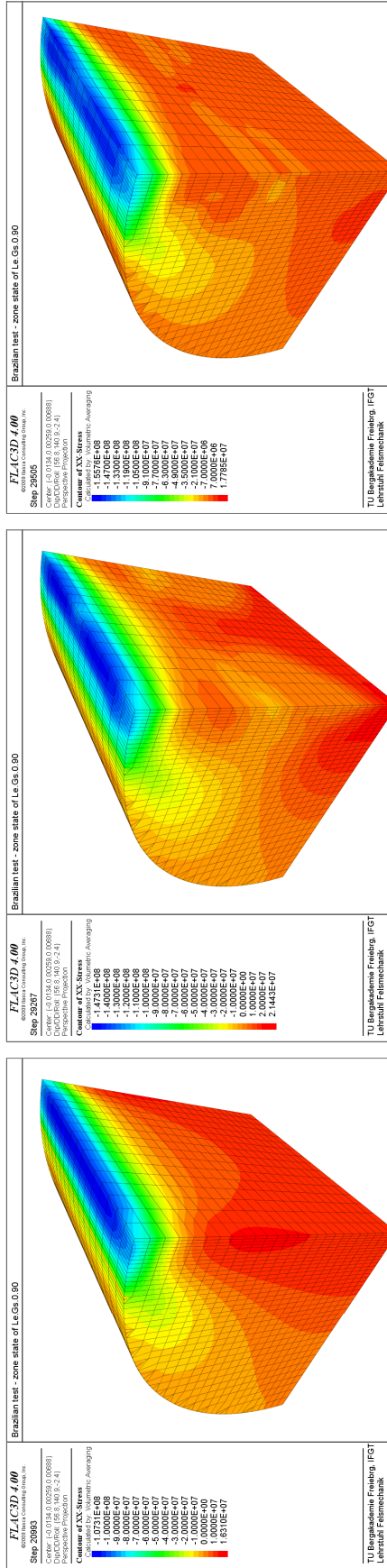
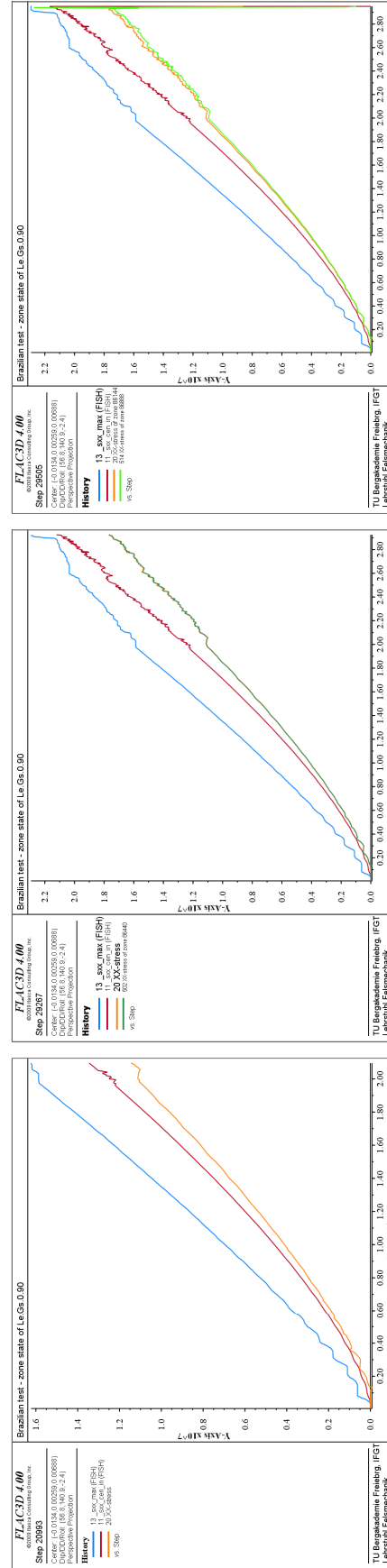Max. principal stress (Pa)

(Continued)

Volume strain increment (-)

Vertical stress component (Pa)

(Continued)

Horizontal stress component (Pa)

(a) calculating at step 20993   (b) calculating at step 29267   (c) calculating at step 29505

Tensile stress (Pa) at selected points of observation close to the center of the disc

Figure 5-21: Damage development in the Le.Gs.0.90 specimen

5.5.6   Fracture patterns – Comparison of lab results and numerical simulations

Figure 5-22 shows a comparison of typical fracture patterns observed in the Le.Gs Gneiss during the lab tests and revealed by the numerical simulations as well. Notice that photos for lab results show front side, but numerical simulations view behind.

(a) Typical fracture pattern I ($\psi = 0°$): single fracture develops along the central line.

(b) Typical fracture pattern II ($15° \leq \psi \leq 45°$): a more diffuse inclined fracture network (fracture coalescence) develops within a wider area along the center of the disc.

(c) Typical fracture pattern III (60° ≤ ψ ≤ 75°): fracture development away from the center line of the disc begins at the rim.
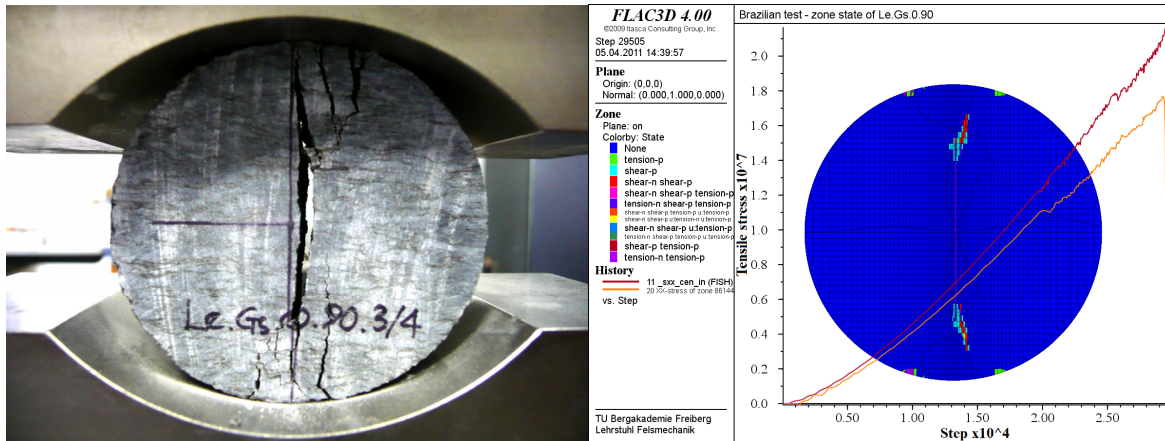
(d) Typical fracture pattern IV (ψ = 90°): initial fractures appear at the rim near the loading area followed by fracture across the center line of the disc.

Figure 5-22: Typical fracture patterns observed in lab tests compared with numerical simulation results (see also Appendices).

5.6 Tensile strength – Comparison of lab results and numerical simulations

In this section, the numerical simulation results will be compared with the results from lab tests. Special attention will be paid to the stress component perpendicular to the disc axis at the center of the specimen (sxx_cen) since the classical evaluation is based on the assumption that the maximum tensile stress and the tensile cracking are respectively created and initiated there. Also of major interest is the calculated tensile strength from Eq. 1.2 (theoretical sxx_cen). This is based on either the measured peak load observed during the lab tests or the peak load transferred through the interface from the loading jaws to the disc during the numerical simulations.

Figure 5-23 to Figure 5-26 compare lab results and selected results obtained from the numerical simulations.

5.6.1   Tensile strength of Le.Gs Gneiss

	$\psi = 0°$	$\psi = 15°$	$\psi = 30°$	$\psi = 45°$	$\psi = 60°$	$\psi = 75°$	$\psi = 90°$
$\beta = 0°$	7.25	8.23	12.44	16.38	18.18	17.98	21.07
$\beta = 15°$	8.90	8.98	12.55	15.66	18.38	17.93	21.07
$\beta = 30°$	11.09	11.44	13.57	15.04	15.07	18.16	21.07
$\beta = 45°$	12.87	13.73	15.60	16.35	14.66	16.21	21.07
$\beta = 60°$	13.46	15.11	13.96	16.28	14.84	15.56	21.07
$\beta = 75°$	15.04	14.78	12.80	15.73	14.79	15.54	21.07
$\beta = 90°$	17.77	17.60	17.66	17.29	14.71	15.48	21.07

**Table 5-2:** Numerical tensile strength (numerical sxx_cen) results of Le.Gs Gneiss (MPa).

	$\psi = 0°$	$\psi = 15°$	$\psi = 30°$	$\psi = 45°$	$\psi = 60°$	$\psi = 75°$	$\psi = 90°$
$\beta = 0°$	7.75	9.40	14.87	19.17	21.23	21.51	23.72
$\beta = 15°$	10.49	10.40	14.59	18.08	21.29	21.30	23.72
$\beta = 30°$	11.47	12.61	12.86	18.04	17.46	21.13	23.72
$\beta = 45°$	14.62	15.02	17.37	17.35	17.39	18.83	23.72
$\beta = 60°$	16.26	15.15	16.90	18.05	17.23	18.27	23.72
$\beta = 75°$	17.25	17.33	15.22	18.13	17.26	18.05	23.72
$\beta = 90°$	21.29	21.40	21.45	20.72	17.16	17.95	23.72

**Table 5-3:** Theoretical tensile strength (theoretical sxx_cen) results of Le.Gs Gneiss (MPa).

	$\psi = 0°$	$\psi = 15°$	$\psi = 30°$	$\psi = 45°$	$\psi = 60°$	$\psi = 75°$	$\psi = 90°$
$\beta = 0°$	6%	12%	16%	15%	14%	16%	11%
$\beta = 15°$	15%	14%	14%	13%	14%	16%	11%
$\beta = 30°$	3%	9%	-5%	17%	14%	14%	11%
$\beta = 45°$	12%	9%	10%	6%	16%	14%	11%
$\beta = 60°$	17%	0%	17%	10%	14%	15%	11%
$\beta = 75°$	13%	15%	16%	13%	14%	14%	11%
$\beta = 90°$	17%	18%	18%	17%	14%	14%	11%

Table 5-4: Differences between theoretical and numerical tensile strength of Le.Gs Gneiss.
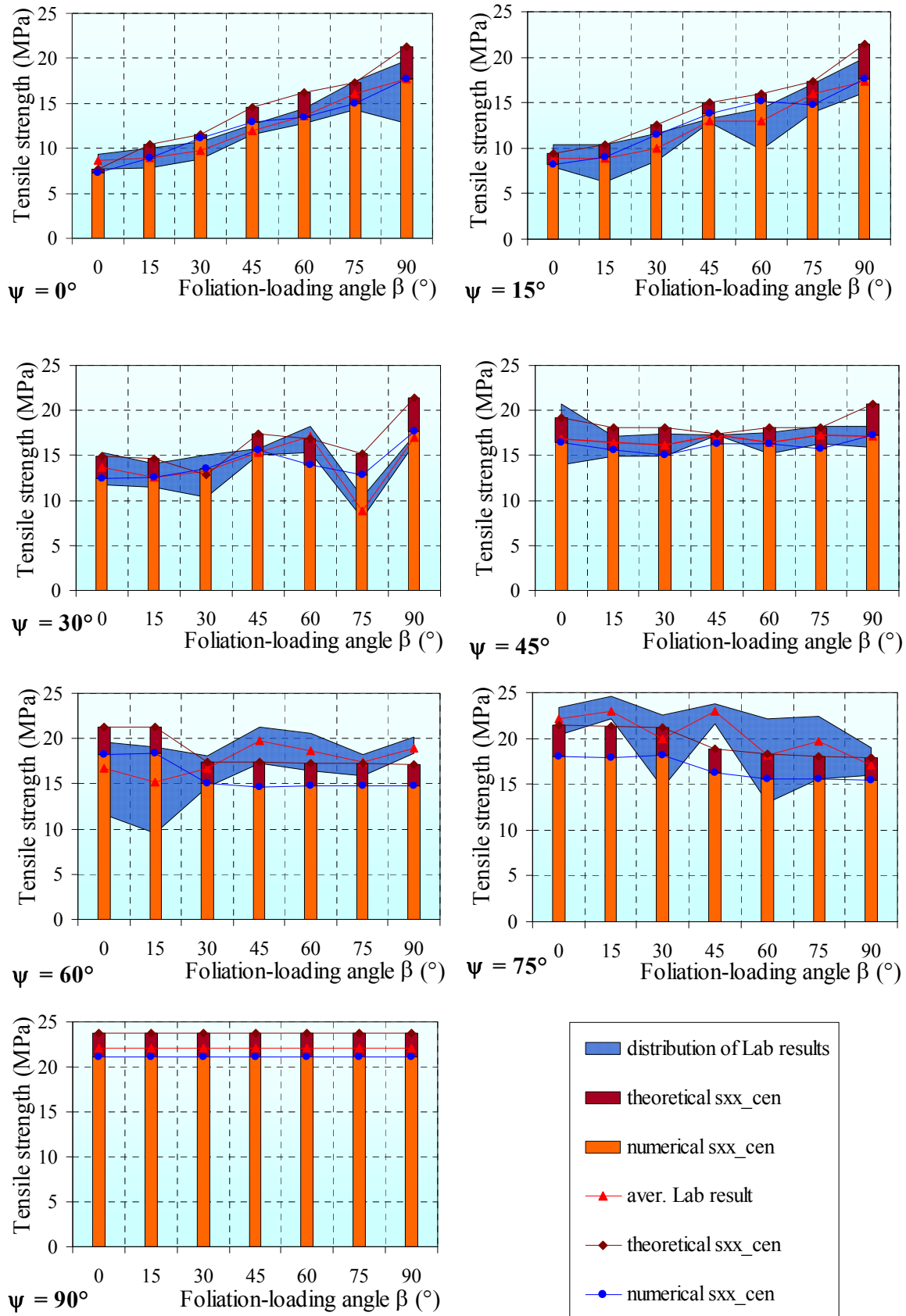
Figure 5-23: Tensile strengths of Le.Gs Gneiss relative to the orientation angle (ψ)
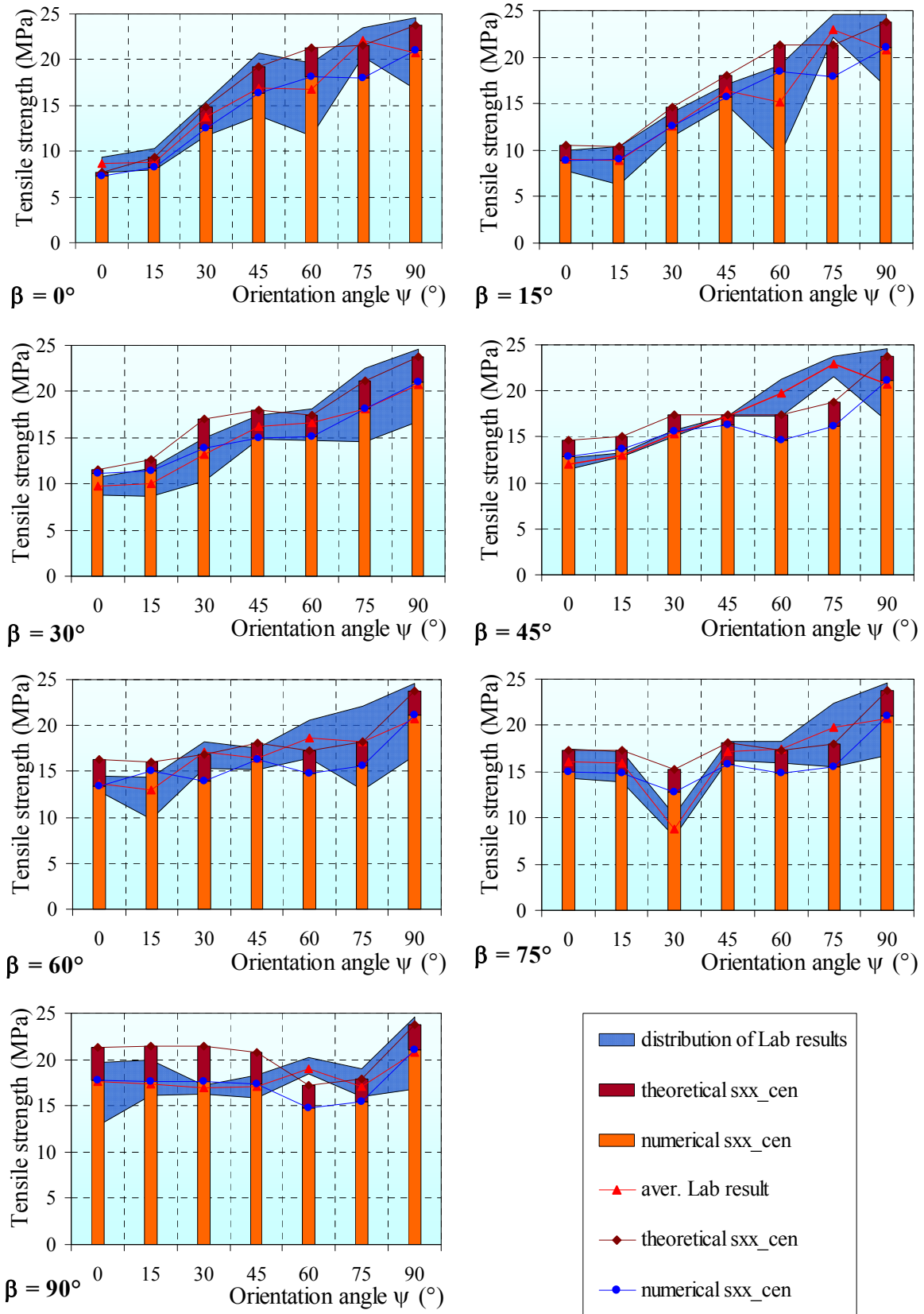
Figure 5-24: Tensile strengths of Le.Gs Gneiss relative to the foliation-loading angle (β)

Tensile strength values obtained by different approaches with regard to different orientation (ψ) and foliation-loading (β) angles are displayed in Table 5-2 & 5-4 and Figure 5-23 & 5-24 for the Le.Gs Gneiss. The comparison shows that the determined numerical values are close to experimental ones. Both methods reveal a significant influence of ψ and β.

Assessment of numerically determined tensile strength relative to the orientation angle (ψ):

➢ At $\psi \leq 15°$, tensile strength values show a strong dependence on the foliation-loading angle (β). Tensile strength significantly increases with increasing β-values, with the ratio of $\beta = 90°$ to $\beta = 0°$ at its maximum value $\beta_{\psi=0°}^{\overline{\frac{90°}{0°}}} = 2.45$.

➢ At $30° \leq \psi \leq 45°$, no clear tendency can be detected; the maximum tensile strength ratio equal to $\beta_{\psi=30°}^{\overline{\frac{90°}{0°}}} = 1.42$ for $\psi = 30°$ and $\beta_{\psi=45°}^{\frac{90°}{30°}} = 1.15$ for $\psi = 45°$.

➢ At $60° \leq \psi \leq 75°$, bisection becomes visible. The tensile strength is slightly higher at low β-values (smaller than about $40°$), the maximum ratio at $\psi = 60°$ equal to $\beta_{\psi=60°}^{\overline{\frac{90°}{0°}}} = 0.81$ and $\beta_{\psi=75°}^{\overline{\frac{90°}{0°}}} = 0.86$ at $\psi = 75°$.

➢ $\psi = 90°$ is a special case. Tensile strength here does not depend on β because the weakness planes always occur parallel to the loading direction. In this case, the maximum tensile strength value is 21.07 (MPa).

Assessment of the numerically determined tensile strength relative to the foliation-loading angle (β):

➢ At $\beta \leq 60°$, a significant increase in tensile strength is observed with increasing orientation angle (ψ). With increasing β-values, this increase is decrescent, the ratio varying between $\psi_{\beta=0°}^{\overline{\frac{90°}{0°}}} = 2.91$ at $\beta = 0°$ and $\psi_{\beta=60°}^{\overline{\frac{90°}{0°}}} = 1.56$ at $\beta = 60°$.

➢ Where $\beta \geq 75°$, the influence of ψ on the tensile strength is small. It would seem that up to about $\psi = 45°$, a near tensile strength constancy is valid followed by a small decrease and a final strong increase. The maximum tensile strength ratio is then equal to $\psi_{\beta=75°}^{\overline{\frac{90°}{30°}}} = 1.65$ and $\psi_{\beta=90°}^{\overline{\frac{90°}{60°}}} = 1.43$ at $\beta = 75°$ and $\beta = 90°$, respectively.

Based on the gradients in Figure 5-23 & 5-24, it becomes clear that the influence of ψ is larger than that of β in the Le.Gs Gneiss, especially when both ψ and β are small.

Analysis of failure state (see also Appendix 5.1)

➢ At $\psi < 30°$ and $\beta = 0°$ pure tensile failure occurs exactly along the weakness plane across the disc center. Failure is completely governed by the tensile failure joint.

➢ At $\beta = 15°$ and $90°$, plastic zones develop first under the loading jaws and then quickly spread towards the center line. Mixed tensile-shear failure appears along the center line of the disc but tensile failure dominates. Tensile failure also dominates only in the joints at $\beta = 15°$ and in the matrix at all $\beta = 90°$. At $15° \leq \beta \leq 75°$, the plasticized area becomes wider and more complicated in detail though a symmetric pattern is still observed with respect to the loading direction. Shear plastification dominates and tensile failure appears to be ubiquitous within the plasticized area (several parallel tensile fractures). Failure is along the joints and also in the matrix.

➢ At $\psi = 30°$, mixed tensile-shear failure appears to be ubiquitously within the plasticized area at all β except where $\psi = 30°$, $\beta = 30°$, pure shear failure occurring along the joints in this case.

➢ Where $\psi > 30°$, the plasticized area, though becoming wider relative to the loading direction, shows a symmetric pattern. Mixed shear-tensile failure appears ubiquitously within the plasticized area except at $\psi = 45°$, $\beta = 30°$, where shear failure dominates in the joint plane.

5.6.2   Tensile strength of My.Sc Slate

	ψ = 0°	ψ = 15°	ψ = 30°	ψ = 45°	ψ = 60°	ψ = 75°	ψ = 90°
β = 0°	4.14	5.07	6.12	11.98	14.42	17.24	19.15
β = 15°	4.33	5.15	6.23	11.00	14.26	17.13	19.15
β = 30°	6.33	6.22	7.49	9.54	13.44	17.00	19.15
β = 45°	8.16	6.17	9.36	9.77	13.18	17.70	19.15
β = 60°	9.40	8.15	10.47	10.94	12.07	17.88	19.15
β = 75°	10.00	8.71	11.11	11.41	10.82	17.80	19.15
β = 90°	15.20	12.84	12.74	12.45	10.77	18.05	19.15

Table 5-5: Numerical tensile strength (numerical sxx_cen) results of My.Sc Slate (MPa).

	ψ = 0°	ψ = 15°	ψ = 30°	ψ = 45°	ψ = 60°	ψ = 75°	ψ = 90°
β = 0°	4.69	5.77	6.93	14.50	17.02	20.42	19.92
β = 15°	4.98	5.89	7.24	13.50	15.54	20.47	19.92
β = 30°	7.19	7.30	8.54	11.58	14.59	20.45	19.92
β = 45°	9.33	7.12	11.33	11.32	14.47	19.21	19.92
β = 60°	11.32	9.48	11.83	11.72	13.55	19.36	19.92
β = 75°	11.60	9.54	13.17	13.00	12.67	19.49	19.92
β = 90°	17.90	15.51	15.07	14.74	12.74	19.54	19.92

Table 5-6: Theoretical tensile strength (theoretical sxx_cen) results of My.Sc Slate (MPa).

	ψ = 0°	ψ = 15°	ψ = 30°	ψ = 45°	ψ = 60°	ψ = 75°	ψ = 90°
β = 0°	12%	12%	12%	17%	15%	16%	4%
β = 15°	13%	13%	14%	19%	8%	16%	4%
β = 30°	12%	15%	12%	18%	8%	17%	4%
β = 45°	13%	13%	17%	14%	9%	8%	4%
β = 60°	17%	14%	11%	7%	11%	8%	4%
β = 75°	14%	9%	16%	12%	15%	9%	4%
β = 90°	15%	17%	15%	16%	15%	8%	4%

Table 5-7: Differences in the theoretical and numerical tensile strength of My.Sc Slate.
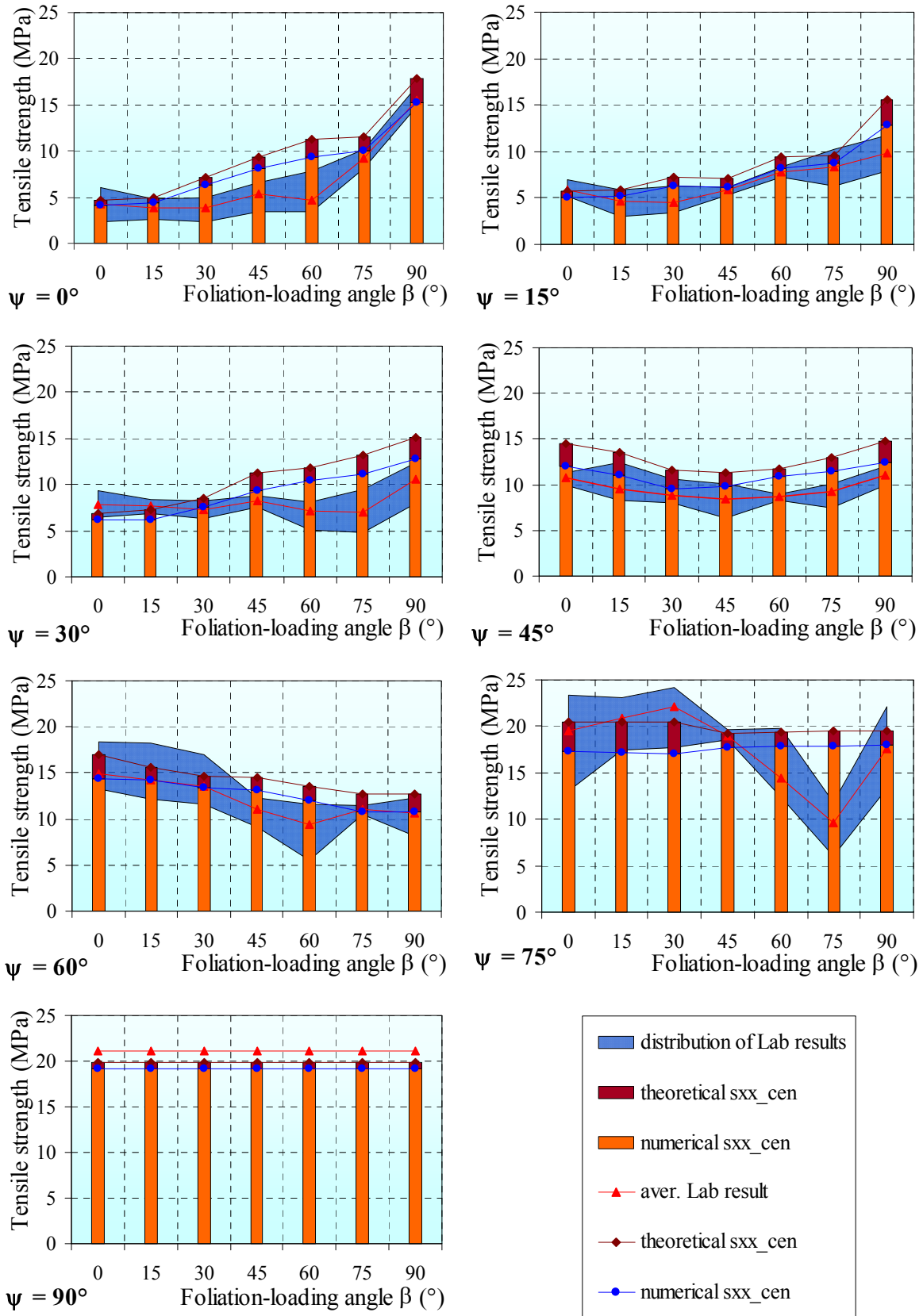
Figure 5-25: Tensile strengths of My.Sc Slate relative to the orientation angle (ψ)
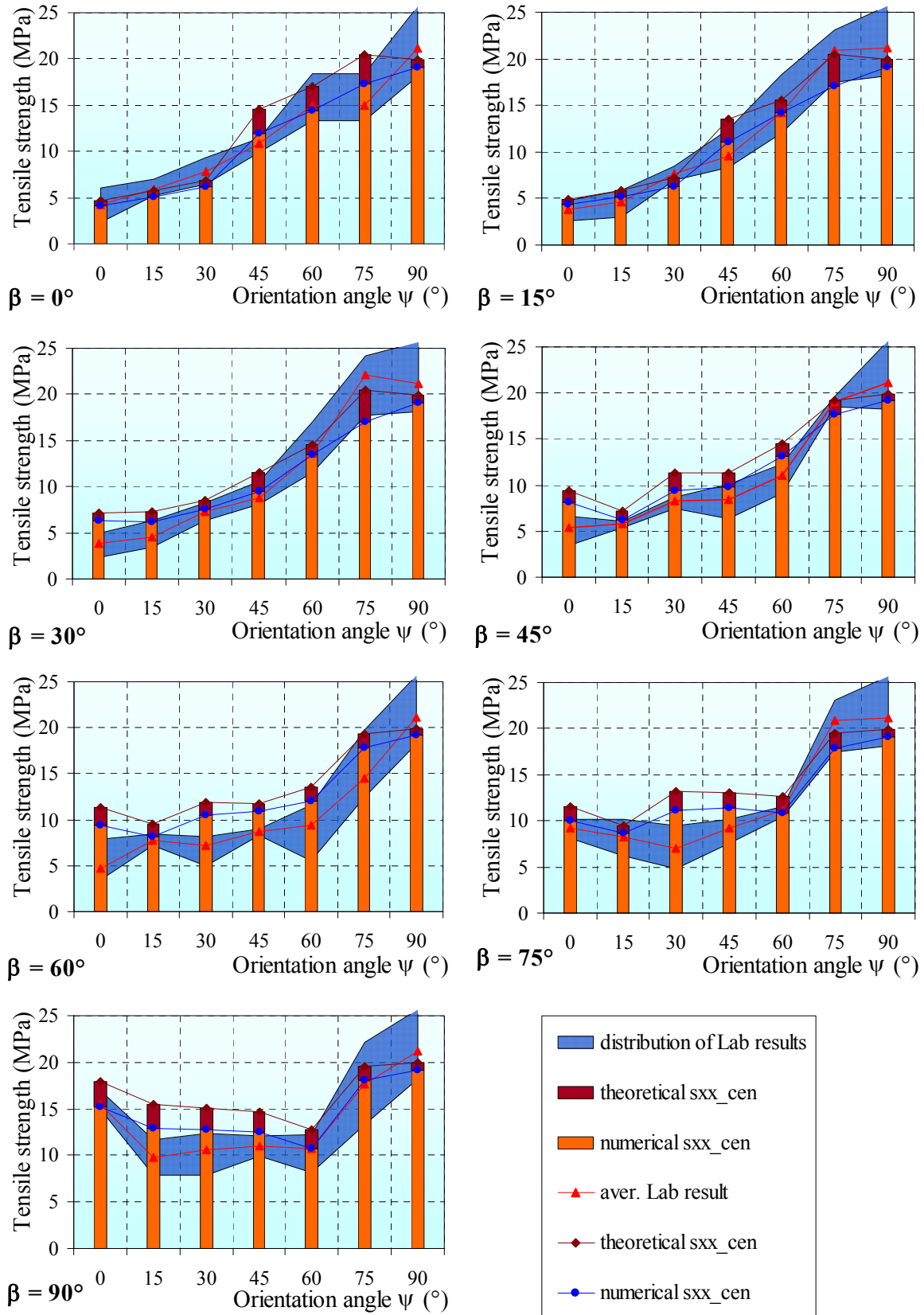
Figure 5-26: Tensile strengths of My.Sc Slate relative to the foliation-loading angle (β)

The results displayed in Table 5-5, 5-6 & 5-7 and Figure 5-25 & 5-26 are analogous to the section above and show the tensile strength of My.Sc Slate relative to different orientation (ψ) and foliation-loading (β) angles. Again, a satisfactory agreement is observed between lab and numerical simulation results.

Assessment of the tensile strength with respect to the orientation angle (ψ):

➢ At ψ < 45°, tensile strength increases with increasing foliation-loading angle (β). The maximum tensile strength ratio is $\beta_{\psi=0°}^{\overline{0°}^{90°}} = 3.67$; $\beta_{\psi=15°}^{\overline{0°}^{90°}} = 2.53$ and $\beta_{\psi=30°}^{\overline{0°}^{90°}} = 2.08$ at ψ = 0°, 15° and 30°, respectively.

➢ A ψ = 45°, a minimum is observed at β = 45° with slight symmetrically increasing values in both directions, towards β = 0° and β = 90°.

➢ At ψ = 60°, tensile strength slightly decreases with increasing β-values. The maximum tensile strength ratio is $\beta_{\psi=60°}^{\overline{0°}^{90°}} = 0.75$.

➢ At ψ = 75°, the values show no dependence on β.

➢ ψ = 90° is a special case. Tensile strength does not depend on the foliation-loading angle β because the weakness planes are inherently parallel to the loading direction. Here, the maximum tensile strength of about 20 MPa is reached.

Assessment of the tensile strength with respect to the foliation-loading angle (β):

➢ At 0° ≤ β ≤ 45°, tensile strength strongly increases with increasing ψ. The maximum tensile strength ratio is $\psi_{\beta=0°}^{\overline{0°}^{90°}} = 4.63$ at β = 0°.

➢ At 60 ≤ β and β ≥ 75°, the tensile strength is relatively low and constant at ψ ≤ 60° although it shows a remarkable increase at ψ ≥ 60°.

➢ At β = 90°, a small decrease in tensile strength is observed up to about ψ = 60°, followed by a sharp increase at ψ > 60°.

As observed in Figure 5-25 & 5-26 in the Slate, the influence of ψ is stronger than that of β, especially where both ψ and β are small.

Analysis of failure state (see also Appendix 5.2):

➢ At ψ < 45°: β = 0° and in the special cases (ψ = 15°, β = 15°) and (ψ = 30°, β = 90°) pure tensile failure appears exactly along the weakness planes at the center of the disc. For the remaining constellations, mixed shear-tensile failure is observed. In these cases, failure is governed by the joint plane except at β = 90° where matrix failure is observed and (ψ = 0°, β = 15°) as well as (ψ = 15°, β = 60°), failure here occurring along joints and the matrix.

➢ At ψ = 45°: mixed mode failure is observed for all β-values, whereby failure dominates along joints at β = 0°, 30°, 60° and 75° and inside the matrix at β = 15°, 45° and 90°.

➢ At ψ > 45°: the plasticized area becomes wider relative to the loading direction and has a symmetric pattern. Plastification is dominated by mixed shear-tensile failure.

In general, the numerical results in Table 5-2 to Table 5-6 and the diagrams in Figure 5-23 to Figure 5-26 clearly show that the tensile strength value is strongly dependent on both the orientation (ψ) and foliation-loading (β) angles relative to the weak foliation planes in anisotropic rocks.

5.7 Summary and Review

The finite difference code FLAC^{3D} was successfully adopted to simulate the Brazilian test by using the *bilinear strain-hardening/softening ubiquitous-joint* model. The results obtained from the numerical simulations are in close agreement with the observations made in the experimental tests. The behavior of anisotropic rocks varies with foliation and loading directions as discovered in the evaluation of laboratory and simulating results.
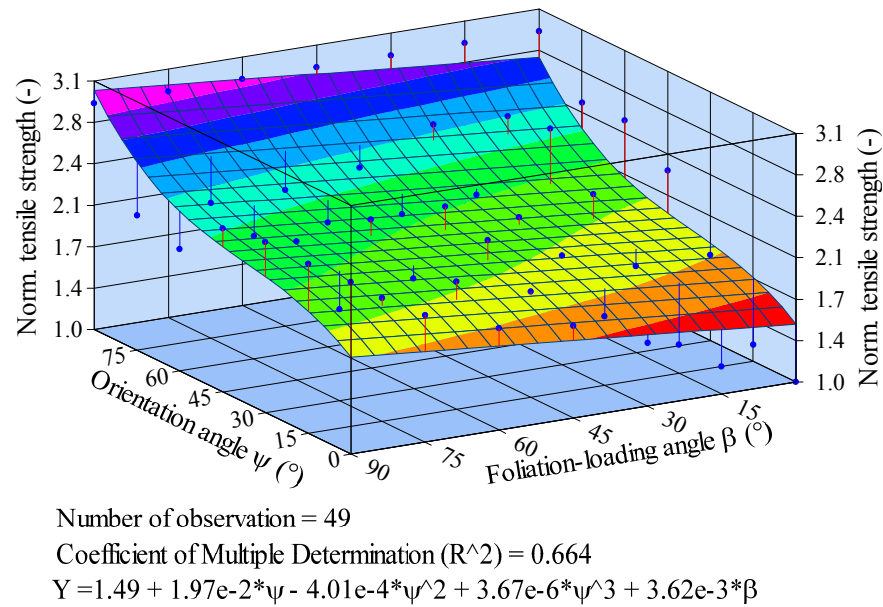
5.7.1 Potential failure state deduced from pure elastic considerations

The pure elastic considerations have revealed that tensile failure are only possible in joints (weak planes) if ψ < 60°. Within the range 8° ≤ ψ ≤ 60°, tensile failure and shear failure
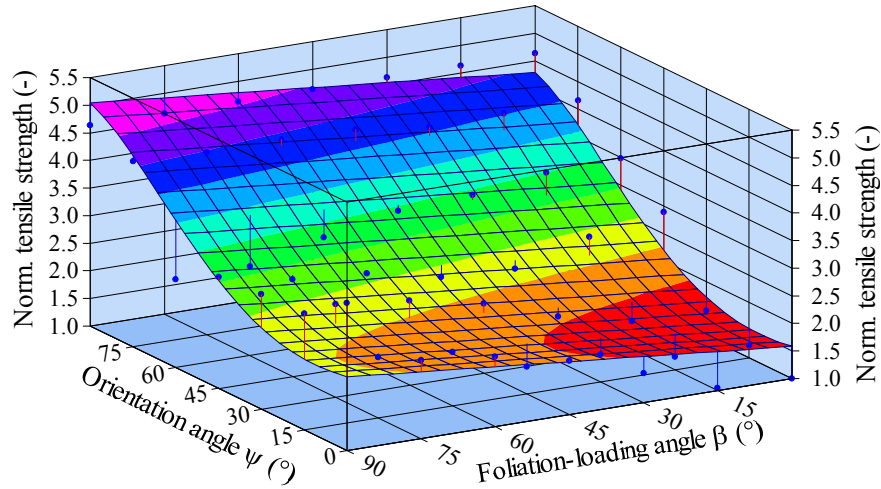
are possible depending on β. At ψ < 8°, only tensile failure is possible, the actual failure type also depending on the ratio of the strength between matrix and joints.

5.7.2 Tensile strength distribution

In order to assess the effect of loading direction and weakness plane orientation on tensile strength of the Gneiss and the Slate, the results were normalized by exact numerical values at ψ = 0° and β = 0° (Figure 5-27 & 5-28).

Number of observation = 49
Coefficient of Multiple Determination (R^2) = 0.664
Y =1.49 + 1.97e-2*ψ - 4.01e-4*ψ^2 + 3.67e-6*ψ^3 + 3.62e-3*β

Figure 5-27: Normalized tensile strength as functions of β and ψ of Le.Gs Gneiss

Number of observation = 49
Coefficient of Multiple Determination (R^2) = 0.857
Y= 1.58 - 8.43e-3*ψ + 1.86e-4*ψ^2 + 1.09e-5*ψ^3 - 9.12e-8*ψ^4 + 8.37e-3*β

Figure 5-28: Normalized tensile strength as functions of β and ψ of My.Sc Slate

The regression analyses allow a prediction of the tensile strength with respect to any arbitrary orientation and foliation-loading angle with just one single conducted test:

Gneiss (Le.Gs, see also Figure 5-27) yields the following:

$$\sigma_t^{\psi,\beta} = 1.49 + 1.97e-2*\psi - 4.01e-4*\psi^2 + 3.67e-6*\psi^3 + 3.62e-3*\beta \tag{5.10}$$

Slate (My.Sc, see also Figure 5-28) yields the following:

$$\sigma_t^{\psi,\beta} = 1.58 - 8.43e-3*\psi + 1.86e-4*\psi^2 + 1.09e-5*\psi^3 - 9.12e-8*\psi^4 + 8.37e-3*\beta \tag{5.11}$$

The coefficient of multiple determination is relatively low (0.86 for slate and 0.66 for gneiss) but it has to be taken into account that only one data set and constitutive law each was used for any constellation of β and ψ. As expected, the anisotropic strength is more pronounced in the slate whereas the qualitative relations are similar.

5.7.3 Tensile strength – determining the anisotropy factor

The strength anisotropy factor, normalized to 1 at β = 0 and ψ = 0, for Le.Gs and My.Sc is shown in Figure 5-29 & 5-30. The anisotropy ratio of the tensile strength can reach values of up to 2.75 and 4.50 for Gneiss and Slate, respectively.
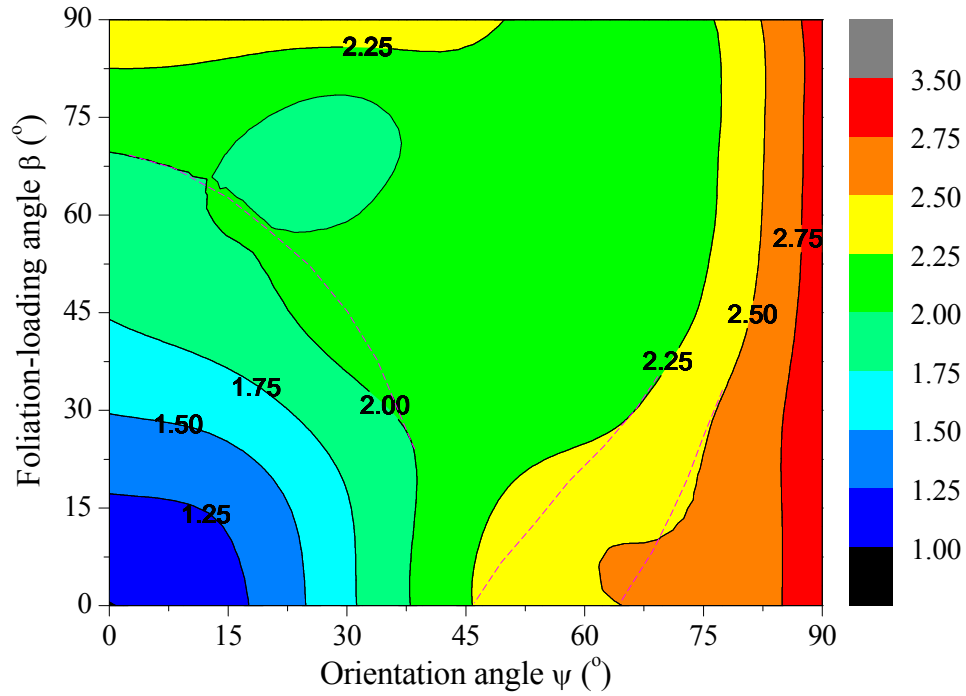
Figure 5-29: Normalized tensile strength of Le.Gs Gneiss
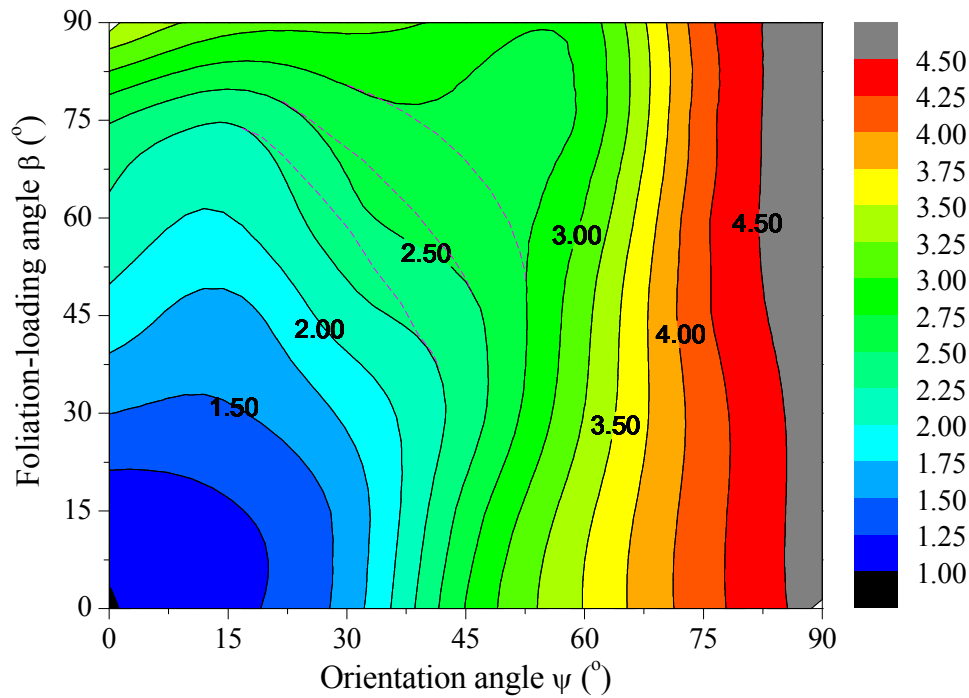
Figure 5-30: Normalized tensile strength of My.Sc Slate

Figure 5-30 indicates that the highest tensile strength anisotropy factor for My.Sc slate reaches 4.5. Also, at $\psi > 45°$, the tensile strength seems to be nearly independent of β.

5.7.4   Tensile strength – different procedures - different results

To get a better idea of the Brazilian test limitations, it is necessary that the stress distribution within specimens be carefully considered. Actually, the tensile strength can be determined by several different procedures: direct tensile tests and different indirect tensile tests like 3- or 4-point bending tests or the Brazilian test. Although all these tests enable measurement of tensile strength, they do not necessarily give the same results because stress distributions or effective volumes are not the same in all of them [99].

Comparison between direct and indirect tensile strength values of rocks show that these can largely differ. Several authors have come to the conclusion that $\sigma_t^{Direct\ test} \geq \sigma_t^{Brazilian\ test}$, e.g. Jaeger [82] for Carrara marble, Hardy and Jayaraman [100] for Berea sandstone, Indiana limestone, Leuders limestone, Crab Orchard sandstone and Barre granite as well as Alehossein [101] for Australian granite. But Jaeger [82] also obtained the result $\sigma_t^{Direct\ test} \cong \sigma_t^{Brazilian\ test}$ for Gosford sandstone and $\sigma_t^{Direct\ test} \leq \sigma_t^{Brazilian\ test}$ for Bowral trachyte. According to Tang [4], the ratio of Brazilian tensile strength and direct tensile strength for isotropic materials varies from 1.005 (5%) to 1.214 (21%) depending on the relative load-bearing strip width (a) where (a/D) is from 0.04 to 0.16. It should be noted however that the aforementioned tests were carried out almost exclusively on isotropic rocks. According to Classon [94], the error in the approximate formulas of the principal tensile and compressive stresses at the center of a 2D disc for transversely anisotropic materials ranges from 0.1% to 10.8% depending on the anisotropy of stiffness

$$b = \frac{\sqrt{EE'}}{2}\left(\frac{1}{G'} - \frac{2\mu'}{E'}\right)$$ and (E'/E).

The classical model for the evaluation of the Brazilian test (isotropic materials under 2D conditions) assumes that tensile strength can be calculated at failure from the applied force. It assumes further that failure starts at the center of the loaded diameter. If that is the case, the specimens would break down into two half-discs and the tensile strength could now be determined by Eq. 1.2 with $\sigma_t = -\dfrac{2P}{\pi Dt}$. However, the numerical simulations have shown that the damage and fracture mode during the Brazilian test are not comparable to the one in a direct tension test. Also, the failure state is often not a pure tension mode.

The simulation results indicate that the tensile strength determined by the conventional theoretical formula (Eq. 1.2) is almost slightly higher than the maximum tensile stress observed at the center. The deviation here is equal to -5% to 18% for the Le.Gs Gneiss (Table 5-4) and 4% to 19% for the My.Sc Slate (Table 5-7), depended on the orientation of the anisotropic planes. This result indicates that the critical stress state (initial failure state) is not always located at the center of the disc. These results are similar to the difference in tensile strength of the Brazilian test and the direct tensile test.

Chapter 6

Conclusion and Recommendations

The Brazilian test is a simple way of determining the tensile strength of brittle materials. Tensile strength of rocks counts amongst the most important geotechnical parameters influencing rock strength, deformability, damage, fracturing and crushing.

Research results indicate that the material anisotropy has significant influence on the stress distribution, crack initiation, fracture pattern and peak load. In transverse anisotropy, the key parameter is the orientation of the cleavage, bedding or schistosity planes with respect to the direction of the applied load. The results obtained from the numerical simulations show a close agreement with the observations made during the experimental tests. The behavior of anisotropic rocks varies with the foliation and loading directions as observed in the laboratory and the simulations.

The results of the present research can be summarized thus:

> ➢ The laboratory tests show that the character anisotropy has a strong influence on the measured peak strength obtained in a Brazilian test. Whereas the relation sample orientation to loading direction is unimportant for nearly isotropic materials, strongly anisotropic materials like Gneiss and Slate reveal a strong dependence of the peak strength on this interrelation.

> ➢ The formula usually used for calculating the tensile strength is derived from an analytical 2D elastic solution which ignores the effect of the loading angle (2α), the thickness-to-diameter ratio (L/D) and the Poisson's ratio (μ). However, the local stress concentration phenomena and induced tensile stresses inside the disc greatly depend on the above-mentioned conditions.

➢ The stress distribution near the center of a disc under diametral loading is largely the same in isotropic materials, whether in 2D, 3D analytical solutions or 3D numerical simulations.

➢ The tensile stresses in the edge sections (border region) of the disc can be slightly smaller or even higher, as the case may be, than those at the center depending on the loading angle, Poisson's ratio and thickness-to-diameter ratio L/D. This has important influence on the location of the fracture initiation and the interpretation of the test results.

➢ Small loading angles ($2\alpha < 20°$) produce the maximum tensile stresses at the center of the disc. Larger loading angles ($2\alpha > 20°$) produce this same effect closer to the rim of the disc. Very small loading angles ($2\alpha < 10°$) may lead to damage at the load entry points. The recommended loading angle is therefore, $10° \leq 2\alpha \leq 20°$.

➢ The thin disc produces maximum tensile stresses at the center of the disc. With increasing thickness, e.g. for an L/D from ¼ to $\frac{1}{1}$, the tensile stress along the center plane becomes smaller and increases for planes towards the end of the cylinder, by about 12.5% for an L/D = ¼ sample as against one with an L/D = $\frac{1}{1}$, for example. Although from a theoretical point of view a very small thickness is advantageous, in order to avoid eccentric loading, misalignment and buckling, it is recommended that the lower and upper limits of the length to thickness ratio range between ¼ ≤ L/D ≤ $\frac{1}{1}$. An L/D = ½ ratio is recommended here.

➢ The tensile stress component is independent of the Poisson's ratio along the middle plane of the disc. In contrast, the higher the Poisson's ratio induced, the further the observation plane for stress distributions move away from the center of the disc, the more pronounced the stress peaks close to the load entry area.

➢ Present analytical solutions only consider plane-stress situations. The 3-dimensional quasi-analytical solution after Wijk shows some agreement with numerical simulations for the center plane. Away from the center however, very questionable results were obtained. According to Wijk's formulations, the horizontal stress component yields extreme values close to the load entry point so that the largest tensile stress is not found at the center of the disc but closer to the boundary.

➢ The FG.Ss Sandstone shows relatively low standard deviations and consequently, low coefficients of variation equal to 13% for the determined peak (tensile) strength. Gneisses and Slate on the other hand, document large tensile strength deviation values with coefficients of variation 31%, 26% and 61% for FG.Gs Gneiss, Le.Gs Gneiss and Le.Sc Slate respectively. Large coefficient of variation values indicates anisotropic behavior.

➢ Lab results of FG.Ss Sandstone show a distinct fracture pattern which is characterized by the sample splitting into two halves. Sometimes, wedges are formed immediately under the loading jaws. The fracture pattern was more or less identical for all FG.Ss samples and is characterized by a central tensile crack independent of the sample orientation. In the FG.Gs and Le.Gs Gneisses in contrast, and especially in the My.Sc Slate, the fracture pattern is strongly influenced by the orientation of the weak planes. In many cases, the fracture pattern is characterized by sub-parallel cracks like in step faults or staircase-shaped fractures along the existing weak planes.

type 1: tensile failure type 2: tensile-shear failure type 3: shear failure
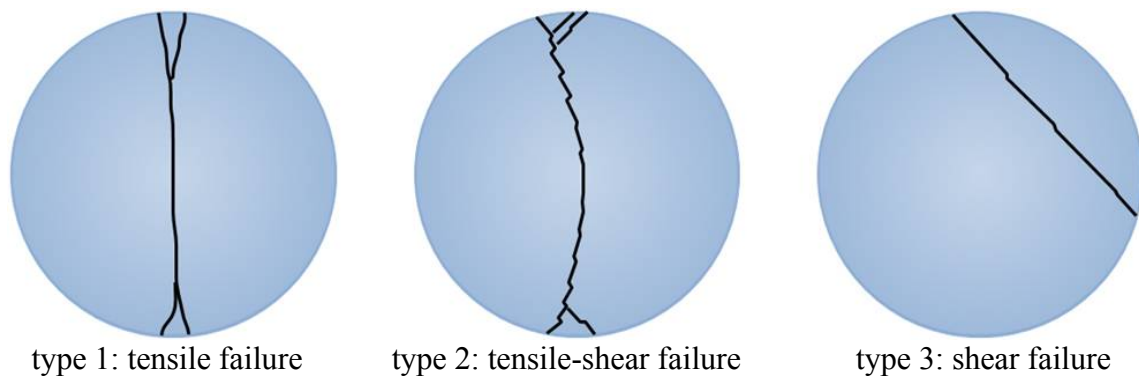
Figure 6-1: Typical failure mechanisms in the Brazilian test

➢ The specimen can be initially fractured by stress concentration at the loading jaws. That means that fracture initiation can be triggered off in this region instead of at the center of the disc as is usually assumed.

➢ Exact analytical solutions for anisotropic rocks are not available so that either numerical analysis or semi-analytical solutions had to be used.

➢ The simulation results indicate that the tensile strength determined by the conventional theoretical formula is often slightly lower than the maximum tensile strength. The maximum deviation is equal to 18% in the Gneisses and 19% in the Slates, depending on the orientation of the anisotropy planes. This result indicates that the critical stress state (initial failure state) is not always located at the center of the disc if anisotropic strength is considered.

➢ The anisotropic character and loading direction strongly influence failure mechanisms of the sample. Pure tensile failure along weakness planes occurs only at $\psi \leq 15°$ for Gneiss and $\psi \leq 30°$ for Slate as loading directions parallel to planes of weakness. In all other constellations, plastifications are characterized by mixed mode (shear-tensile) damage and final failure appears in a smear manner within the plasticized area.

➢ The normalized tensile strength of transverse anisotropic rocks could reach quite high values of deviation from 2.65 to 5.24 in lab results and from 2.75 to 4.5 in simulation results for Gneiss and Slate respectively.

➢ The regression analyses enable a prediction of the peak (tensile) strength with respect to any arbitrary orientation and foliation-loading angle from one single test:

Le.Gs Gneiss yields the following:

$$\sigma_t^{\psi,\beta} = 1.49 + 1.97e - 2 * \psi - 4.01e - 4 * \psi^2 + 3.67e - 6 * \psi^3 + 3.62e - 3 * \beta$$

and My.Sc Slate yields:

$$\sigma_t^{\psi,\beta} = 1.58 - 8.43e - 3 * \psi + 1.86e - 4 * \psi^2 + 1.09e - 5 * \psi^3 - 9.12e - 8 * \psi^4 + 8.37e - 3 * \beta$$

Recommendations for future research

Although this research has made great progress in relation to the influence of anisotropy on tensile strength as determined by the Brazilian test, further efforts are necessary in order to enhance points like:

➢ The development of inhomogeneous material models as in natural rocks (see Figure 6-2).
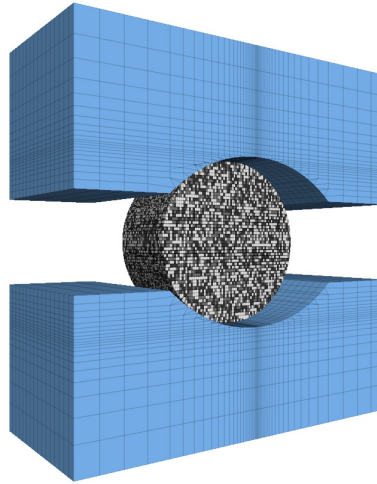
Figure 6-2: Inhomogeneous continuum model of Gneiss with a random distribution of minerals: mica 10% (white), quartz 30% (grey) and feldspar 60% (black).

➢ Extension of the lab tests and numerical simulations to encompass stiffness anisotropy in addition to determining the strength anisotropy. The following parameters have to be determined when examining transverse anisotropy: E, E', μ, μ', G, C, C', ϕ, ϕ' and σ_t, σ_t'.

➢ Incorporating additional measuring techniques, e.g. high-speed camera, seismoacoustic analyses, etc. to capture damage and fracture process as a function of time and location in more detail.

➢ Using the discontinuum mechanics method to better understand the fracture process.

➢ Investigation of the influence of stiffness and frictional behavior of the interface between rock disc and loading jaws.

APPENDICES

Appendix 3.1 - Fracture patterns in FG.Ss samples

FG.Ss.0.0-90 (β = 0°, 15°, 30°, 45°, 60°, 75°, 90° from top to bottom)
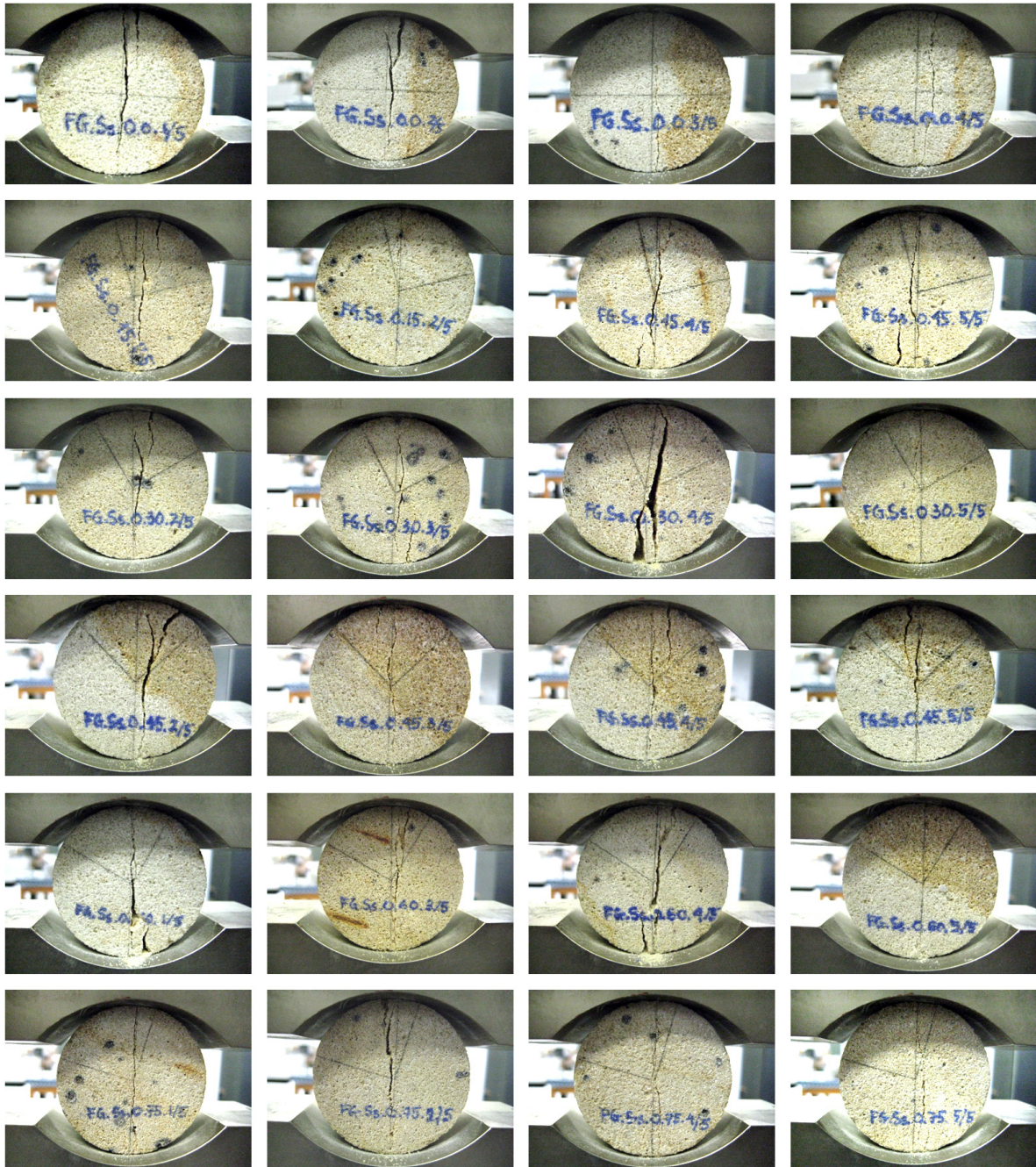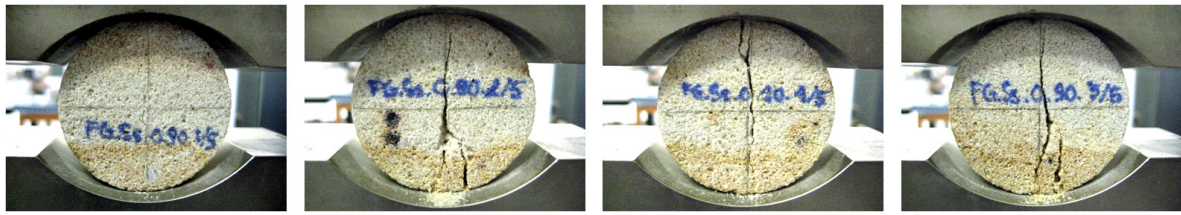
FG.Ss.15.0-90 (β = 0°, 15°, 30°, 45°, 60°, 75°, 90° from top to bottom)
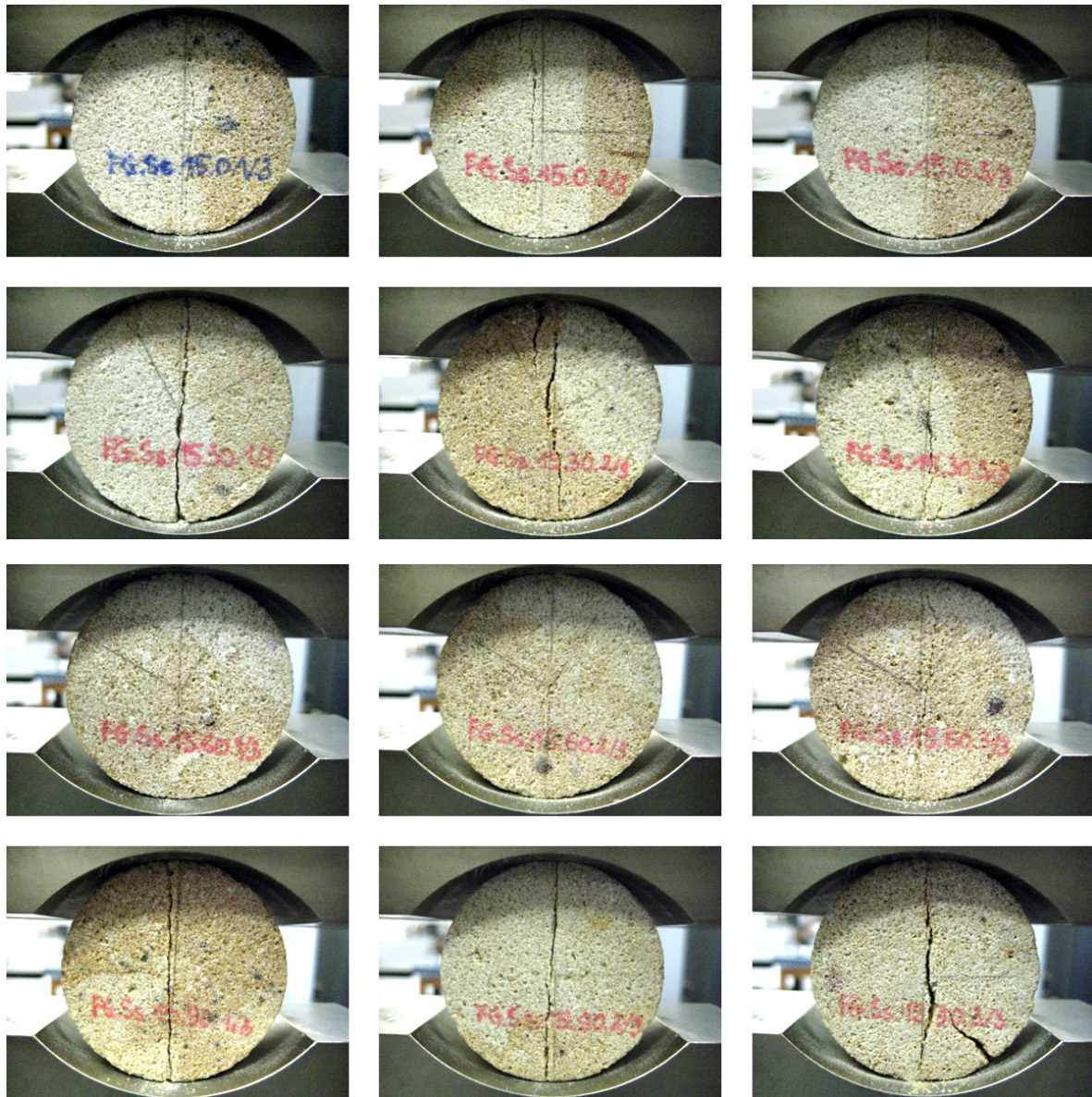
FG.Ss.30.0-90 (β = 0°, 15°, 30°, 45°, 60°, 75°, 90° from top to bottom)
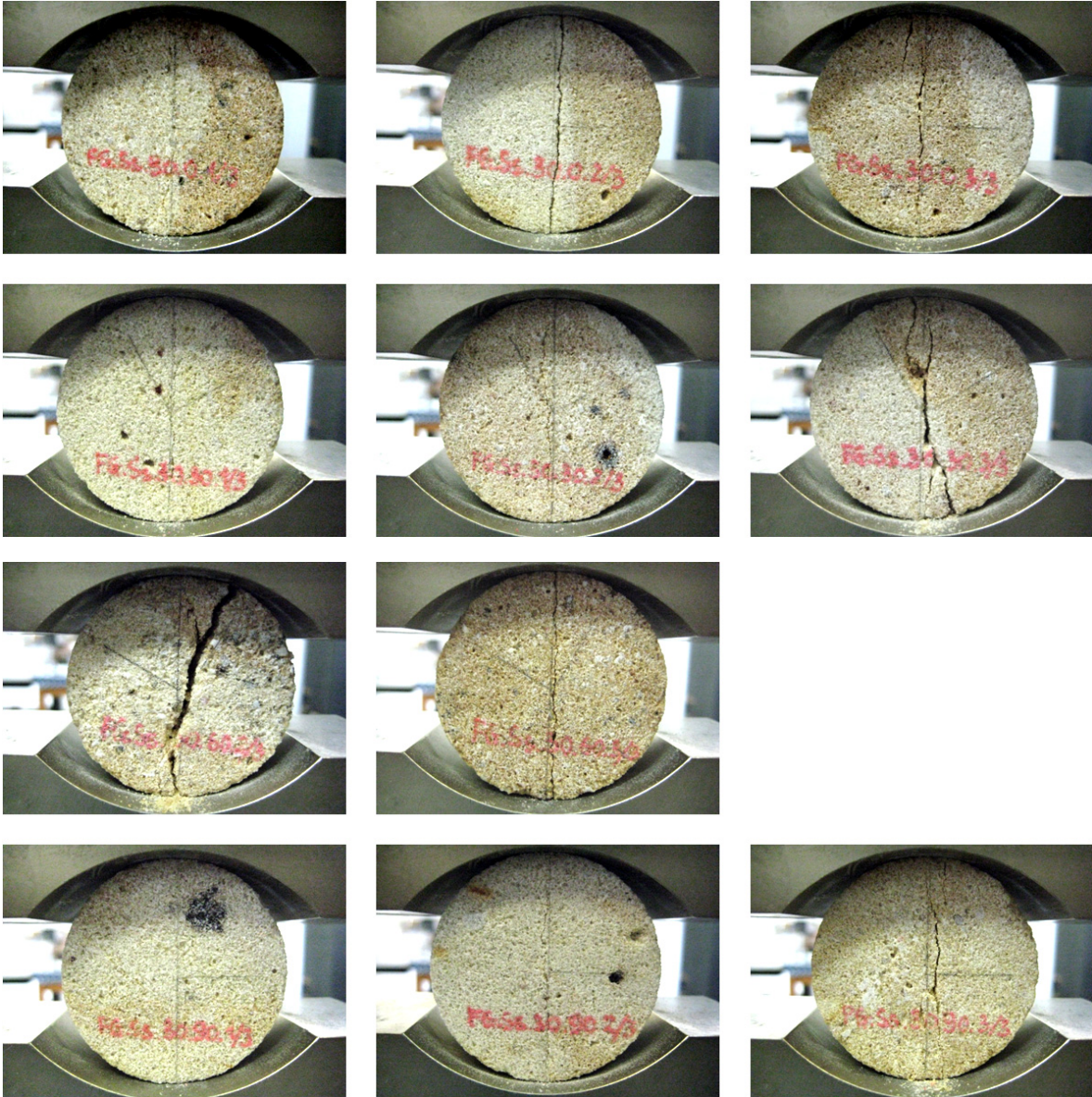
FG.Ss.45.0-90 (β = 0°, 15°, 30°, 45°, 60°, 75°, 90° from top to bottom)
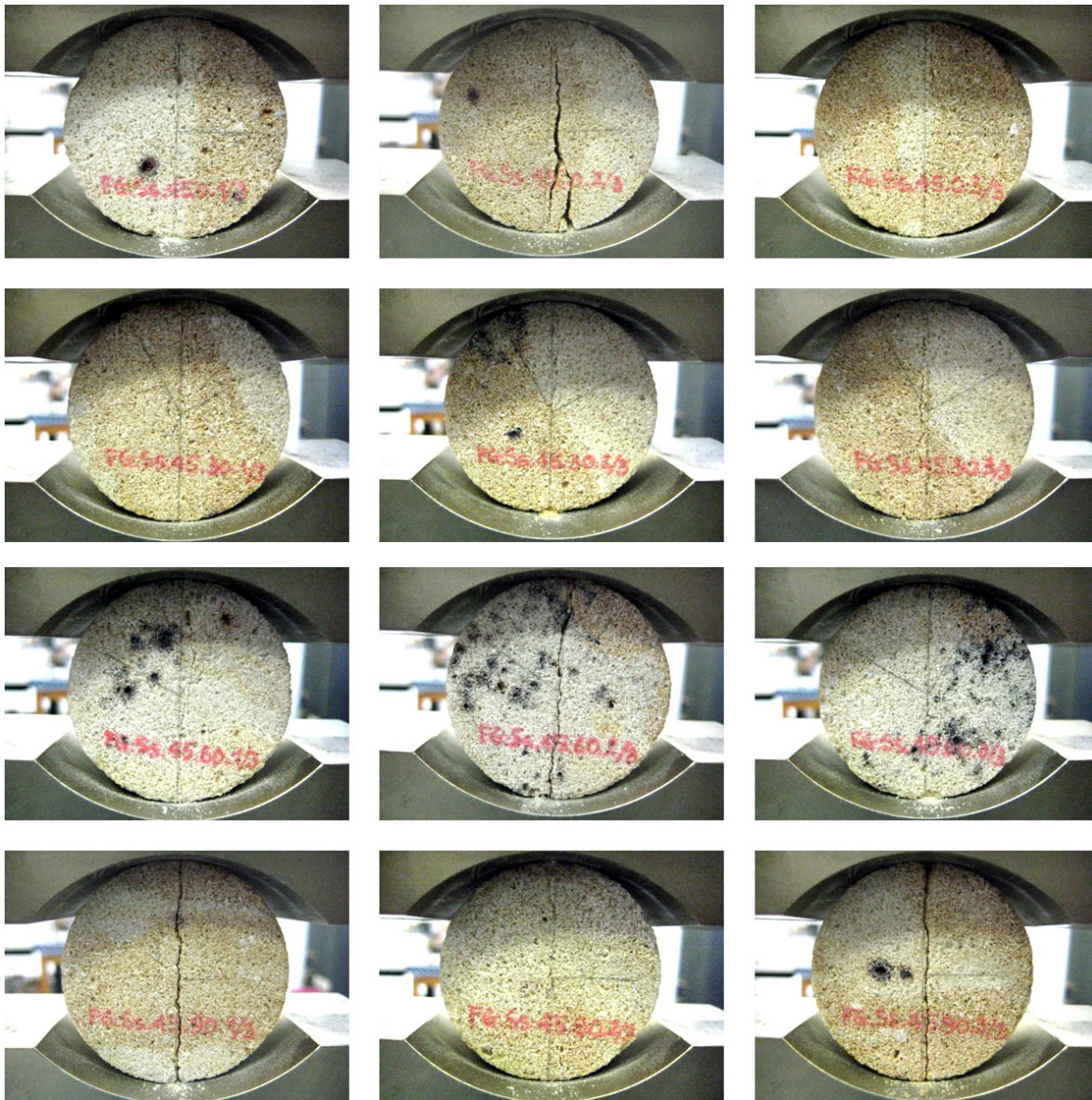
FG.Ss.60.0-90 (β = 0°, 15°, 30°, 45°, 60°, 75°, 90° from top to bottom)
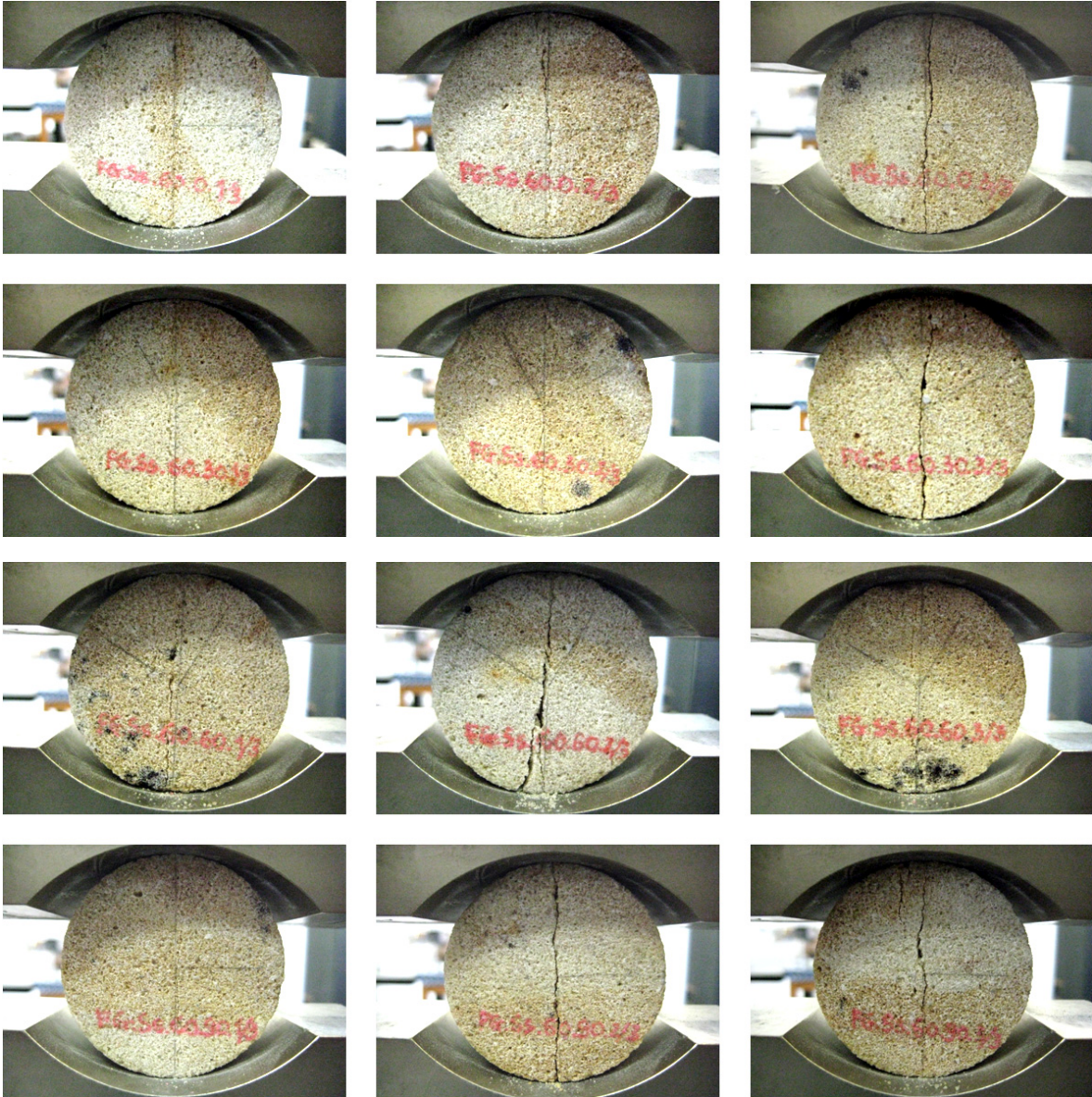
FG.Ss.75.0-90 (β = 0°, 15°, 30°, 45°, 60°, 75°, 90° from top to bottom)
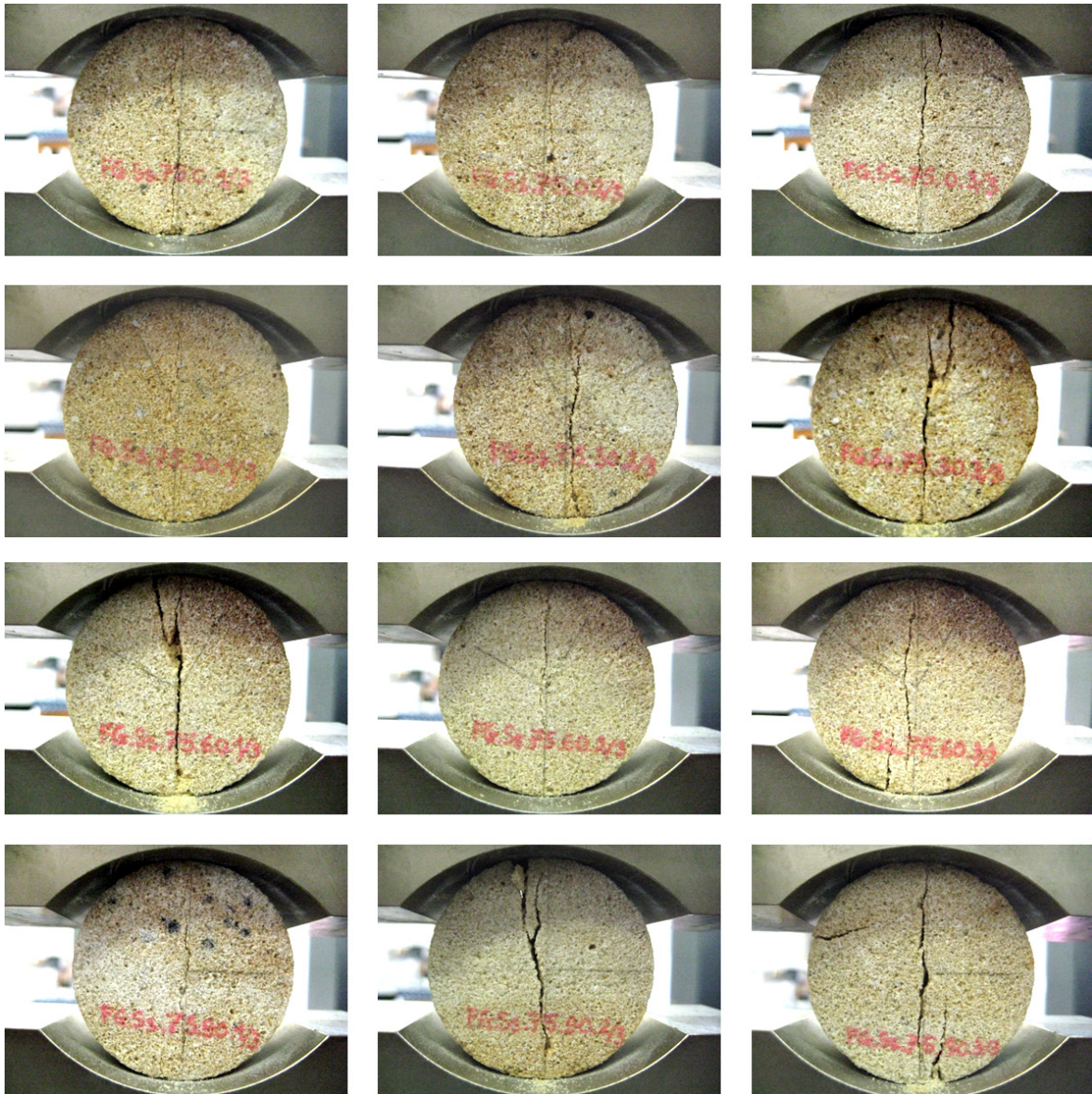
Appendix 3.2 - Fracture patterns in FG.Gs samples

FG.Gs.0.0-90 (β = 0°, 15°, 30°, 45°, 60°, 75°, 90° from top to bottom)
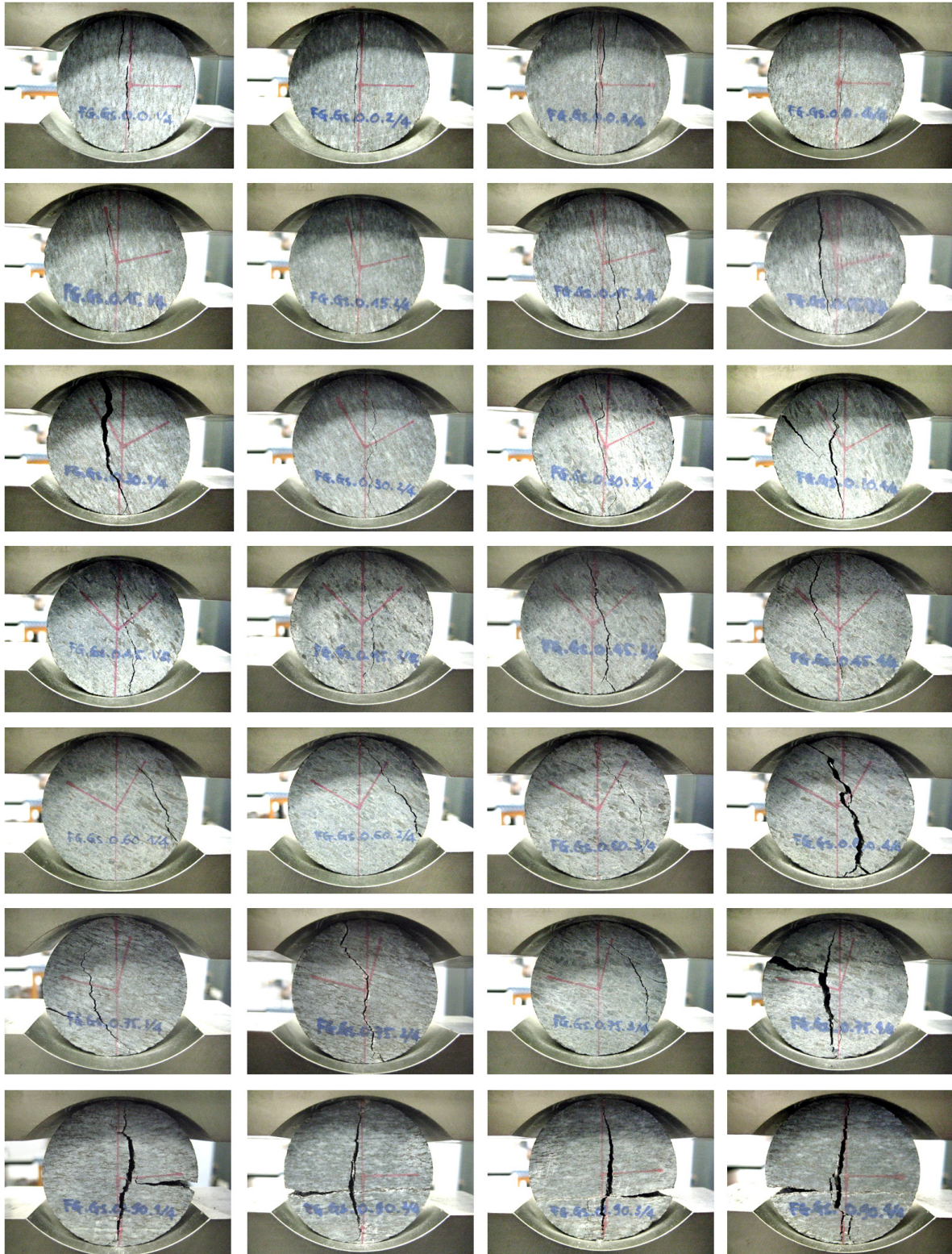
FG.Gs.15.0-90 (β = 0°, 15°, 30°, 45°, 60°, 75°, 90° from top to bottom)
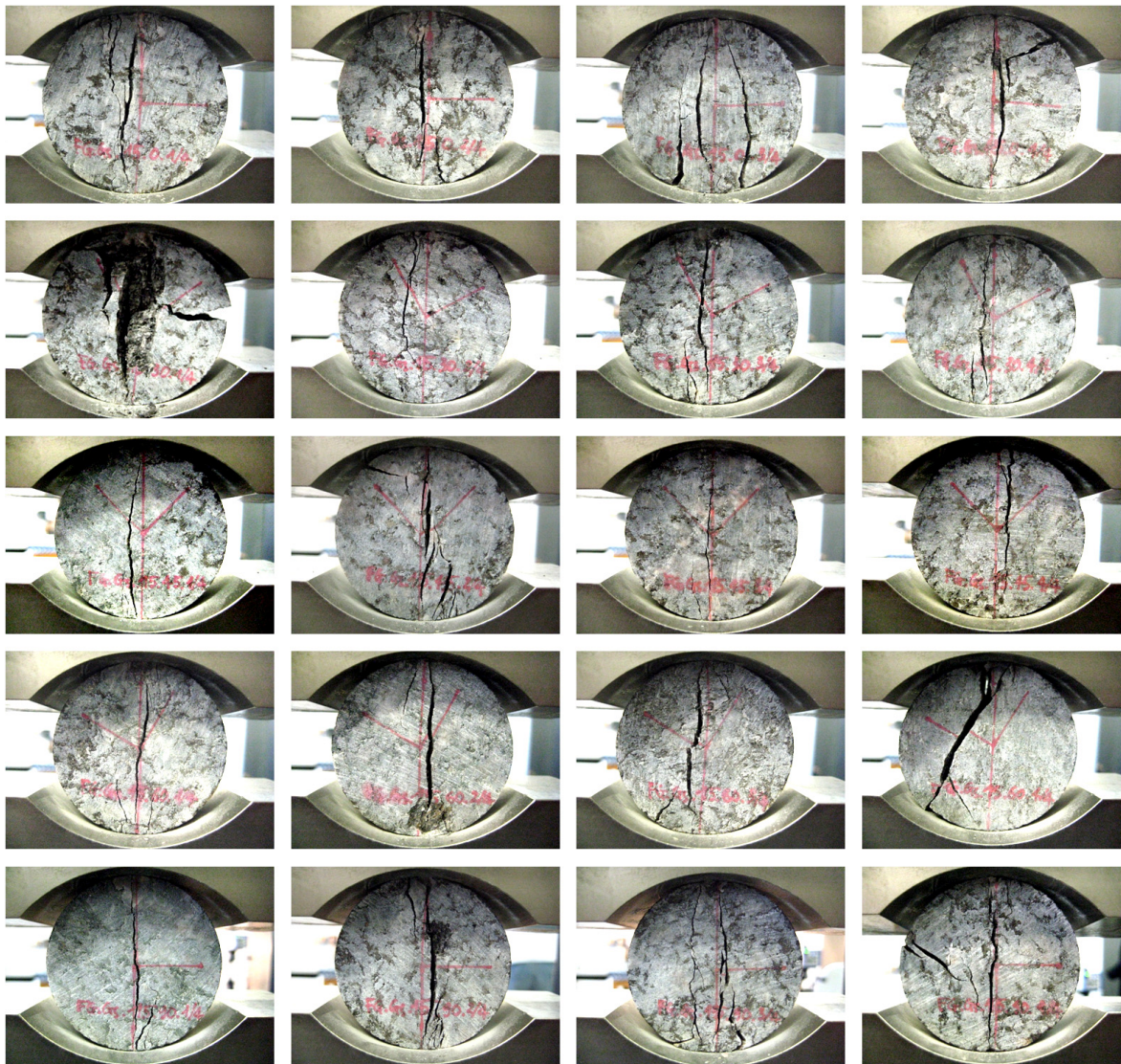
FG.Gs.30.0-90 (β = 0°, 15°, 30°, 45°, 60°, 75°, 90° from top to bottom)
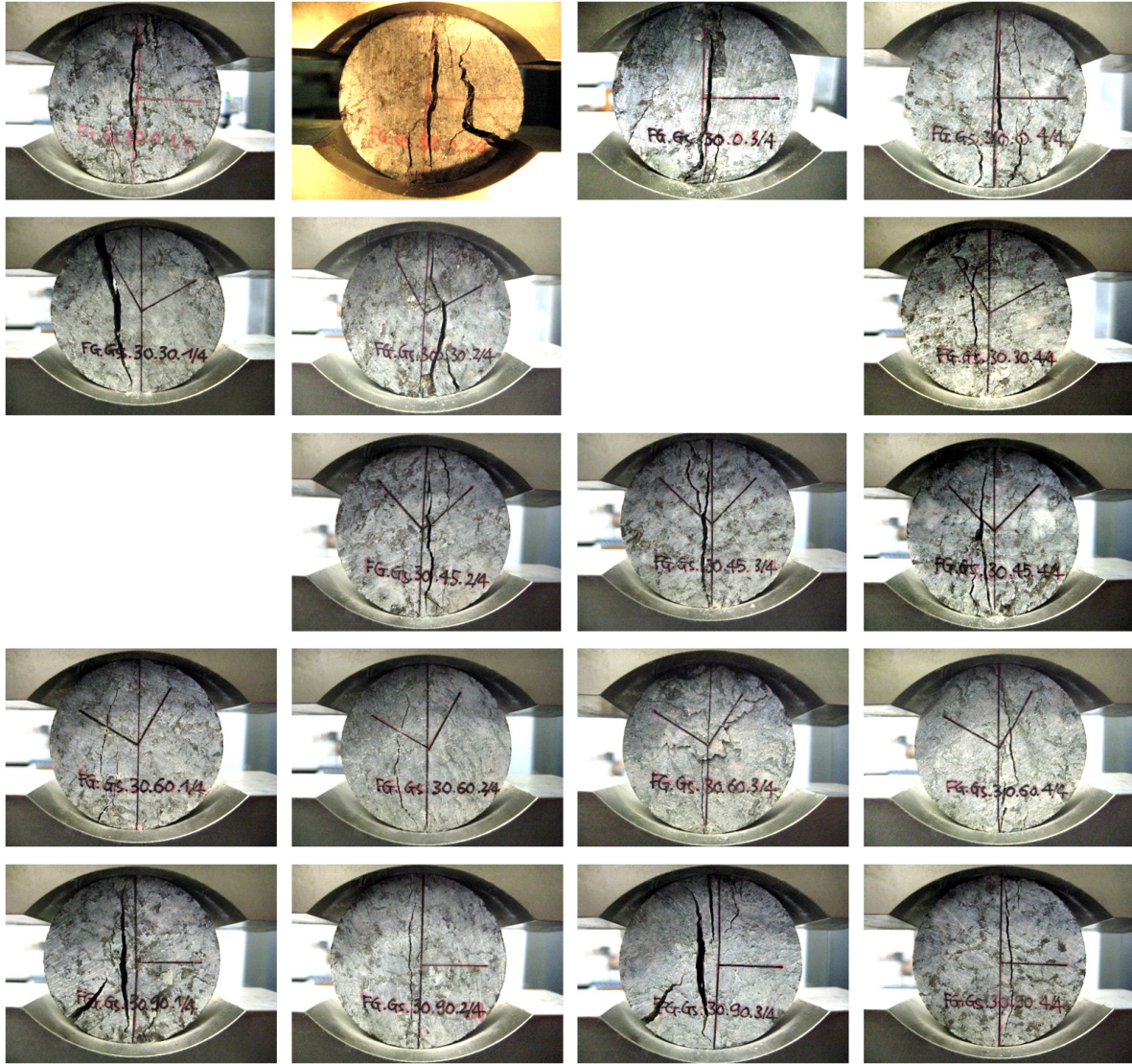
FG.Gs.45.0-90 (β = 0°, 15°, 30°, 45°, 60°, 75°, 90° from top to bottom)
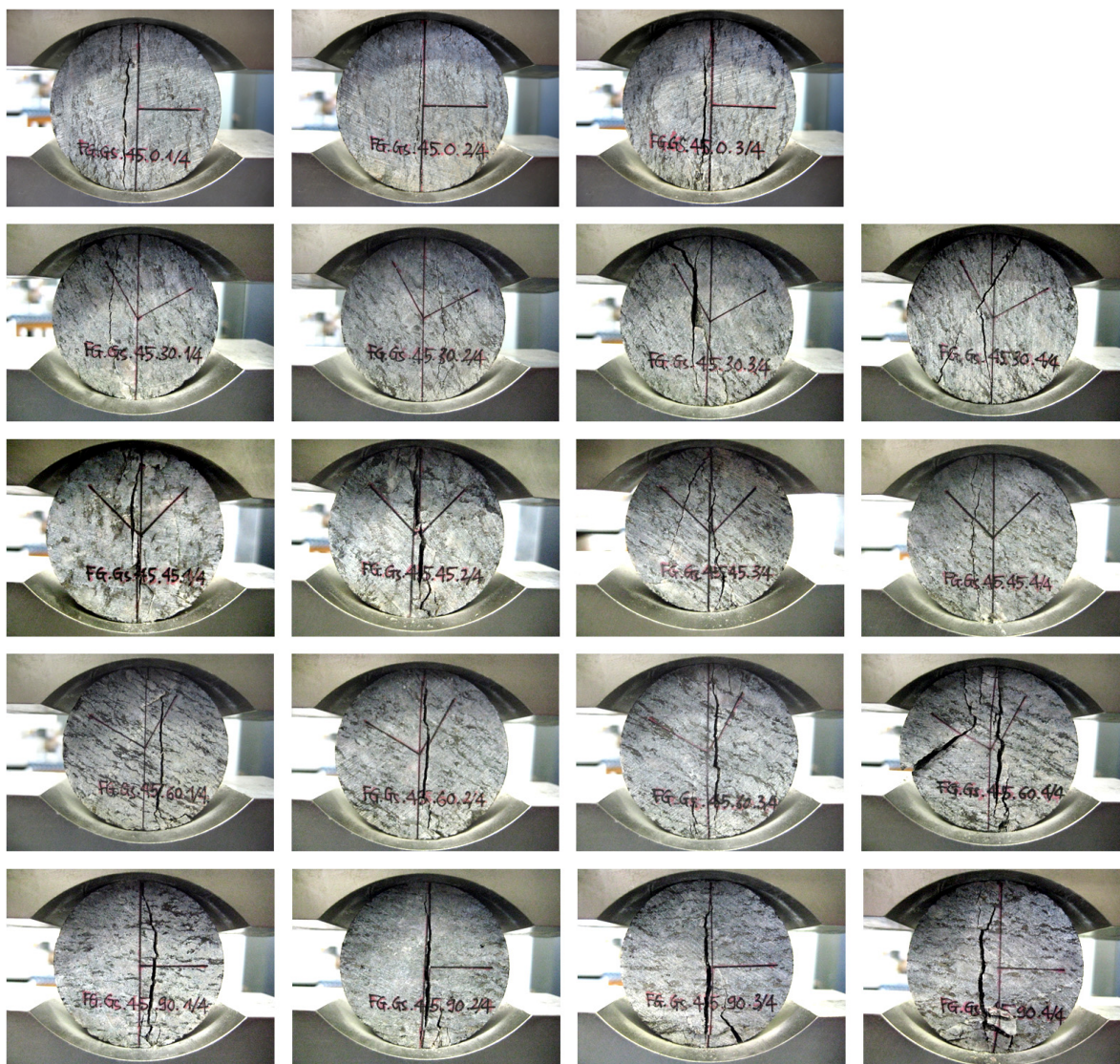
FG.Gs.60.0-90 (β = 0°, 15°, 30°, 45°, 60°, 75°, 90° from top to bottom)
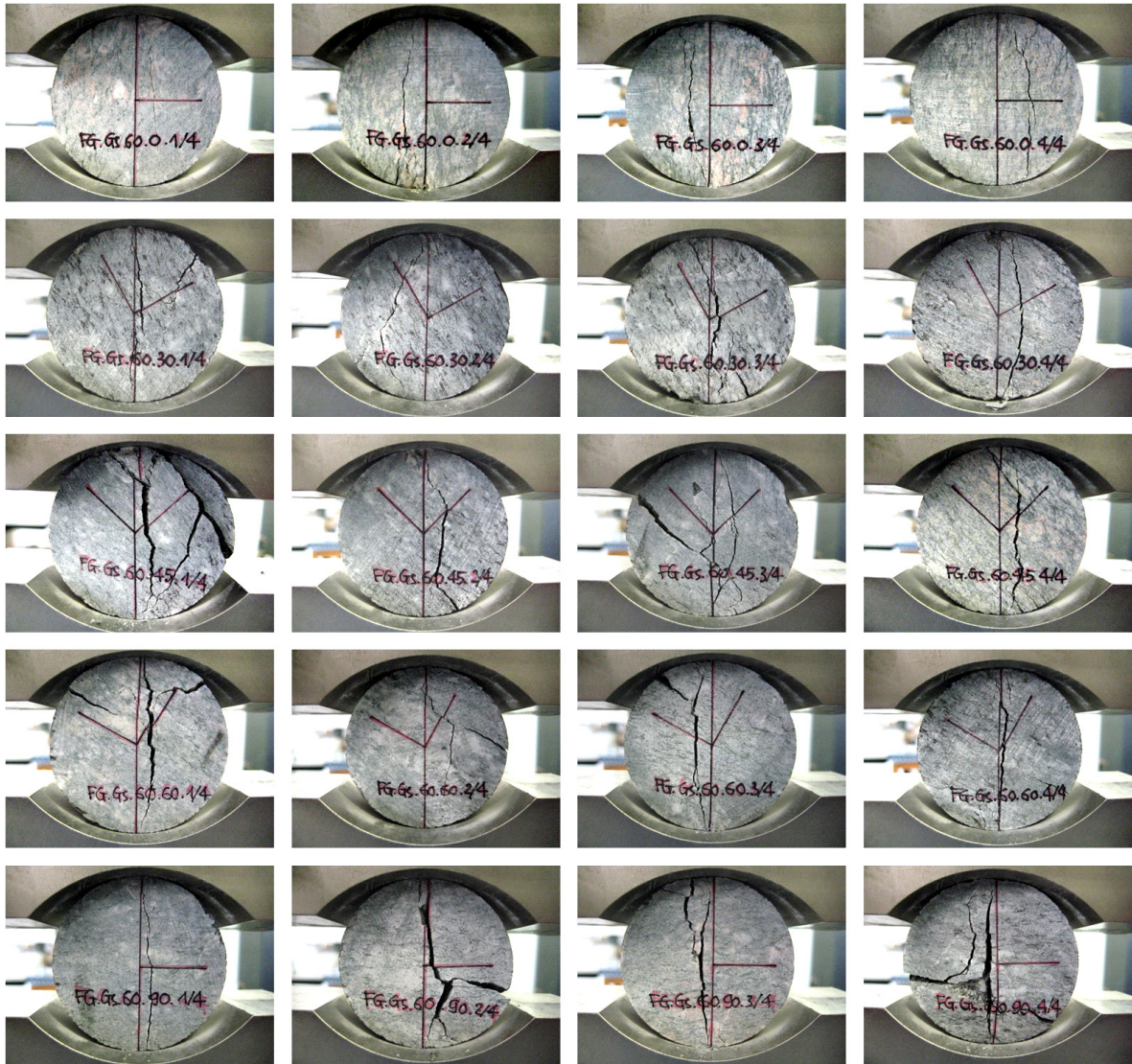
FG.Gs.75.0-90 (β = 0°, 15°, 30°, 45°, 60°, 75°, 90° from top to bottom)
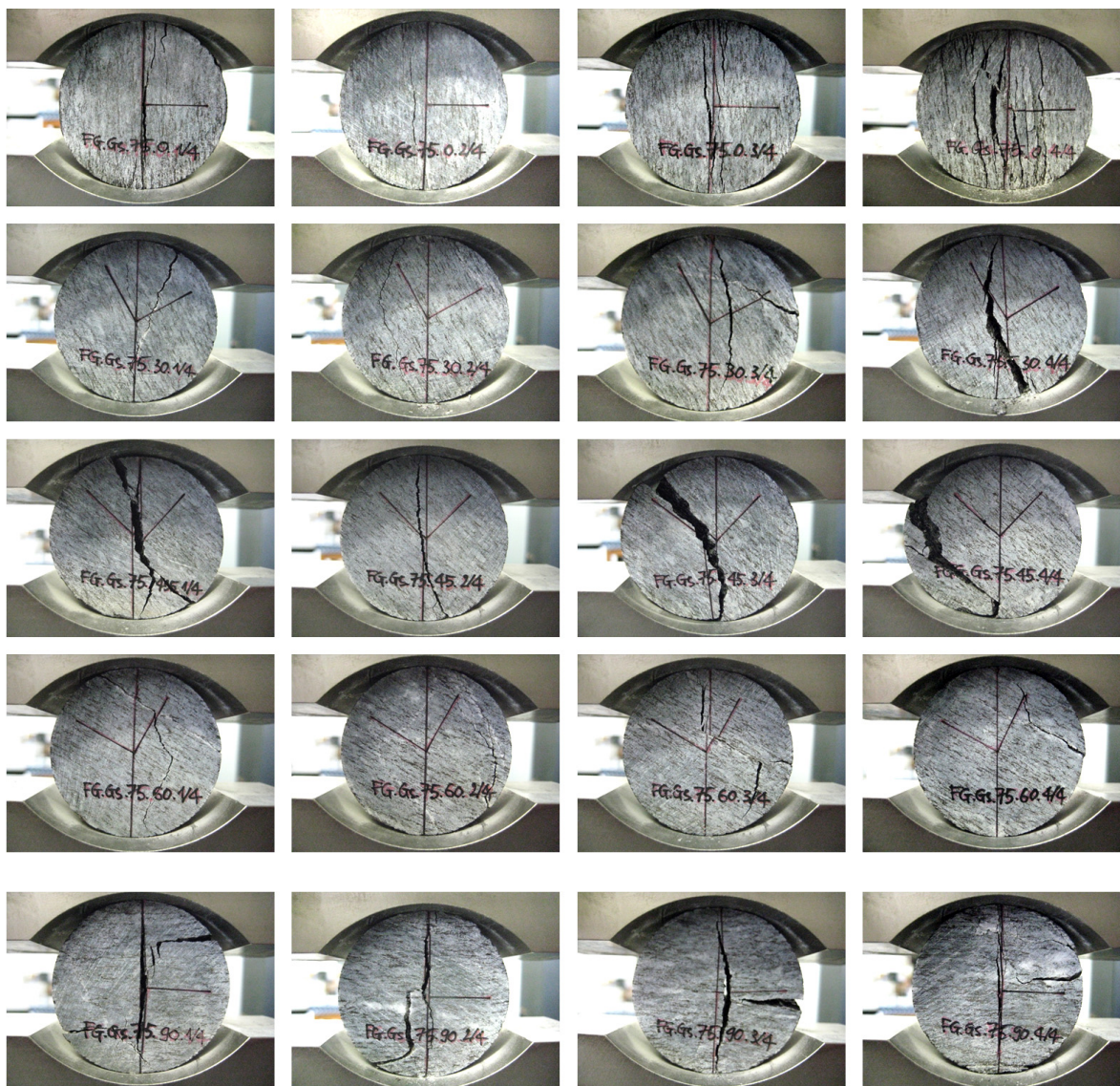
FG.Gs.90 (SPZ1)
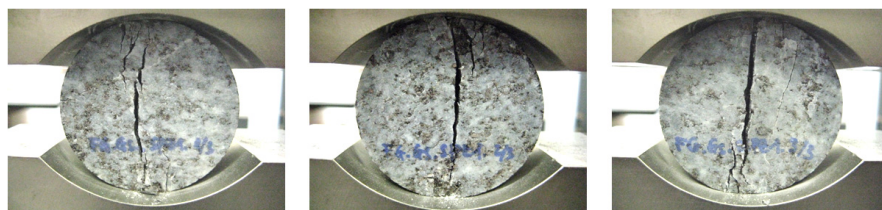
Appendix 3.3 - Fracture patterns in Le.Gs samples

Le.Gs.0.0-90 (β = 0°, 15°, 30°, 45°, 60°, 75°, 90° from top to bottom)
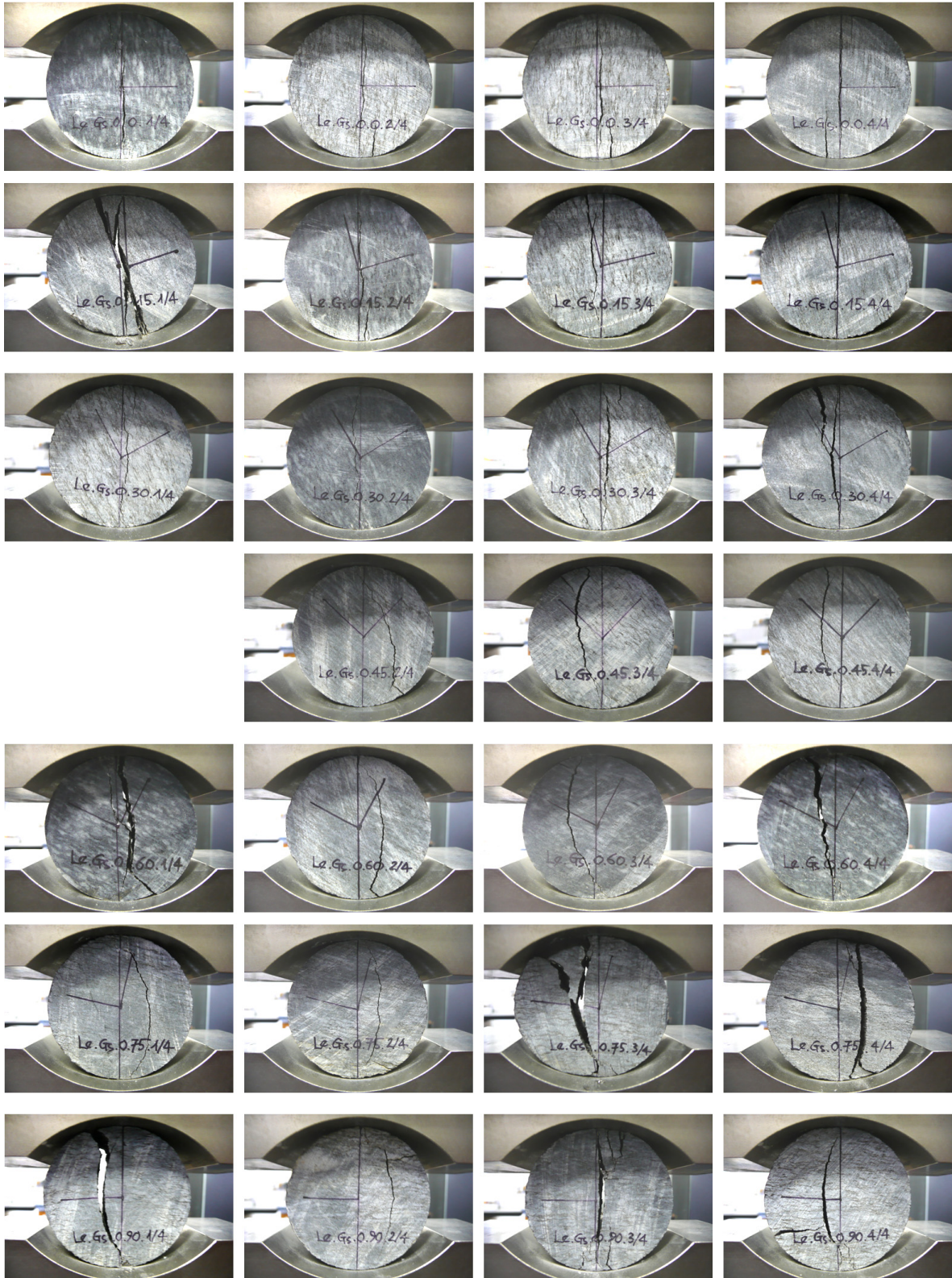
Le.Gs.15.0-90 (β = 0°, 15°, 30°, 45°, 60°, 75°, 90° from top to bottom)
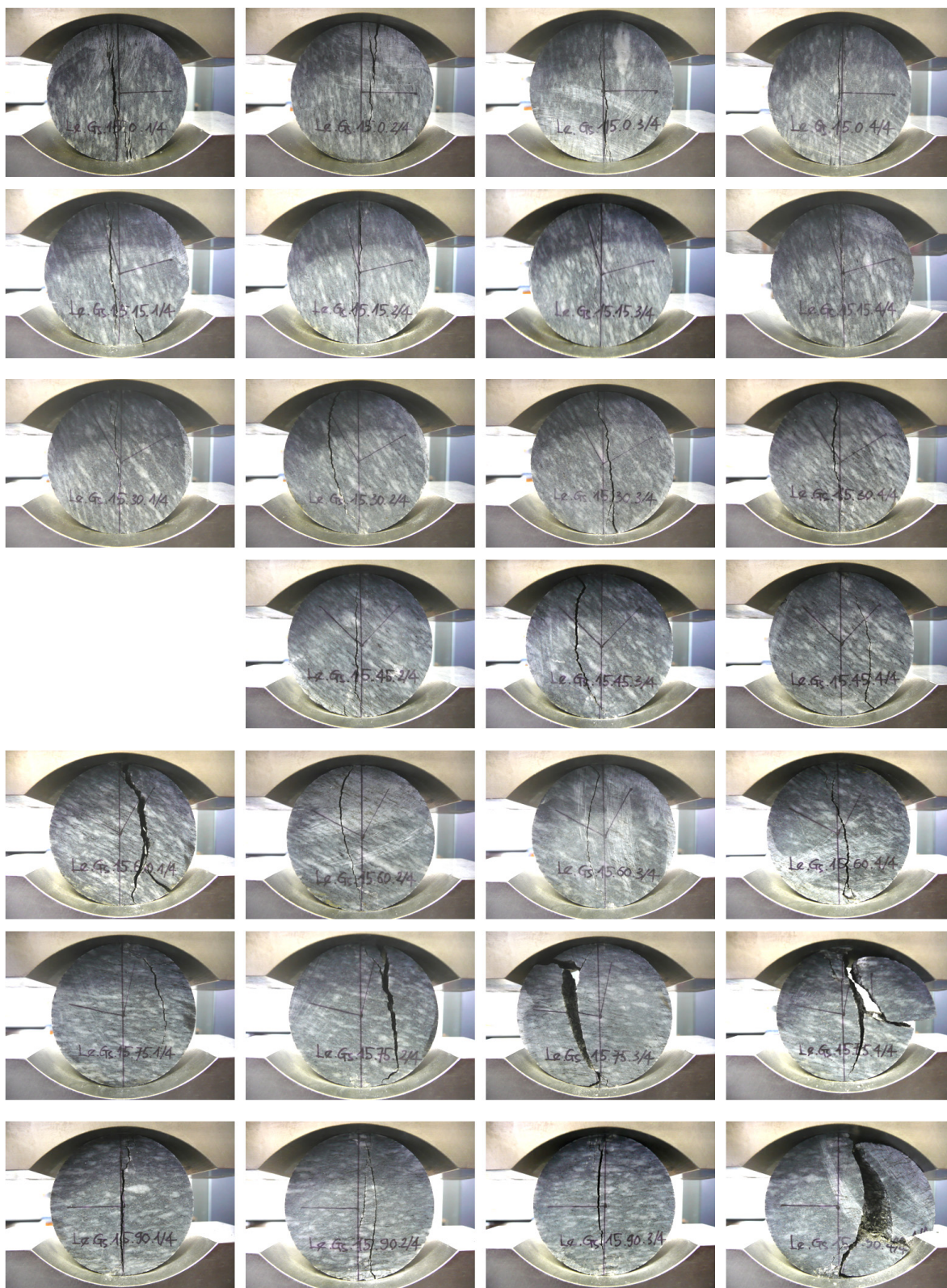
Le.Gs.30.0-90 (β = 0°, 15°, 30°, 45°, 60°, 75°, 90° from top to bottom)
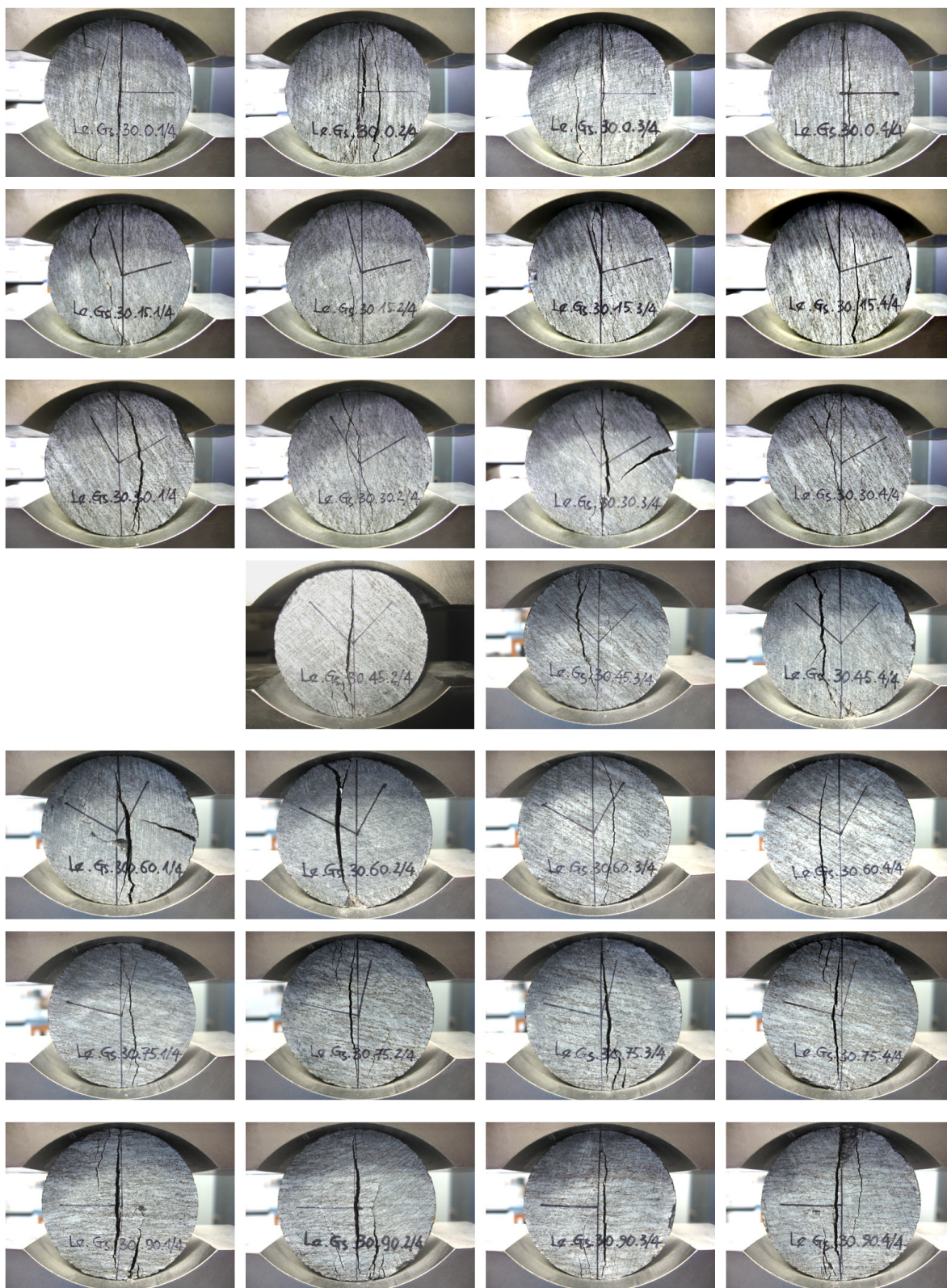
Le.Gs.45.0-90 (β = 0°, 15°, 30°, 45°, 60°, 75°, 90° from top to bottom)
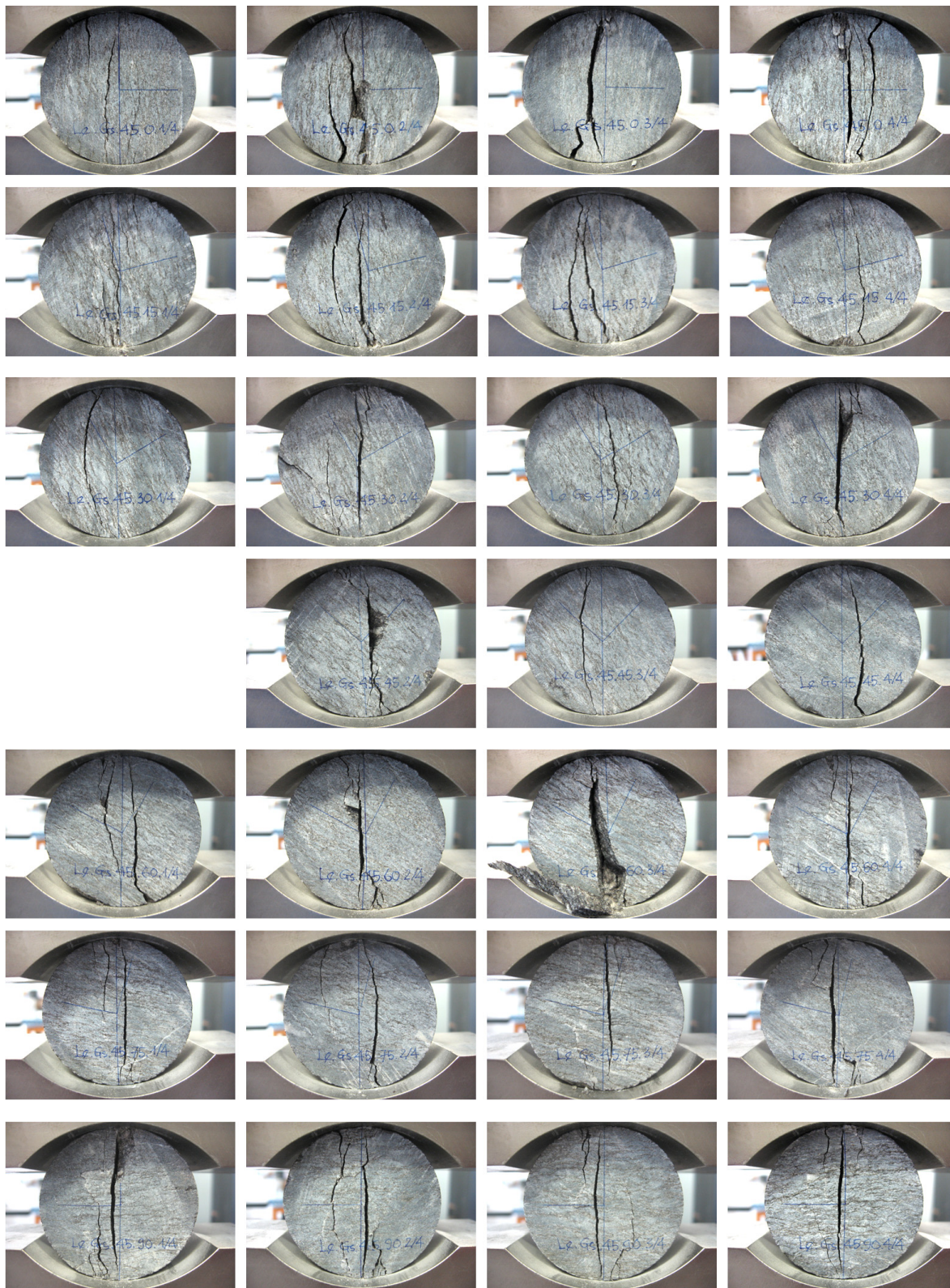
Le.Gs.60.0-90 (β = 0°, 15°, 30°, 45°, 60°, 75°, 90° from top to bottom)
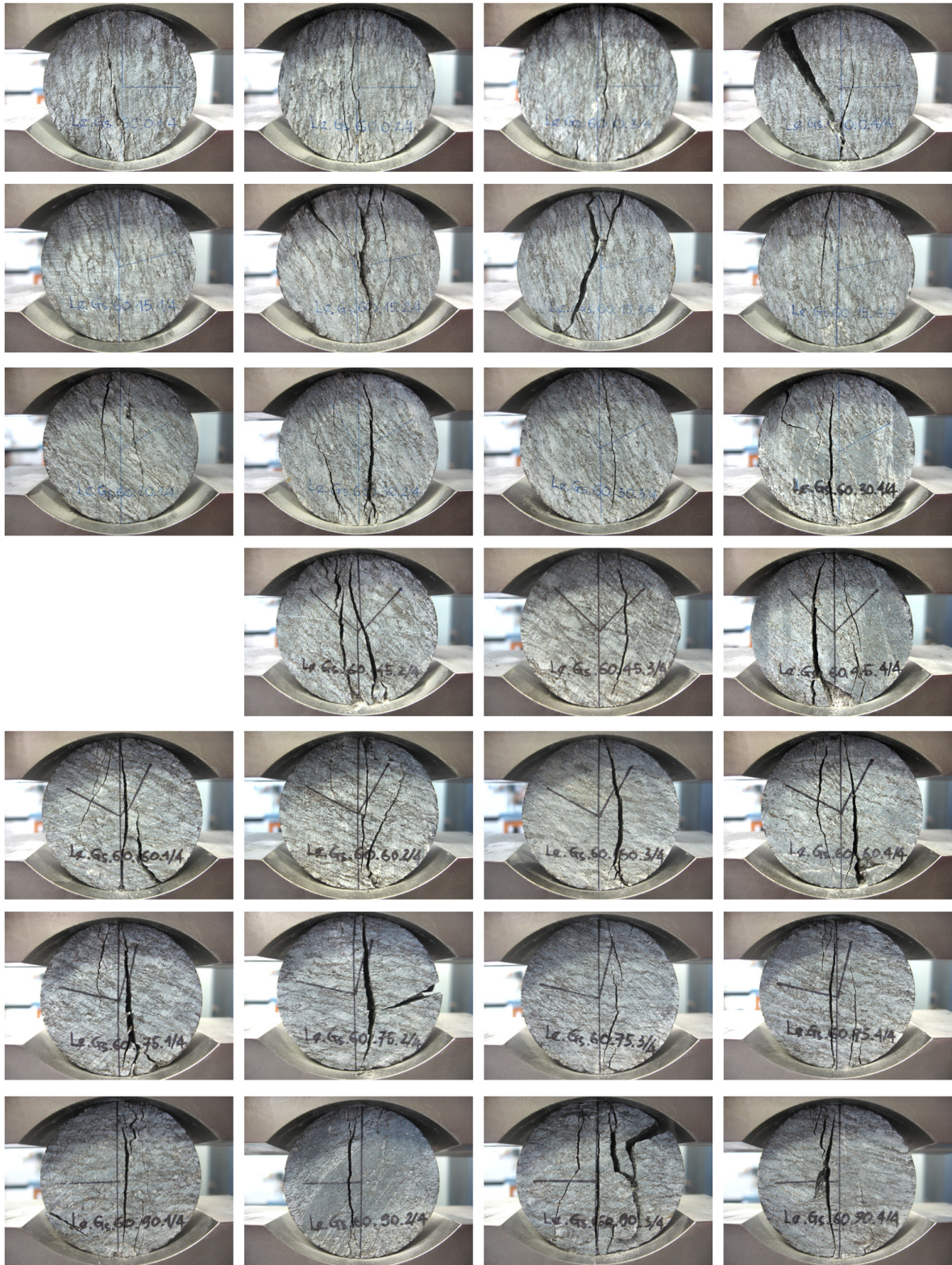
Le.Gs.75.0-90 (β = 0°, 15°, 30°, 45°, 60°, 75°, 90° from top to bottom)
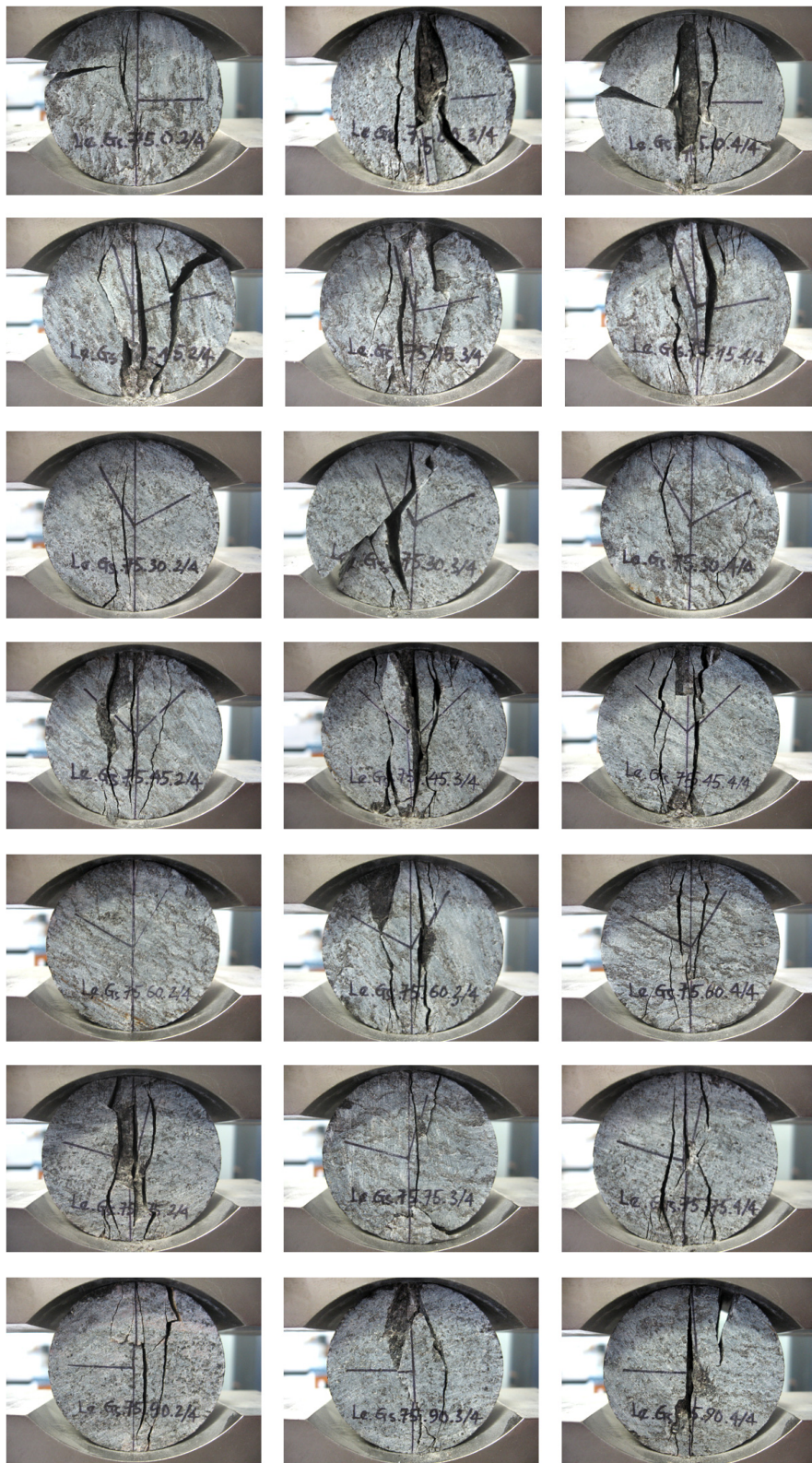
Le.Gs.90 (SPZ1)
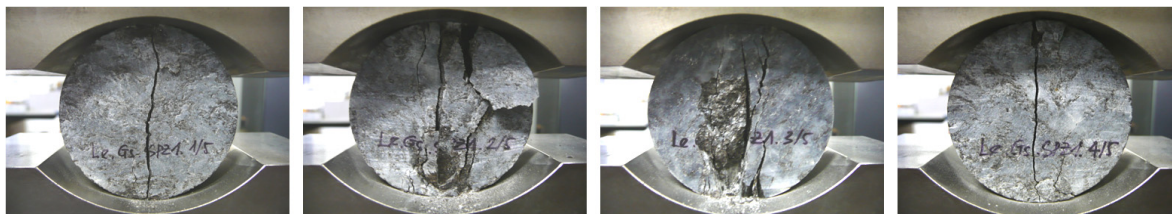
Appendix 3.4 - Fracture patterns in My.Sc samples

My.Sc.0.0-90 (β = 0°, 15°, 30°, 45°, 60°, 75°, 90° from top to bottom)
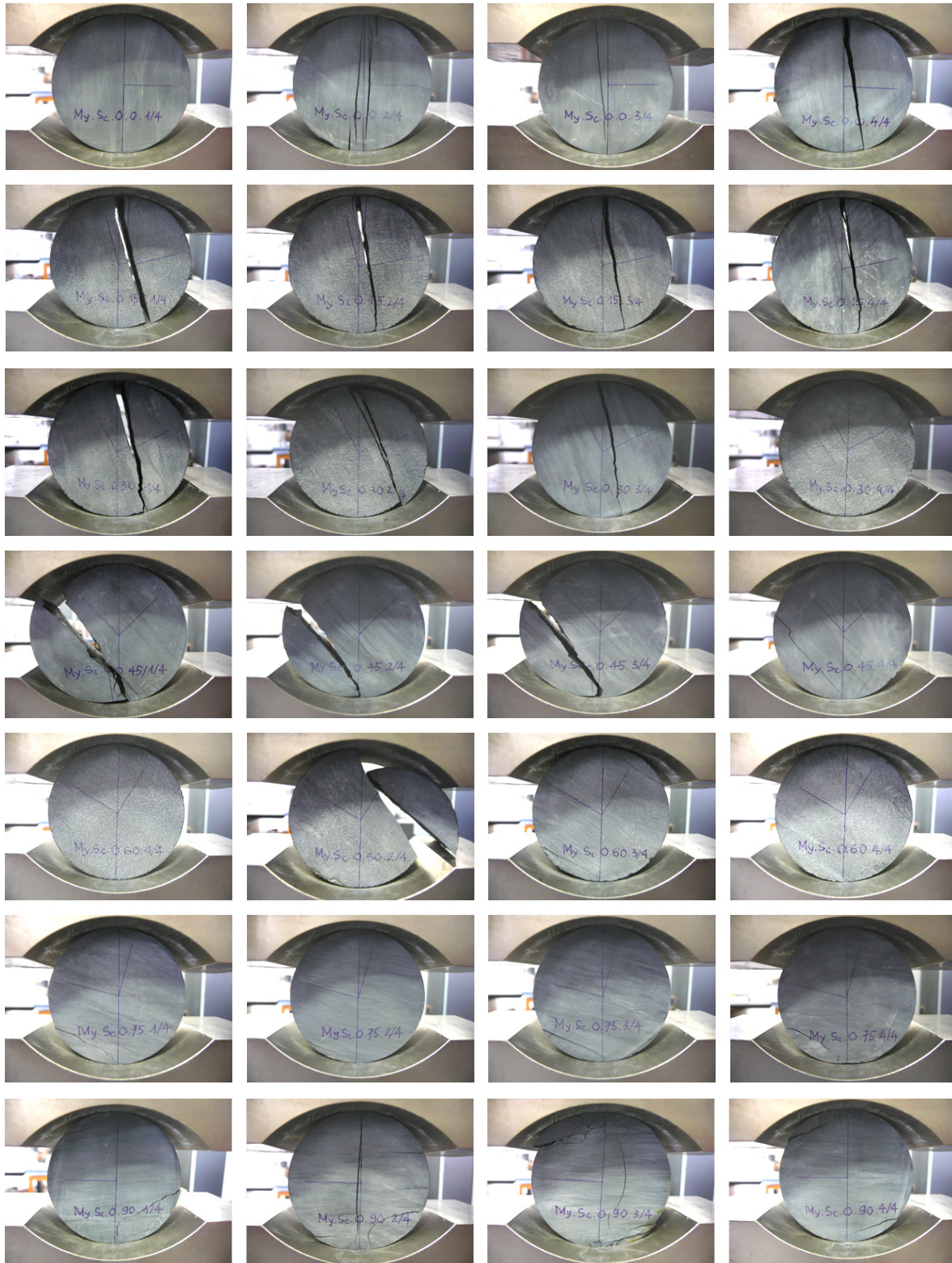
My.Sc.15.0-90 (β = 0°, 15°, 30°, 45°, 60°, 75°, 90° from top to bottom)
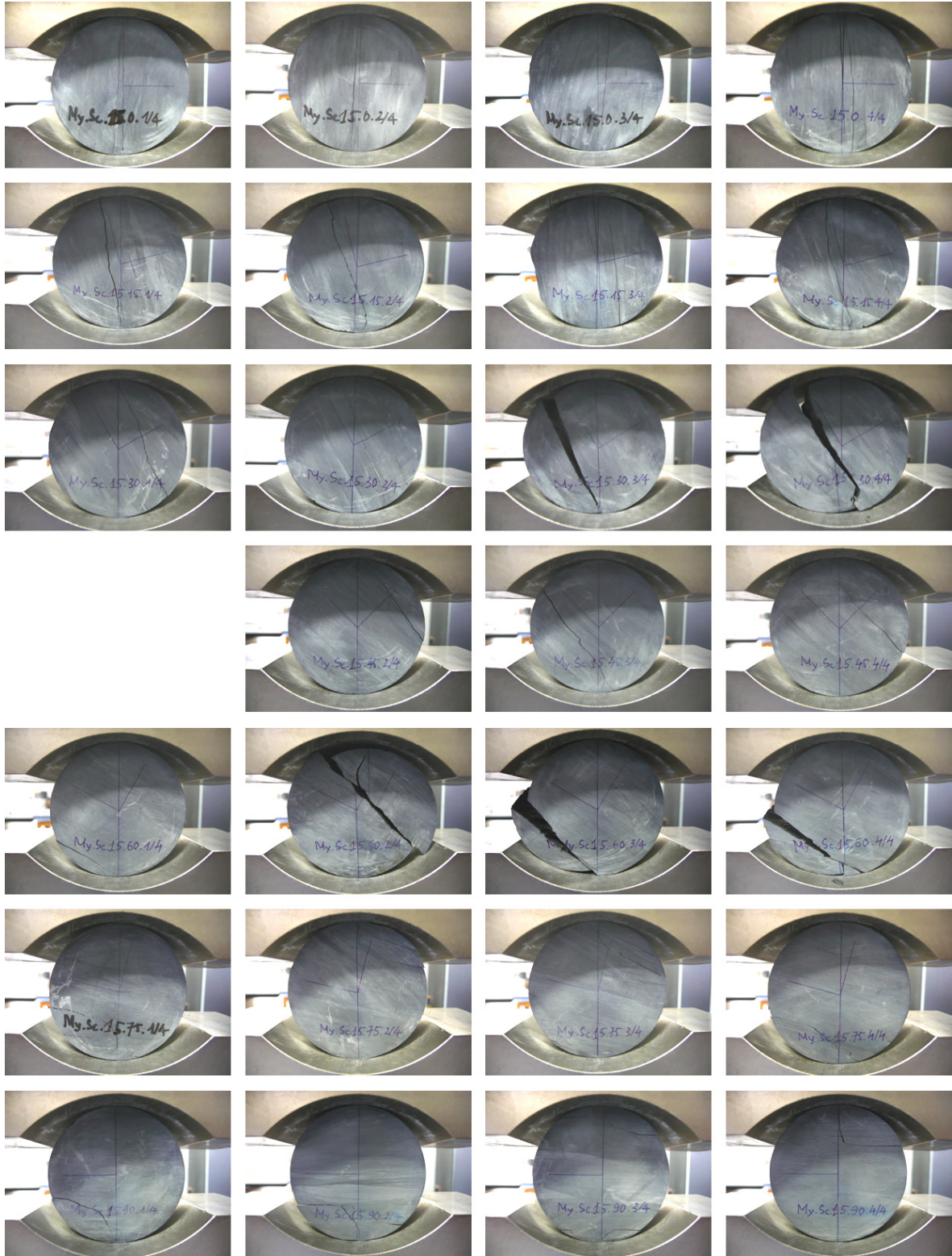
My.Sc.30.0-90 (β = 0°, 15°, 30°, 45°, 60°, 75°, 90° from top to bottom)
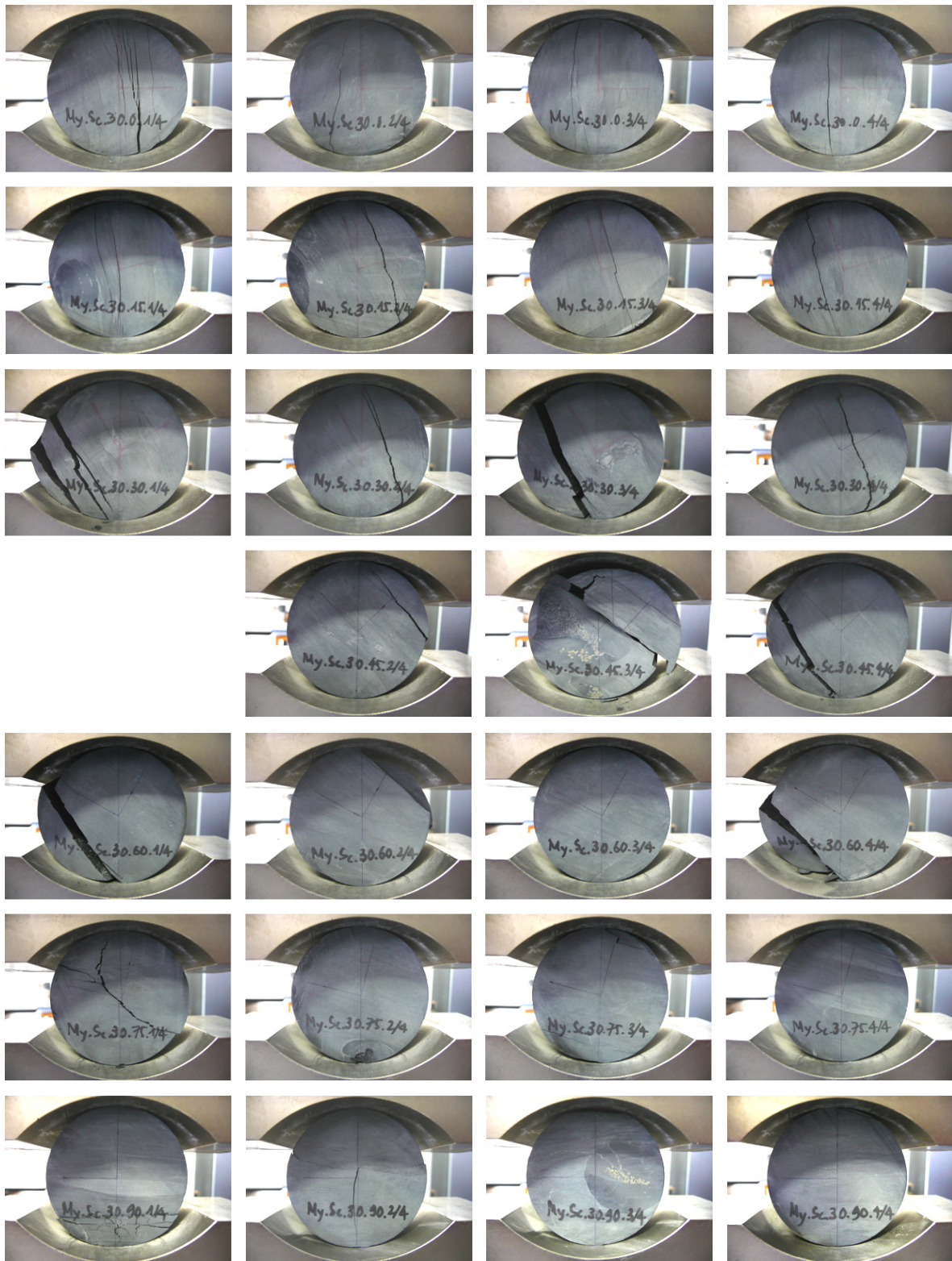
My.Sc.45.0-90 (β = 0°, 15°, 30°, 45°, 60°, 75°, 90° from top to bottom)
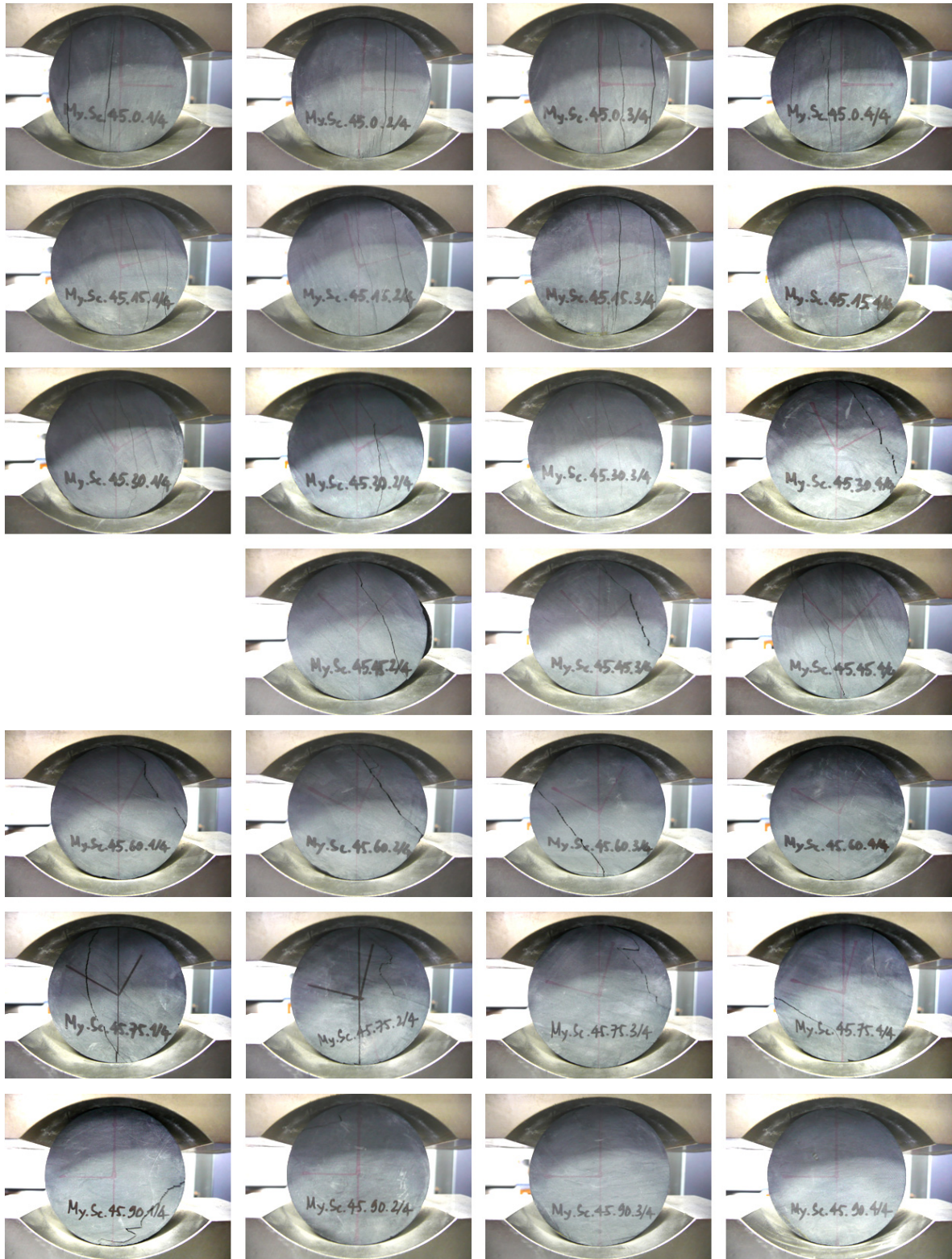
My.Sc.60.0-90 (β = 0°, 15°, 30°, 45°, 60°, 75°, 90° from top to bottom)
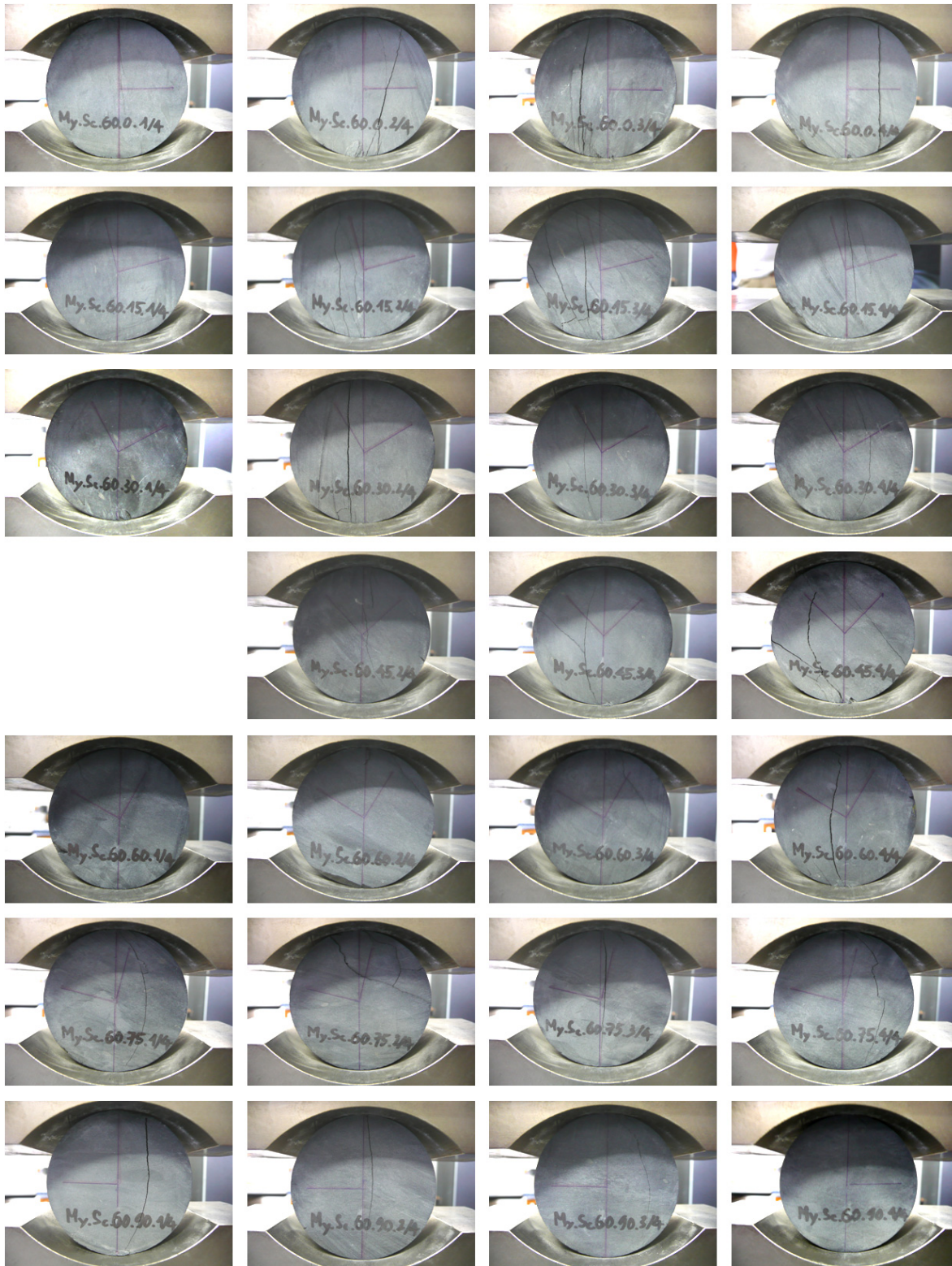
My.Sc.75.0-90 (β = 0°, 15°, 30°, 45°, 60°, 75°, 90° from top to bottom)
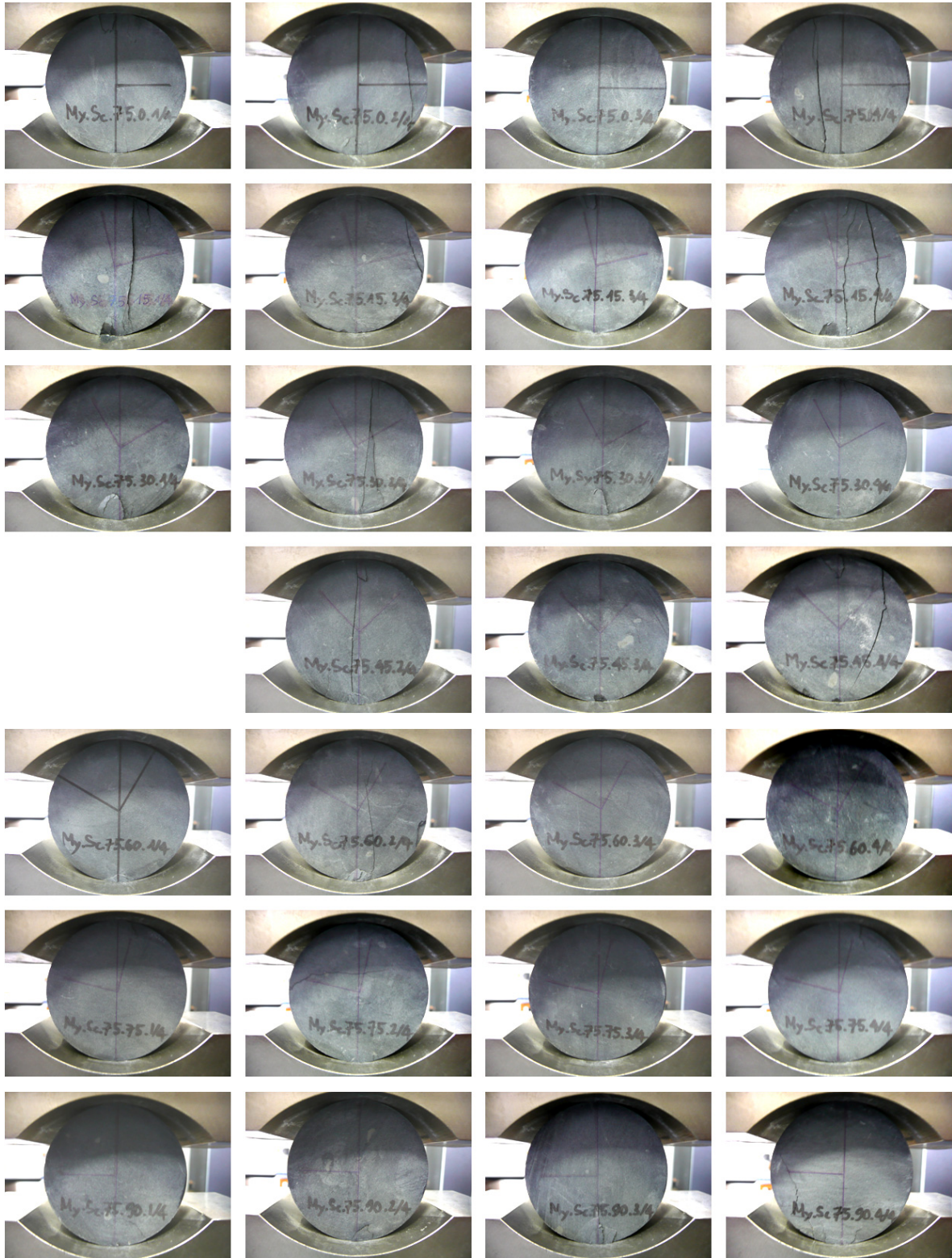
My.Sc.90 (SPZ1)
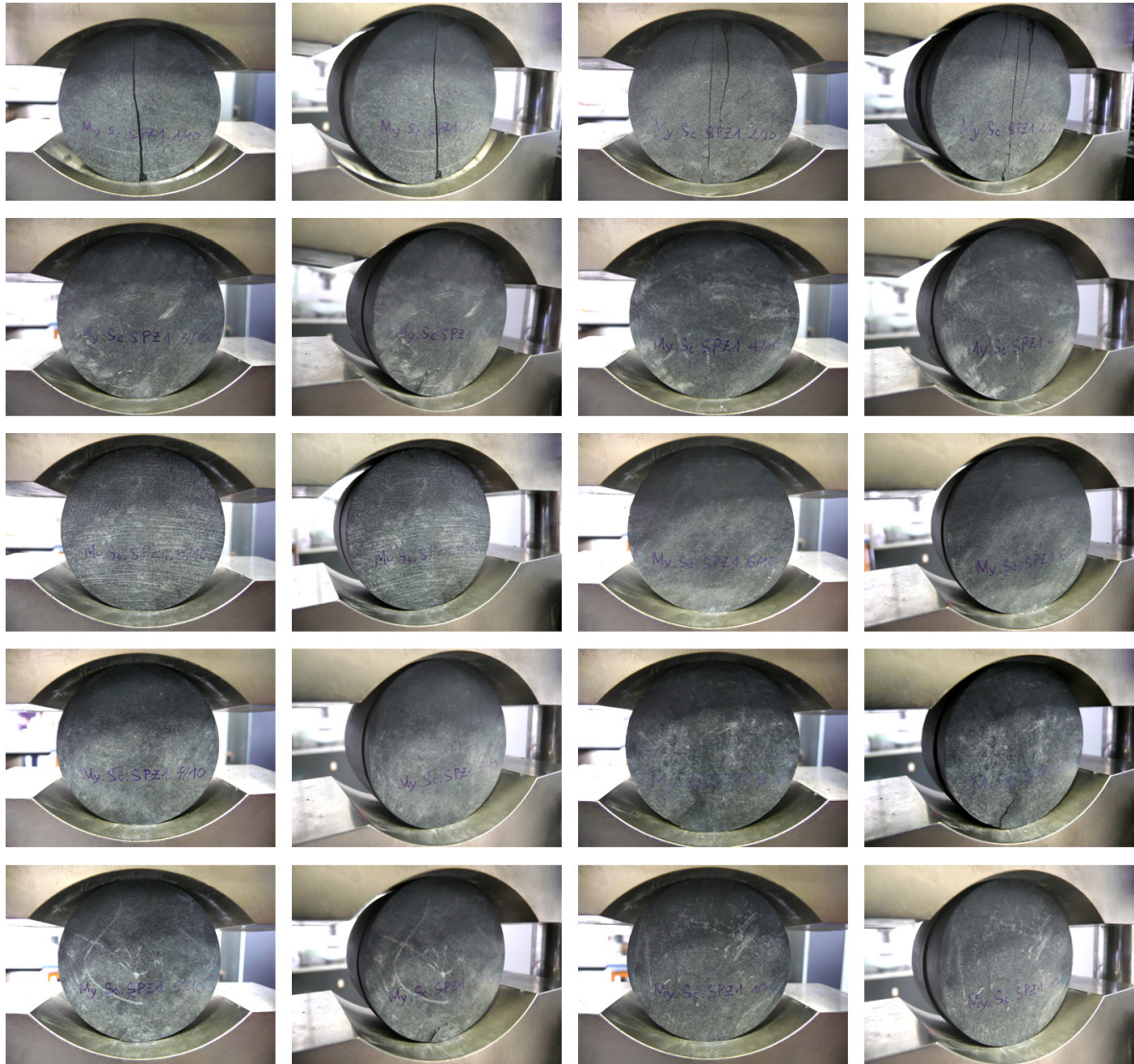
Appendix 4.1 - Influence of loading angle

4.1.1 Results of the radial model
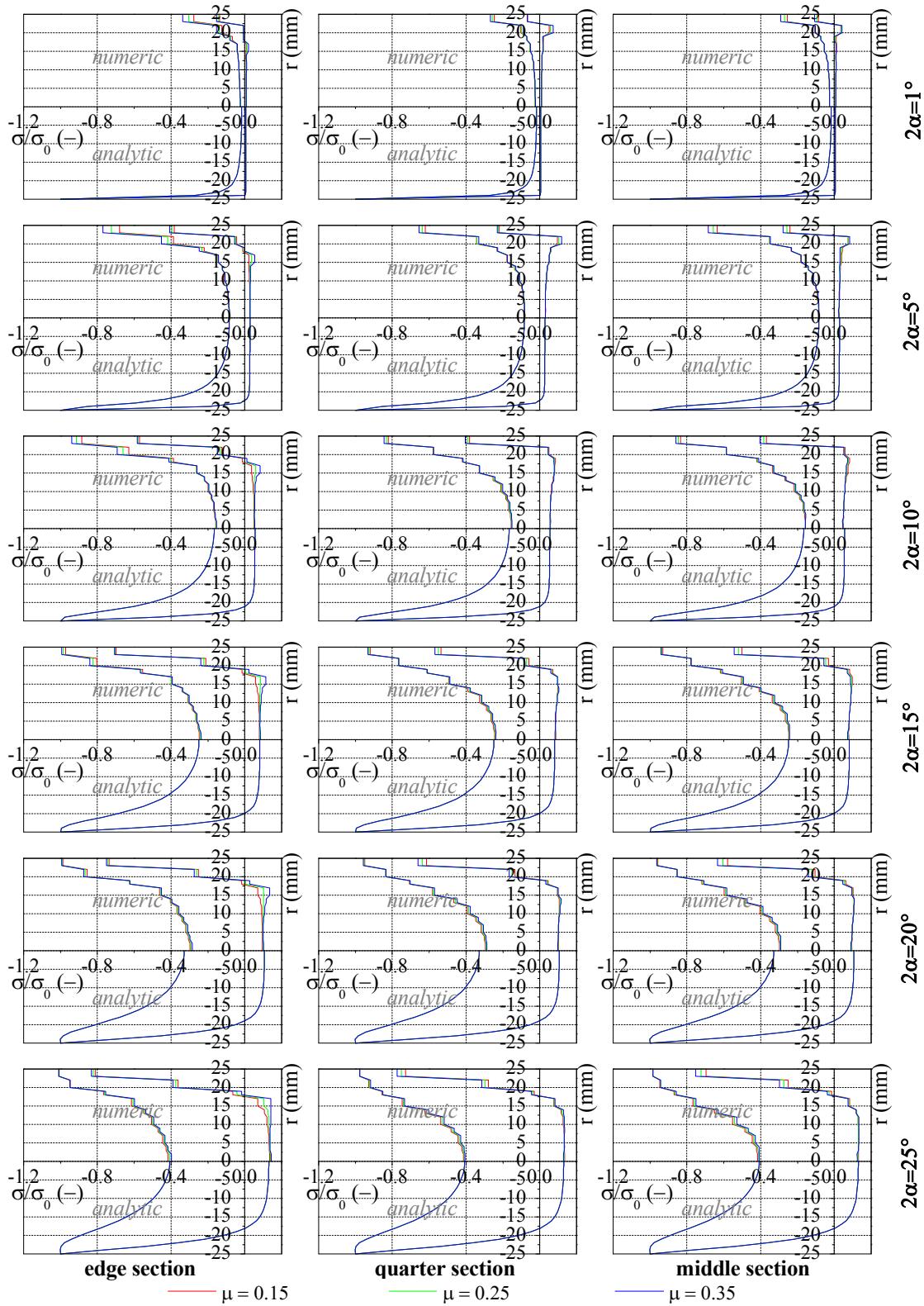
Figure A4.1-1: Influence of loading angle on σ_x and σ_y in the radial model with a thickness to diameter ratio L/D = ¼
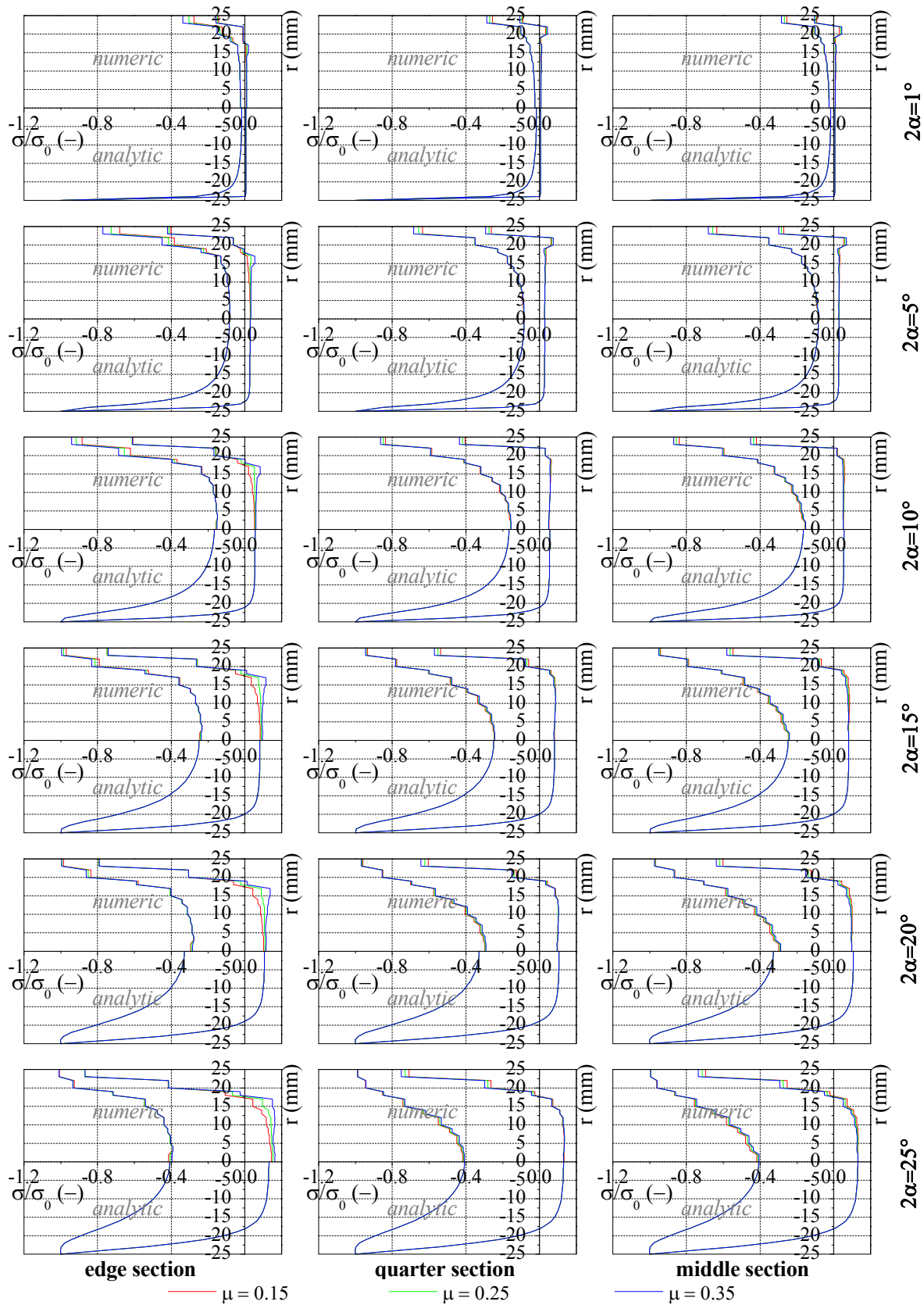
Figure A4.1-2: Influence of loading angle on σ_x and σ_y in the radial model with a thickness to diameter ratio L/D = ½

Figure A4.1-3: Influence of loading angle on σ_x and σ_y in the radial model with a thickness to diameter ratio L/D = $\frac{1}{1}$

4.1.2 Comparison of the results of the orthogonal model

Figure A4.1-4: Influence of loading angle on σ_x and σ_y in the orthogonal model with a thickness to diameter ratio L/D = ¼

Figure A4.1-5: Influence of loading angle on σ_x and σ_y in the orthogonal model with a thickness to diameter ratio L/D = ½

Figure A4.1-6: Influence of loading angle on σ_x and σ_y in the orthogonal model with a thickness to diameter ratio L/D = $\frac{1}{1}$

Appendix 4.2 - Influence of material properties

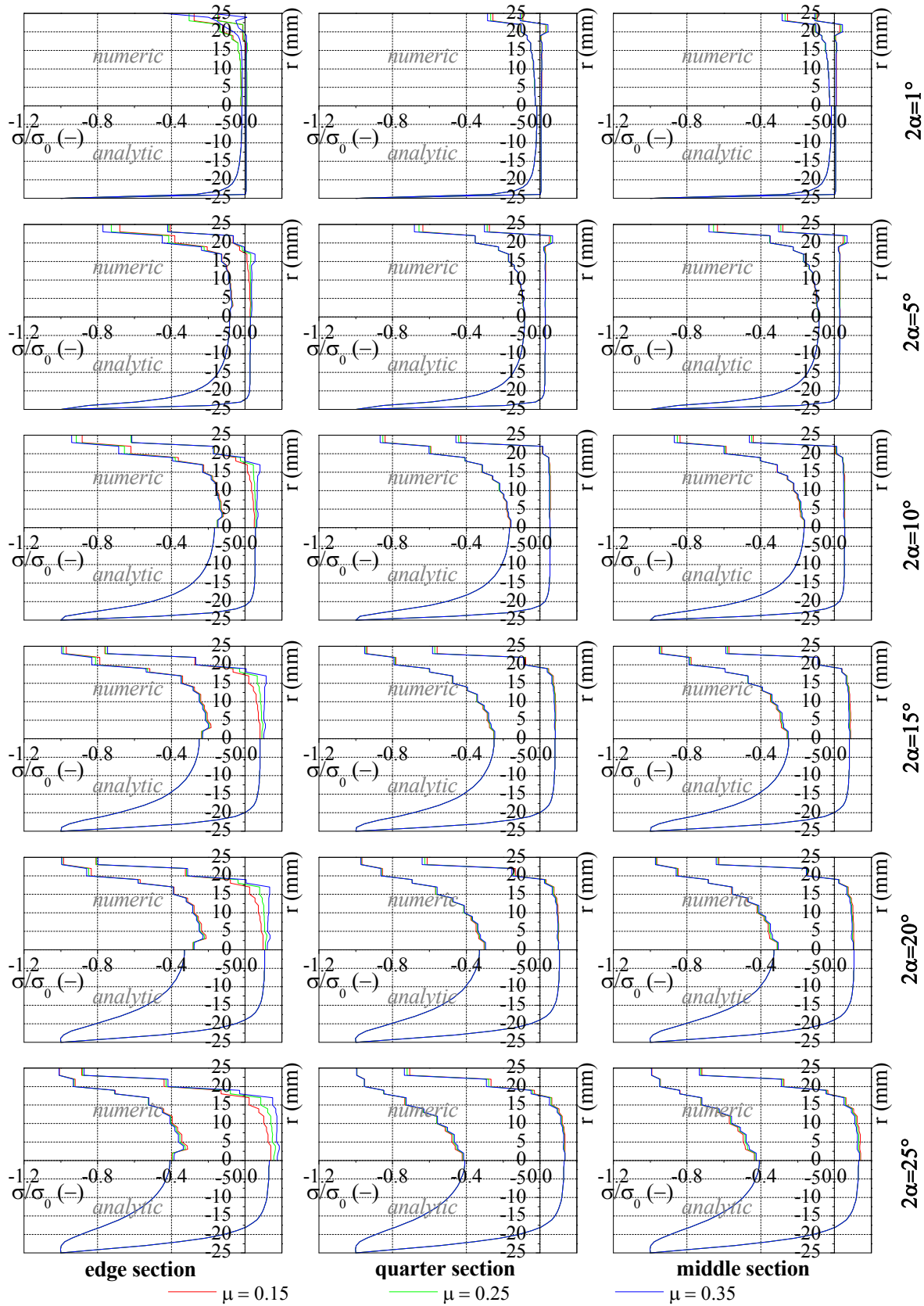## 4.2.1 Results of the radial model

Figure A4.2-1: Influence of material on σ_x and σ_y in the radial model with a thickness to diameter ratio L/D = ¼
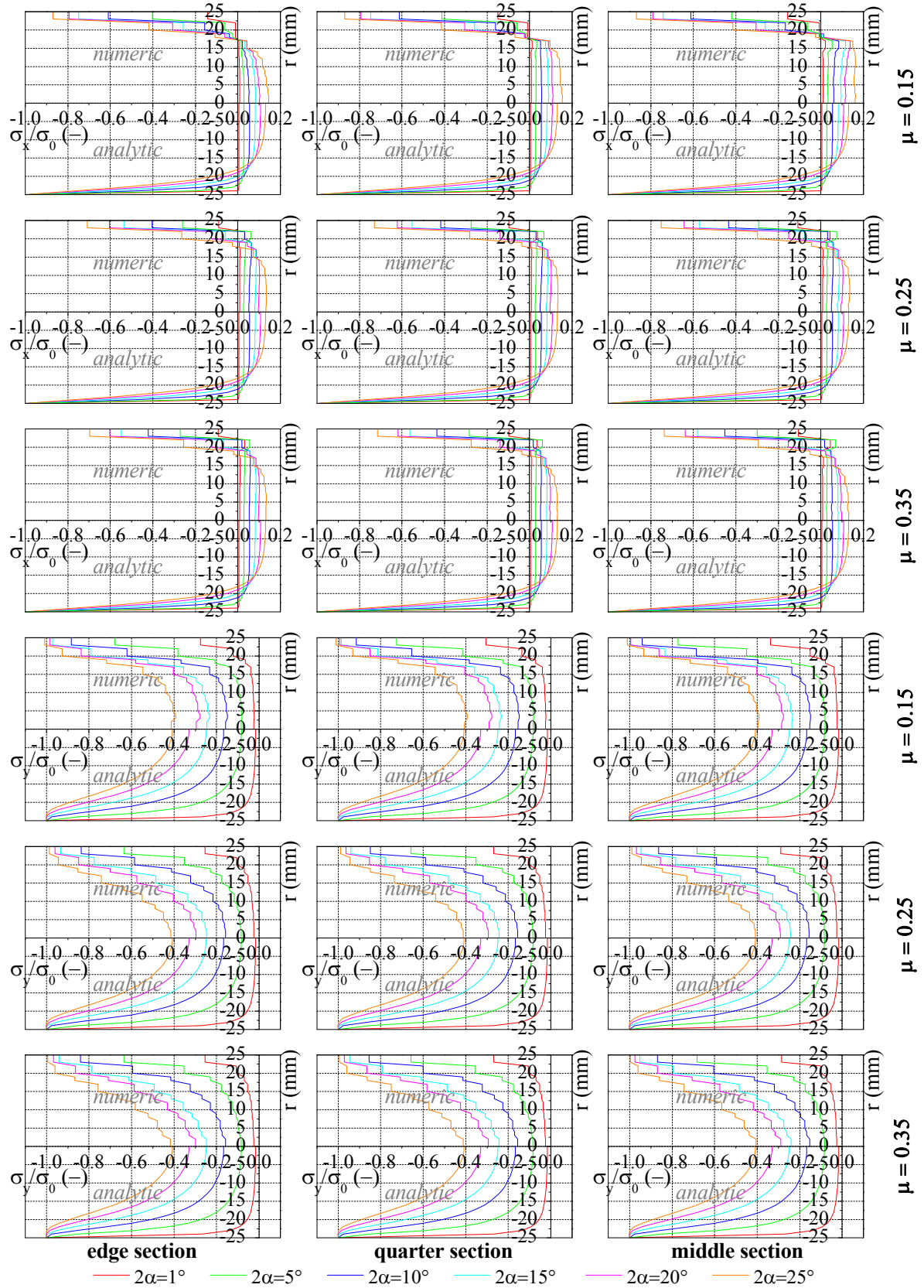
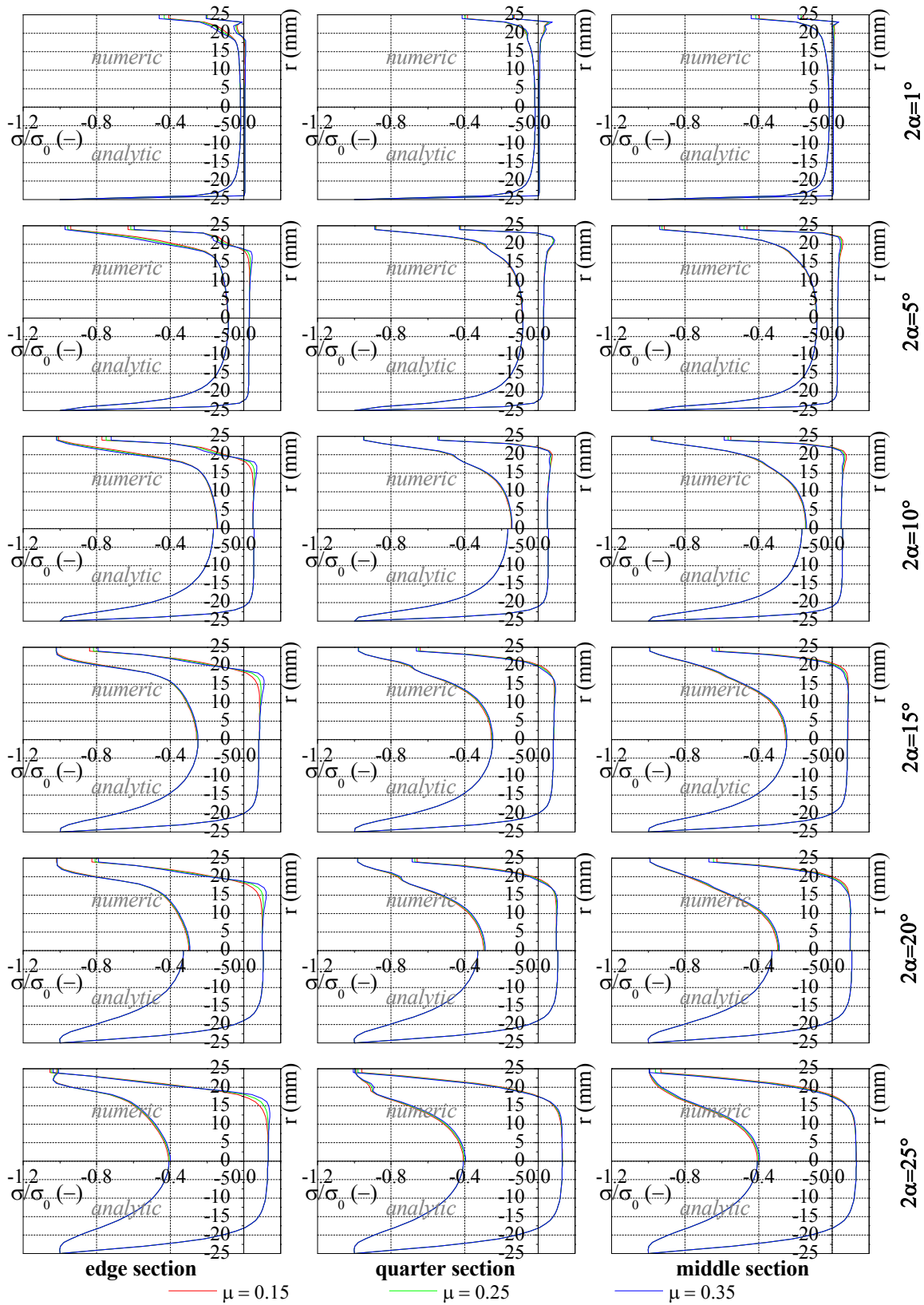**Figure A4.2-2:** Influence of material on σ_x and σ_y in the radial model with a thickness to diameter ratio L/D = ½
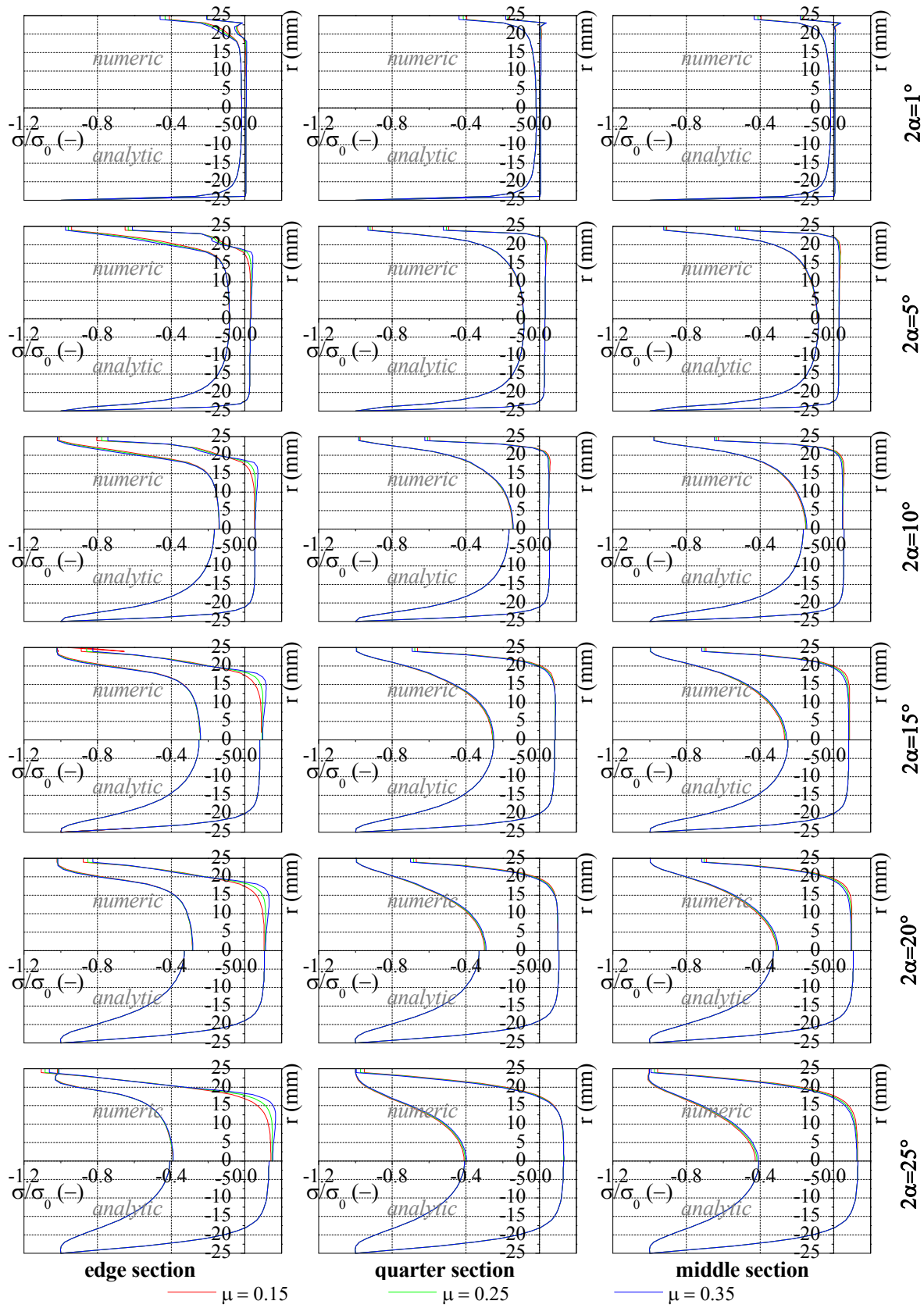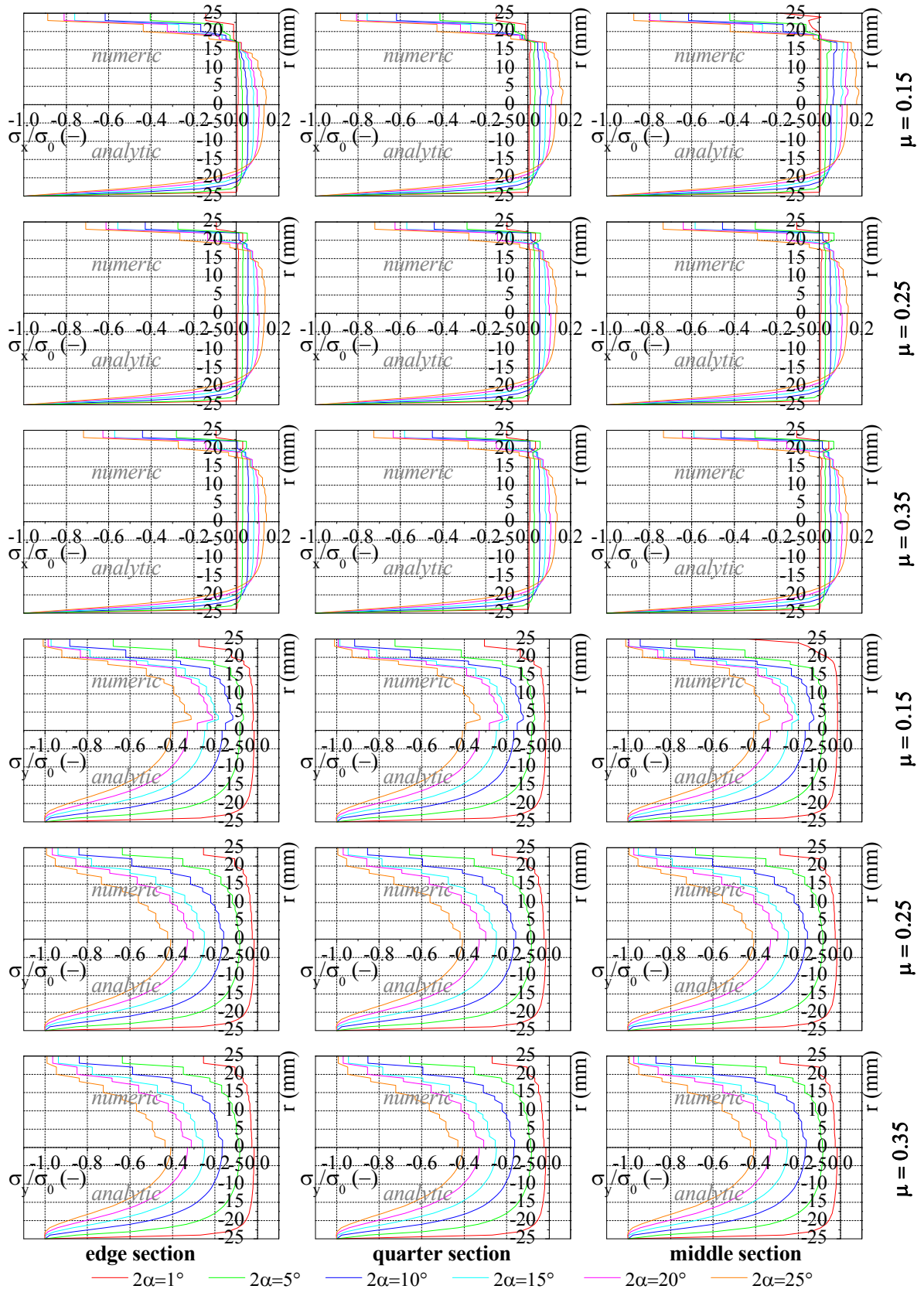
Figure A4.2-3: Influence of material on σ_x and σ_y in the radial model with a thickness to diameter ratio L/D = $\frac{1}{1}$
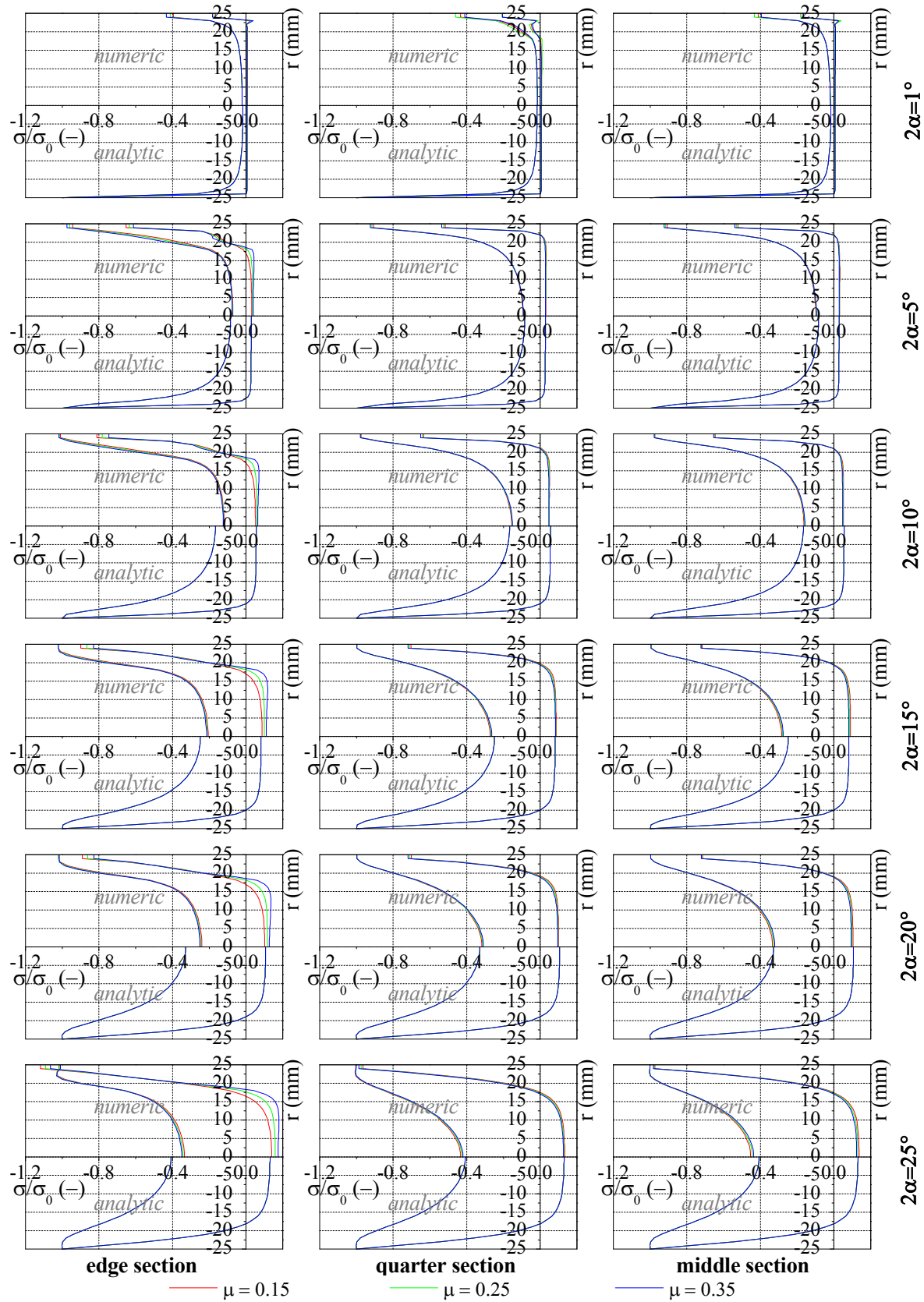
4.2.2 Comparison of the results of the orthogonal model
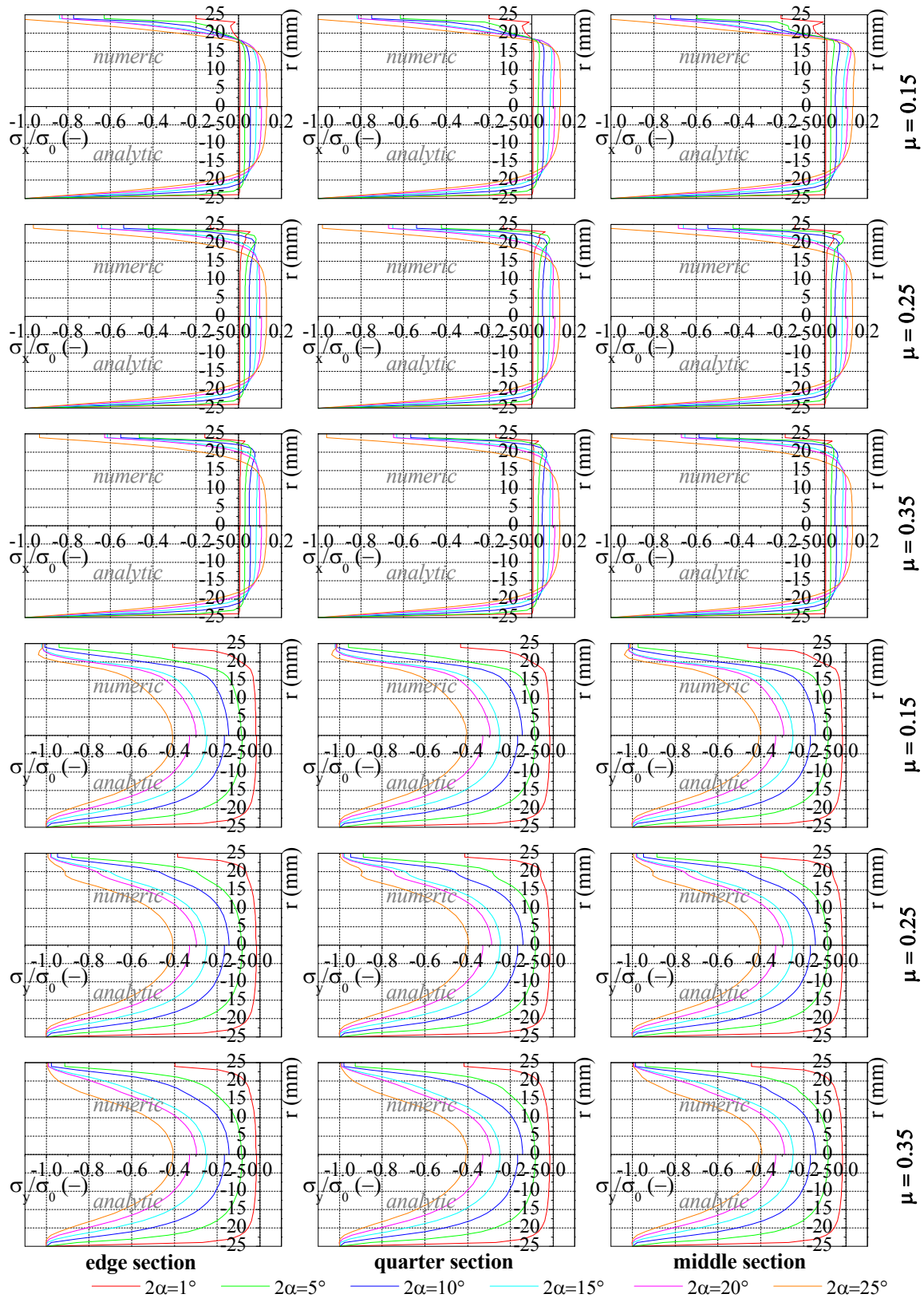
Figure A4.2-4: Influence of material on σ_x and σ_y in the orthogonal model with a thickness to diameter ratio L/D = ¼
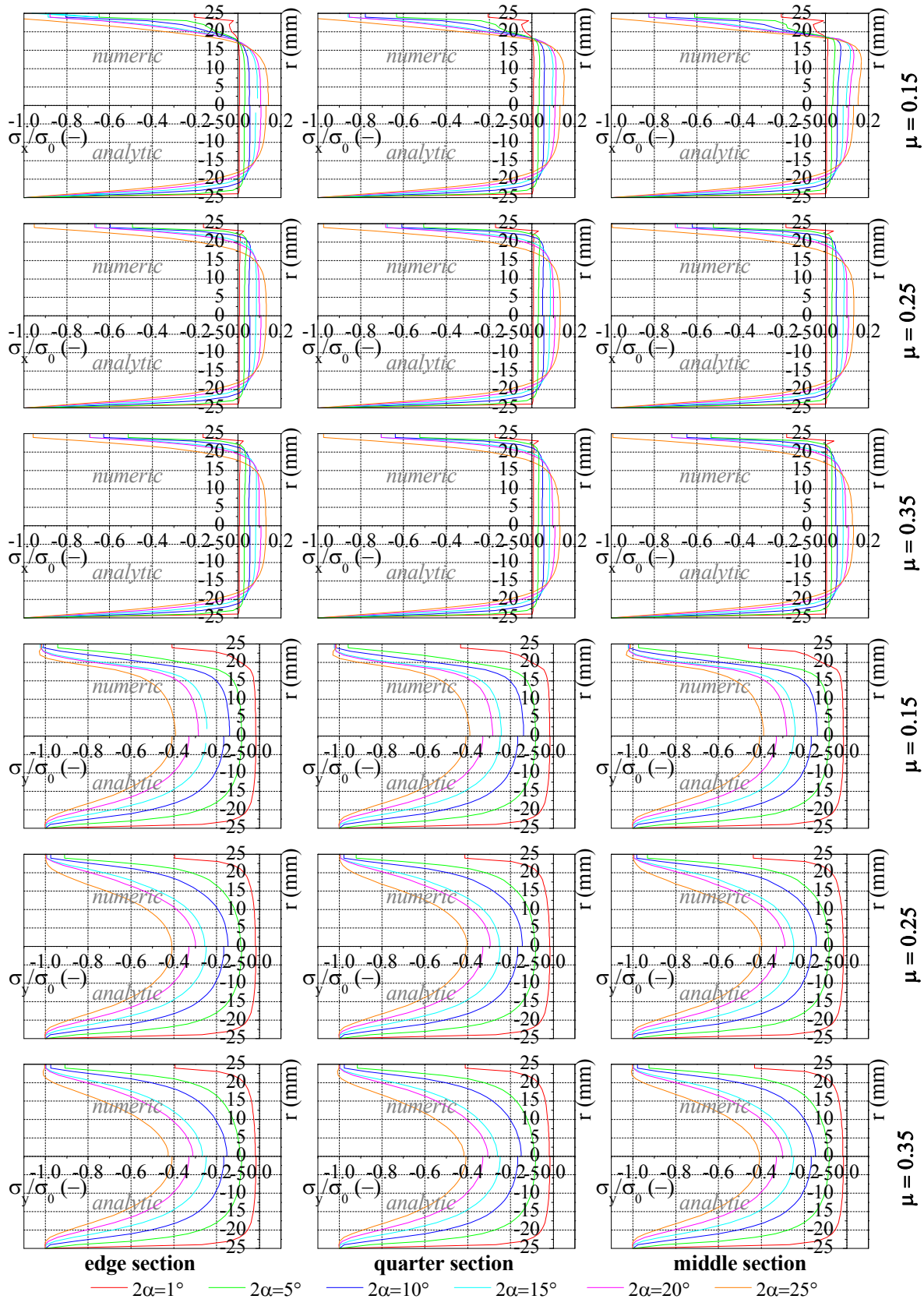
Figure A4.2-5: Influence of material on σ_x and σ_y in the orthogonal model with a thickness to diameter ratio L/D = ½

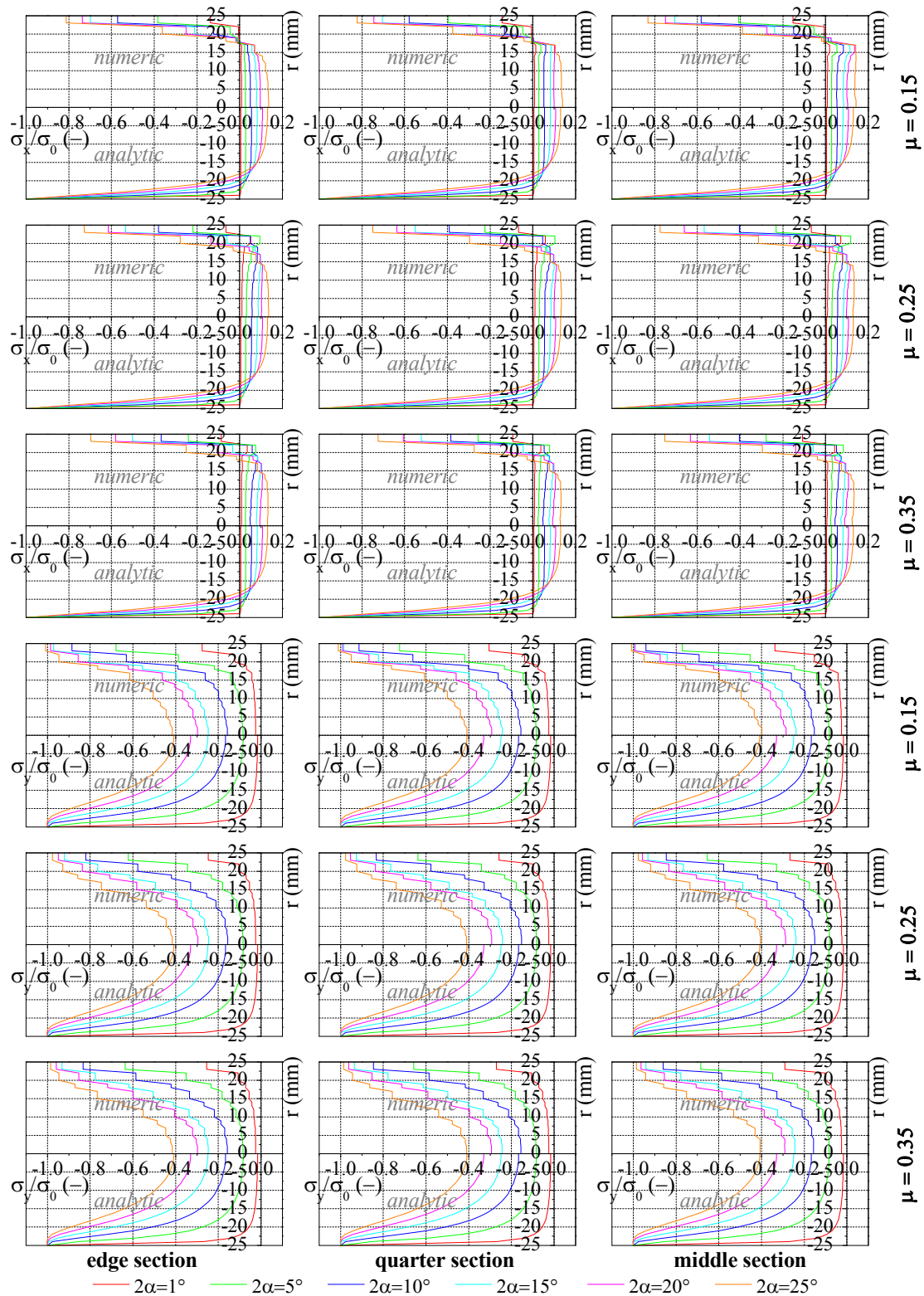**Figure A4.2-6:** Influence of material on σ_x and σ_y in the orthogonal model with a thickness to diameter ratio $L/D = \frac{1}{1}$
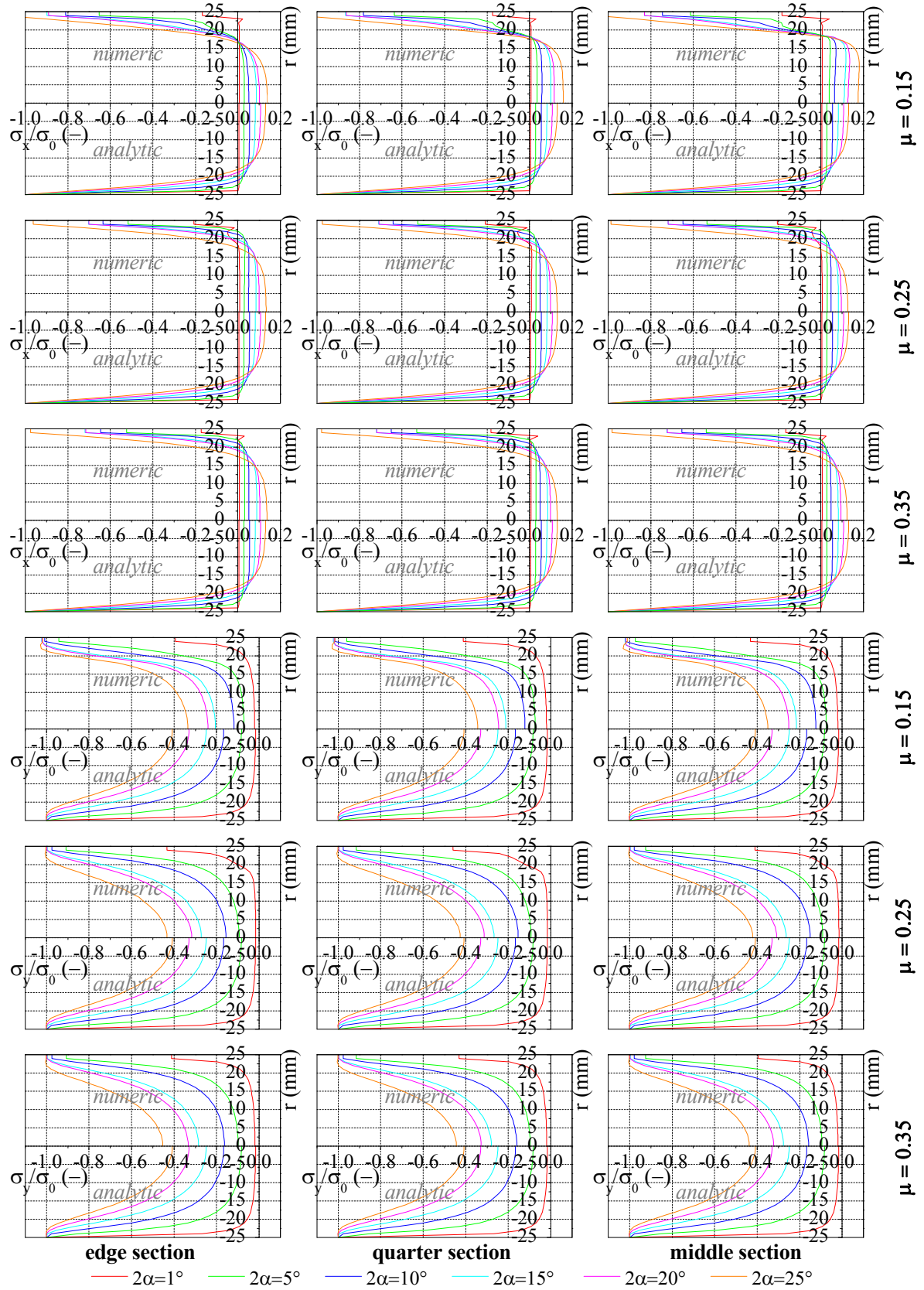
Appendix 5.1 - Failure zone state in Le.Gs Gneiss
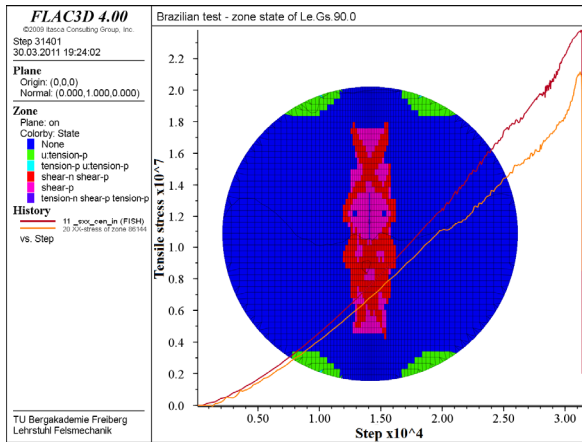
Figure A5.1-1: Failure zone state in Le.Gs Gneiss where ψ = 90°
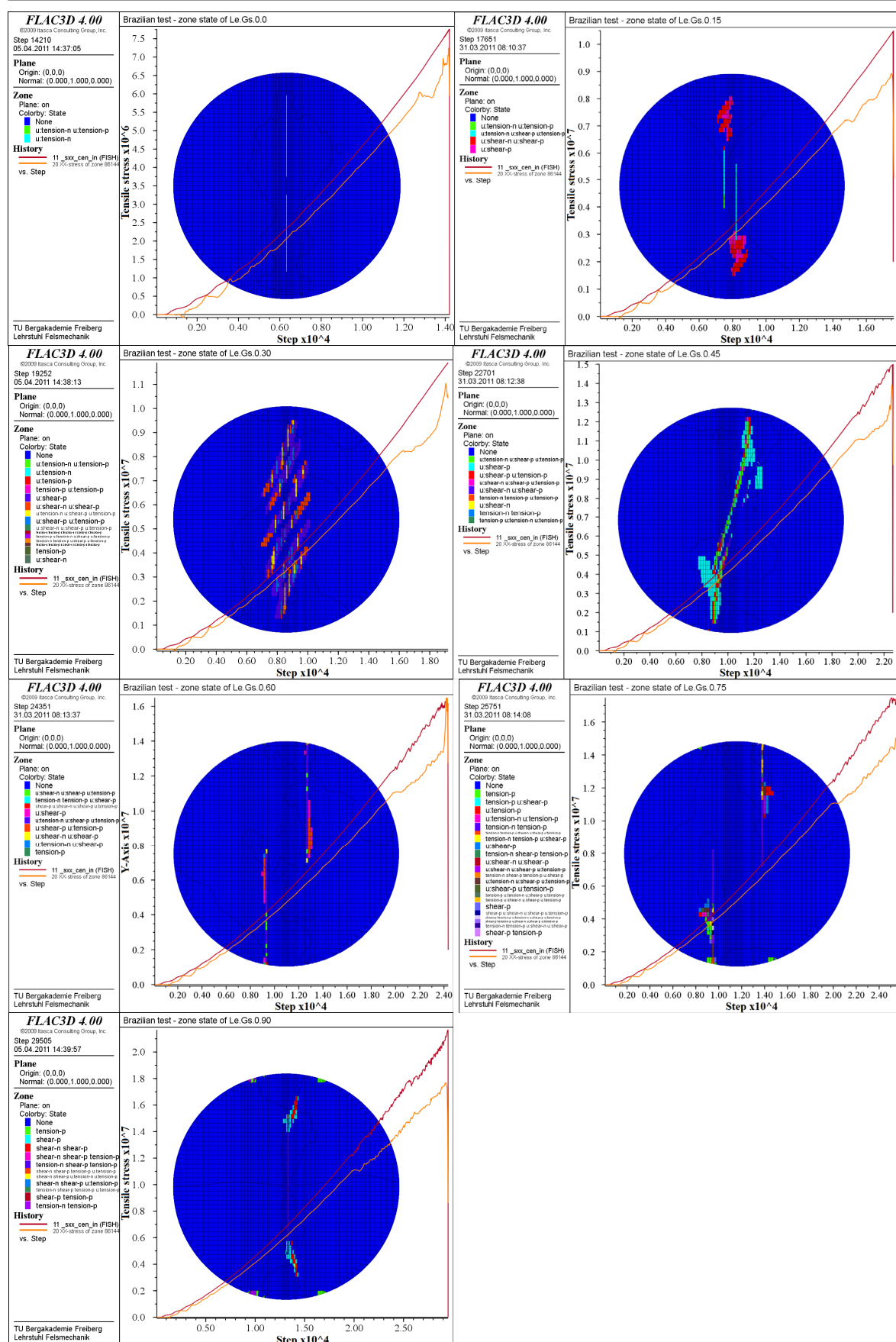
Figure A5.1-2: Failure zone state in Le.Gs Gneiss where ψ = 0°

Figure A5.1-3: Failure zone state in Le.Gs Gneiss where ψ = 15°
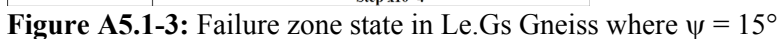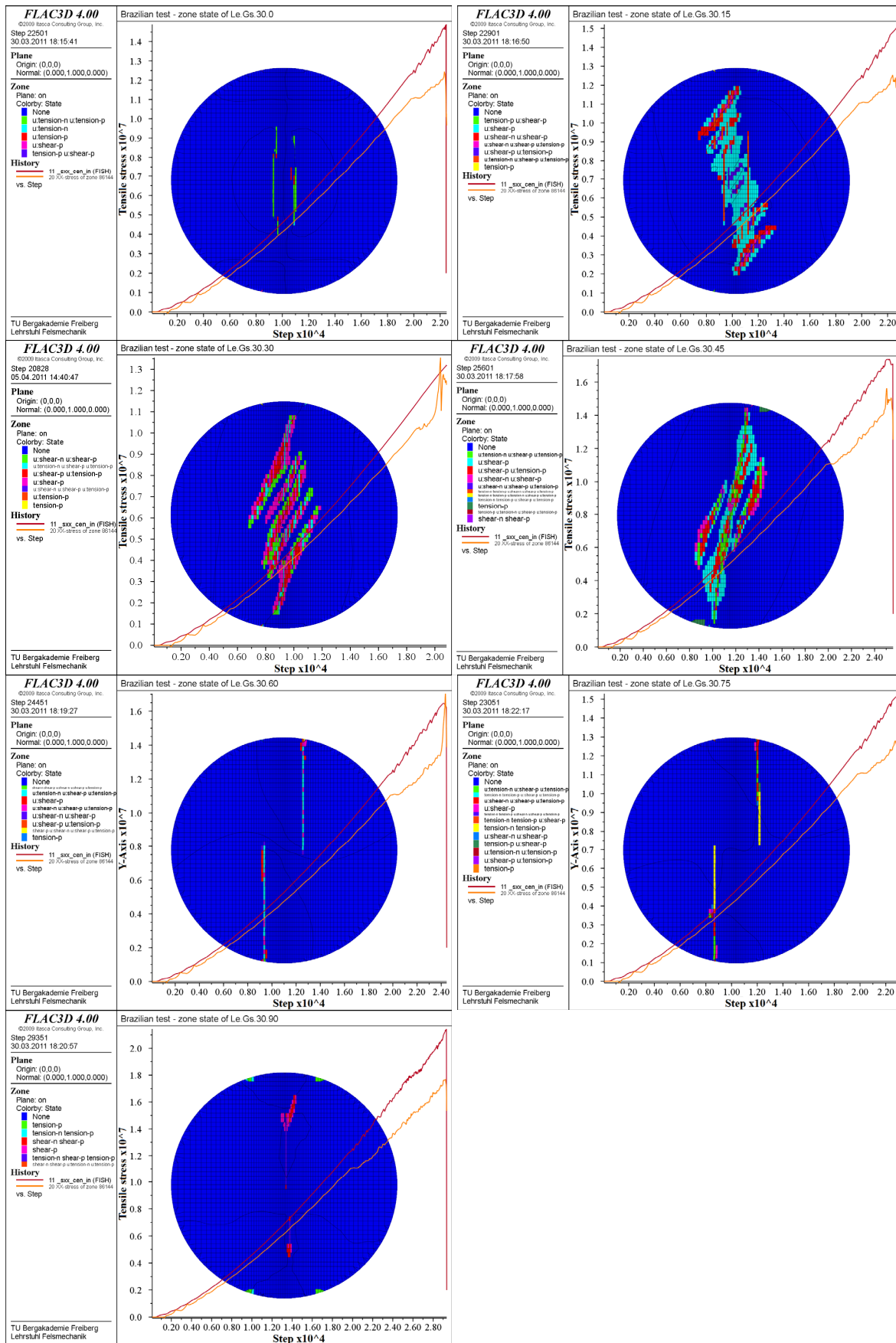
Figure A5.1-4: Failure zone state in Le.Gs Gneiss where ψ = 30°
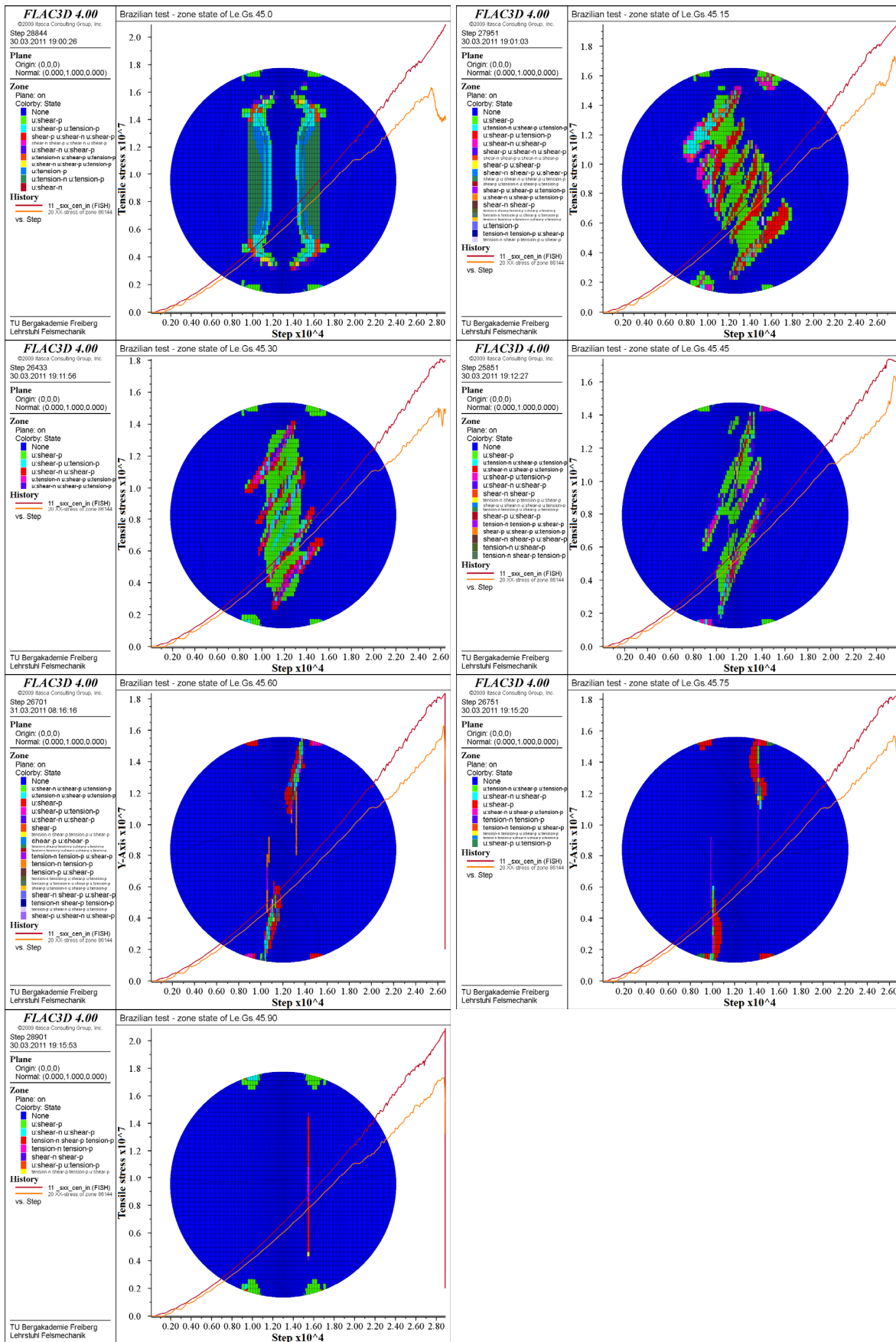
Figure A5.1-5: Failure zone state in Le.Gs Gneiss where ψ = 45°
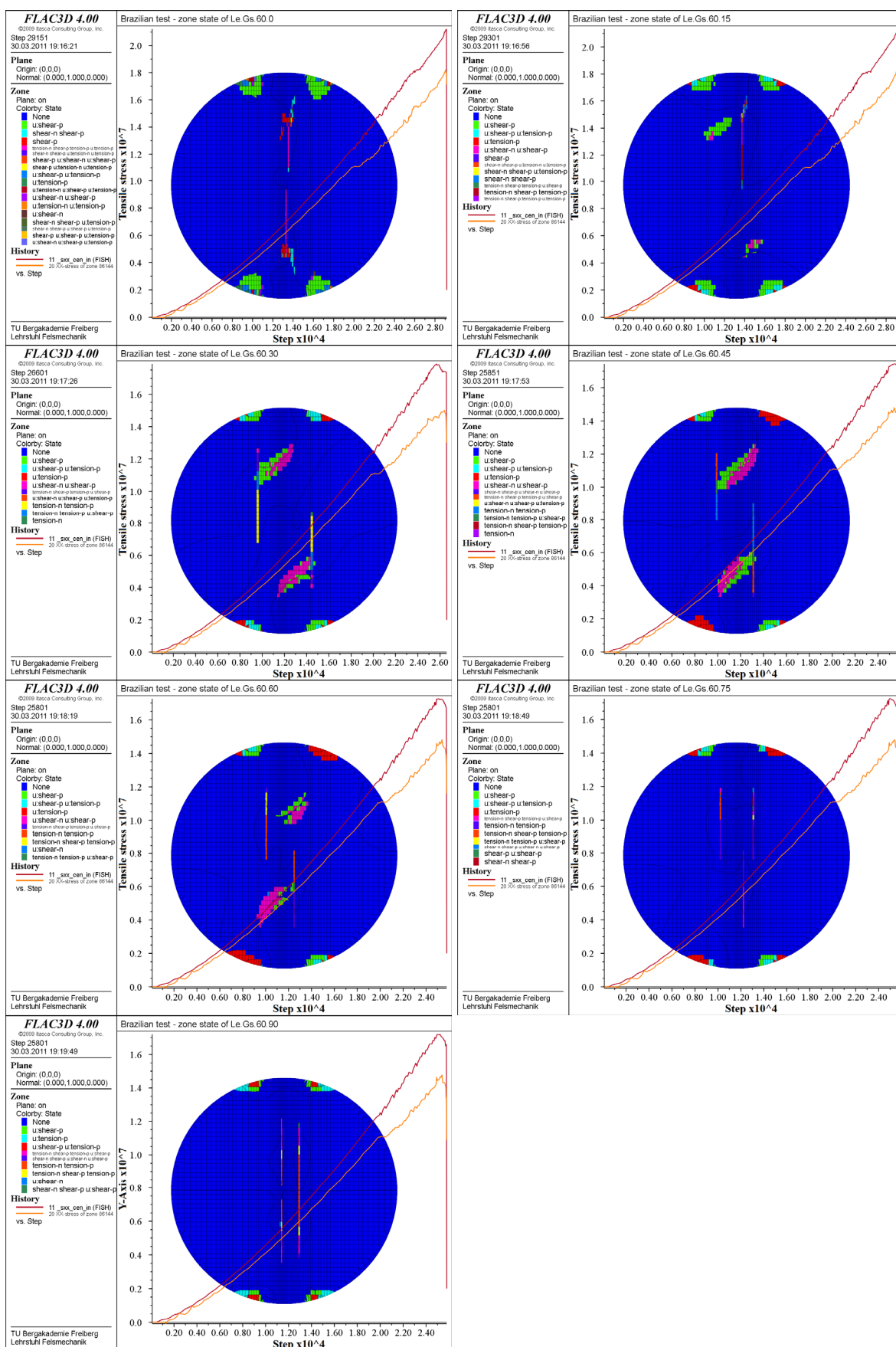
Figure A5.1-6: Failure zone state in Le.Gs Gneiss where ψ = 60°

Figure A5.1-7: Failure zone state in Le.Gs Gneiss where ψ = 75°
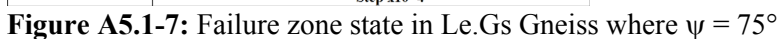
Appendix 5.2: Failure zone state in My.Sc Slate
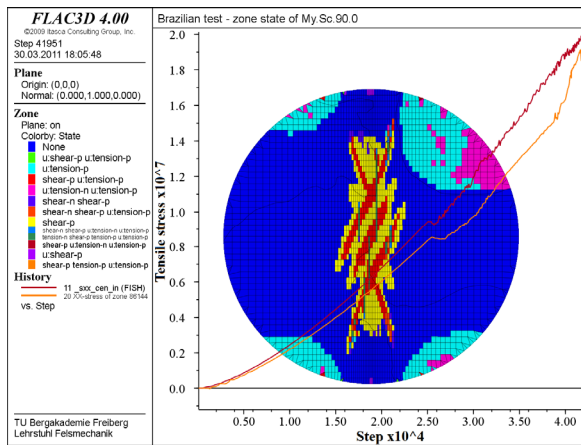
Figure A5.2-1: Failure zone state in My.Sc slate where ψ = 90°
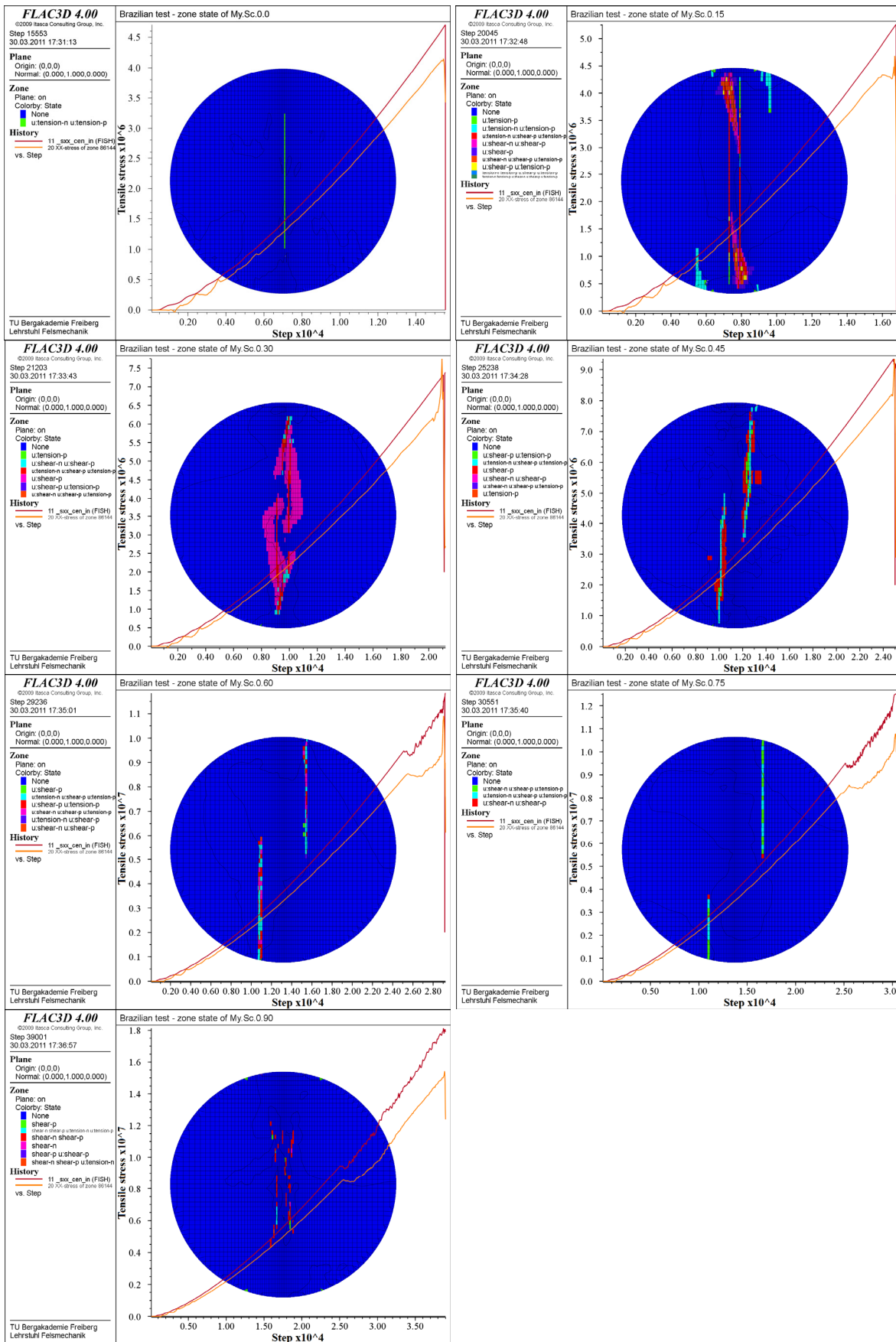
Figure A5.2-2: Failure zone state in My.Sc Slate where ψ = 0°
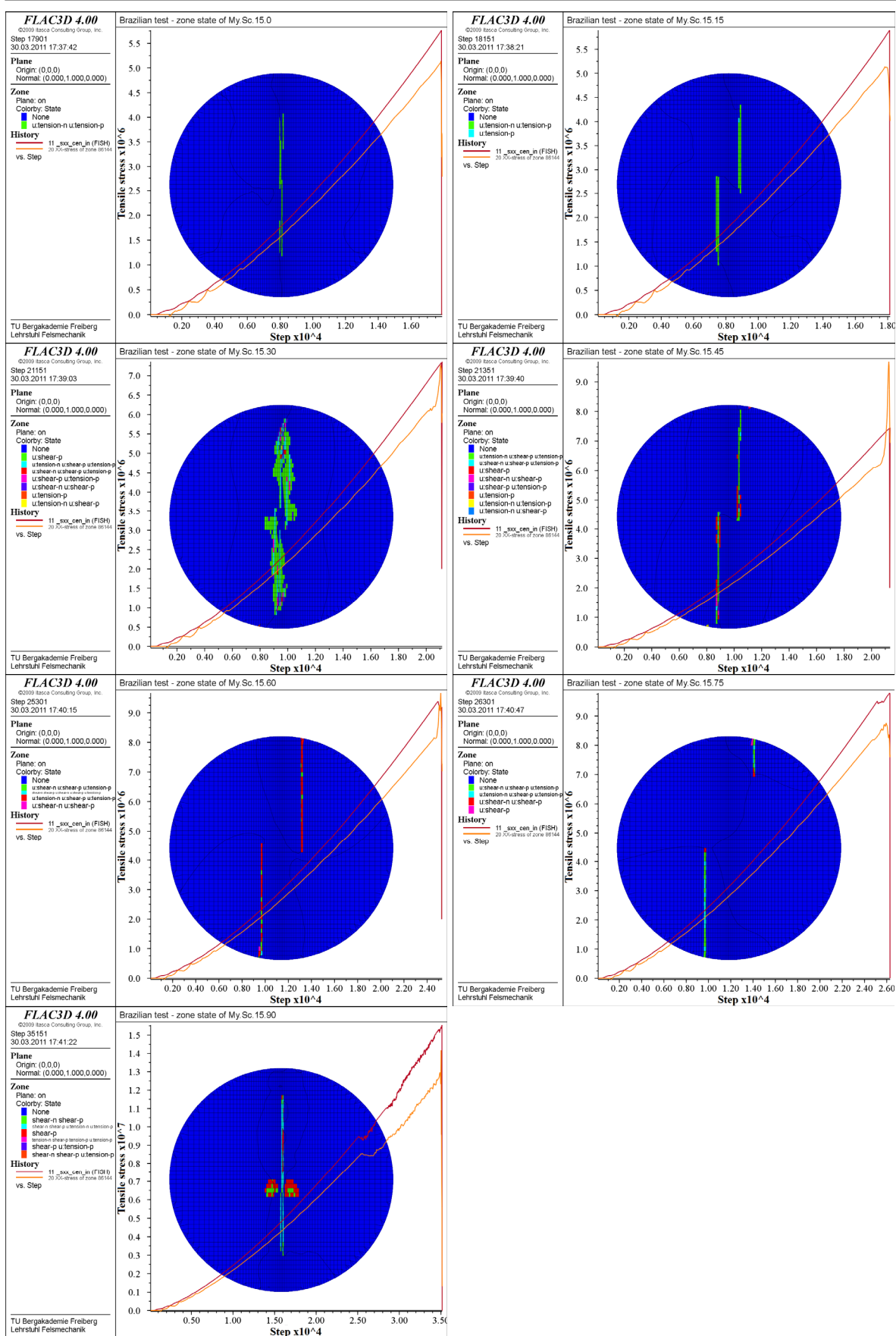
Figure A5.2-3: Failure zone state in My.Sc Slate where ψ = 15°
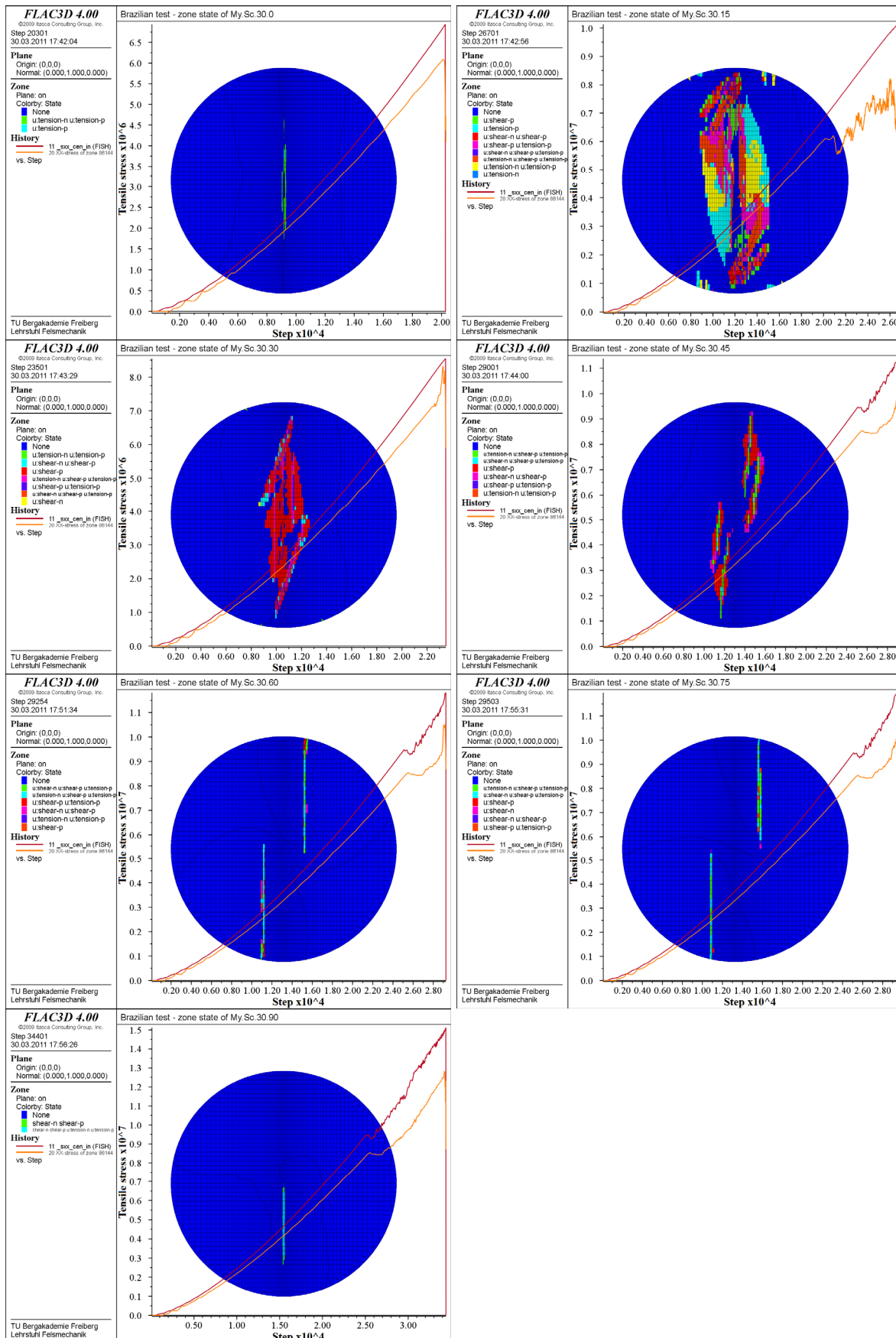
Figure A5.2-4: Failure zone state in My.Sc Slate where ψ = 30°
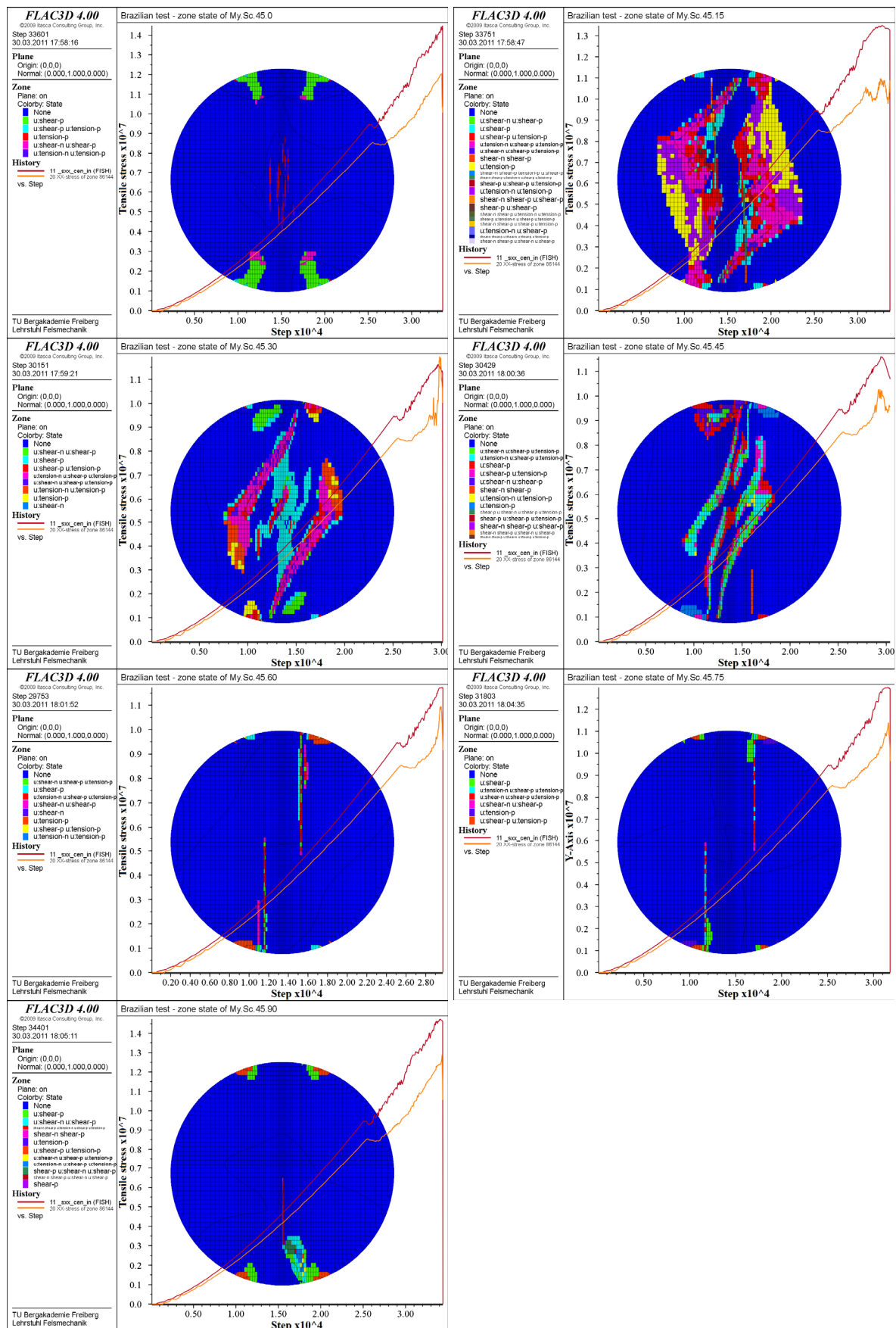
Figure A5.2-5: Failure zone state in My.Sc Slate where ψ = 45°
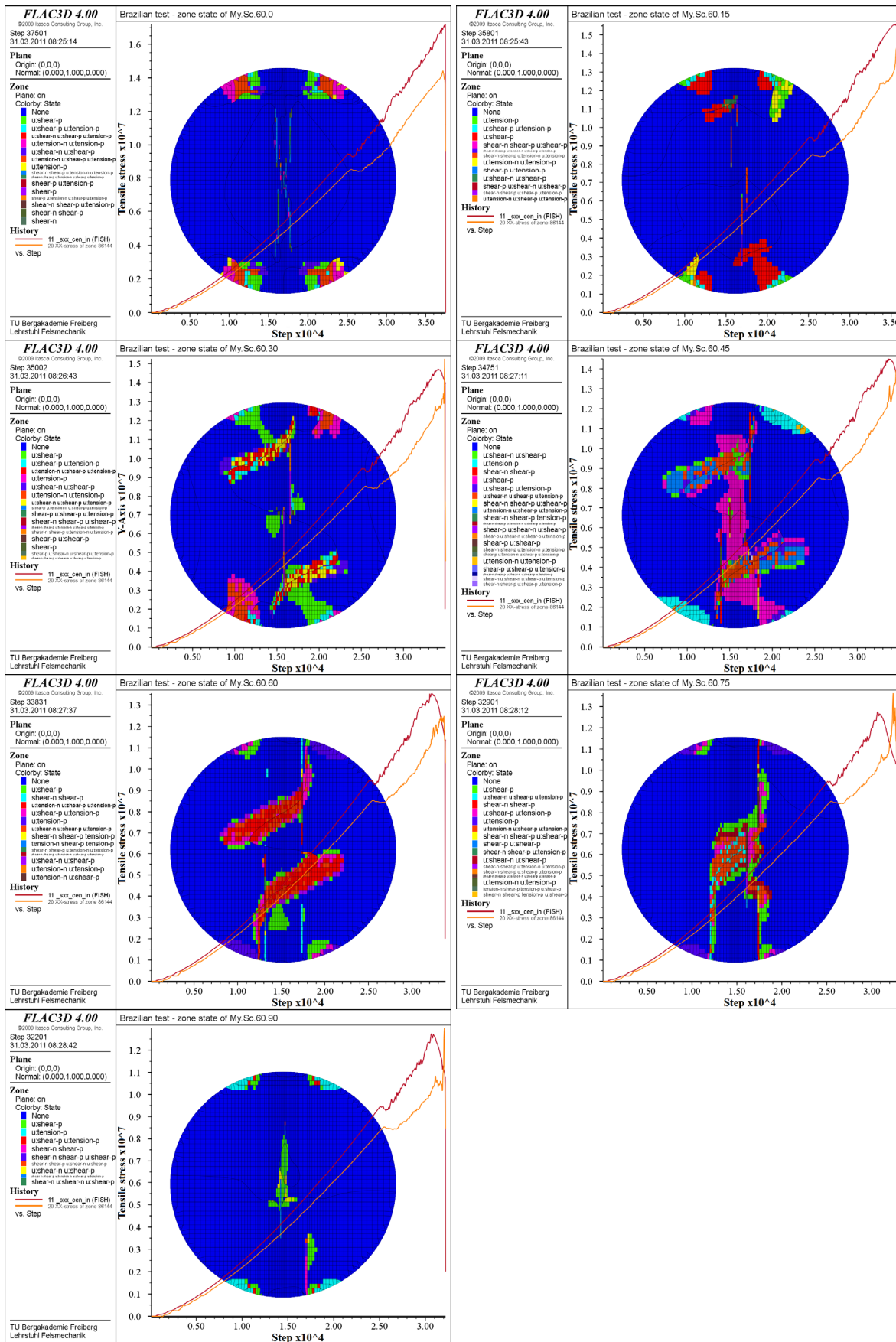
Figure A5.2-6: Failure zone state in My.Sc Slate where ψ = 60°
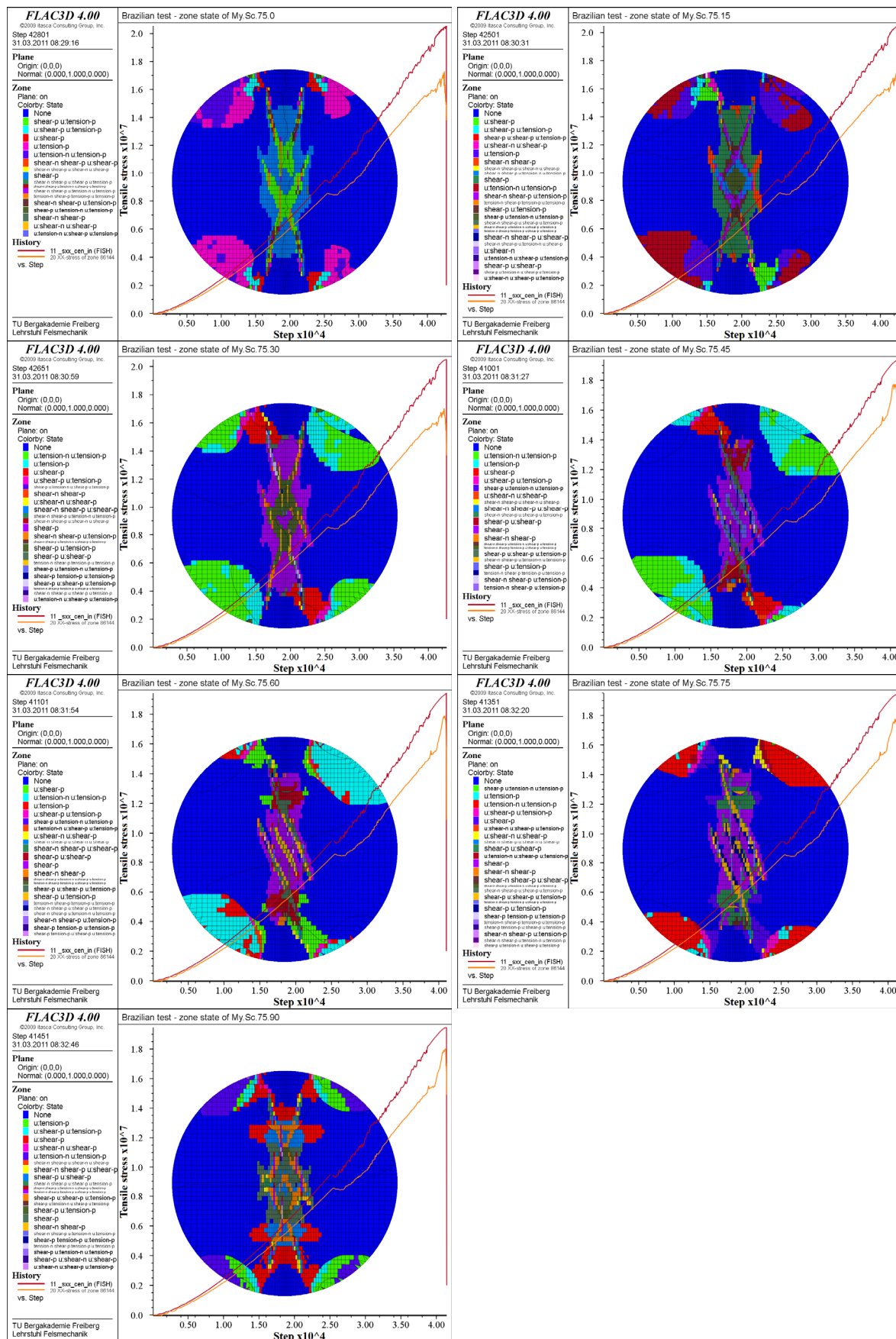
Figure A5.2-7: Failure zone state in My.Sc Slate where ψ = 75°

REFERENCES

1.   Carneiro, F., *Une novelle methode d'sssai pour determiner la resistance a la traction du beton.* Paris: Reunion des Laboratoires d' Essai de Materiaux, 1947.

2.   Goodman, R.E., *Rock Mechanics*. 2nd Edition ed. 1989: John Wiley & Sons.

3.   Amadei, B., *Importance of anisotropy when estimating and measuring in situ stresses in rock.* International Journal of Rock Mechanics and Mining Science & Geomechanics, 1996. 33(3): p. 293-325.

4.   Tang, C.A. and Hudson, J.A., *Rock Failure Mechanisms*. 2010: A.A Balkema.

5.   ISRM, *Suggested methods for determining tensile strength of rock materials*, in *International Journal of Rock Mechanics and Mining Sciences & Geomechanics*. 1978. p. 99-103.

6.   Itasca Consulting Group Inc., ed. *FLAC3D - **F**ast **L**agrangian **A**nalysis of **C**ontinua in **3** **D**imensions - User's Guide*. 2009: Minneapolis, USA.

7.   Mellor, M. and Hawkes, I., *Measurement of tensile strength by diametral compression of discs and annuli.* Engineering Geology, 1971. 5(3): p. 173-225.

8.   Ma, C.-C. and Hung, K.-M., *Exact full-field analysis of strain and displacement for circular disks subjected to partially distributed compressions.* International Journal of Mechanical Sciences, 2008. 50(2): p. 275-292.

9.   Markides, C.F., Pazis, D.N., and Kourkoulis, S.K., *Closed fullfield solutions for stresses and displacements.* International Journal of Rock Mechanics & Mining Sciences, 2010. 47: p. 227-237.

10.   ASTM, *ASTM D3967 – 08: Standard Test Method for Splitting Tensile Strength of Intact Rock Core Specimens*. 2008, ASTM international.

11.   BS EN, *BS EN 12390-6: Testing hardened concrete. Tensile splitting strength of test specimens*. 2009, British Standards.

12.   Deutschen Gesellschaft für Geotechnik, *lndirekter Zugversuch an Gesteinsproben - Spaltzugversuch*, in *Bautechnik, 8-b*. 2008, Ernst & Sohn Verlag. p. 623-627.

13.   Nova, R. and Zaninetti, A., *An investigation into the tensile behaviour of a schistose rock.* International Journal of Rock Mechanics and Mining Sciences & Geomechanics, 1990. 27(4): p. 231-242.

14.   Kourkoulis, S.K. *The problem of direct tension experiments in marble specimens.* in *Proceedings of the sixth international conference achievements in mechanical and materials Engineering* 1997. Miskolc, Hungary.

15.   Andreev, G.E., ed. *Brittle failure of rock materials*. 1995, A.A Balkema

16.   Akazawa, T., *Tension test method for concrete.* Int Assoc Test Res Labs Mater Struct, 1953. 16: p. 13-23.

17.   Berenbaum, R. and Brodie, I., *Measurement of the tensile strength of brittle materials.* British Journal of Applied Physics, 1958. 10: p. 281-286.

18.   Hondros, G., *The evaluation of poisson's ratio and the modulus of materials of a low tensile resistance by the Brazilian (indirect tensile) test with particular reference to concrete.* G. Aust. J. appl. Sci., 1959. 3: p. 243-268.

19.   Fairhurst, C., *On the validity of the 'Brazilian' test for brittle materials.* International Journal of Rock Mechanics and Mining Sciences & Geomechanics, 1964. 1(4): p. 535-546.

20.   Hobbs, D.W., *The tensile strength of rocks.* International Journal of Rock Mechanics and Mining Sciences & Geomechanics, 1964. 1(3): p. 385-388, IN17-IN18, 389-396.

21.   Hooper, J.A., *The failure of glass cylinders in diametral compression.* Journal of the Mechanics and Physics of Solids, 1971. 19(4): p. 179-188.

22.   Minh Phong, L., *Tensile and shear strengths of concrete and rock.* Engineering Fracture Mechanics, 1990. 35(1-3): p. 127-135.

23.   Newman, D.A. and Bennett, D.G., *Effect of specimen size and stress rate for the Brazilian test -- a statistical analysis.* International Journal of Rock Mechanics and Mining Sciences & Geomechanics, 1990. 27(6): p. 330-330.

24.   Tay, W.M. and Braden, M., *Load deformation behaviour during a diametral test.* Biomaterials, 1990. 11(5): p. 361-366.

25.   Andreev, G.E., *A review of the Brazilian test for rock tensile strength determination. Part I: calculation formula.* Mining Science and Technology, 1991. 13(3): p. 445-456.

26.   Andreev, G.E., *A review of the Brazilian test for rock tensile strength determination. Part II: contact conditions.* Mining Science and Technology, 1991. 13(3): p. 457-465.

27.   Corthésy, R., Gill, D.E., and Leite, M.H., *An integrated approach to rock stress measurement in anisotropic non-linear elastic rock.* International Journal of Rock Mechanics and Mining Sciences & Geomechanics, 1993. 30(4): p. 395-411.

28.   Guo, H., Aziz, N.I., and Schmidth, L.C., *Rock fracture-toughness determination by the Brazilian test.* International Journal of Rock Mechanics and Mining Sciences & Geomechanics, 1993. 30(5): p. 331-331.

29.   Cauwelaert, F.V. and Eckmann, B., *Indirect tensile test applied to anisotropic materials* Materials and Structures, 1994. Volume 27, Number 1 / January, 1994.

30.   Fahad, M.K., *Stresses and failure in the diametral compression test.* Journal of Materials Science, 1996. 31(14): p. 3723-3729.

31.   Lemmon, R.K. and Blackketter, D.M., *Stress analysis of an orthotropic material under diametral compression* Experimental Mechanics, 1996. 36(3): p. 204-211.

32.   Jyh Jong, L., Yang, M.-T., and Hsieh, H.-Y., *Direct tensile behavior of a transversely isotropic rock.* International Journal of Rock Mechanics and Mining Sciences, 1997. 34(5): p. 837-849.

33.   Chen, C.-S., Pan, E., and Amadei, B., *Fracture mechanics analysis of cracked discs of anisotropic rock using the boundary element method.* International Journal of Rock Mechanics and Mining Sciences, 1998. 35(2): p. 195-218.

34.   Rocco, C., et al., *Size effect and boundary conditions in the brazilian test: theoretical analysis* Materials and Structures, 1999. 32: p. 437-444.

35.   Wijk, G., *Some new theoritical aspects of indirect mesurements of the tensile strength of rocks.* Int. J. Rock Mech. Min. Sci. & Geomech, 1978. 15(4): p. 149-160.

36.   Sarris, E., et al. *Numerical Simulation of the Cracked Brazilian Disc under Diametral Compression* in *7th International Workshop on Bifurcation, Instabilities and Degradation in Geomechanics (IW BIDG 2005)*. 2005. Hania.

37.   Hung, K.-M. and Ma, C.-C., *Theoretical Analysis and Digital Photoelastic Measurement of Circular Disks Subjected to Partially Distributed Compressions* Experimental Mechanics, 2003. 43(2): p. 216-224.

38.   Zhu, W.C. and Tang, C.A., *Numerical simulation of Brazilian disk rock failure under static and dynamic loading.* International Journal of Rock Mechanics and Mining Sciences, 2006. 43(2): p. 236-252.

39.   Chen, S., Yue, Z.Q., and Tham, L.G., *Digital Image Based Approach for Three-Dimensional Mechanical Analysis of Heterogeneous Rocks.* Rock Mechanics and Rock Engineering, 2007. 40(2): p. 145-168.

40.   Lanaro, F., Sato, T., and Stephansson, O., *Microcrack modelling of Brazilian tensile tests with the boundary element method.* International Journal of Rock Mechanics and Mining Sciences, 2008. In Press, Corrected Proof.

41.   Wang, Q.Z., et al., *The flattened Brazilian disc specimen used for testing elastic modulus, tensile strength and fracture toughness of brittle rocks: analytical and numerical results.* International Journal of Rock Mechanics and Mining Sciences, 2004. 41(2): p. 245-253.

42.   Li, J. and Zhang, X.B., *A criterion study for non-singular stress concentrations in brittle or quasi-brittle materials.* Engineering Fracture Mechanics, 2006. 73(4): p. 505-523.

43.   Hakala, M., Kuula, H., and Hudson, J.A., *Estimating the transversely isotropic elastic intact rock properties for in situ stress measurement data reduction: A case study of the Olkiluoto mica gneiss, Finland.* International Journal of Rock Mechanics and Mining Sciences, 2007. 44(1): p. 14-46.

44.   Jonsén, P., Häggblad, H.Å., and Sommer, K., *Tensile strength and fracture energy of pressed metal powder by diametral compression test.* Powder Technology, 2007. 176(2-3): p. 148-155.

45.   Tang, C.A., et al., *A numerical study of the influence of heterogeneity on the strength characterization of rock under uniaxial tension.* Mechanics of Materials, 2007. 39(4): p. 326-339.

46.   Ke, C., Chen, C., and Tu, C., *Determination of fracture toughness of anisotropic rock by boundary element method.* Rock Mech. Rock Eng, 2008. 41(4): p. 509-538.

47.   Corthésy, R. and Leite, M.H., *A strain-softening numerical model of core discing and damage.* International Journal of Rock Mechanics and Mining Sciences, 2008. 45(3): p. 329-350.

48.   Vasconcelos, G., et al., *Experimental characterization of the tensile behaviour of granites.* International Journal of Rock Mechanics and Mining Sciences, 2008. 45(2): p. 268-277.

49.   Wang, T.-T. and Huang, T.-H., *A constitutive model for the deformation of a rock mass containing sets of ubiquitous joints.* International Journal of Rock Mechanics and Mining Sciences, 2009. 46(3): p. 521-530.

50.   Tavallali, A. and Vervoort, A., *Effect of layer orientation on the failure of layered sandstone under Brazilian test conditions.* International Journal of Rock Mechanics and Mining Sciences, 2010. 47(2): p. 313-322.

51.   Kwaśniewski, M. *Testing and modeling of the anisotropy of tensile strength of rocks*. in *Proceedings of the International Conference on Rock Joints and Jointed Rock Masses*. January 7-8, 2009. Tucson, Arizona, USA.

52.   Gonzaga, G.G., Leite, M.H., and Corthésy, R., *Determination of anisotropic deformability parameters from a single standard rock specimen*. International Journal of Rock Mechanics and Mining Sciences, 2008. 45(8): p. 1420-1438.

53.   Gao, Z., Zhao, J., and Yao, Y., *A generalized anisotropic failure criterion for geomaterials*. International Journal of Solids and Structures, 2010. 47(22-23): p. 3166-3185.

54.   Shahnazari, H., Dehnavi, Y., and Alavi, A.H., *Numerical modeling of stress-strain behavior of sand under cyclic loading*. Engineering Geology, 2010. 116(1-2): p. 53-72.

55.   Chen, C.-S., Pan, E., and Amadei, B., *Determination of deformability and tensile strength of anisotropic rock using Brazilian tests*. International Journal of Rock Mechanics and Mining Sciences, 1998. 35(1): p. 43-61.

56.   Cai, M. and Kaiser, P.K., *Numerical simulation of the Brazilian test and the tensile strength of anisotropic rocks and rocks with the pre-existing cracks*. SINOROCK2004 Symposium. Int. J. Rock Mech. Min. Sci., 2004. 41(3).

57.   Ljunggren, C., et al., *An overview of rock stress measurement methods*. International Journal of Rock Mechanics and Mining Sciences, 2003. 40(7-8): p. 975-989.

58.   Yu, Y. and Meng, C., *3-D distribution of tensile stress in rock specimens for the Brazilian test*. Journal of University of Science and Technology Beijing, 2005. 12(6): p. 495-507.

59.   Wright, P.J.F., *Comments on an Indirect Tensile Test on Concrete Cylinders*. Cement and Concrete Association, London, 1955. 7(20): p. 87-96.

60.   Hudson, J.A., Brown, E.T., and Rummel, F., *The controlled failure of rock discs and rings loaded in diametral compression*. Int. J. Rock Mech. Min. Sci. Geomech, 1972. 9: p. 8.

61.   Yu, Y., Yin, J., and Zhong, Z., *Shape effects in the Brazilian tensile strength test and a 3D FEM correction*. International Journal of Rock Mechanics and Mining Sciences, 2006. 43(4): p. 623-627.

62.   Markides, C., et al., *Marble Discs under Distributed Loading: Theoretical, Numerical and Experimental Study*. Fracture of Nano and Engineering Materials and Structures, 2006. 2(14): p. 413-414.

63.   Yu, Y., Zhang, J., and Zhang, J., *A modified Brazilian disk tension test*. International Journal of Rock Mechanics and Mining Sciences, 2009. 46(2): p. 421-425.

64.   Hoek, E. and Brown, E.T., *Practical estimates of rock mass strength*. Int. J Rock Mech. Min. Sci., 1997. 34(8): p. 1165-1186.

65.   Hoek, E., Carranza-Torres, C., and Corkum, B., *Hoek-Brown failure criterion - 2002 edition*. 2002.

66.   Nasseri, M.H.B. and Mohanty, B., *Fracture toughness anisotropy in granitic rocks*. International Journal of Rock Mechanics and Mining Sciences, 2008. 45(2): p. 167-193.

67.   Itasca Consulting Group Inc., ed. *PFC2D **P**raticle **F**low **C**ode in **2 D**imensions - User's guide*. 2008.

68.   Malan, D.F., Napier, J.A.L., and Watson, B.P., *Propagation of fractures from an interface in a Brazilian test specimen.* International Journal of Rock Mechanics and Mining Sciences & Geomechanics, 1994. 31(6): p. 581-596.

69.   Wang, Q.-Z. and Xing, L., *Determination of fracture toughness KIC by using the flattened Brazilian disk specimen for rocks.* Engineering Fracture Mechanics, 1999. 64(2): p. 193-201.

70.   Pan, E., Amadei, B., and Kim, Y.I., *2-D BEM analysis of anisotropic half-plane problems--application to rock mechanics.* International Journal of Rock Mechanics and Mining Sciences, 1998. 35(1): p. 69-74.

71.   Van de Steen, B., Vervoort, A., and Sahin, K., *Influence of internal structure of crinoidal limestone on fracture paths.* Engineering Geology, 2002. 67(1-2): p. 109-125.

72.   Frocht, M.M., ed. *Photoelasticity II.* 1948, Wiley: New York.

73.   Timoshenko, S. and Goodier, J.N., eds. *Theory of Elasticity.* 1951, Mcraw-Hill: New York - Toronto - London.

74.   Sokolnikoff, I.S., ed. *Mathematical theory of elasticity.* 1956, McGraw-Hill: Singapore.

75.   Muskhelishvili, N.I., ed. *Some basic problems of the mathematical theory of elasticity.* 1975, Noordhoff International Publishing: The Netherlands.

76.   Timoshenko, S.P. and Goodier, J.N., eds. *Theory of elasticity.* ed. 3rd. 1982, McGraw-Hill: Singapore.

77.   Poulos, H.G. and Davis, E.H., eds. *Elastic solutions for soil and rock mechanics.* 1991.

78.   Martin, H.S., ed. *Elasticity - Theory Applications and Numerics.* 2005, Elsevier Butterworth–Heinemann: Oxford - Paris - San Diego - San Francisco - Singapore - Sydney - Tokyo.

79.   ISO, *ISO 4108: Concrete - Determination of tensile splitting strength of test specimens.* 1980.

80.   Liu, C., *Elastic Constants Determination and Deformation Observation Using Brazilian Disk Geometry.* Experimental Mechanics, 2010. 50(7): p. 1025-1039.

81.   Jianhong, Y., Wu, F.Q., and Sun, J.Z., *Estimation of the tensile elastic modulus using Brazilian disc by applying diametrically opposed concentrated loads.* International Journal of Rock Mechanics and Mining Sciences, 2009. 46(3): p. 568-576.

82.   Jaeger, J.C., *Failure of rocks under tensile conditions.* International Journal of Rock Mechanics and Mining Science & Geomechanics, 1967. 4(2): p. 219-227.

83.   Colback, P.S.B. *An Analysis of Brittle Fracture Initiation and Propagation in the Brazilian test.* in *Proc. 1st Cong. Int. Soc. of Rock Mechanics.* 1967.

84.   Lekhnitskii, S.G., ed. *Theory of Elasticity of an Anisotropic Body.* 1981, Mir Publishes: Moscow.

85.   V.A.Lularda, ed. *ElastoPlasticity Theory.* 2002, CRC Press: Boca Raton - London - New York - Washington.

86.   Mindlin, R.D., *Force at a point in the interior of a semi-infinite solid.* Physics, 1936. 7: p. 195-202.

87.   Amadei, B., *In situ stress measurements in anisotropic rock.* International Journal of Rock Mechanics and Mining Science & Geomechanics, 1984. 21(6): p. 327-338.

88.   Davison, T., Wadley, H.N., and Pindera, M.J., *Elastic response of a layered cylinder subjected to diametral loading.* Composites Engineering, 1994. 4: p. 995-1009.

89.   Chen, C.S., Pan, E., and Amadei, B. *Evaluation of properties of anisotropic rocks using Brazilian tests.* in *Proc. 2nd NAMS, Montreal.* 1996.

90.   Amadei, B. and Jonsson, T. *Tensile strength of anisotropic rocks measured with the splitting tension test.* in *Proc. 12th Southeastern Conf. Theoret. Appl. Mech.,.* 1984.

91.   Barla, G. and Innaurato, N., *Indirect tensile testing of anisotropic rocks.* Rock Mech, 1973. 5: p. 215-230.

92.   Wittke, W., ed. *Rock Mechanics - Theory and applications with case histories.* 1990, Springer-Verlag: Berlin - Heidelberg - New York - London - Paris - Tokyo - Hong Kong - Barcelona.

93.   Amadei, B., Rogers, J.D., and Goodman, R.E. *Elastic constants and tensile strength of anisotropic rocks.* in *Proc. 5th ISRM Congr.* 1983. Melbourne.

94.   Claesson, J. and Bohloli, B., *Brazilian test: stress field and tensile strength of anisotropic rocks using an analytical solution.* International Journal of Rock Mechanics and Mining Sciences, 2002. 39(8): p. 991-1004.

95.   Exadaktylos, G.E. and Kaklis, K.N., *Applications of an explicit solution for the transversely isotropic circular disc compressed diametrically.* International Journal of Rock Mechanics and Mining Sciences, 2001. 38(2): p. 227-243.

96.   Hudson, J.A., *Tensile strength and the ring test.* International Journal of Rock Mechanics and Mining Sciences & Geomechanics, 1969. 6(1): p. 91-97.

97.   Itasca Consulting Group Inc., *FLAC3D - **F**ast **L**agrangian **A**nalysis of **C**ontinua in **3** **D**imensions - User's Guide.* 2009: Minneapolis, Minnesota 55401 USA.

98.   Itasca Consulting Group Inc., *FLAC3D - **F**ast **L**agrangian **A**nalysis of **C**ontinua in **3** **D**imensions - Theory and Background.* 2009: Minneapolis, Minnesota 55401 USA.

99.   Pittet, C. and J., L., *Mechanical Characterization of Brushite Cements: A MohrCircles' Approach.* Journal of Biomedical Materials Research, 2000. 53(6): p. 759-780.

100.   Hardy, H.R. and Jayaraman, N.I. *An investigation of methods for the determination of the tensile strength of rock.* in *Proc. 2nd Congr. Int. Soc. Rock Mech., Belgrade.* 1970.

101.   Alehossein, H. and Boland, J.N. *Strength, toughness, damage and fatigue of rock.* in *Structural Integrity and Fracture International Conference (SIF'04).* Sept. 26-29, 2004. Brisbane, Australia.